UNIVERSITÀ DEGLI STUDI DI MESSINA
DIPARTIMENTO DI SCIENZE CHIMICHE, BIOLOGICHE, FARMACEUTICHE ED AMBIENTALI
CORSO DI DOTTORATO IN SCIENZE CHIMICHE - XXXI CICLO
PROGETTAZIONE, SINTESI, ANALISI E PROPRIETÀ DI SISTEMI MOLECOLARI FUNZIONALI

Playing with light on molecular and hybrid nanomaterials

Emanuele La Mazza

Supervisor
Prof. Fausto Puntoriero

Coordinator
Prof. Sebastiano Campagna

2015-2018

TABLE OF CONTENTS

Chapter 4

Chapter 5

Chapter 6

Chapter 7

Introduction

"I remember in college, another guy and I had an idea. We wanted to find out what made the grass grow green. That sounds silly, but that's the biggest research problem in the world today and I'll tell you why. Because there's a tiny little engine in the green of this grass and in the green of the trees that has the mysterious gift of being able to take energy from the rays of the Sun and store it up. You see that's how the heat, and power, and coal, and oil, and wood is stored up. We thought that if we could find the secret of all those millions of little engines in this green stuff we can make big ones and then we can take power we can ever need right from the sunrays."

(J. Stewart in "You Can't Take It With You" by Frank Capra - 1938)

Watching this movie one can realise how huge is the importance of this particular problem. That someone 80 years ago in a movie explained the difficulty of using solar light for large-scale energy applications is amazing, as it is hard to believe how long we took (in a famous address presented before the VIII International Congress of Applied Chemistry, held in New York in 1912, G. Ciamician strongly suggested to replace "fossil solar energy" with the energy that the Earth receives from the Sun every day) to understand how photosynthesis works.

Combustion of fossil fuels is today the main source of energy useful for several sectors, such as industry, transportation, communication, welfare and so on.[1] However, despite the relatively abundance and ease of extraction, supplies of fossil fuels are not limitless.[1] They are *not* a long-term solution for a durable Earth energy supply; the average worldwide energy consumption in a year is 16.2 TW[2,3] and this value is doomed to rise. Moreover, another problem that is getting worse year by year is related to the pollution due to the combustion of such fuels: from combustion processes there derive an huge amount of CO_2 (causing the greenhouse effect) and several sub-products that are extremely toxic for the ecosystems. So, it will not be far

the age in which seeking alternative energy sources will not be just an alternative, but a dreadful reality to face.

One of the most promising alternative energy sources may derive by the photochemical conversion of solar energy. Sunlight is, in fact, a source of energy that is renewable, environmentally clean, inexpensive, available everywhere and abundant.[4,5] Earth receives an inconceivable power flow from the Sun: 120,000 TW per year of electromagnetic radiation of various wavelengths. So, the quantity of energy that continuously arrives from the Sun largely exceeds human needs.[5,6,7] Unluckily, light energy is intermittent and too diffuse to be optimally used as such, so it is necessary converting it in other types of energy: heat and electric energy might be valid choices, but the most convenient way is storing solar energy as chemical one; after all, this is what Nature does everyday, as well as the reason why all of us exist on this planet. Natural photosynthesis is, indeed, an efficacious example of such photochemical conversion process and mimicking it could grant us high-energy content chemicals (fuels) from low-energy content materials. A possible example is the photoinduced water splitting process.[8] This process leads to obtaining molecular oxygen and, above all, molecular hydrogen, which is considered the fuel of the future, thanks its several advantages: it has a high specific enthalpy value[9,10,11] and the combustion of its regenerates water, releasing energy, which leads to a sustainable cycle that is environmentally safe and generates no polluting subproducts.[8,11]

By learning the lesson from Nature, an artificial photosynthetic system should include: i) an antenna system, ii) a reaction centre, and iii) multielectron transfer catalysts.

The first step in this direction lies on catching solar light. A mechanism by which natural systems accomplish this task relies on the use of spatial constraints to assemble multiple pigments into highly organised light-harvesting antennae. Although, in these systems, the various pigment subunits are basically identical one another, the driving force for energy migration is generated by slightly differences on their excited-state energy, as a consequence of their position within the supramolecular structure and therefore of their environment. This is realised by using protein membranes as scaffolds that allow chlorophyll chromophores to convey excitation energy to suitable reaction centres, in an overall system able to damp

thermal losses and provide long-term stability.[12, 13, 14] In doing so, nature has evolved to combine the versatility of molecular systems with the organisation of nanomaterials.

The present thesis collects the principal results I obtained during the three-year Ph.D. course in Chemical Sciences, on systems able to collect light and elaborate the information transmitted by photons. The research work has been performed in the Laboratory of Photochemistry of the Department of Chemical, Biological, Pharmaceutical and Environmental Sciences at the University of Messina under the supervision of Prof. Fausto Puntoriero and partially in the Laboratory of Photochemistry of the School of Natural and Environmental Sciences at Newcastle University of Newcastle upon Tyne, UK, under the supervision of Prof. Fabio Cucinotta. The entire work of this thesis arises from the desire to develop light-harvesting antennas by using coordination compounds, organic dyes and host-guest hybrid system assembled on mesoporous silica nanomaterials. All the results are resumed as follow.

Outlines of the thesis

Chapter 1 contains basic information about *energy transfer* process, which is fundamental in photosynthetic systems.

Chapter 2 focuses on *dendrimers*, which, in virtue of their properties, are particularly suitable to be used as photoactive well-organised multicomponent molecular nanomaterial. It deals also with the photophysical properties of dendrimeric antenna systems based on Ru(II) and Os(II) polypyridine subunits, previously studied by photochemistry research group in Messina.

Chapter 3 describes *mesoporous silica nanoparticles* as host systems for molecules, in particular species that undergoes energy transfer processes.

Chapter 4 focuses on the synthesis and on the discussion of the photo- and electrochemical properties of a series of metal containing complexes and in particular of a heptanuclear dendrimer based on Ru(II) and Os(II) subunits on a new tris-chelating bridging ligand.

Chapter 5 and Chapter 6 deal with hybrid mesoporous silica nanomaterials as host-guest systems. The species used as guests are organic dyes (Chapter 5) and Ru(II) metal complex (Chapter 6). In Chapter 5 there are discussed the photophysical properties of two organic dyes once trapped, both separately and mixed, in silica nanoparticles (MCM-41 type). In Chapter 6 there are reported the preparation and the study of a hybrid antenna system trapped in two types of silica nanoparticles (MCM-41 and mesoporous silica spheres). The possibility of integrating other active species (iridium oxide nanoparticles in this case) to introduce new functionalities has been explored too.

It is evident that light has become one of the most powerful and extensively used tool not only in chemistry and material sciences but also in cell biology and related areas of the biomedical sciences, this because light allows for performing non-invasive measurements, extremely good precision, accuracy and modularity. So, in Chapter 7 I report on preliminary study of the efficiency of a dinuclear complex discussed in Chapter 4 to act as light switch for DNA. The ability of this compound to permeate the cellular membrane of erythrocytes, as well as the cellular internalisation behaviour of the hybrid materials discussed Chapter 7, have been preliminary discussed.

References

1) M. Hambourger, G. F. Moore, D.M. Kramer, D. Gust, A. L. Moore, T. A. Moore, *Chem. Soc. Rev.*, **2009**, 38, 25.

2) (a) Energy Information Association; U.S. Department of Energy; Washington DC; www.eia.doe.gov (accessed January 2010); (b) J. R. McKone, N. S. Lewis, H. G. Gray, *Chem. Mater.*, **2014**, 26, 407.

3) T. R. Cook, D. K. Dogutan, S. Y. Reece, Y. Surendranath, T. S. Teets, D. G. Nocera, *Chem. Rev.*, **2010**, 110, 6474.

4) (a) N. Armaroli, V. Balzani, *Angew. Chem., Int. Ed.*, **2007**, 46, 52; (b) M. H. V. Huynh, T. J. Meyer, *Chem. Rev.*, **2007**, 107, 5004; (c) J. P. McEvoy, G. W. Brudvig, *Chem. Rev.*, **2006**, 106, 4455; (d) M. Wasielewski, *Acc. Chem. Res.*, **2009**, 42, 1910; (e) D. Gust, T. A. Moore, A. L. Moore, *Acc. Chem. Res.*, **2009**, 42, 1890; (f) C. Herrero, A. Quaranta, W. Leibl, A. W. Rutherford, A. Aukauloo, *Energy Environ. Sci.*, **2001**, 4, 2353.

5) (a) N. Armaroli, V. Balzani, *Energy for a Sustainable World: From the Oil Age to a Sun-Powered Future, Wiley-VCH*, Weinheim, **2011**; (b) N. Armaroli, V. Balzani, N. Serpone, *Powering Planet Earth, Wiley-VCH*, Weinheim, **2013**.

6) (a) A. J. Bard, M. A. Fox, *Acc. Chem. Res.*, **1995**, 28, 141; (b) N. S. Lewis, D. G. Nocera, *Proc. Natl. Acad. Sci. USA*, **2006**, 103, 15729; (c) H. B. Gray, *Nature Chem.*, **2009**, 1, 7.

7) B. D. Sherman, M.D. Vaughn, J. J. Bergkamp, D. Gust, A. L. Moore, T. A. Moore, *Photosynth. Res.*, **2014**, 120, 59.

8) (a) T. J. Meyer, *Nature*, **2008**, 451, 778; (b) F. Liu, J. J. Conception, J. W. Jurss, T. Cardolaccia, J. L. Templeton, T. J. Meyer, *Inorg. Chem.*, **2008**, 47, 1727; (c) J. W. Jurss, J. C. Concepcion, M. R. Norris, J. L. Templeton, T. J. Meyer, *Inorg. Chem.*, **2010**, 49, 3980; (d) S. Y. Reece, J. A. Hamel, K. Sung, T. D. Jarvi, A. J. Esswein, J. J. H. Pijpers, D. G. Nocera, *Science*, **2011**, 334, 645; (e) L. Kohler, N. Kaveevivitchai, R. Zong, R. P. Thummel, *Inorg. Chem.*, **2014**, 53, 912.

9) (a) S. M. Arachchige, K. J. Brewer, *R. Crabtree (Ed.), Energy Production and Storage; Inorganic Chemical Strategies for a Warming World, John Wiley & Sons*, Chichester, West Sussex, UK, **2010**, 143-171; (b) T. S. Teets, D. G. Nocera, *Chem. Commun.*, **2011**, 47, 9268.

10) (a) F. Wang, W. G. Wang, H. Y. Wang, G. Si, C. H. Tung, L. Z. Wu, *ACS Catal.*, **2012**, 2, 407; (b) *The Hydrogen Economy: Opportunities, Costs, Barriers, and R&D Needs*, U.S. National Research Council and U.S. National Academy of Engineering, **2004**.

11) D. Gust, T. A. Moore, A. L. Moore, *Faraday Discuss.*, **2012**, 155, 9.

12) J. Deisenhofer, O. Epp, K. Miki, R. Huber, H. Michel, *Nature* **1985**, 318, 618-624.

13) W. Kuhlbrandt, N. W. Da, F. Yoshinori, *Nature* **1994**, 367, 614-621

14) G. D. Scholes, G. R. Fleming, A. Olaya-Castro, R. van Grondelle, *Nat. Chem.,* **2011**, 3, 763-774.

Chapter 1

Photoinduced Energy Transfer: a Brief Description

Photoinduced energy transfer plays a key role in both natural and artificial systems. Examples are natural photosynthesis as well as synthetic assemblies for solar energy conversion and information technologies.

Generally speaking, when electronic excitation energy absorbed by a chromophore D (donor) is transferred to a chemically different chromophore A (acceptor) a photoinduced energy transfer process takes place, according to:

$$D^* + A \rightarrow D + A^*$$

In this case the process is called heterotransfer. This process is possible provided that the donor emission spectrum partially overlaps the acceptor absorption spectrum.

If donor and acceptor are identical, it is called homotransfer:

$$D^* + D \rightarrow D + D^*$$

When the process can repeat itself so that the energy migrates over several molecules, it is called *energy migration*.

It is important to distinguish between radiative and non-radiative transfer, in fact they have different effects on the characteristics of fluorescence emission from the donor, which allows us to make a distinction between these two types of transfer. Moreover, the factors governing the efficiency of radiative and non-radiative transfers are not the same (apart from the spectral overlap, which is required for both processes).

Radiative transfer is a two-step process by which D* emits a photon that is resorbed by A and is observed when the average distance between D and A (or D) is larger than the excitation wavelength:

1) $D^* \rightarrow D + h\nu$

2) $h\nu + A \rightarrow A^*$ or $h\nu + D \rightarrow D^*$

Such a transfer is also called *trivial energy transfer*, does not require any

interaction between the partners and is not dependent on the distance between them, while depends on the concentration of A, the optical path length of emitted photons across the sample and the spectral overlap. This process does not affect the lifetime of the D* excited state, but can lead to distortions of the emission spectrum from D*.

This process is often called *trivial transfer* because of the simplicity of the phenomenon, but in reality the quantitative description is quite complicated because it depends on the size of the sample and its configuration with respect to excitation and observation.

Radiative transfer results in a decrease of the donor fluorescence intensity in the region of spectral overlap. Such a distortion of the fluorescence spectrum is called the inner filter effect.

Non-radiative transfer of excitation energy occurs without any emission of photons at distances less than the wavelength and result from shot- or long-range interactions between molecules. Consequently, such a transfer provides a tool for determining distances of a few tens of ångströms between chromophores. The transfer of excitation energy plays a major role in photosynthetic systems.

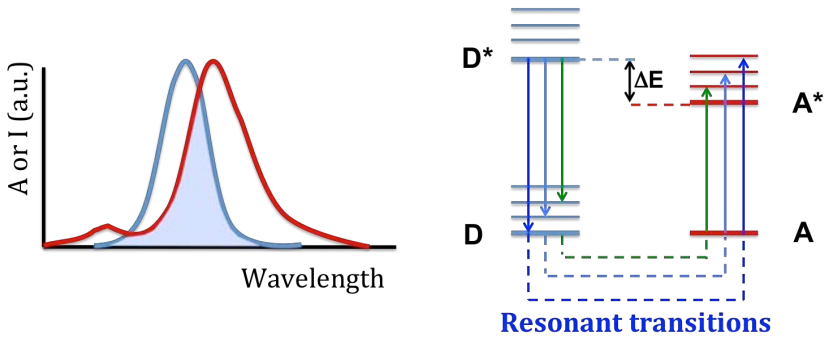

Figure 1.2 *(Left): illustration of the integral overlap between the emission spectrum (blue) of the donor and the absorption spectrum (red) of the acceptor. (Right): energy level scheme of donor and acceptor molecules showing the coupled transitions.*

Non-radiative transfer process requires some interaction between a donor molecule and an acceptor molecule, and it can occur if the emission spectrum of the donor overlaps the absorption spectrum of the acceptor, so that several vibronic transitions in the donor have practically the same energy as the corresponding

transitions in the acceptor. Such transitions are coupled (see **Figure 1.2**), *i.e.* are in resonance.

From the spectroscopic viewpoint both for molecular and supramolecular systems the transfer can be dealt with as an isoenergetic non-radiative deactivation between two ''localised'' electronically excited states:

D*–L–A ⟶ D–L–A*

The rate constant can be obtained by an appropriate Fermi golden rule expression (**Equation 1.1**):

$$k_{en} = \frac{2\pi}{\hbar}\left\langle \Psi_{D^*\cdot A} \mid \hat{H}^{en} \mid \Psi_{D\cdot A^*} \right\rangle^2 FC^{en} \qquad \text{(eq. 1.1)}$$

where $\hat{H}^{en}$ is the electronic coupling operator between the two excited states interconverted by the energy-transfer process and FC^{en} is an appropriate Franck–Condon factor.

The Franck–Condon factor can be cast either in classical[1] or quantum mechanical[2] terms. Classically, it accounts for the combined effects of energy gradient and nuclear reorganisation on the rate constant. In quantum mechanical terms, the FC factor is a thermally averaged sum of vibrational overlap integrals (**Equation 1.2**):

$$FC^{en} = \sum_{m,n}\left\langle \theta^0_{D^*}\theta^0_A \mid \theta^m_D\theta^n_{A^*} \right\rangle^2 = \sum_{m,n}\left\langle \theta^0_{D^*}\theta^m_D \mid \theta^0_A\theta^n_{A^*} \right\rangle^2 \qquad \text{(eq. 1.2)}$$

Experimental information on this term can be obtained from the overlap integral between the emission spectrum of the donor and the absorption spectrum of the acceptor: FC^{en} is negligible if D* lies at lower energy than A* (**Figure 1.3a**), quite small if the two excited states are isoenergetic (**Figure 1.3b**) and large if D* is higher than A* in energy (**Figure 1.3c**).

As shown in **Figure 1.3**, energy transfer is an isoenergetic process that takes place after vibrational relaxation. This is usually the case for radiationless transitions. As a consequence, it is a unidirectional process, unless the two excited states are practically isoenergetic.

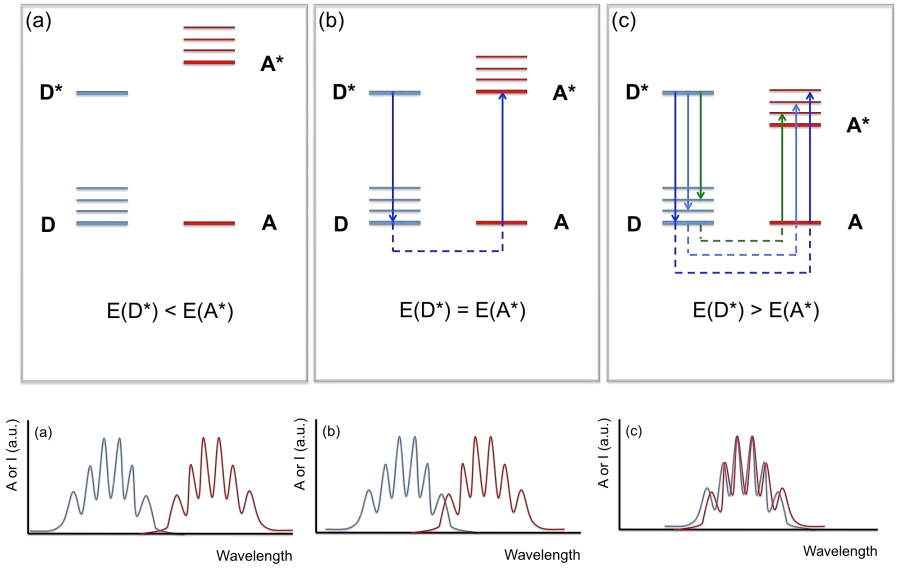

Figure 1.3 *Schematic energy levels (top) and spectral overlap (bottom) between emission of the donor D (blue line) and absorption of the acceptor A (red line) for three different cases: (a) E(D*)>E(A*); (b) E(D*)=E(A*); (c) E(D*)>E(A*).*

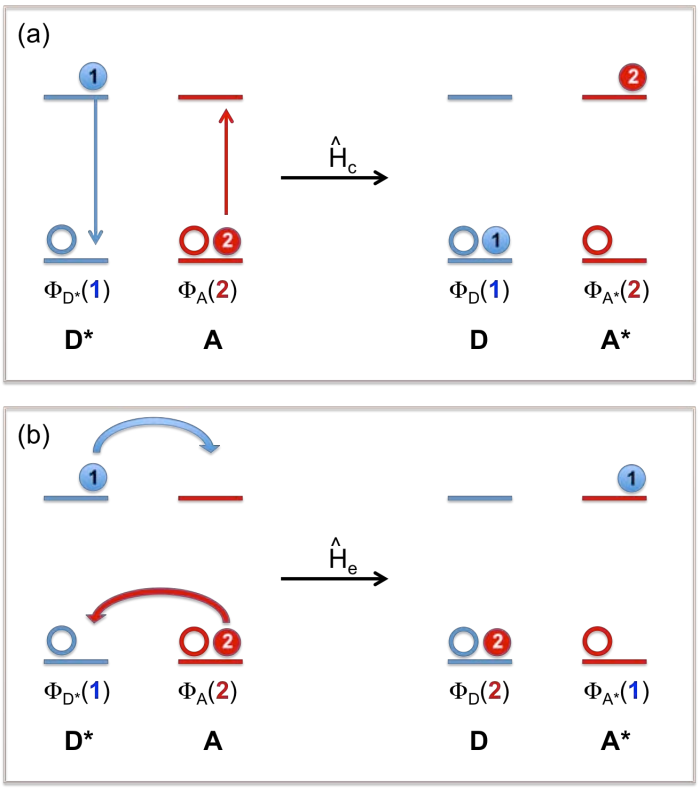

Figure 1.4 *Pictorial representations of the coulombic (a) and exchange (b) energy transfer mechanism.*

The electronic operator $\hat{H}^{en}$ involves the HOMO (highest occupied molecular orbital) and LUMO (lowest unoccupied molecular orbital) of the energy-donor and energy-acceptor components. Non-radiative energy transfer can result from different mechanisms: the interactions may be coulombic and/or due to intermolecular orbital overlap. Hence, $\hat{H}^{en}$ can be split in two additive terms, a *coulombic* term ($\hat{H}_C$) and an *exchange* term ($\hat{H}_E$) (**Figure 1.4**). The two terms depend differently on the parameters of the system (spin of ground and excited states, door-acceptor distance, etc.). Each can become predominant depending on the specific system and experimental conditions.

1.1 *Coulombic mechanism*

The coulombic mechanism (also called resonance, Förster resonance energy transfer (FRET))[3,4], is a long-range mechanism that does not require physical contact between donor and acceptor. It can be shown that the most important term, within the coulombic interaction, is the dipole–dipole term, which obeys the same selection rules as the corresponding electric dipole transitions of the two partners (D*→D and A→A*, **Figure 1.4a**). Coulombic energy transfer is therefore expected to be efficient in systems in which the radiative transitions connecting the ground and the excited state of each partner have high oscillator strength and in which each partner does not change its spin multiplicity. The rate constant for the dipole–dipole coulombic energy transfer is proportional to $\left\langle \Psi_{D^*\cdot A} \mid \hat{H}^{en} \mid \Psi_{D\cdot A^*} \right\rangle^2$; as the interaction between two point dipoles falls off with the third power of the distance, the rate constant falls off with the sixth power of the distance r_{AB} between the two partners. The rate constant can be expressed as a function of the spectroscopic and photophysical properties of the two molecular components (**Equation 1.3**):

$$k_{en}^{F} = 8.8\cdot 10^{-25} \frac{K^2 \Phi}{n^4 r_{AB}^6 \tau} J_F \qquad \text{(eq. 1.3)}$$

where K is an orientation factor which accounts for the directional nature of the dipole-dipole interaction (from statistics considerations, assumed as 0.66), Φ and τ

are the luminescence quantum yield and lifetime of the donor, respectively, n is the solvent refractive index, r_{AB} is the distance between donor and acceptor. The spectral overlap J_F is given by **Equation 1.4**:

$$J_F = \frac{\int F(\bar{\nu})\varepsilon(\bar{\nu}) / \bar{\nu}^4 \, d\nu}{\int F(\bar{\nu}) d\nu} \qquad \text{(eq. 1.4)}$$

where $F(\bar{\nu})$ is the luminescence spectrum of the donor and $\varepsilon(\bar{\nu})$ is the absorption spectrum of the acceptor on an energy scale (cm^{-1}). Note that the rate constant (in s^{-1}) is a first-order rate constant, representing the energy transfer between D* and A held at a fixed distance and relative orientation.

The overlap integral can be expressed in terms of wavelength, in which case appropriate proportionally constant should be considered that match those of **Equation 1.4**:

$$J_F = \frac{\int F(\lambda)\varepsilon(\lambda) / \lambda^4 \, d\lambda}{\int F(\lambda) d\lambda} \qquad \text{(eq. 1.5)}$$

The rate constant k^F_{en} can also be expressed in terms of **Equation 1.6**:

$$k_{en}^F = \frac{R_0^6}{r_{AB}^6 \tau} \qquad \text{(eq. 1.6)}$$

where τ is the lifetime of the donor in the absence of the acceptor and R_0, named *critical transfer distance*, is the distance in which energy transfer has 50% efficiency (half of D* decays by intrinsic paths and half energy transfer to A). Förster energy transfer is thus widely applied in determining the distance between D and A markers attached to biopolymers.[5]

With good spectral overlap integral and appropriate photophysical properties, the $1/r^6_{AB}$ distance dependence enables energy transfer to occur efficiently over distances substantially exceeding the molecular diameters. The typical example of an efficient coulombic mechanism is that of singlet–singlet energy transfer between large aromatic molecules, a process used by nature in the antenna systems of the

photosynthetic apparatus.[6] On the basis of spin considerations, the process here illustrated is doubly forbidden by the coulombic mechanism:

$$D^*(T_1) + A(S_0) \rightarrow D(S_0) + A^*(T_1)$$

However, if D exhibits a high phosphorescence quantum yield and good overlap with the singlet absorption of A, coulombic energy transfer can occur, thanks to the long lifetime of the donor species.

As this energy transfer mechanism does not require close contact between D* and A, the rate constant can exceed the rate constant of diffusion and Stern-Volmer plots deviate from linearity.

In the case of an energy migration process (A=D), it does not bring about any change in lifetime of D* or in its emission intensity, but does yield depolarisation of fluorescence.

1.2 *Exchange mechanism*

The rate constant for the exchange (also called *Dexter-type*)[7] mechanism can be expressed by **Equation 1.7**:

$$k_{en}^{D} = \frac{2\pi}{\hbar}\left\langle \Psi_{D^*\cdot A} \mid \hat{H}^{en} \mid \Psi_{D\cdot A^*} \right\rangle^2 J_D \qquad \text{(eq. 1.7)}$$

where the electronic term $\hat{H}^{en}$ is obtained from the electronic coupling between donor and acceptor, and is exponentially dependent on distance.

$$\left\langle \Psi_{D^*\cdot A} \mid \hat{H}^{en} \mid \Psi_{D\cdot A^*} \right\rangle^2 = H^{en} = H^{en}(0)\exp\left[-\frac{\beta^{en}}{2}(r_{AB} - r_0)\right] \qquad \text{(eq. 1.8)}$$

the nuclear factor J_D is the Dexter overlap integral between the emission spectrum of the donor and the absorption spectrum of the acceptor (**Equation 1.9**):

$$J_D = \frac{\int F(\bar{\nu})\varepsilon(\bar{\nu})\, d\bar{\nu}}{\int F(\bar{\nu})\, d\bar{\nu} \int \varepsilon(\bar{\nu})\, d\bar{\nu}} \qquad \text{(eq. 1.9)}$$

It is worth noting that J_D is different from J_F (**Equation 1.5**) because the normalisation is done not only on the emission spectrum of the donor but also on the absorption spectrum of the acceptor, so that J_D is independent of the oscillator strengths of both partners.

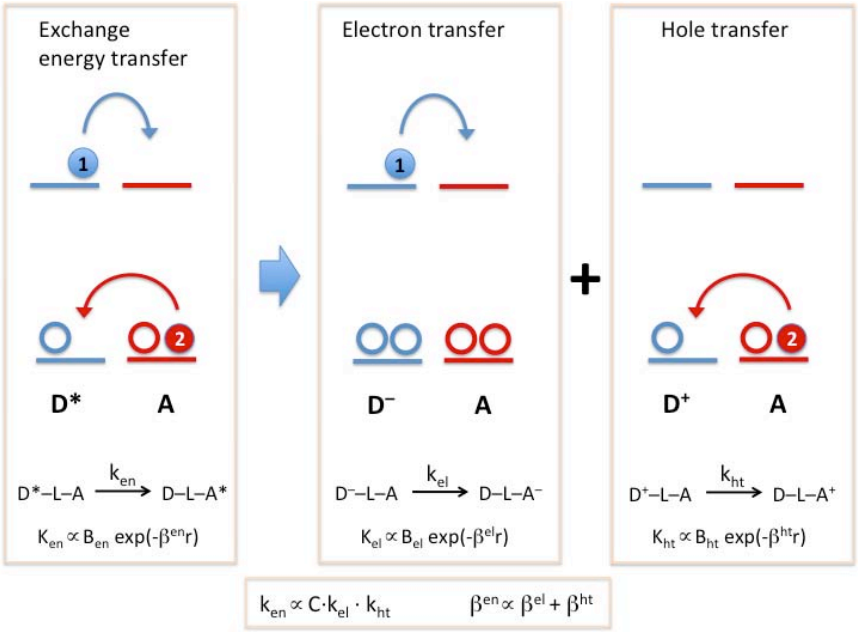

Figure 1.5 *Exchange energy transfer can be represented as an electron and a hole transfer. The relationship between the rate constants and the attenuation factors of the three processes are also shown.*

The exchange interaction (**Figure 1.4b**) can best regarded as a double electron transfer process, one electron is moving from the LUMO of the excited donor to the LUMO of the acceptor, and the other from the acceptor HOMO to the donor HOMO. This important insight is illustrated in **Figure 1.5**, from which it is clear that the attenuation factor β^{en} for the exchange energy transfer should be approximately equal to the sum of the attenuation factors for two separated electron transfer processes, that is β^{el} for electron transfer between the LUMO of the donor and acceptor, and β^{ht} for the electron transfer between the HOMOs (superscript *ht* denotes hole transfer from the donor to the acceptor).[8]

The spin selection rules for this type of mechanism arise from the need to obey spin conservation in the reacting pair as a whole, Wigner's rule.[9] This enables the

exchange mechanism to be operative in many instances in which the excited states involved are spin-forbidden in the usual spectroscopic sense. Thus, the typical example of an efficient exchange mechanism is that of triplet-triplet energy transfer:

$$D^*(T_1) + A(S_0) \rightarrow D(S_0) + A^*(T_1)$$

This sensitisation process is often used to selectively populate triplet states of molecules that do not undergo efficient intersystem crossing following direct excitation: it can be useful for a variety of purposes, including energy upconversion, preparative photochemistry and elucidation of photoreaction mechanisms.

Although the exchange mechanism was originally formulated in terms of direct overlap between donor and acceptor orbitals, it can be extended to coupling mediated by the intervening medium (*i.e.*, a connecting bridge).[10]

To summarise, the most important differences between the two non-radiative mechanisms are:

1. Range: coulombic mechanism is a dipole-dipole long-range mechanism (in favourable conditions, efficient over 5 nm); exchange mechanism is a short-range (collisional) mechanism (less than 1 nm) and has an exponential dependence on distance as orbital overlap is required.
2. Media: coulombic mechanism is efficient in rigid media (sphere-of-action kinetics); exchange mechanism is blocked in rigid media when D and A are two species dissolved in diluted solutions.
3. Oscillator strength: coulombic mechanism is fast when both donor and acceptor have large oscillator strength; exchange-mechanism rate is independent from oscillator strength.
4. Stern–Volmer behaviour: coulombic mechanism in fluid solutions shows non-Stern–Volmer kinetics; exchange mechanism in fluid solutions shows Stern–Volmer behaviour.
5. Treatment: for coulombic mechanism it is applied the Förster equation for calculating energy transfer rate constants from experimental data on D and A molecules; for exchange mechanism the Marcus-type treatment is applied.

Moreover, both coulombic and exchange mechanism follow the following rules,

based on energetic considerations:

1. Very endothermic energy transfer processes are in general inefficient (even if spin-allowed) because there is no overlap between donor emission spectrum and acceptor absorption one.
2. Exothermic spin-allowed energy transfer processes are generally efficient.
3. There is no general rule for exothermic spin-forbidden energy transfer processes.

References

1) V. Balzani, F. Bolletta, F. Scandola, *J. Am. Chem. Soc.*, **1980**, 102, 2152–2163.

2) G. Orlandi, S. Monti, F. Barigelletti, V. Balzani, *Chem. Phys.*, **1980**, 52, 313–319.

3) T. Förster, 10th spiers memorial lecture. Transfer mechanisms of electronic excitation, *Discuss. Faraday Soc.*, **1959**, 27, 7–17.

4) F. Barigelletti, L. Flamigni,, *Chem. Soc. Rev.*, **2000**, 29, 1–12.

5) J. R. Lakowicz, *Principle of Fluorescence Spectroscopy, 3rd edn, Springer*, New York, **2006**.

6) T Pullerits, V. Sundström, *Acc. Chem. Res 29*, **1996**, 381 and references therein.,

7) D. L. Dexter, *J. Chem. Phys.*, **1953**, 21, 836–850.

8) G. L. Closs, M. D. Johnson, J. R. Miller, P. Piotrowiak, *J. Am. Chem. Soc.*, **1989**, 111, 3751–3753.

9) P. Klán, J. Wirz, *Photochemistry of Organic Compounds: From Concepts to Practice, John Wiley & Sons, Ltd*, Chichester, **2009**

10) P. Piotrowiak*, Relationship between electron and electronic excitation transfer, in Electron Transfer in Chemistry (ed. V. Balzani), Wiley-VCH Verlag GmbH*, Weinheim, **2001**, 215–237.

Chapter 2

Artificial Light Harvesting and Dendrimer as Antenna Systems

Introduction

Several photosynthetic organisms exist that perform the photosynthetic process and all of them use the same strategy. The photosynthetic machinery uses three components to drive solar fuel production: (i) the antenna system, (ii) the reaction centre, and (iii) systems for the multielectronic catalysis. They work is sequence, as following: firstly sunlight is absorbed by the antenna systems, which are collections of chromophores that absorb a large range of solar light spectrum. Then, they transfer excitation energy among one another via Föster singlet-singlet energy transfer, and finally to the next component:[1] the reaction centre protein. Here, the energy received is used for a charge separation process. The so-formed charges are used to obtain the products of the photosynthesis (organic compounds, biomass, fossil fuels, and so on) by multielectronic catalysis. The burning of such products with oxygen by combustion forms the original compounds (water and carbon dioxide) and releases the energy originated from sunlight.[2]

As explicative example to understand the mechanisms behind the photosynthetic components, deep investigations have been carried out on the Rhodopseudomonas acidophila. Herein, the antenna apparatus is composed by two systems: LH2 and LH1. The first one consists of two organised sets of bacteriochlorophylls, absorbing each at 800 nm and at 850 nm.[3] Sunlight absorbed by the higher-energy absorbing set (800 nm) is transferred to the lower-energy absorbing set of chlorophylls (850 nm). The energy is then transferred to LH1, which is larger than LH2 and it is composed by 32 bacteriochlorophylls, even if the structure of the system is not well known. LH1 absorbs at 880 nm and the short distance (30 Å) between the two systems allows a fast energy transfer (3 ps) from LH2 to LH1. In the antenna systems (in particular in LH2), auxiliary chromophores (like carotenoids, phycoerythrins, and phycocyanins) are employed to absorb light in regions where chlorophyll does not absorb, and then they transfer the energy to chlorophylls. Antenna systems are also involved in photoregulation and photoprotection of the photosynthetic apparatus.[1]

From LH1, energy transfer occurs in 35 ps to the reaction centre, which is located

inside the LH1 system. Then, a photoinduced electron transfer process yields to the formation of a charge separated species, whose charges are captured by the multielectronic catalysts.

Among the others, the photosynthetic mechanisms occurring in the plants appear the most attractive to study and to mimic. In the plants, absorption of light by photosynthetic pigments is followed by a series of energy transfers and charge separation processes which lead to the oxidation of water to molecular oxygen, while the reducing equivalents are used for the reduction of CO_2 into carbohydrates.

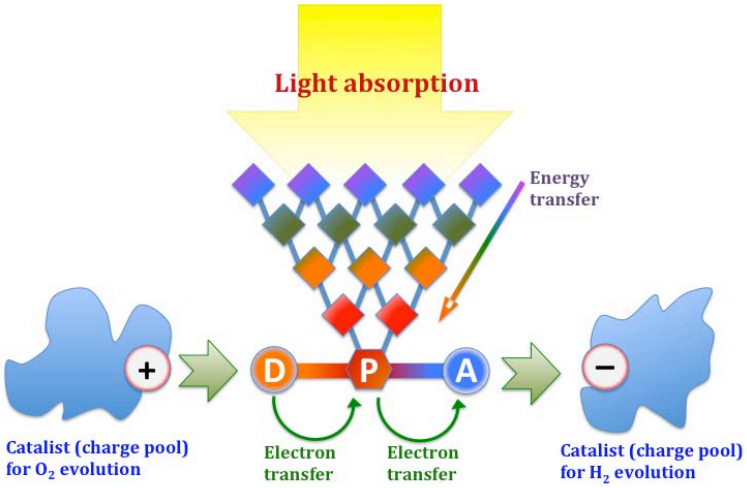

Figure 2.1 *Schematic representation of an artificial photosynthetic device.*

To perform an artificial photosynthesis many structurally-organised and functionally-integrated components, inspired by natural photosynthetic systems, are needed (schematised in **Figure 2.1**): (i) the antenna system, an assembly of chromophores which has the function of collecting light energy and conveying it by a series of elementary energy transfer steps to a specific subunit;[4,5,6] (ii) the charge-separation component, which essentially should transform electronic energy into chemical (redox) energy; (iii) multi-electron storage systems, which have to collect more than one electron (or hole) in reversible ways, also in successive steps, and deliver all the collected electrons (or holes) to suitable substrates in a single shot (most of the species which are potentially used to store chemical energy in usable forms need multi-electron processes – this is the case for water splitting or carbon dioxide reduction, for example). It could be noted that each component of this

artificial photosynthetic device is itself a multicomponent system, so a hierarchical supramolecular organisation is required.[7]

Despite the complexity of this kind of system, the outstanding developments in supramolecular chemistry[8,9] and ultrafast spectroscopy[10] in the last decades granted us a better knowledge to design multicomponent systems. A rational way to design efficient artificial photosynthetic systems is studying the various components separately. Since an optimal antenna system needs a lot of chromophores, a good way to achieve this is using dendrimers;[11,12] in fact, because their structure, they can concentrate a lot of chromophores in a limited space by few synthetic steps. Moreover, choosing between divergent and convergent synthetic strategy allows tuning the system energy gradient. In the research group where I have worked it has been studied dendritic antenna systems based on Ru(II) and Os(II) polypyridine subunits, also in collaboration with research groups in Bologna and Pisa[13,14,15].

2.1 Dendrimers

Dendrimers[16,17] are well-defined macromolecules exhibiting a tree-like structure which can be built via an iterative sequence of reaction steps. In a dendrimer it is possible recognise a core and one or more layers of concentric shells containing several repetitive subunits and the number of layers defines the generation of the dendrimer (**Figure 2.2**).

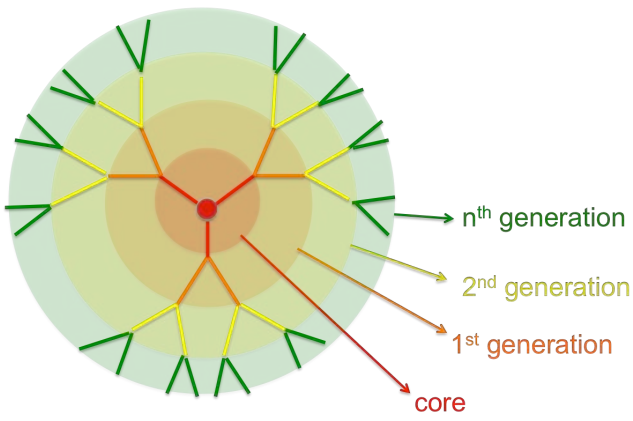

Figure 2.2 *Schematic representation of a generic dendrimer.*

The interest on dendrimer chemistry has evolved from the simple construction of these intriguing molecules to their characterisation, and finally toward their functionalisation, in view of potential applications in many different fields, such as chemistry, physics, engineering, biology and medicine. Both organic and inorganic units have been introduced in each of the topologically different positions available within the dendrimer structure, *i.e.* in the core, in the branches, and on the surface. Multiple functionalisations have also been achieved by placing two or more different active units in distinct regions of the same dendrimer. Furthermore, host–guest chemistry can be used to incorporate functional species in the cavities present in the dendrimer's interior. The interaction of different components, modulated by the dendritic structure, may give rise to a molecular-level device,[18,19] that is an assembly of a discrete number of molecular components designed to achieve a complex function, resulting from the cooperation of the various units.

Molecular level devices, like macroscopic devices, need energy to operate and signals to communicate with the operator. Photons and electrons constitute the most viable answer to this dual requirement. Light is indeed used by Nature, where photons are used as energy in the devices involved in the photosynthetic processes and as signals by the devices involved in vision-related processes. Electrical energy is another simple way to induce molecular-level functions, and electrochemistry is a very useful means to monitor the occurrence of such functions. For all these reasons, it is appealing to design and construct dendrimers containing photo- and redox-active units, which could thus play the role of molecular-level photonic and electronic devices.

It is worth emphasising that the photochemical and photophysical properties of dendrimers are particularly interesting since (i) cooperation among the photoactive components can allow the dendrimer to perform useful functions such as light harvesting and frequency converting, (ii) changes in the photophysical properties can be exploited for sensing purposes with signal amplification, and (iii) the presence of luminescence signals can offer a valuable handle to better understand the dendritic structure and superstructure. On the other hand, the electrochemical properties of dendrimers are interesting since (iv) redox active units present at the core of a dendrimer can be "encapsulated" by the surrounding branches, thus modulating the

electron transfer rate, (v) the presence of multiple equivalent, non-interacting units gives rise to the simultaneous exchange of a large and predetermined number of electrons, and (vi) electroactive units of the same or different types can be placed in topologically equivalent or non-equivalent sites of a dendrimer to obtain specific redox patterns. Many new valuable functions can be obtained by introducing photo- and redox-active units in appropriate sites of the dendritic structure. As a consequence, new are foreseen in several different fields, ranging from biology and medicine (tissue engineering, diagnostics, artificial proteins, drug-delivery systems) to nano-engineering (photoresponsive molecules, light-emitting diodes, electrochemical sensors, molecular batteries), data processing (information storage, fiber optics), catalysis (multielectron transfer and asymmetric catalysis), and energy harvesting devices, mimics of the natural photosynthetic system.

Photoactive units (metal-based subunits) can be directly incorporated or appended with covalent or coordination bonds in different regions of a dendritic structure. From a topological point of view, metal-based dendrimers may be classified in four groups:

1. Dendrimers with a metal subunit as core: these compounds can be treated as metal complexes whose ligands have dendritic substituents. Most common metal complexes used as core are porphyrin and polypyridine complexes and ferrocene compounds.
2. Dendrimers with peripheral metal subunits: these dendrimers are functionalised on the surface.[20]
3. Dendrimers with metal subunits among branches: in these dendrimers the metal subunits are the connectors of the dendritic structure, or can be attached to specific sites.[21]
4. Dendrimers where metals occupy every branches site: in these dendrimers the ligands in the structure can coordinate two or more metal centres. Besides ion metals and bridging ligands, they contain terminal ligands.[22]

There are also metal-based dendrimers that can be part of more of a single group. The kinds of dendrimer structures are schematised in **Figure 2.3**.

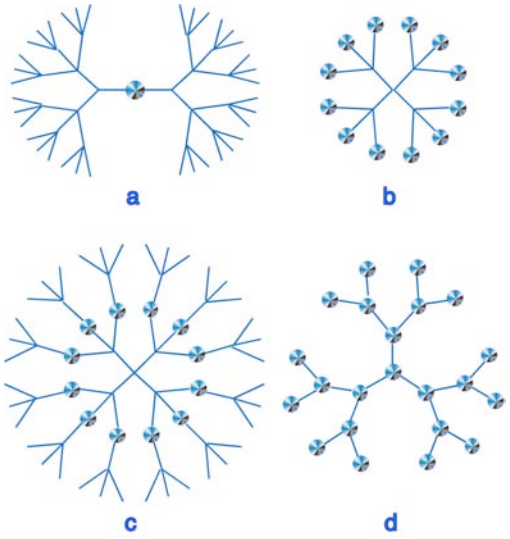

Figure 2.3 *Schematic representations of the different typologies of metal-based dendrimers. Circles represent generic metal subunits.*

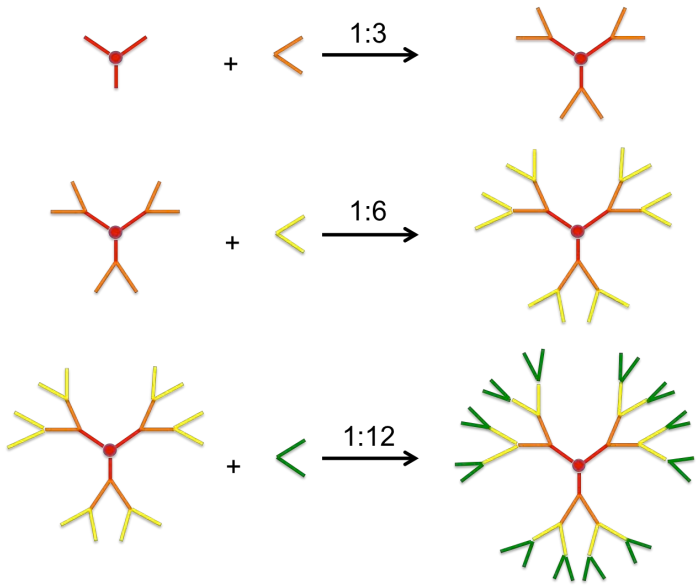

Figure 2.4 *Schematic representation of a divergent methodology.*

Synthetic methodologies to obtain dendrimers consist usually in a divergent or convergent approach.

In a *divergent* approach the dendrimer is synthesised starting from the core and proceeding towards the periphery adding the repetitive subunits. More specifically, the core at first reacts with suitable building blocks to form a first generation

dendrimer. If the peripheral subunits have free or reactive sites, the dendrimer can further react. This process can be iterated and at each growing step a new layer of branching units is added, thus increasing by one the generation number (**Figure 2.4**).

A significant characteristic of the divergent approach is the rapid increasing of peripheral reactive site number; such thing can lead to possible issues about growing process: any incomplete reaction centred on a terminal subunit may lead to imperfections and failures for successive steps. Moreover, it is necessary using a great amount of reagents, getting purification harder.

In a *convergent* method, on the contrary, the synthesis starts at the periphery and proceeds towards the core. A small dendron is initially formed by connecting two peripheral groups to a branching unit. Then, two of these dendrons can again be connected to a branching unit to generate a higher generation dendron, and this coupling process can be repeated doubling each time the dendron size. Finally, a symmetrical dendrimer can be formed by connecting these dendrons to a polyfunctional core through their focal point (**Figure 2.5**). In the convergent approach the number of reacting partners does not change on increasing generation, so that structural defects can be more easily avoided. However, the preparation of high-generation dendrons is hampered for steric reasons because coupling must occur at the focal point.

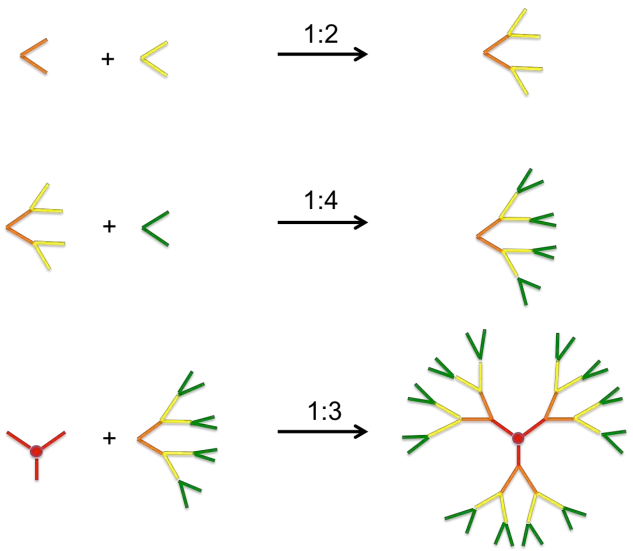

Figure 2.5 *Schematic representation of a convergent methodology.*

To develop an antenna system is useful, like Nature does, maintaining a modular approach, so it is important focusing on the single modules, which can be used as building blocks to prepare dendrimeric antenna systems. The building blocks' features to design a good photoactive system are several: ground and excited state stability (especially because, differently from natural systems, artificial ones cannot self-repair); efficient UV/Vis absorption; relatively long-lived excited states, to grant minimal loss of energy when energy transfer processes occur. There were chosen Ru(II) and Os(II) polypyridine complexes as building blocks because their optimal properties for such photoactive systems:[23,24] good stability of ground, excited and redox states; presence of intense metal-to-ligand charge transfer (MLCT) bands which allow a good absorption in the visible region; relatively long-lived and luminescent excited state (in the order of microseconds) due to radiative deactivation of the lowest-lying ^{3}MLCT level(s); reversible metal-centred oxidation and ligand-centred reduction processes at accessible potential; tunability of all the properties by varying the ligands.

2.2 *Ru(II) and Os(II) polypyridine complexes*

Ruthenium and osmium, in oxidation state of +2, have a d^6 electronic configuration. Polypyridines are strong field ligands that act as σ-donor by the orbitals localised on N atoms and as π-acceptor by π^* orbitals delocalised within the aromatic rings. A typical absorption spectrum of this kind of complexes shows several bands characterised by different molar attenuation coefficient in the UV/Vis region. Ground, low energy excited and redox states can be described by localised molecular orbitals approximation.[25] This approximation makes easier band-assignment of spectra.

Electron promotion from a π_M metal orbital to a π_L^* ligand orbital generates a MLCT (metal-to-ligand charge transfer) excited state; the one from a π_M orbital to a σ_M^* orbital generates a MC (metal centred) excited state; the one from a π_L orbital to a π_L^* generates a LC (ligand centred) excited state (**Figure 2.6**); LMCT (ligand-to-metal charge transfer) excited states may not be considered because in low spin octahedral complexes $\pi_M(t_{2g})$ are full so it is not possible observing these kinds of transition at

low energy. In general, MC excited states energy depends on ligand field strength, which depends on π-acceptor and σ-donor properties, steric hindrance and polydentate ligand bite angle.

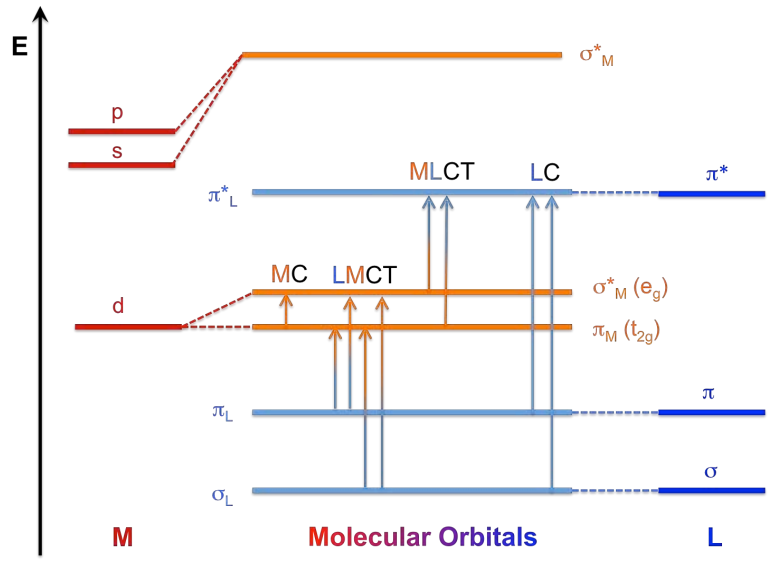

Figure 2.6 *Scheme of possible electronic transitions in a complex.*

MLCT excited states energy depends on ligand reduction potentials, metal oxidation potentials (which are influenced by ligands themselves) and charge separation derived from the transition. LC excited states energy derives from the ligand intrinsic properties, such as HOMO-LUMO energy difference and singlet-triplet separation. All of these states can have a singlet or triplet multiplicity, although spin-orbit interaction may cause a combination between singlet and triplet states.

Cation complexes $[M(L)_3]^{2+}$ (M = Ru and Os; L is a generic bidentate polypyridine ligand) have a D_2 symmetry.[26] π* orbitals can be symmetric or asymmetric referring to C_2 rotation axis of each M(L) subunit (χ and φ respectively, according to Orgel notation).[27] In **Figure 2.7** there are schematised the possible MLCT transitions for these kinds of systems.

Highest occupied molecular orbitals (HOMO) are $\pi_M a_1(d)$ and $\pi_M e(d)$, that are localised on metal. Lowest unoccupied molecular orbitals (LUMO) are $\pi_L a_2(\varphi)$ and $\pi_L e(\varphi)$, that are localised on ligands. Such complexes' ground state is a singlet derived from $\pi_M e(d)^4 \pi_M a_1(d)^2$ electronic configuration. In transition metal complexes, high

energy excited states lead to fast non-radiative decays, so only lowest energy state (and all the states which can be populated according to Boltzmann distribution) can be implicated in luminescent and bimolecular processes.[28]

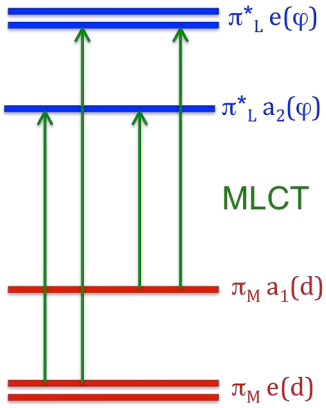

Figure 2.7 *A more detailed representation of MLCT transitions in an octahedral complex with a D_2 symmetry.*

In Ru(II) and Os(II) complexes, LMCT excited states have high energy because the elevated metal electronic affinity; so, the lowest energy excited state may be a MLCT or LC state.[29]

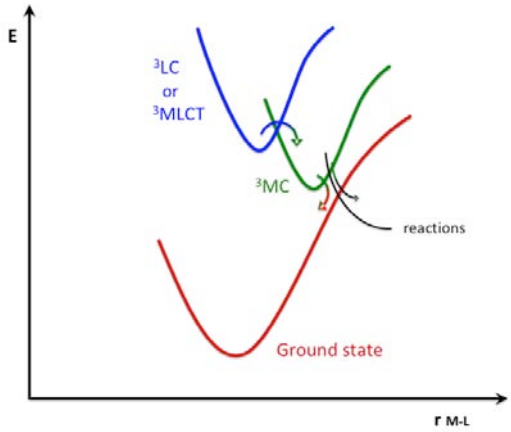

Figure 2.8 *Schematic representation of processes that take part when a MC state is the lowest-energy excited level.*

MC excited state of d^6 metals octahedral complexes exhibit a very distorted geometry along metal-ligand vibration coordinates compared to ground state one.[25,30] Therefore, a MC excited state leads to a non-radiative decay or to ligand dissociation

(**Figure 2.8**); at room temperature, excited states lifetimes are very short and it is not possible observing luminescent processes or bimolecular reactions.[31]

On the other hand, MLCT and LC excited states geometries are not highly distorted compared to ground state one, so it is more probable a radiative decay, with the exception of high temperatures because the population of higher energy non-radiative states can be thermically promoted (**Figure 2.9**).

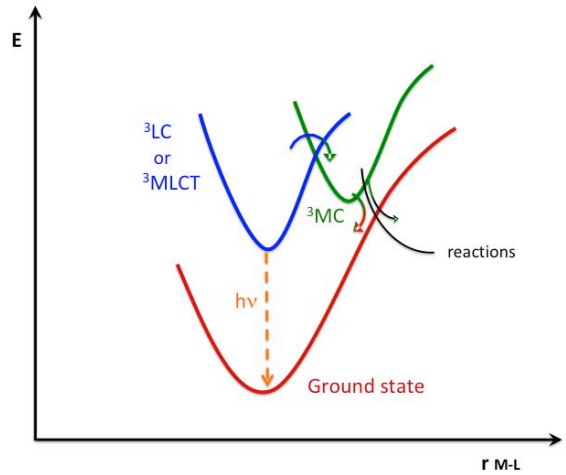

Figure 2.9 *Schematic representation of processes that take part when a LC or a MLCT state is the lowest-energy excited level.*

^{3}MLCT, compared to ^{3}LC excited states, are more influenced by spin-orbit interaction (in particular in Os(II) compounds), resulting in greater radiative decay constant rates. Because of this, at low temperature in rigid matrix it is more probable the emission is due to a deactivation from ^{3}LC excited states; at room temperature in liquid solution such states easily are deactivated, populating non-radiative MC excited states. So, in these experimental conditions, emission from ^{3}MLCT excited states dominate the spectrum.

In Ru(II) and Os(II) polypyridine complexes the excited states which produce luminescence are only MLCT excited states formally spin-forbidden.[32] The energy of luminescent state is correlated to both nature of metal and nature of ligands. As it is easier oxidising Os(II) than Ru(II), the luminescent excited state of an Os(II) complex is lower in energy than the one of the equivalent Ru(II) complex.[33] Moreover, the energy can be modulated using different polypyridine ligands.[32,34] For instance, luminescent level of $[M(bpy)_3]^{2+}$ (bpy = 2,2'-bipyridine) is higher in energy than the

one of $[M(biq)_3]^{2+}$ (biq = 2,2'-biquinoline) because biquinoline is easier to be reduced than bipyridine. Nature of ancillary ligands (that are ligands which do not take part in the MLCT transition) influences energy of luminescent energy level too; for instance, if a ligand X in a ML_nX_m complex is replaced by a better electron-donor ligand, the ^{3}MLCT state gets lower in energy because the increased electron density (that leads to a lower oxidation potential) around the metal.

Polypyridine complexes show an intense absorption in UV/Vis region. Their spectra are dominated in UV region by intense bands due to spin-allowed LC transitions ($\pi \rightarrow \pi^*$) and bands in visible region due to spin-allowed MLCT transitions. In polynuclear complexes, the presence of different or non-equivalent metal centres (due to non-equivalent chemical environments) or different ligands lead to different MLCT transitions and the bands overlap, causing broadened bands. On the basis of previous text, it is possible determining the energies correlated to the several MLCT transitions:

1. Os(II)→ligand transition occurs at a lower energy than Ru(II)→ligand transition (considering equivalent acceptor and ancillary ligands);
2. The energy of M→bpy transition is higher than M→biq one (considering equivalent metals and ancillary ligands).

In Os(II) complexes the presence of such heavy metal permits partially spin-forbidden MLCT transitions, with significant absorption bands at low energy.

The oxidation processes in Ru(II) and Os(II) complexes are generally centred on metal orbitals, and Ru(III) and Os(III) (with low-spin d^5 electronic configuration) form. Commonly, they do not undergo further reactions, permitting the electrochemical reversibility.

Oxidation potentials are strongly dependent on nature of metals (Os(II) is easier to be oxidised than Ru(II)) and on acceptor and donor properties of ligands: electron-acceptor ligands get the potentials higher; electron-donor ligands get the potentials lower.

Reduction processes in Ru(II) and Os(II) polypyridine complexes involve usually π^* ligand orbitals. Reduced species keep a d^6 electronic configuration, which is in general inert enough to make the process reversible.

As previously said, in almost every of this kind of complexes the lowest-energy

excited state (so, the one mainly involved in photophysical and electrochemical processes) is a MLCT state. Even overlooking an accurate description of spin and symmetry properties, it may be questionable whether the orbital can be described as a delocalised orbital over the multichelated system or localised on a single chelated unit. From low-temperature cyclic voltammetry, electronic absorption, Raman spectroscopy, NMR and EPR, the second hypothesis seems to be the actual behaviour of these systems.

Reduction potential of every ligand depends on its electronic properties and, to a lesser extent, on the nature of the metal centre and the other ligands coordinated to it.

2.3 Bridging ligand

When the bridging ligand is conjugated, processes like electron and energy transfer can occur from one metal to the other via the ligand; the rate can then be quite sensitive to the nature of the ligand. For example, a pyrazine ligand and a 1,2-bis(diphenylphosphino)methane ligand give approximately the same length of the bridge, but the rate of the electron transport over the bridge is 30-fold as fast for the pyrazine bridge, since the process can involve the bridge, rather than just tunnel around (or under) it.[35]

To build up multinuclear metal complexes for intercomponent electron transfer and energy migration, the bridging ligands among the metal centres should allow a relative weak electronic coupling between the subunits, letting them maintaining their own individual properties, but, at the same time, be strong enough to allow fast and efficient energy and/or electron transfer processes between the metal subunits. This means the system has to be supramolecular[36] and not delocalised, but it does not forbid that the properties of the individual building blocks can be largely perturbed in the assembly, in comparison with the isolated subunits. It is clear that there is a strong similitude to the realm of mixed-valence chemistry, in which two redox-active subunits are connected by some covalent spacer, or bridging ligand. In particular, the bridging ligand must give origin to a dinuclear species (and in general to multinuclear species) that resembles the Class II limit of mixed-metal compounds, according to the Robin–Day definition.[37] Actually, Robin–Day definition classifies dinuclear metal compounds as belonging to three general classes: Class I, where the electronic

coupling between the two subunits is negligible; Class III, in which the electronic coupling is so large that each component losses its individuality and the dinuclear species can be regarded as a new large molecule; Class II, an intermediate case, somehow the most interesting, since the components keep their individuality – although slightly changed – but the dinuclear system exhibits new properties compared to the separated units.

Such is the reason why the research group where I have worked used 2,3-dpp and 2,5-dpp (dpp = bis(2'-pyridyl)pyrazine) as bridging ligand for previous works based on Ru(II) and Os(II) polypyridine complexes.

2.4 *Synthetic strategy*

An optimal synthetic strategy to assemble a high number of chromophores in the fewest steps possible is "cal/cam" (complex as ligand/complex as metal) approach.[38] Basically, it is convenient preparing simpler (multi)component structures and assembling them into structurally organised systems by taking advantage of some specific and complementary reaction sites, to obtain large supramolecular structures. This strategy contemplates three kinds of precursor for the synthesis, classified by the nature of their reactive sites:

1. complexes as metals, in the case they are coordinated to easy-replaceable ligands so that they can act as metal with other ligands;
2. complexes as ligands, if it is present in the coordination sphere at least one polydentate ligand which has one or more free coordinating sites;
3. closed complexes, if there are no further reactive sites unless extreme conditions.

Mononuclear transition metal complexes are typically synthesised by the reaction between metal ion (M) and free ligands (L) following the scheme $M+nL \rightarrow ML_n$; "cal/cam" strategy is instead based on using complexes in the place of metal ion and free ligands.[38,39] The place of the metal is taken by mono- or oligonuclear complexes which have ligands easily replaceable (*complex-metal*); the place of free ligands is taken by mono- or oligonuclear complexes which contain free chelating sites (*complex-ligand*).

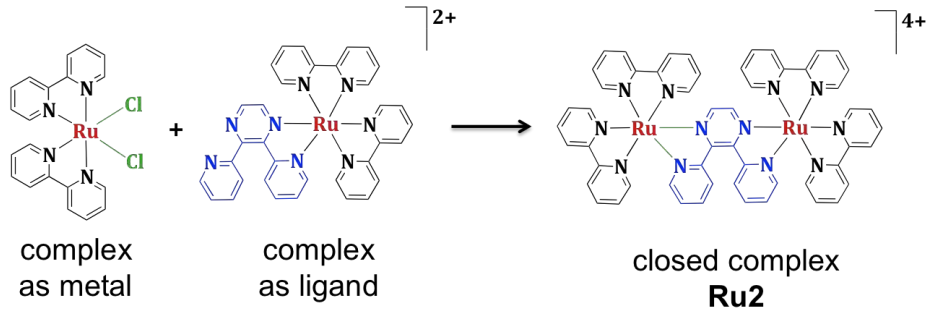

Figure 2.10 *Reaction between a complex as metal and a complex as ligand to obtain a dinuclear complex.*

A simple application of this methodology is shown in **Figure 2.10**, where $Ru(bpy)_2Cl_2$ acts as complex-metal because its two chloride ligands are easily removable under reflux, leaving the Ru(II) complex unsaturated; $[Ru(bpy)_2(2,3\text{-dpp})]^{2+}$ plays instead the role of complex-ligand because its free-chelating site of 2,3-dpp which can coordinate the unsaturated complex-metal, after the removal of chlorides. By this reaction, complex **Ru2** is obtained.

However, this example has been shown just to clarify the cal/cam methodology, as the **Ru2** complex can be synthesised with easier paths. Cal/cam strategy is more useful when polynuclear and/or multifunctional complex-metals and complex-ligands are available. An example is shown in **Figure 2.11**, where a monofunctional, trinuclear complex-metal and a trifunctional mononuclear complex-ligand (with free chelating sites) react to form a decanuclear complex.[43]

The reaction in **Figure 2.11** warrants some comments: (i) a high-nuclearity complex is formed in a single step by taking advantage of the functionalities of the reaction partners. (ii) The topography of the final compound is fully controlled by synthesis: the metal centre in the central position (M_c) of the decanuclear species is the metal initially belonging to the trifunctional complex ligand; the intermediate positions metal centres (M_i) are the metals of the trinuclear complex metal with the leaving chloride ligands; and the metals in the peripheral positions (M_p) are the terminal metals of the parent trinuclear complex metal. Similarly, the positions of the bridging ligands in the final structure are also determined by the metal precursors used in the synthetic reaction. (iii) The decanuclear species can be considered a second-generation dendrimer. It should be noted that point (ii) in particular is due to the stability of the metal-polypyridine linkages, typical (with some exceptions) of

Ru(II) and Os(II) polypyridine compounds: a prerequisite for the application of this method is indeed that ligand scrambling does not occur, as it is the case for Ru(II) and Os(II) complexes.

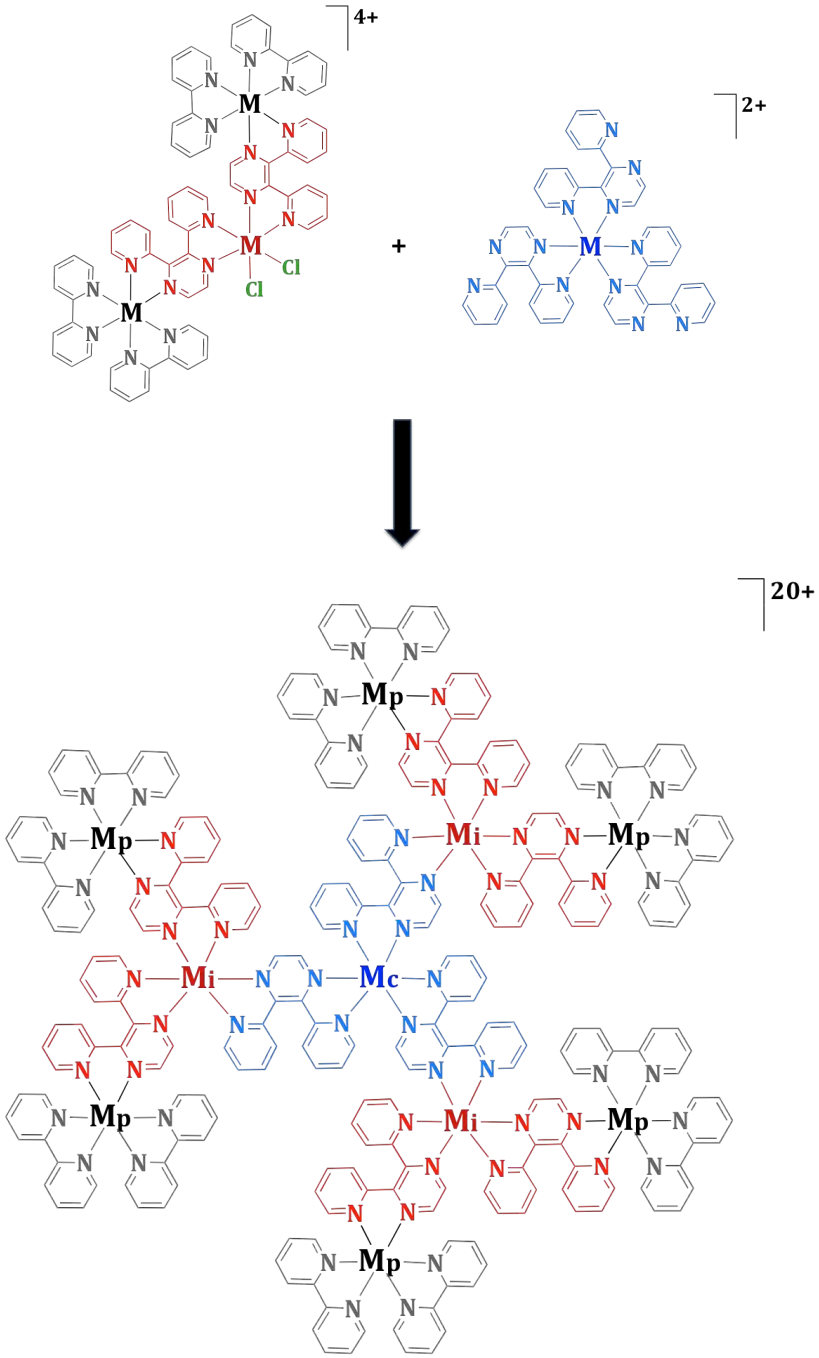

Figure 2.11 *Synthetic approach for the synthesis of a decanuclear complex. The topography of the final product (i.e., the position of the various metal centres in the dendritic structure) is governed by the synthons used. M can be Ru(II) and/or Os(II).*

2.5 Complexes previously studied as antenna systems

The research group where I have worked in these years studied in the past several Ru(II) and Os(II) polypyridine dendrimers based on, as previously said, 2,3-dpp and 2,5-dpp as bridging ligand (**Figure 2.12**). Main aim was using such dendrimers for photoinduced energy migration across the dendritic arrays, with predetermined redox patterns.[40]

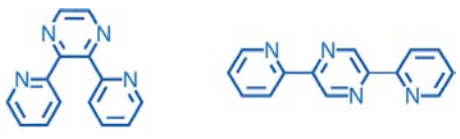

Figure 1.12 *Molecular structures of dpp-based bridging ligands.*

It is necessary explaining briefly the general properties of these dendritic species.

(i) As said previously, each metal-based subunit exhibits specific photophysical and redox properties, but in the assemblies the electronic properties (which are correlated to photophysical and redox ones) of the 2,3-dpp and 2,5-dpp ligands change substantially whether they act as bridging ligands (bis-coordination) of terminal ligands (mono-coordination). More specifically, their reduction potential gets less negative values by several hundreds of mV on double coordination. For example, the dpp-based reduction moves from about -1.10 V in $[Ru(bpy)_2(2,3\text{-dpp})]^{2+}$ to -0.60 V in $[(bpy)_2Ru(\mu\text{-}2,3\text{-dpp})Ru(bpy)_2]^{4+}$ (reported potentials are in acetonitrile *vs.* SCE). As a consequence, the ^{3}MLCT state (that is, a formally Ru→μ-2,3-dpp CT state) undergoes a strong decrease in energy. So, although the dendrimers contain a number of monometallic Ru(II) subunits, the "individual" subunits that contain dpp ligands in their "bridging" form and properties. In other words, the mononuclear species, which does not contain bridging ligands, are not good model as building block for the monometallic units of the dendrimers, as far as their electronic properties are concerned, but rather we should consider building blocks with bridged dpp.

(ii) Since the MLCT state depends on the oxidation potential of the metal centre (which depends on all the ligands whose it is coordinated) and on the reduction potential of the easiest ligand to reduce connected, the $[Ru(\mu\text{-}2,3\text{-dpp}_3)]^{2+}$ subunit has

a MLCT state higher in energy than the $[Ru(bpy)_2(\mu\text{-}2,3\text{-}dpp)]^{2+}$ subunit, although in both cases the lowest-energy MLCT is a Ru→μ-2,3-dpp CT state. Therefore, the peripheral subunits have MLCT levels lying at lower energies than the inner ones, so it is possible referring to a gradient for a directional energy transfer from the centre to the periphery of the dendrimer. An example of this is $[Ru\{(\mu\text{-}2,3\text{-}dpp)Ru(bpy)_2\}_3]^{8+}$ (**Ru4**).

(iii) In mixed metal Ru/Os dendrimers, energy transfer from Ru(II) centres to Os(II) centres is thermodynamically favourable.

(iv) Metal-metal interaction between bridging ligand is not negligible, so oxidising a metal centre cause a rising of oxidation values of the oxidation processes of all the metal centres directly connected to. It is the same for ligand-ligand interaction via metal centres.

The above points (i)-(iv) explain the properties of the metal dendrimers. In the tetranuclear, first generation mixed-metal dendrimer $[Os\{(\mu\text{-}2,3\text{-}dpp)Ru(bpy)_2\}_3]^{8+}$ (**OsRu3**), made of an Os-based core and three peripheral Ru-based chromophores, all the light energy absorbed by the peripheral Ru-based chromophores is efficiently transferred to the Os core (**Figure 2.13**), that is a quantitative energy transfer takes place from the upper-lying MLCT states involving the Ru peripheral units to the lower-lying MLCT state of the Os core, whose MLCT triplet state is the only emissive state of the dendrimer.[41] In fact, emission spectra present only an emission band at 860 nm, which is typical of radiative deactivation of $[Os(\mu\text{-}2,3\text{-}dpp_3)]^{2+}$ subunit. It has been needed waiting for the development of fs pump-probe transient absorption spectroscopy to kinetically determine the rate constant of such a periphery-to-centre energy transfer process. Indeed it has been possible demonstrating that such energy transfer occurs via triplet–triplet energy transfer with a time constant of 600 fs, and that for excitation wavelengths shorter than 540 nm the process mostly takes place via non-equilibrated states, possibly also involving singlet MLCT levels, with time constants shorter than 60 fs.[42] For the all-ruthenium first, second- (shown in **Figure 2.13**) and third-generation dendrimers a reverse, centre-to-periphery energy transfer takes place, with energy transfer from the upper-energy centre (and intermediate) $[Ru(\mu\text{-}2,3\text{-}dpp)]^{2+}$ subunit(s) to the lower-energy $\{(\mu\text{-}2,3\text{-}dpp)Ru(bpy)_2\}^{2+}$ subunits.

The above-mentioned results, together with a large series of photophysical studies regarding other dendrimers of this family, allowed concluding that down-hill energy transfer, as well as isoergonic energy transfer, between subunits connected by the same bridging ligands are extremely fast (subpicosecond timescale) and efficient. In all cases, the main mechanism for energy transfer is Dexter electron exchange.

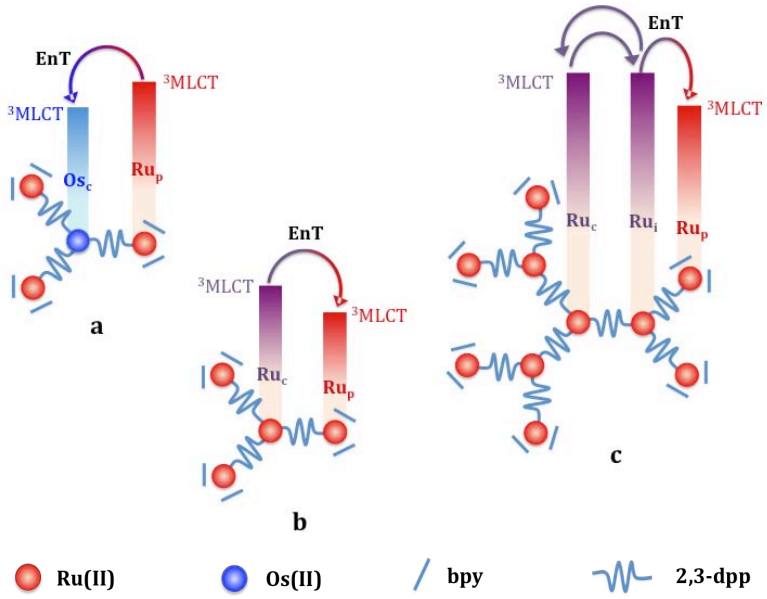

Figure 2.13 *Energy order of the ^{3}MLCT states of the various subunits and energy transfer (EnT) processes occurring in* ***Ru3Os*** *(a),* ***Ru4*** *(b) and* ***Ru10*** *(c).*

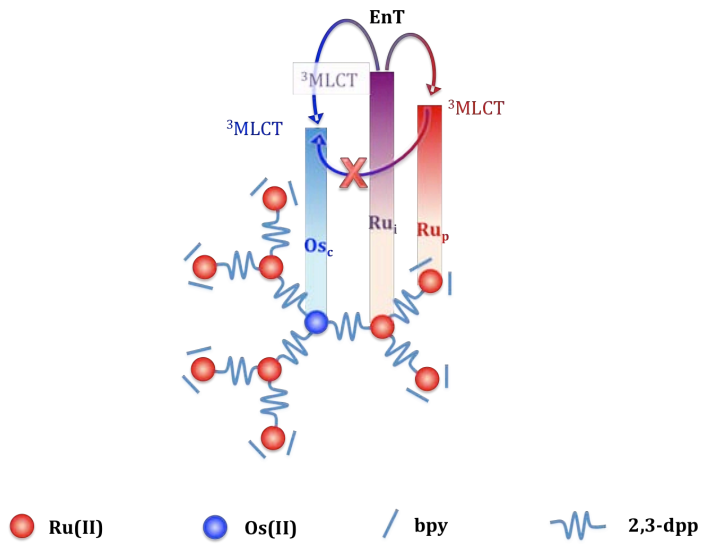

Figure 2.14 *Schematization of the energy order of the ^{3}MLCT states and energy transfer (EnT) processes occurring in* ***Ru9Os****.*

The situation is different when up-hill energy transfer steps are present, that is when metal-based units having higher-energy MLCT states ("high-energy subunits") are interposed between donor and acceptor energy transfer subunits. This was the case for the decanuclear mixed-metal compound $[Os\{(\mu\text{-}2,3\text{-}dpp)Ru\{(\mu\text{-}2,3\text{-}dpp)Ru(bpy)_2\}_2\}_3]^{20+}$ (**Ru9Os**; see **Figure 2.14**).[43] Due to the different oxidation potential of Os(II) compared to Ru(II) units and of the inner Ru(II) centres compared to the outer Ru(II) centers, the energy order of the three types of subunits of **Ru9Os** is $[Os(\mu\text{-}2,3\text{-}dpp)_3]^{2+}$ (the core chromophore, Osc) < $[(\mu\text{-}2,3\text{-}dpp)Ru(bpy)_2]^{2+}$ [the outer chromophore(s), Ru_p] < $[Ru(\mu\text{-}2,3\text{-}dpp)_3]^{2+}$ (the intermediate chromophores, Ru_{int}).[43] So, in principle all the absorbed light should be conveyed into the Os_c subunit. However, the emission spectrum is dominated by emission from the peripheral Rup-type chromophores, with only a very small contribute from the core Os_c chromophore.[43,44] Evidently, energy transfer from Ru_p to Os_c across the higher-energy Ru_{int} interposed subunit is not effective. This is even more evident in the docosanuclear species **Ru21Os**, where the Os(II) contribution is negligible.[45] In both **Ru9Os** and **Ru21Os**, as well as in a similar mixed-metal decanuclear species in which 2,2′-biquinoline (biq) replaces bpy as the terminal ligands,[43] the emission lifetimes recorded at the Rup dominant emission are also unchanged with respect to the emission lifetimes of the corresponding all-Ru dendrimers, so confirming that Ru_p-to-Os_c energy transfer is not a useful decay route in the presence of high-energy interposed chromophores.

Solutions to the problem of this energy gradient from intermediate subunits to peripheral and central ones may be several, focusing on modifying the excited state energy of the subunits:

1) increasing excited state energy of peripheral chromophores, modifying the nature of metal centres and/or the nature of terminal ligands;
2) decreasing excited state energy localised on intermediate chromophore;
3) decreasing excited state energy localised on central chromophore.

My work on this topic was focused on the synthesis and study of a new heptanuclear dendrimer, containing an Os(II) core and six Ru(II) polypiridine subunits. In this new species, the Os(II)-based core is directly connected (via a novel

bridging ligand) to six Ru(II)- based chromophores. The presence of interposed high-energy metal-based components is therefore avoided, so overcoming the above-cited problem in the EnT efficiency of light-harvesting metal-based dendrimers of high nuclearity, see Chapter 4.

References

1) D. Gust, T. A. Moore, A. L. Moore, *Faraday Discuss*., **2012**, 155, 9.

2) V. Balzani, P. Ceroni, A. Juris, Photochemistry and Photophysics. Concepts, Research, Perspectives, Wiley-VCH, Weinheim, **2014**.

3) (a) G. MacDermott, S. M. Prince, A. A. Freer, A. M. Hawthornthwaite-Lawless, M. Z. Papiz, R. J. Cogdell, N. W. Isaacs, *Nature*, **1995**, 374, 517; (b) T. Pullerits, V. Sundström, *Acc. Chem. Res*., **1996**, 29, 381 and refs therein; (c) S. Karrash, P.A. Bullough, R. Ghosh, *EMBO J*., **1995**, 14, 631.

4) G. MacDermott, S. M. Prince, A.A. Freer, A.M. Hawthornthwaite- Lawless, M. Z. Papiz, R. J. Cogdell, N. W. Isaacs, *Nature 374*, **1995**, 517.

5) T. Pullerits, V. Sundström, *Acc. Chem. Res 29*, **1996**, 381 and references therein.

6) S. Campagna, S. Serroni, F. Puntoriero, C. Di Pietro, V. Ricevuto, in: V. Balzani (Ed.), *Electron Transfer in Chemistry,Vol. 5,Wiley-VCH,Weinheim*, **2001**, p. 186.

7) S. Serroni, S. Campagna, F. Puntoriero, F. Loiseau, V. Ricevuto, R. Passalacqua, M. Galletta, *C. R. Chimie 6*, **2003**, 883–893.

8) J. M. Lehn, *Supramolecular Chemistry, VCH-Wiley, Weinheim*, Germany, **1995**.

9) J. M. Lehn (Ed.), *Comprehensive Supramolecular Chemistry, VCH-Wiley*, **2001**.

10) A.H. Zewail, *Angew. Chem. Int. Ed. Engl. 39*, **2000**, 2586.

11) G.R. Newkome, C. Moorefield, F. Vögtle, *Dendrimers and Dendrons, Wiley-VCH, Weinheim*, **2001**.

12) S. Campagna, S. Serroni, F. Puntoriero, C. Di Pietro, V. Ricevuto, in: V. Balzani (Ed.), *Electron Transfer in Chemistry, vol. 5 (and refs. therein)*, *Wiley-VCH*, **2001**, p. 186.

13) V. Balzani, S. Campagna, G. Denti, A. Juris, S. Serroni, M. Venturi, *Acc. Chem. Res. 31,* **1998**, 26.

14) E.C. Constable*, Chem. Commun.*, 1997, 1073.

15) (a) G. Denti, S. Campagna, L. Sabatino, S. Serroni, M. Ciano, V. Balzani, *Inorg. Chem. 29*, **1990**, 4750; (b) G. Denti, S. Campagna, S. Serroni, M. Ciano, V. Balzani, *J. Am. Chem. Soc. 114,* **1992**, 2944; (c) S. Campagna, G. Denti, S. Serroni, A. Juris, M. Venturi, V. Ricevuto, V. Balzani, *Chem. Eur. J. 1,* **1995**, 211; (d) S. Serroni, A. Juris, M. Venturi, S. Campagna, I. Resino Resino, G. Denti, A. Credi, V. Balzani, *J. Mater. Chem. 7,* **1997**, 1227;

16) (a) D.A. Tomalia, H.D. Durst, *Top. Curr. Chem.*, **1993**, 165, 193; (b) J. M. J. Fréchet, *Science*, **1994**, 263, 1710; (c) N. Ardoin, D. Astruc, *Bull. Soc. Chim. Fr.*, **1995**, 132, 875; (d) G. R. Newkome, C. Moorefield, F. Vögtle, *Dendritic Molecules: Concepts, Syntheses, Perspectives, VCH, Weinheim*, **1996**; (e) F. Zeng, S.C. Zimmerman, *Chem. Rev.*, **1997**, 97, 1681; (f) J. P. Majoral, A. M. Caminade, *Top. Curr. Chem.*, **1998**, 197, 79; (g) O. A. Matthews, A. N. Shipway,

J. F. Stoddart, *Prog. Polym. Sci.*, **1998**, 23, 10; (h) D. K. Smith, F. Diederich, *Chem. Eur. J.*, **1998**, 4, 1353; (i) H. F. Chow, T. K. K. Mong, M.F. Nongrum, C. W. Wan, *Tetrahedron*, **1998**, 54, 8543; (j) M. Fischer, F. Vögtle, Angew. *Chem. Int. Ed.*, **1999**, 38, 884; (k) A. W. Bosman, H. M. Janssen, E. W. Meijer, *Chem. Rev.*, **1999**, 99, 1665; (l) G. R. Newkome, E. He, C. Moorefield, *Chem. Rev.*, **1999**, 99, 1689.

17) A. Juris, *Annu. Rep. Prog. Chem., Sect. C*, **2003**, 99, 177–241.

18) V. Balzani, A. Credi and M. Venturi, in *Stimulating Concepts in Chemistry*, ed. M. Shibasaki, J. F. Stoddart and F. Vögtle, Wiley-VCH, Weinheim, **2000**, 255.

19) V. Balzani, A. Credi and M. Venturi, *Molecular Devices and Machines – A Journey into the Nano World*, Wiley-VCH, Weinheim, **2003**.

20) (a) Y. H. Liao, J. R. Moss, *Organometallics* **1996**, 15, 4307. (b) I. Cuadrado, M. Moràn, C. M. Casado, B. Alonso, F. Lobete, B. Garcìa, M. Ibisate, J. Losada, *Organometallics* **1996**, 15, 5278; (c) M. Slany, M. Bardajì, M. J. Casanove, A. M. Caminade, J. P. Majoral, B. J. Chaudret, *Am. Chem. Soc.* **1995**, 117, 9764.

21) (a) G. R. Newkome, F. Cardullo, E. C. Constable, C. N. Moorefield, Cargill Thompson A.M.W., *J. Chem. Soc. Chem. Commun.* **1993**, 925. (b) G. R. Newkome, C. N. Moorefield, G. R. Baker, A. L. Johnson, R. K. Behera, *Angew Chem Int Ed Engl.,* **1991**, 30, 1176.

22) (a) V. Balzani, A. Juris, M. Venturi, S. Campagna, S. Serroni, *Chem*. *Rev.,* **1996**, 96, 759. (b) S. Serroni, G. Denti, S. Campagna, A. Juris, M. Ciano, V. Balzani, *Angew Chem Int Ed Engl,* **1992**, 31, 1493. (c) S. Achar, R. J. Puddephatt, *J. Chem. Soc. Chem. Commun.,* **1994**, 1895; (d) S. Achar, J. J. Vittal, R. J. Puddephatt, *Organometallics,* **1996**, 15, 43. (e) W. T. S. Huck, F. G. J. M. Vanveggel, D. N. Reinhoudt, *Angew Chem Int Ed Engl.,* **1996**, 35, 1213.

23) A. Juris, V. Balzani, F. Barigelletti, S. Campagna, P. Belser, A. von Zelewsky, *Coord. Chem. Rev.*, 84, **1988**, 85.

24) T. J. Meyer, *Acc. Chem. Res.*, 22, **1989**, 163.

25) V. Balzani, V. Carassiti, *Photochemistry of Coordination Compounds, Academic Press*, London, **1970**.

26) D.P. Rillema, D.S. Jones, H.A. Levy, J. *Chem. Soc. Chem. Commun.*, **1979**, 849.

27) L.E. Orgel, *J. Chem. Soc.*, **1961**, 3683

28) J. N. Demas, *J. Chem. Ed.*, **1983**, 60, 803.

29) C.K. Jörgensen, *Mol. Phys.*, **1959**, 2, 309.

30) A.W. Adamson, *J. Chem. Ed.*, **1983**, 60, 797.

31) P.D. Fleischauer, P. Fleischauer, *Chem. Rev.*, **1970**, 70, 199.

32) F. Puntoriero, F. Nastasi, M. Galletta, S. Campagna, *Comprehensive Inorganic Chemistry II: From Elements to Applications*, **2013**, 8, 255-337 and references.

33) G. Denti, S. Serroni, L. Sabatino M. Ciano, V. Ricevuto, S. Campagna, *Gazz. Chim. Ital.* **1991**, 121, 37.

34) (a) A. Juris, F. Barigelletti, S. Campagna, V. Balzani, P. Belser, A. von Zelewsky, *Coord. Chem. Rev.*, **1988**, 84, 85; (b) T. J. Meyer, *Pure Appl. Chem.*, **1986**, 58, 1193; (c) V. Balzani, G. Bergamini, S. Campagna, F. Puntoriero, *Top. Curr. Chem.*, **2007**, 280, 136; (d) S. Campagna, F. Puntoriero, F. Nastasi, G. Bergamini, V. Balzani, *Top. Curr. Chem.*, **2007**, 280, 117-214

35) G. Wulfsberg, Inorganic Chemistry, *University Science Books*, **2000**, 886.

36) V. Balzani, F. Scandola, *Supramolecular Photochemistry, Horwood, Chichester, UK*, **1991**.

37) (a) M. B. Robin, P. Day, *Adv. Inorg. Chem. Radiochem.*, **1968**, 10, 247; (b) C. Creutz, H. Taube, *J. Am. Chem. Soc.*, **1973**, 95, 1086; (c) C. Creutz, *Prog. Inorg. Chem.*, **1983**, 30, 1; (d) D. E. Richardson, H. Taube, *J. Am. Chem. Soc.*, **1983**, 105, 40; (e) B. S. Brunschwig, C. Creutz, N. Sutin, *Chem. Soc. Rev.*, **2002**, 31, 168; (f) A. Petitjean, F. Puntoriero, S. Campagna, A. Jutis, J. M. Lehn, *Eur. J. Inorg. Chem.*, **2006**, 3878.

38) S. Serroni, S. Campagna, F. Puntoriero, C. Di Pietro, F. Loiseau, N. D. McClenaghan, *Chem. Soc. Rev.*, **2001**, 30, 367, and refs. therein.

39) V. Balzani, S. Campagna, G. Denti, A. Juris, S. Serroni, M. Venturi, *Acc. Chem. Res.*, **1998**, 31, 26.

40) Fausto Puntoriero, Scolastica Serroni, Giuseppina La Ganga, Antonio Santoro, Maurilio Galletta, Francesco Nastasi, Emanuele La Mazza, Ambra M. Cancelliere, Sebastiano Campagna, *Eur. J. Inorg. Chem.*, **2018**, 3887–3899.

41) S. Campagna, G. Denti, L. Sabatino, S. Serroni, M. Ciano, V. Balzani, *J. Chem. Soc., Chem. Commun.*, **1989**, 1500.

42) (a) J. Andersson, F. Puntoriero, S. Serroni, A. Yartsev, T. Pascher, T. Polivka, S. Campagna, V. Sundström, *Chem. Phys. Lett.*, **2004**, 386, 336; (b) J. Andersson, F. Puntoriero, S. Serroni, A. Yartsev, T. Pascher, T. Polivka, S. Campagna, V. Sundström, *Faraday Discuss.*, **2004**, 127, 295; (c) J. Larsen, F. Puntoriero, T. Pascher, N. McClenaghan, S. Campagna, E. Åkesson, V. Sundström, *ChemPhysChem*, **2007**, 8, 2643.

43) G. Denti, S. Campagna, S. Serroni, M. Ciano, V. Balzani, *J. Am. Chem. Soc.*, **1992**, 114, 2944.

44) V. Balzani, S. Campagna, G. Denti, A. Juris, S. Serroni, M. Venturi, Acc. Chem. Res. 1998, 31, 26.

45) S. Serroni, A. Juris, M. Venturi, S. Campagna, I. Resino Resino, G. Denti, A. Credi, V. Balzani, *J. Mater. Chem.*, **1997**, 7, 1227.

Chapter 3

Mesoporous silica nanoparticles as host-guest systems

3.1 Mesoporous structures

The development of porous materials with large specific areas is an interesting field of research, in fact their potential applications include areas such adsorption, chromatography, catalysis, sensor technology, gas storage, and so on. In 1992, with the development by the Mobil Oil Company of the class of periodic mesoporous silicas known as the M41S phase (which is formed by a sol-gel process)[1], an upsurge started: these materials little by little superseded zeolite molecular sieves, whose pores size is restricted between 0.4 and 2 nm.[2]

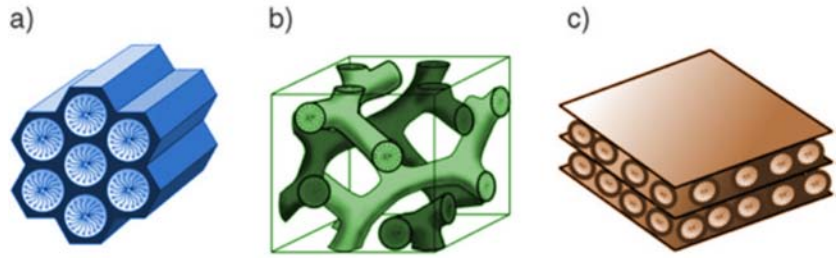

Figure 3.1 Structure of mesoporous silica materials: (a) MCM-41, (b) MCM-48 and (c) MCM-50.[3]

Like the nanoporous crystalline zeolites, this class of materials is characterised by very large specific surface areas, ordered and tunable pore system, well-defined pore radius distributions and a structural rigidity that enhances the mechanical and thermal stability of the whole system.[4,5,6] Furthermore, M41S materials, unlike zeolites, exhibit pore diameters from about 2 to 10 nm, amorphous pore walls and specific inner surface areas of typically ~1000 m^2g^{-1}. The most well-known structures of this class include the silica solid MCM-41 (with a hexagonal arrangement of the mesopores, space group *p6mm*), MCM-48 (with a cubic arrangement of the mesopores, space group $Ia\bar{3}d$) and MCM-50 (with a laminar structure, space group *p2*), whereas "MCM" stands for "Mobile Composition of Matter" (**Figure 3.1**).[4,7] The use of supramolecular aggregates of ionic surfactants (long-chain alkyltrimethylammonium halides) as structure-directing agents (SDAs) was revolutionary in the synthesis of these materials. These SDAs, in the form of a

lyotropic liquid-crystalline phase, lead to the assembly of an ordered mesostructured composite during the condensation of the silica precursor under basic conditions. The mesoporous materials are obtained by subsequent removal of the surfactant by extraction or calcination.

It was investigated the formation process of these composite materials and it was found that two different mechanisms are involved:

1. In the true liquid-crystal templating (TLCT), the concentration of the surfactant is so high that under the prevailing conditions (temperature, pH) a lyotropic liquid-crystalline phase is formed without requiring the presence of the precursor inorganic framework materials (usually tetraethyl- or tetramethylortosilica, TEOS and TMOS respectively).[8]
2. It is also possible that the lyotropic liquid-crystalline phase forms even at lower concentration of surfactant molecules, for example, when there is cooperative self-assembly of the SDA and the already added inorganic species, in which case a liquid-crystal phase with hexagonal, cubic or laminar arrangement can develop (**Scheme 3.1**).[9]

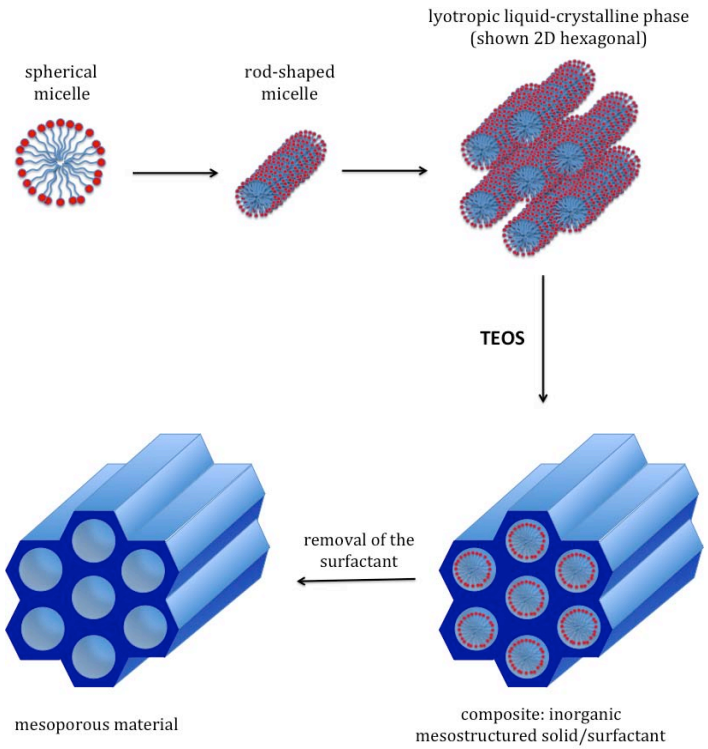

Scheme 3.1 *True liquid-crystal template mechanism for the formation of mesoporous materials.*

In the meantime, there have been explored new original approaches to synthesise these mesoporous silicas, for instance by the use of triblock copolymer templates under acidic conditions by which means the so-called SBA (Santa Barbara Amorphous) silica phases may be synthesised.

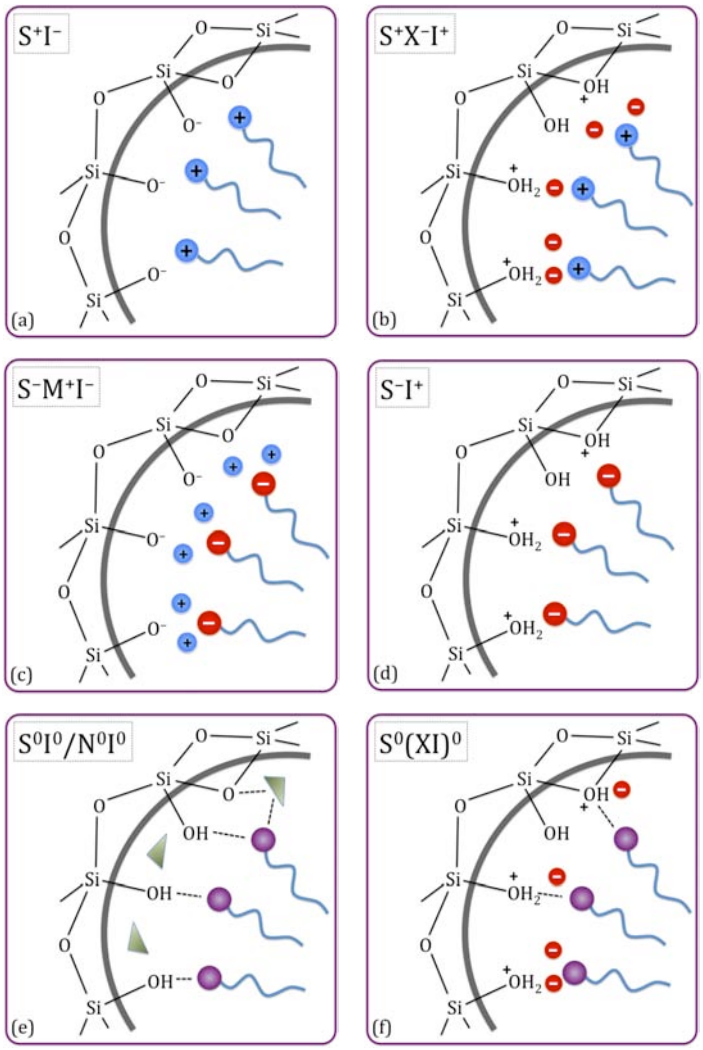

Figure 3.2 *Interaction between the inorganic species and the head group of the surfactant, considering the several synthetic methodologies in acidic, basic or neutral media. Electrostatic: (a), (b), (c) and (d); through hydrogen bonds: (e) and (f).*

It is relevant underlining that, for the second mechanism, an attractive interaction between the template and the silica precursor has to be produced to ensure inclusion of the structure director without phase separation might take place. The different interactions that can take place between the inorganic components and the head

groups of the surfactants are shown in **Figure 3.2**). These interactions, according to Huo *et al.*,[10,11] are classified as follow: (i) if the reaction takes place under basic conditions (silica species present in the mixture as anions) and cationic quaternary ammonium surfactants are used as SDA, the synthetic pathway is called S^+I^- (**Figure 3.2a**; S: surfactants; I: inorganic species). (ii) The synthesis can also take place under acidic conditions (below the isoelectric point of the Si–OH-bearing inorganic species; pH≈2), so the silica species in the mixture are positively charged. In this kind of preparation it is necessary adding a mediator ion X^- (halides, generally) to induce an interaction between the cationic head of surfactant and the positively charged silica species ($S^+X^-I^+$; **Figure 3.2b**). (iii) On the other hand, if negatively charged surfactants (such as long-chain alkyl phosphates) are used as SDA, it is possible working in basic media provided that, as before seen, a mediator ion M^+ is added to ensure interaction the surfactant molecules and the negatively charged silica species ($S^-M^+I^-$; **Figure 3.2c**). (iv) Similarly to (i), in acidic media a mediator ion is not required (S^-I^+; **Figure 3.2d**). In all of these cases, the dominating interactions are of an electrostatic nature, but it is also possible for the attractive interactions being mediated through hydrogen bonds. This happens when non-ionic surfactants are used (such as long-chained amines (S^0) or polyethylene oxide (N^0)), whereby (v) uncharged silica species (S^0I^0; **Figure 3.2e**) or (vi) ion pairs ($S^0(XI)^0$; **Figure 3.2f**) can be present.

The above-described synthetic methodologies for ordered mesoporous solids are classified as *endotemplate* methods ("soft-matter templating"). In *exotemplate* methods ("nanocasting") it is used as the template a porous solid, instead of the surfactant; this method is also known as "hard-matter templating". The hollow spaces provided by the exotemplate framework are filled with an inorganic precursor, which is transformed (cured) under suitable conditions. In this way, the pore system of the template is copied as a "negative image". After removal of the now-filled exotemplate framework, the incorporated material is obtained with a large specific surface area. Examples of periodic porous solids employed as exotemplate are ordered mesoporous silica phases (such as MCM-48 and SBA-15 types).[12,13]

A series of review articles cover the syntheses of mesoporous materials, whether they are pure silica phases or metal oxides, and their applications.[14-21]

The variables that involve controlling the size and morphology of mesoporous

silica nanoparticles include: (i) rate of hydrolysis; (ii) the level of interaction between assembled template and silica polymer; (iii) condensation of silica source. As previously said, by controlling the pH, using different templates and co-solvent it is possible controlling the above variables.[22,23,24] Stirring rate plays a key role in controlling the particle size of mesoporous silica nanoparticles; if the rate is slow, long fiver produced whereas upon fast stirring fine powder is formed.[25] The effect of pH on morphology of MSNs was studied by Ozin *et al.* and demonstrates that under mild acidic condition spherical mesoporous particles with the range of 1-10 μm are formed.[26] Brinker *et al.* used a technique to synthesise MSNs ranging from 100 to 500 nm by evaporating solvent from aerosol containing silica source and surfactant.[27]

The parameters that are used to control the pore size of mesoporous silica nanoparticles are the amount of silica source and surfactant[28] and the packing capacity of surfactant.[24] The aggregation of surfactant in solution depends on pH and the concentration of the solution. Mesoporous silica nanoparticles are synthesised at both acidic and basic pH with different pore structures. For example, lamellar meso phases are synthesised at high pH (>12), while hexagonal structures are produced at basic pH (10-12).[22]

Hydrothermal treatment during synthesis or post-synthesis is used to adjust the pore width. The selection of surfactant with different hydrophobic chain length or by using molecules (like the mesitylene) as swelling agent plays an important role in production of desired pore size.[29,30] Pore expansion can be done by using additives during synthesis and for this purpose additional tuning is required because additives have a property to change the hydrophobic-hydrophilic balance; for example, mesitylene is used as a pore expander of mesoporous silica nanoparticles from 3-5 nm without altering its particle size.

In hydrothermal treatment during post-synthesis a freshly prepared material is subjected to autogenic pressure at temperature ranging from 373 K to 423 K with or without additives, is done to increase the pore size without changing the morphology of pre-formed particles.[24,31,32,33]

3.2 *Functionalisation*

Interestingly, in contrast to the thermal stability, the hydrothermal stability of the

mesoporous silica nanoparticles is remarkably low, pointing to the fact the reaction of the sol-gel process are, in principle, reversible: putting MCM-41/MCM-48 samples into boiling water for 12 hours will lead to a complete loss of their structural integrity due to silicate hydrolysis.[34]

Apart from their use as solid-state acids in heterogeneous catalysis applications,[35] mesoporous silica phases themselves are a rather functionally limited class of materials, in particular from a chemical point of view. Therefore, considerable efforts have been undertaken to incorporate organic components within an inorganic silica framework to achieve symbiosis of the properties of both components. It was found out mesoporous silica phases are ideal candidates to develop organic-inorganic hybrid materials, to chemically revitalise the formerly pure inorganic silica matrix. In fact, they constitute an ideal starting point for placing organic functional groups onto a stable solid substrate bearing very large (inner) surfaces, a defined surrounding and pores which are large enough to accommodate relatively sterically demanding molecules, meaning that, potentially, a large number of accessible functional centres could be anchored onto a thermally stable and robust inorganic matrix.

The synergy of organic and inorganic components can lead to materials whose properties differ considerably from those of their individual, isolated components. Adjustment of the polarity of the pore surfaces of an inorganic matrix by the addition of organic building blocks extends considerably the range of materials that can be used, for example, in chromatography. Equally interesting is modification with organic functionalities such as C–C multiple bonds, alcohols, thiols, sulfonic and carboxylic acids, and amines, etc., which allow, for example, localised organic or biochemical reactions to be carried out on a stable, solid inorganic matrix.

It is worth considering some aspects why it is more convenient having ordered/uniform porous materials than non-ordered counterparts (not forgetting at the same time it always depends on the intended use):

1. a narrow pore size distribution is advantageous in all size-selective applications, for instance in catalysis or chromatography;
2. a broad pore size distribution is often connected with the presence of very narrow pores too, *i.e.* constricted openings like bottle-neck or slit-like pores; these would restrict significantly the accessibility of the

active/functional centres, and an efficient mass transport of the species inside the material towards and back from the active sites;

3. inversely, it should be easier to place as many functional centres within the material as possible if the whole inner surface area can be reached;
4. it is advantageous in terms of the reproducibility of the fabricated samples, if the pore sizes are uniform *and* tunable;
5. a regular arrangement of the channels bears the opportunity to design materials with completely new properties with regard to, for instance, confinement effects or collective properties of adsorbed species inside the pores (e.g. magnetic coupling effects).

Three pathways are available for the synthesis of porous hybrid materials based on organosilica units: (i) the subsequent modification of the pore surface of a purely inorganic silica material ("grafting"), (ii) the simultaneous condensation of corresponding silica and organosilica precursors ("co-condensation"), and (iii) the incorporation of organic groups as bridging components directly and specifically into the pore walls by the use of bissilylated single-source organosilica precursors ("production of periodic mesoporous organosilicas"). These pathways are below explained.

In the post-synthetic functionalisation of silicas (i) the *grafting* term refers to the subsequent modification of the inner surfaces of mesostructured silica phases with organic groups. This process is carried out primarily by reaction of organosilanes of the type $(R'O)_3SiR$, or less frequently chlorosilanes $ClSiR_3$ or silazanes $HN(SiR_3)_3$, with the free silanol groups of the pore surfaces (**Scheme 3.2**). By variation of the organic residue R, functionalisation with a variety of organic groups can be realised in this way. The advantage of such method is that the mesostructure of the starting silica phase is usually retained, whereas the lining of the walls is accompanied by a reduction in the porosity of the hybrid material (although depending upon the size of the organic residue and the degree of occupation). In the case of the preferential reaction of the organosilanes at the pore openings during the initial stages of the synthetic process, the diffusion of further molecules into the centre of the pores can be reduced. So, a nonhomogeneous distribution of the organic groups within the

pores may be obtained, with a lower degree of occupation. In the case of very bulky organic residues this can lead to complete closure of the pores (pore blocking).

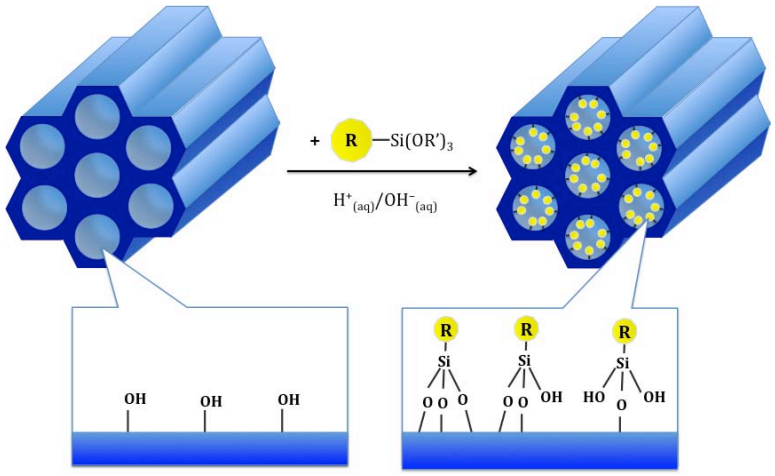

Scheme 3.2 *Postsynthetic functionalisation for organic modification of mesoporous silica materials with terminal organosilanes. R = organic functional group.*

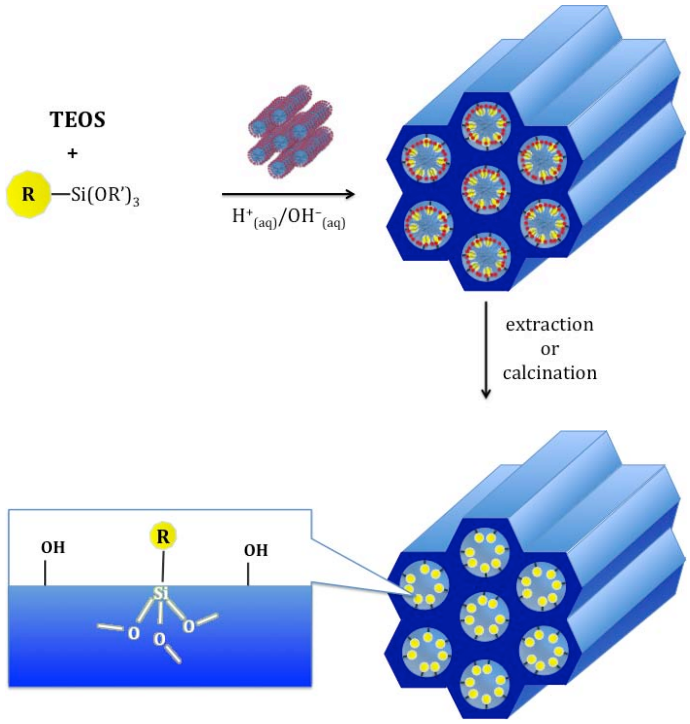

Scheme 3.3 *Co-condensation method for the functionalisation of mesoporous silica materials. R = organic functional group.*

The second method to synthesise mesoporous silica nanoparticles with an organically functionalised surface is the *co-condensation* method (ii), which is a one-pot synthesis. It is based on the co-condensation of tetraalkyloxysilane (TEOS or TMOS) with terminal trialkoxyorganosilanes ($(R'O)_3SiR$) in the presence of structure-directing agents, leading to nanoparticles with organic residues bonded covalently to the pore walls (**Scheme 3.3**). By using structure-directing agents known from the synthesis of pure mesoporous silica phases (for instance, MCM or SBA silica phases), organically modified silicas can be prepared in such a way that the organic functionalities project into the pores. Since through this method the organic functionalities are direct components of the silica matrix, pore blocking is not a problem. Moreover, the distribution of the organic units is generally more homogeneous than the one in functionalised mesoporous silica obtained by grafting method.

However, there are some disadvantages in co-condensation method: in general, the higher the concentration of ($(R'O)_3SiR$) in the reaction mixture is, the more the degree of mesoscopic order decreases, which ultimately leads to totally disordered silica structure. As a consequence, the content of organic functionalities in the modified silica phases does not normally exceed 40 mol %. Furthermore, the proportion of terminal organic groups that are incorporated into the pore-wall network is generally lower than would correspond to the starting concentration of the reaction mixture. This is due to homocondensation reactions, which are favoured in the case of a high proportion of $(R'O)_3SiR$ in the reaction mixture, at the cost of cross-linking co-condensation reactions with the silica precursors. The tendency towards homocondensation reactions is a constant problem in co-condensation because the homogeneous distribution of different organic functionalities in the framework cannot be guaranteed. Moreover, an increase in loading of the incorporated organic groups can lead to a reduction in the pore diameter, pore volume, and specific surface areas. Another disadvantage is that care must be taken not to destroy the organic functionality during removal of the surfactant, which is why commonly only extractive methods can be used, and calcination is not suitable in most cases.

The third method (iii) to prepare ordered mesoporous hybrid materials is based,

again, on the sol-gel approach in presence of a SDA, but instead of applying tetraalkoxysilanes, bridged silsesquioxane precursors of the type $(R'O)_3Si–R–Si(OR')_3$ are used, *i.e.* precursors that are capable of undergoing cross-linking reactions and concurrently carry the organic functionality R *a priori* on board, leading to materials in which the density of the organic functional groups cannot be higher (**Scheme 3.4**). Through this pathway, the so-called *periodic mesoporous organosilica* (PMOs) are obtained.[36]

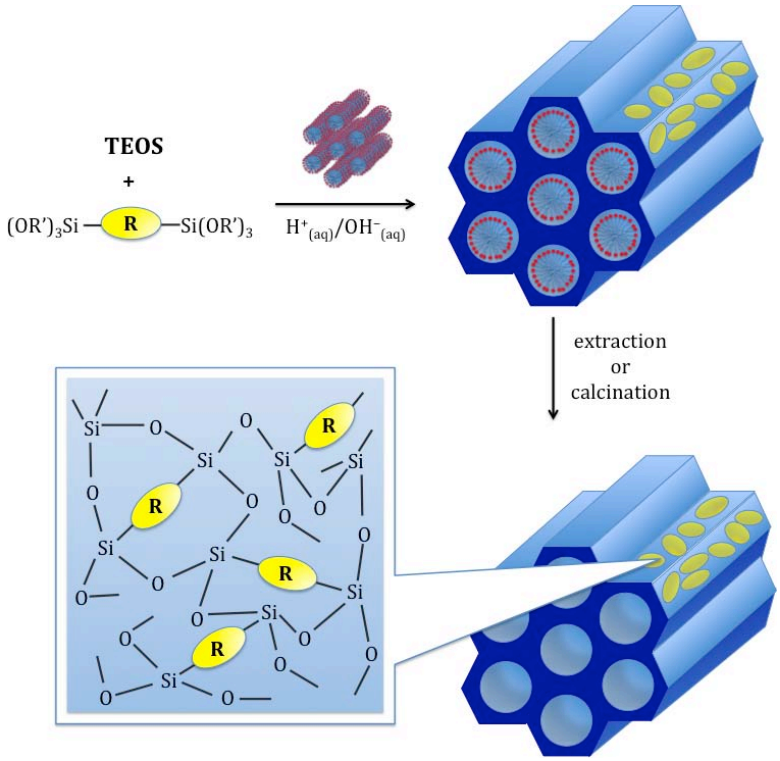

Scheme 3.4 *Schematic synthesis of PMO silica nanoparticles. R = organic bridge.*

As it may be expected, since the organic groups are covalently bonded and embedded within the mesoporous silica matrix, they are indeed an integral part of the pore walls, leading the framework itself being modified. The organic and inorganic parts are completely homogeneously mixed at the molecular scale within the whole sample. This is different from the material obtained from (i) and (ii) methodologies, in which a more or less unaffected pure inorganic substrate is functionalised on the surface with organic groups; PMOs might be probably better described as materials with mixed compartments.

As long as only one type of a bis- or multi-silylated precursor is employed the formation of PMOs belongs to the single-source precursor method. However, it is also possible to carry out SDA mediated sol-gel processes with two or more bridged silsesquioxanes to give PMOs in which two or more different organic groups are homogeneously incorporated. Furthermore, the "PMO approach" can be combined with, in particular, the co-condensation method, *i.e.* using mixtures of bridged bis(trialkoxysilyl)organosilanes [$(R'O)_3Si–R–Si(OR')_3$] and terminal trialkoxysilylorganosilanes [$(R'O)_3SiR''$]. If an appropriate precursor is chosen, post modification of PMOs is also possible.

3.3 *Host-guest systems*

The insertion of guest species into mesoporous silica nanoparticles can be achieved in to way: (i) the introduction of guest species into silica-surfactant mesostructures during the synthesis and (ii) the introduction of guest species into the mesoporous solids, after the micellar template is extracted.

Method (ii) consists in extracting, after the synthesis, the micellar template, leaving the pores hollow, which can be loaded with guest molecules by diffusion.[37] However, this method presents two disadvantages: a considerable amount of material (*e.g.* the surfactant used for the template) is entirely discarded, a factor that, at industrial scales, drives up costs; secondly, guests tends to get placed near the pore entrances, so it is difficult obtaining a uniform organisation of dye molecules along the entire pores via diffusion.

Method (i), can be performed at least via three approaches that allow for the introduction of guest species/functional units into the host-guest systems based on silica-surfactant mesostructures:

(1) solidification from precursor solution containing soluble silica source and surfactant with dissolved functional guest species;

(2) complexation of silica source with amphiphilic molecules working as supramolecular template and functional unit;

(3) polymerisation of organosilanes, bearing covalently bound functional units, with surfactant (co-polymerisation of functional organosilanes with tetraethoxysilane has also been employed), that correspond to the functionalisation of silica materials

seen above (so, it will not further discussed).

It is possible to convert the inorganic-surfactant mesostructured materials prepared by approach 3 into mesoporous ones by template removal keeping the organic functionality. The materials obtained by approaches 1 and 2 can also be transformed into mesoporous silicas, after the extraction (or just decomposition) of guest species. In these cases, the guest species were used to modify the size and shape of the resulting mesopores.

3.3.1 *Approach 1: solidification from precursor solution containing soluble silica source and surfactant with dissolved functional guest species*

This method was the very first approach to complex chromophores with silica-surfactant mesostructured materials (**Scheme 3.5**). Hydophobic dyes, such as pyrene and pyranine, have been incorporated as luminescence probes into silica-surfactant mesostructured materials.

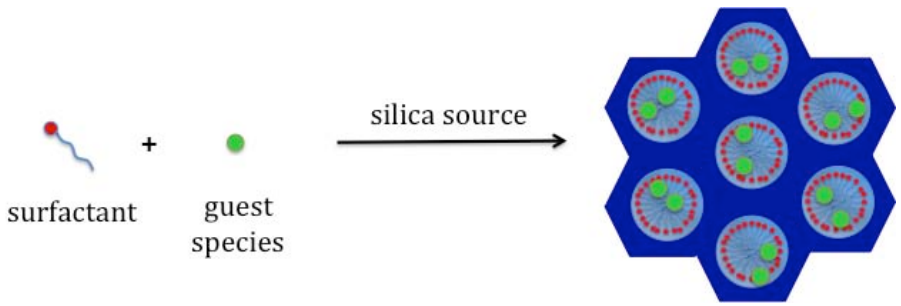

Scheme 3.5 *Approach 1: solubilising guest species into the silica-surfactant mesophase.*

Photoluminescence spectra (and in particular the monomer to excimer intensity ratio) showed that pyrene was incorporated into the hydrophobic part (probably surrounded by alkyl chains of surfactant) of the silica-CTAC (CTAC = hexadecyltrimethylammonium chloride) mesostructured materials without evidence of aggregation even at a high loading level; the molar ratio of included pyrene to surfactant (CTAC) was as high as 1:9, which is extremely high if compared with their solubilisation into surfactant mesophases in aqueous solutions.[38,39] Pyrene was solubilised molecularly in the silica-CTAC mesostructured material and the diffusion of pyrene was restricted significantly. The mesophase of CTAC aggregate was determined by the synthetic conditions (mainly the concentration and the silica to surfactant ratio) and the transformation between mesophases (for example,

lamellar, hexagonal and cubic) was less plausible after the solidification with silica.

The pyrene luminescence (monomer to excimer intensity ratio) as a function of temperature revealed, in this kind of systems, that the microviscosity of the microenvironments surrounding the probe molecule (surfactant mesostructures immobilised by silica) was lower at lower temperature, as confirmed by temperature-dependent changes of the infrared absorption bands due to C–H stretching vibration.[38-49] Thus, the photoluminescence probe study using pyrene provided a fundamental understanding of silica-CTAC mesostructured materials films: (i) inclusion capacity for the guest is comparable if compared with that for CTAC aggregates in aqueous CTAC solution (it will be different when applying different surfactant and guest); (ii) the guest was molecularly isolated surrounded by the alkyl chain; (iii) diffusion of guest is limited due to the dense packing of CTAC; (iv) transition of gel-to-liquid crystalline states was observed; (v) the transformation between different mesophases is less plausible if compared with surfactant aggregates in solution.

The solidification from precursor solution containing soluble silica source and surfactant with dissolved functional species mentioned above has been utilised, for instance, to prepare hybrids with immobilised functional dyes. Chlorophyll and phthalocyanines have been employed to construct the silica-surfactant mesostructures, where the dye aggregation was suppressed as indicated by the visible absorption spectra of the solid products.[43-46] Luminescence of pyranine was utilised to examine the formation of mesostructure during dip-coating of the precursor solution containing soluble silica source and surfactant with dissolved pyranine on substrate by solvent evaporation.[41,47]

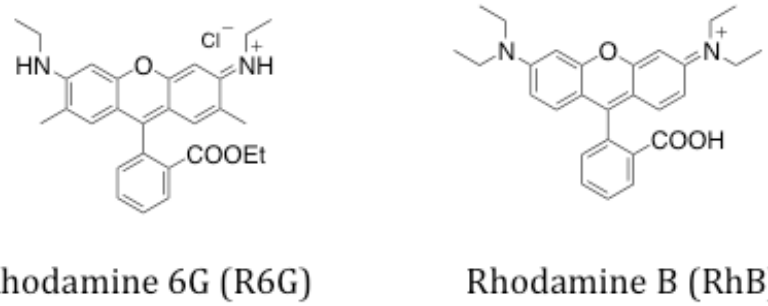

Figure 3.3 *Molecular structure of rhodamines trapped in silica nanoparticles in previous works.*

Rhodamines have been immobilised into optically transparent solids (organic polymers and silica gels) for the application to solid-state lasing device. Hoppe *et al.* has reported, for the first time, the inclusion of Rhodamine B (RhB, **Figure 3.3**) into mesoporous silica, titanium-containing MCM-41.[44] Marlow *et al.* synthesised Rhodamine 6G (R6G, **Figure 3.3**) included silica-hexadecyltrimethylammonium bromide (CTAB) mesostructured materials in the form of fiber[48] and investigated the photoemission from the fiber as a function of pump intensity utilising second harmonic of a Nd:YAG laser (532 nm). Later on, rhodamine 6G was incorporated into silica-block copolymer ((polyethylene oxide)-(polypropylene oxide)-(polyethylene oxide), PEO-PPO-PEO, product name P123) hybrids to observe amplified spontaneous emission.[49] It should be noted here that since it is possible to obtain silica-tri-block copolymer composites as macroscopically controlled morphologies (film and monolith), accordingly the optical application and the detailed characterisation are more realisable.

In this field, photochemical reactions have been also studied, for example the photochromic reactions of spiropyran and spirooxazine included into silica-triblock copolymer (P123) mesostructured films, probably at the organic domain, prepared by dip-coating using dye-dissolved sol-gel precursor solution.[50] When the dye content (or capacity) is low, thick films could be obtained, which led to an absorbance large enough to evaluate photochemical reactions by conventional instruments. The resulting materials exhibited typical photochromism of spiropyran or spirooxazine, between colourless and coloured upon UV irradiation and thermal bleaching. It was claimed that the response time required for the spirooxazine to the coloured form by light irradiation was very fast, making the materials attractive for optical recording (rapid recording). Ariga *et al.* used an oligopeptide-functionalised surfactant to be complexed with silica, and the resulting mesostructured silica hybrid film was shown to accommodate spiropyran.[51]

In general, for the optical and photochemical applications of the dye-containing silica-surfactant mesostructured materials, the limited capacity of the dye (guest) is not an important problem because dye generally possessed a large enough extinction coefficient to be easily detected by optical spectroscopy and, in the case of films, the thickness can be tailored to obtain sufficient absorption. Thus, silica-surfactant

mesostructured materials are attractive host materials for luminescent and photochromic dyes. The covalently bound (grafted) photochromic moieties on the mesopore surface of mesoporous silicas (not silica-surfactant mesostructures) have another possibility toward various photoresponsive materials.

The solubilisation of various molecular species into surfactant aggregates in solutions such as micelles and vesicles as well as those on substrates (*e.g.* Langmuir-Blodgett film) has been studied quite extensively.[52] As to the synthetic chemistry of mesoporous materials, trimethylbenzene and alkane were solubilised into the quaternary ammonium surfactant during the preparation of MCM-41 in order to expand the pore size.[53] Polyglycerol esters of fatty acids were swollen with n-decane to be used as template for mesoporous silica microsphere with the interconnected pore from the exterior to interior.[54] Furthermore, surfactant mixtures with different alkylchain length were used as a mesostructure template to control pore size precisely.[55] Cationic and anionic surfactant mixture was shown to be useful for the nanostructure design.[56] Thus, the solubilisation (or dissolution) of guest species into surfactant aggregate (mesophase) has been conducted not only as a way to incorporate guest species into inorganic-surfactant mesostructured materials but also from the viewpoints of designing the size, shape, and interconnection of mesopore. It is also interesting to see what will happen when the swelling agent is removed from the silica-surfactant mesostructure leaving surfactant in the products.

3.3.2 *Approach 2: complexation of silica with amphiphilic molecules containing functional groups*

Mesostructured hybrid with densely packed functional units can be obtained by hybridisation of amphiphilic functional compounds with silica source through sol-gel process (**Scheme 3.6a**). The possible dense packing of functional units with periodicity is an important difference between approaches 1 (incorporation of guest species into silicasurfactant mesostructured materials) and 2 (hybridisation of amphiphilic functional compounds with silica). Amphiphilic metallophthalocyanine was allowed to react with tetraethoxysilane for condensation to give one-dimensional ordered stacking of molecular disk (metallophthalocyanine).[57] Cu-phthalocyanines were stacked as a single column isolated by a silica wall. One-dimensional columnar

charge transfer (CT) complexes were immobilised in mesostructured silica film by sol-gel reaction of the CT complexes of an amphiphilic triphenylene donor and several acceptors.[58] The CT complexes exhibited absorption red shift, suggesting a long-range structural order in the products, which reflects densely packed CT complex maintained by silica. Amphiphilic ferrocene, ferrocenyl-trimethylundecylammonium, was also employed to produce potentially redox active composites with electrochemical interests.[59]

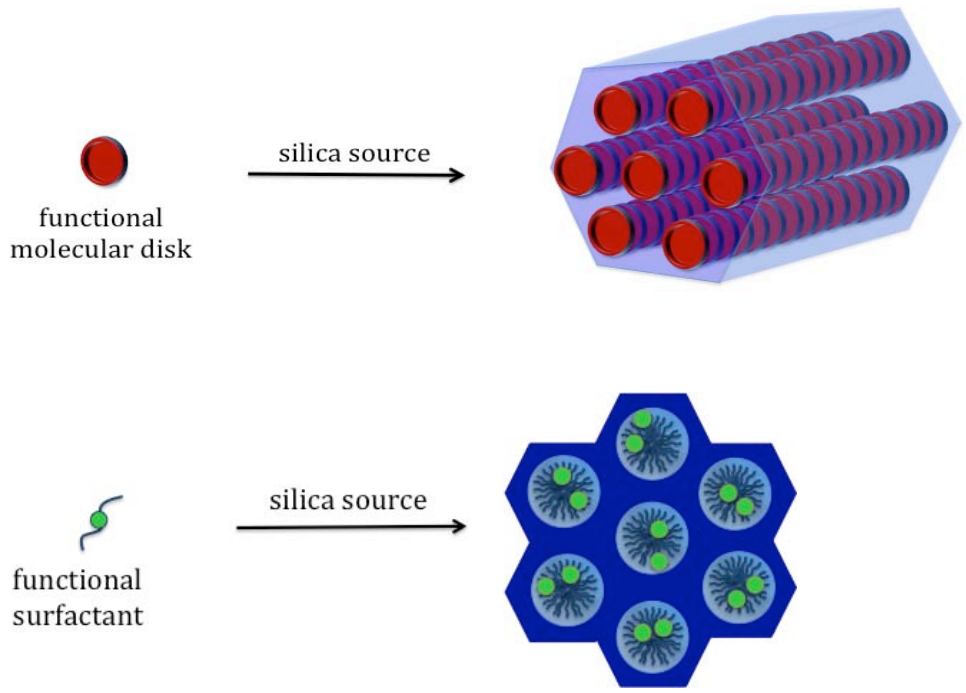

Scheme 3.6 *Approach 2: Use of amphiphilic functional compounds as supramolecular template as well as functional unit; silica-organic hybrids.*

Polymerisation of monomers in the solid state (after complexed with silica) requires appropriate dense packing of monomer (**Scheme 3.6b**). Conjugated polymer-silica mesostructured materials have been prepared using amphiphilic diacetylene monomers.[60] Mesostructures (lamellar, hexagonal and cubic) of the silica-diacetylene mesostructured materials were designed by the head groups of the amphiphilic compounds, since the proximity of the diacetylene moieties strongly influences the polymerisation process.

The effect of the mesostructures on the polymerisation of diacetylene was demonstrated by the fact that the polymerisation of diacetylene was preceded for the

lamellar and hexagonal mesophases by UV irradiation and subsequent heat treatment, while polymerisation was inhibited for the cubic mesophase. The packing of the diacetylene moieties in the lamellar and hexagonal mesostructured materials allowed topochemical polymerisation to produce coloured polydiacetylene.

The design of the diacetylene moiety and the hybridisation with silica led to optically transparent polydiacetylene-silica mesostructured materials, which are mechanically robust if compared with conventional pristine polydiacetylene.

The colour of the hybrid materials changed in response to thermal, mechanical and chemical stimuli, which may be useful for their application as sensors of various targets. One of the advantages of the hybrids of amphiphilic functional compounds is the densely packed periodic mesostructures, which made the efficient intermolecular interactions (and subsequent polymerisation and CT complexation) possible. Since various amphiphilic functional molecules containing a long chain alkyl group as the hydrophobic part and an ionic or polar group as the hydrophilic part are available, approach 2 is versatile and can be combined with approaches 1 and 3 for further variation of the materials. Mesoporous materials were also obtained by the removal of the amphiphilic functional compounds (which act both as structure directing agents and functional guest species) from the hybrids (approach 2) by calcination, as exemplified by the amphiphilic metallophthalocyanine-silica hybrids, which were transformed into mesoporous silica with the pore radius of about 2.35 nm and the Brunauer–Emmett–Teller (BET) surface area of about 1000 m^2g^{-1}.[57]

3.4 *Energy Transfer processes*

As explained in Chapter 1, an energy transfer process, in which an excited D species transfers its energy to an acceptor A, can occur via dipole-dipole interaction (Förster mechanism) and/or via electron exchange (Dexter mechanism). Several review articles have examined energy transfer processes not only in solution and biological system, but also in hybrid materials such as zeolites, clays and polymeric nanoparticles.[61,62,63,64,65,66] Photochemical and photophysical aspects of energy transfer in liquid solutions and hybrid materials have been reviewed, as also ultrafast photochemical reactions in homogeneous liquids including intra- and intermolecular charge-transfer processes, the design of optical artificial antennas using hybrid

materials, dye-doped latex nanoparticles and molecular antennas based on D and A dyes.[65,67]

As discussed in previously, dyes (D and A) can be adsorbed on the silica surfaces or within their nanochannels, in which the cavities of microporous and mesoporous structures provide distance between D and A in a range from 20 to 100 Å. At these distances, a Förster energy transfer process may occur in a timescale of the order of femtoseconds to milliseconds.[65,68,69,70,71] To the best of our knowledge, energy transfer processes occurring in all the systems involving silica-based materials are Förster-type. The confining space afforded by the nanochannels of the mesoporous materials and most of the zeolite structures allows dyes to orient and pack when being encapsulated, thus promoting ways to "control" their relative orientation and distance between different D and A units for the energy transfer process. Consequently, this allows the assembling and tuning of photonic antennas, which *are based* on energy transfer.[63,65,71,72,73,74,75] The related process can also manifest when the excited encapsulated partners directly interact with the silicate framework, thus affecting the efficiency of other competitive processes.

The ability of mesoporous silica materials to encapsulate a variety of aromatic molecules and their silica framework, which its attitude to be easily chemically modifiable, make them the hosts of choice for the fabrication of nanoantenna-based composites. The encapsulation can significantly stabilise the guest species (D and A), leading to a more efficient Förster energy transfer. The narrower space in the nanopores of silica materials may promote molecular events that might not be possible in solution. Some D and A molecules in solutions do not exhibit energy transfer, while, when trapped into the pores, they show intermolecular energy events. For example, TPC1 (**Figure 3.3**) fluorescence behaves normally in solution, but if it is encapsulated in MCM-41 pores, it behaves differently.[76] In dichloromethane solutions, two fluorescence lifetimes (800 and 3.5 ps) are observed, assigned to neutral and anion forms, respectively. When TPC1 is trapped in MCM-41, an additional small and shorter component (180 ps) is observed, attributed to a self-quenching due by an energy transfer process.[76]

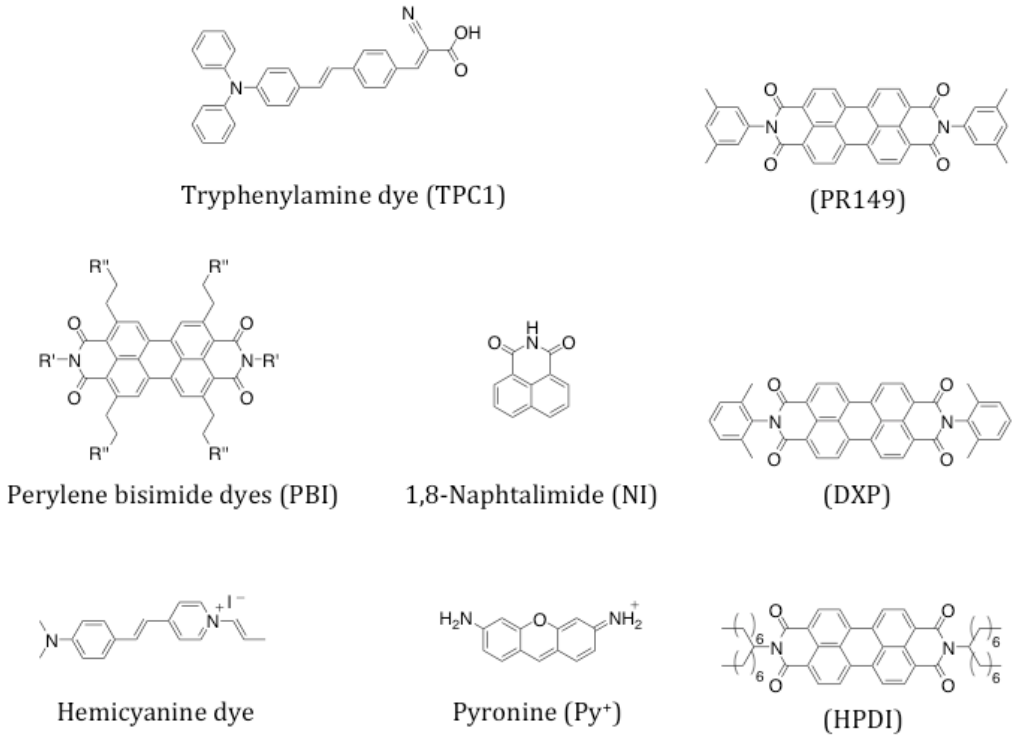

Figure 3.4 *Molecular structures of compounds interacting with silica based materials.*

The strength of the interaction of a trapped guest with the OH groups of the framework surface and the nanosized pores of its channels can also alter the energy transfer between encapsulated dyes. This has been demonstrated in a study in which the Förster energy transfer efficiency between Rhodamine 6G (R6G, **Figure 3.3**), acting as donor, and Rhodamine B (RhB, **Figure 3.3**) as acceptor, was enhanced due to the variation in the strength of interaction of both partners with the MCM-41, MCM-48, and SBA-15 mesoporous materials.[77] The three-dimensional structure of MCM-48 results being the most favourable for the energy transfer process since its channels can highly disperse the dye molecules.

The energy transfer efficiency can also be controlled by modifying the framework properties introducing metal atoms (doping). The effect of doping was demonstrated for MCM-48 materials having Al and Ce atoms in their frameworks.[77] The presence of these metal atoms decreases the energy transfer efficiency because of an increase in the ability of the material to accept an electron from the D molecule (R6G).[77] The energy transfer process between caged dyes can be regulated by doping the framework with metal atoms of different oxidation abilities (here Al and Ce atoms).

Adjusting these properties enables different colours of emission from these composites to be observed, which could be of potential interest in photonics and sensing.

Another methodology for synthesising host-guest antenna systems based on silica materials is doping directly the donor species into the mesoporous material framework or bound it covalently to the inner walls; the acceptor is encapsulated within the nanochannels. There were studied dye-doped PMOs films with different host-guest arrangements, where a fluorescent tetraphenylpyrene (TPPy)-silica mesostructured film acts as the host donor and perylene bisimide (PBI, **Figure 3.4**) acts as the guest acceptor.[74] It was demonstrated changing substituents in the PBI molecular structure alters the energy transfer efficiency, so as leads to competitive processes (energy and electron transfer).[74]

Förster energy transfer was reported between 1,8-naphthalimide (donor) (NI in **Figure 3.4**) covalently linked to the mesoporous silica host and trapped N,N′-bis(2,6-dimethylphenyl)-3,4,9,10-perylenediimide (PR149 in **Figure 3.4**) as acceptor.[78] The optical properties of these complexes can be tuned depending on the concentration of NI in the nanostructure. At lower concentrations of NI, a blue emission is recorded and assigned to monomers; higher NI loading causes a green emission, attributed to aggregate species.[78] The Förster radius was indeed found to be dependent on sample concentration, with an energy transfer more efficient in the case of higher loadings. For these composites, the emission spectra span the whole visible spectrum, making them strong candidates for white-emitting LEDs.

An important factor to consider for the efficiency of the energy transfer processes in these hybrid systems is the concentration of D and A species, also considering the typology of mesoporous silica nanoparticles used as hosts.

In a silica system containing fluorescein as donor and RhB as acceptor (**Figure 3.4**) it has been designed and examined two types of dye-silica nanoconjugates: one based on silica nanoshells (SNS-dye) and another on silica nanoparticles (SNP-dye).[79,80] In both nanosystems the energy transfer efficiency and dynamics are affected by the concentrations of donor species. Moreover, results

indicated that the energy transfer process in SNP-dye is more efficient than the one in SNS-dye.[79] For example, the energy transfer efficiency in SNS-dye and SNP-dye with a 2:1 (D/A) ratio, is 91 and 97%, respectively. The difference was explained as a result of the different methods of synthesis of both nanoconjugates.[79] For the case of dye-doped SNP, the synthesis leads to dye-rich core formation that results in dye molecules with a high proximity, generating an energy transfer process in a more efficient way than in the SNS systems. On the other hand, an increase in the D concentration decreases the energy transfer efficiency of both complexes (60 and 66% for D:A = 3:1 in SNS and D:A = 4:1 in SNP systems) due to competitive self-quenching of D molecules.[79,80] Therefore, the interaction between D and A species within these hybrid systems grants nanostructures where Förster energy transfer is highly efficient, but an optimum concentration of both partners is needed to achieve a maximum energy transfer yield.

3.4.1 *Homo-Energy transfer and Aggregates formations*

Energy transfer between the same dye molecules (Homo-Energy transfer) within silica systems is a special case.[81,82,83] It is strongly related to the formation of molecular aggregates, whose aggregation is favoured in the confining space provided by nanochannel of mesoporous silica nanoparticles.

Many fluorescent dyes with planar molecular structures consisting of three or more fused aromatics rings, such as rhodamines,[84] pyronines, [85] thionines,[86] and oxazines[87] tend to aggregate at relatively low concentrations. This molecular packing may lead to formation of H-aggregates (face-to-face) and J-aggregates (face-to-edge), which have different spectroscopic and dynamical behaviours. Classical exciton theory predicts a splitting of the monomer excited state level to higher and lower exciton bands of the aggregates. H-aggregates are characterised by absorption bands at high energies (S_0–>S_2 transitions), and the S_0–>S_1 transition is not allowed.[88,89] On the other hand, J-aggregates exhibits absorption bands at lower energies (S_0–>S_1 transitions).[88b,90] H- and J-aggregates have different dynamics than their monomer species. Generally, aggregates show emission lifetime shorter than monomer's one because of efficient deactivation processes (such as energy transfer) that are caused by the molecular packing of the monomer.[88,89,90] Furthermore, for H-aggregates, this

emission quenching is high because the low probability of a radiative decay from a S_2 state.[88b,91]

When the monomers are encapsulated within the nanomaterial pores, aggregates formation can be either favoured or inhibited, depending on the molecular structure of the guest an the type of silica-based material used. Hemicyanine dyes (**Figure 3.4**) that were encapsulated in nanosize pores of zeolites show this kind of behaviour.[92] Steady-state experiments indicated high fluorescence quenching as the concentration of the dye increased and the intermolecular distance shortened (from 12.6 to 2.1 nm).[92] The emission quenching was explained in terms of an intermolecular dipole-dipole interaction (Förster mechanism) between the dye molecules (*i.e.*, one excited hemicyanine molecule transfers its electronic energy to a hemicyanine in the ground state). Analysis of the time-resolved data showed that efficient energy transfer occurs when the intermolecular distance is longer than 5 nm (R_0 = 2.2 nm). The emission decays were fit with a biexponential function. The shorter average time constant (800 ps) was assigned to the lifetime of guest molecules near each other, and a 2.2 ns time constant was attributed to monomers that were not interacting with others.[92]

Another example of a molecule that forms caged aggregates is Py, a xanthene-derivative dye (**Figure 3.4**). Different loadings of Py encapsulated in zeolite L have been investigated.[85c] At highly diluted conditions (0.6% loading), the composite exhibits similar behaviour to that observed for the free Py in solution, indicating that the caged Py molecules are present as isolated monomers.[85c] However, at higher concentrations (20% loading), the caged Py molecules form J-aggregates, generating additional red-shifted transitions and shortening the fluorescence lifetimes. At this loading biexponential fluorescence was observed, with lifetimes of 0.7 and 2.9 ns, assigned to J-aggregates and monomers inside the zeolite, respectively.[85c] Similar observations have been reported for perylene dyes (N,N′-bis(2,6-dimethylphenyl)-3,4,9,10-perylenetetracarboxylic diimide (DXP), N,N′-bis(3,5-dimethylphenyl)-3,4,9,10-perylenetetracarboxylic diimide (PR149), and N,N′-bis(1-hexylheptyl)-3,4,9,10-perylenetetracarboxylic diimide (HPDI), **Figure 3.4**) interacting with zeolite L.[93] Interestingly, for these composites, the presence of substituents on the pyrene structure can inhibit or favour the molecular packing.[93] DXP exhibits aggregation,

while PR149 and HPDI do not show it. Another factor that obviously influences the formation of aggregates is the concentration of the dye inside the zeolite cavities. This controllable factor provided to observe interesting behaviour of DXP/zeolite L composites, whose spectroscopic properties strongly depend on the loading. Under diluted dye suspensions, monomers emission is mainly recorded (with a lifetime of 3.8 ns), while at high dye loadings, a significantly shorter lifetime (from 1.7 to 0.7 ns), assigned to J-aggregates, was reported.[93] In contrast, the voluminous groups of PR149 and HPDI prevent these dyes from packing at the sufficiently short centre-to-centre distance that is needed for strong coupling.[93]

Part of my work on this topic, have been focused on preparing and studying the properties of hybrid materials (guest filled mesoporous silica) with peculiar photophysical properties (see Chapter 5) and new structures and functionalities (see Chapter 6).

References

1) C. J. Brinker, G. W. Scherer, *Sol-Gel Science: The Physics and Chemistry of Sol-Gel Processing*, Academic Press, New York, **1990**.

2) D. Brühwiler, G. Calzaferri, T. Torres, J. H. Ramm, N. Gartmann, L.-Q. Dieu, I. López-Duarte, M. V. Martínez-Díaz, *J. Mater. Chem.*, **2009**, 19, 8040;

3) F. Hoffmann, M. Cornelius, J. Morell, M. Fröba, *Angew. Chem. Int. Ed.*, **2006**, 45, 3216 – 3251

4) J. S. Beck, J. C. Vartuli, W. J. Roth, M. E. Leonowicz, C. T. Kresge, K. D. Schmitt, C. T. W. Chu, D. H. Olson, E. W. Sheppard, S. B. McCullen, J. B. Higgins, J. L. Schlenker, *J. Am. Chem. Soc.*, **1992**, 114, 10834-10843.

5) A. Katiyar, S. Yadav, P. G. Smirniotis, N. G. Pinto, *J. Chromatogr. A*, **2006**, 1122, 13-20.

6) J. E. Lofgreen, G. A. Ozin, *Chem. Soc. Rev.*, **2014**, 43, 911-933.

7) C. T. Kresge, M. E. Leonowicz, W. J. Roth, J. C. Vartuli, J. S. Beck, *Nature*, **1992**, 359, 710-712.

8) G. S. Attard, J. C. Glyde, C. G. Göltner, *Nature*, **1995**, 378, 366-368.

9) A. Monnier, F. SchEth, Q. Huo, D. Kumar, D. Margolese, R. S. Maxwell, G. Stucky, M. Krishnamurty, P. Petroff, A. Firouzi, M. Janicke, B. Chmelka, *Science*, **1993**, 261, 1299-1303.

10) Q. Huo, D. I. Margolese, U. Ciesla, P. Feng, T. E. Gier, P. Sieger, R. Leon, P. M. Petroff, F. SchEth, G. D. Stucky, *Nature*, **1994**, 368, 317-321.

11) Q. Huo, D. I. Margolese, U. Ciesla,D. G. Demuth, P. Feng, T. E. Gier, P. Sieger, A. Firouzi, B. F. Chmelka, F. SchEth, G. D. Stucky, *Chem. Mater.*, **1994**, 6, 1176-1191.

12) R. Ryoo, S. H. Joo, S. Jun, *J. Phys. Chem. B*, **1999**, 103, 7743-7746.

13) J. Lee, S. Yoon, T. Hyeon, S. M. Oh, K. B. Kim, *Chem. Commun.*, **1999**, 2177-2178.

14) N. K. Raman, M. T. Anderson, C. J. Brinker, *Chem. Mater.*, **1996**, 8, 1682-1701.

15) D. M. Antonelli, J. Y. Ying, *Curr. Opin. Colloid Interface Sci.*, **1996**, 1, 523-529.

16) P. Behrens, *Angew. Chem.*, **1996**, 108, 561 – 564; *Angew. Chem. Int. Ed. Engl.*, **1996**, 35, 515-518.

17) A. Sayari, *Chem. Mater.*, **1996**, 8, 1840-1852.

18) X. S. Zhao, G. Q. Lu, G. J. Millar, *Ind. Eng. Chem. Res.*, **1996**, 35, 2075-2090.

19) J. Y. Ying, C. P. Mehnert, M. S. Wong, *Angew. Chem.*, **1999**, 111, 58-82; *Angew. Chem. Int. Ed.*, **1999**, 38, 56-77.

20) G. J. de A. A. Soler-Illia, C. Sanchez, B. Lebeau, J. Patarin, *Chem. Rev.*, **2002**, 102, 4093-4138.

21) A. Stein, *Adv. Mater.*, **2003**, 15, 763-775.

22) Y. Wan, D. Zhao, *Chemical Reviews,* **2007**, 107 (7), 2821-2860.

23) D. Zhao, J. Sun, Q. Li, G. D. Stucky, *Chemistry of Materials*, **2000**, 12 (2), 275-279.

24) Q. Huo, D. I. Margolese, G. D. Stucky*, *Chemistry of Materials*, **1996**, 8 (5), 1147-1160.

25) S. Schacht, Q. Huo, I. G. Voigt-Martin, G. D. Stucky, F. Schüth, *Oil-water interface templating*

of mesoporous macroscale structures. Science-New York then Washington, **1996**, 273, 768-770.

26) H. Yang, G. Vovk, N. Coombs, I. Sokolov , G. A. Ozin, *J. Mater. Chem.*, **1998**, 8, 743-750.

27) Y. Lu, H. Fan, A. Stump, T. L. Ward, *Nature*, **1999**, 398, 223-226.

28) J. C. Vartuli, K. D. Schmitt, C. T. Kresge, W. J. Roth, M. E. Leonowicz, S. B. McCullen, S. D. Hellring, J. S. Beck, J. L. Schlenker, and *Chemistry of Materials*, **1994**, 6 (12), 2317-2326.

29) J. S. Beck, J. C. Vartuli, W. J. Roth, M. E. Leonowicz, C. T. Kresge, K. D. Schmitt, C. T. W. Chu, D. H. Olson, E. W. Sheppard, S. B. McCullen, J. B. Higgins, and J. L. Schlenker *Journal of the American Chemical Society*, **1992**, 114 (27), 10834-10843.

30) D. Zhao, J. Feng, Q. Huo, N. Melosh, G. H. Fredrickson, *Science*, **1998**, 279: 548-552.

31) H. P. Lin, C. Y. Mou, *Microporous and mesoporous materials*, **2002**, 55, 69-80.

32) A. Sayari, M. Kruk, M. Jaroniec, I. L. Moudrakovski, *Advanced Materials*, **1998**, 10, 1376-1379.

33) D. Khushalani, A. Kuperman, G. A. Ozin, K. Tanaka, N. Coombs, *Advanced materials*, **1995**, 7, 842-846.

34) J. M. Kim and R. Ryoo, *Bull. Korean Chem. Soc.*, **1996**, 17, 66-68.

35) A. P. Wight, M. E. Davis, *Chem. Rev.*, **2002**, 102, 3589-3614.

36) (a) S. Inagaki, S. Guan, Y. Fukushima, T. Ohsuna, O. Terasaki, *J. Am. Chem. Soc.*, **1999**, 121, 9611-9614; (b) B. J. Melde, B. T. Holland, C. F. Blanford, A. Stein*, Chem. Mater.*, **1999**, 11, 3302-3308; (c) T. Asefa, M. J. MacLachlan, N. Coombs, G. A. Ozin, *Nature*, **1999**, 402, 867-871.

37) (a) F. Hoffmann, M. Fröba, *Chem. Soc. Rev.*, **2011**, 40, 608-620; (b) L. Grösch, Y. J. Lee, F. Hoffmann, M. Fröba*, Chem. Eur. J.*, **2015**, 21, 331-346.

38) M. Ogawa, *Langmuir*, **1995**, 11, 4639-41.

39) M. Ogawa, T. Igarashi, K. Kuroda, *Chem. Mater.*, **1998**, 10, 1382-5.

40) H. Furukawa, T. Watanabe, K. Kuroda, *Chem. Commun.*, **2001**, **2002-2003**.

41) A. Fukuoka, K. Fujishima, M. Chiba, A. Yamagishi, S. Inagaki, Y. Fukushima, M. Ichikawa, *Catal. Lett.*, **2000**, 68, 241-244.

42) S. Subbiah, R. Mokaya, *J. Phys. Chem. B*, **2005**, 109, 5079-5084.

43) H. G. Chen, J. L. Shi, H. R. Chen, Y. S. Li, Z. L. Hua, D. S. Yan, *Appl. Phys. B*, **2003**, 77, 89-91.

44) D. Das, J.-F. Lee, S. Cheng, *Chem. Commun.*, **2001**, 2178-2179.

45) D. Das, J.-F. Lee, S. Cheng, *J. Catal.*, **2004**, 223, 152-160.

46) K. Shimizu, E. Hayashi, T. Hatamachi, T. Kodama, T. Higuchi, A. Satsuma, Y. Kitayama, *J. Catal.*, **2005**, 231, 131-138.

47) B. Sow, S. Hamoudi, M. H. Zahedi-Niaki, S. Kaliaguine, *Microporous Mesoporous Mater.*,

2005, 79, 129-136.

48) F. Marlow, M. D. McGehee, D. Y. Zhao, B. F. Chmelka, G. D. Stucky, *Adv. Mater.*, **1999**, 11, 632-4.

49) G. Wirnsberger, G. D. Stucky, *Chem. Mater.*, **2000**, 12, 2525-7.

50) G. Wirnsberger, B. J. Scott, B. F. Chmelka, G. D. Stucky, *Adv. Mater.*, **2000**, 12, 1450-4.

51) K. Ariga, *Chem. Rec.*, **2004**, 3, 297-307.

52) (a) J. H. Clint, Surfactant Aggregation, New York: Blackie, **1992**; (b) E. D. Goddard , K. P. Anathapadmanabhan, *Interactions of Surfactants with Polymers and Proteins*, Boca Raton, FL: CRC Press, **1993**; (c) A. Ulman, *An Introduction to Ultrathin Organic Films*, San Diego, CA: Academic, **1992**.

53) J. S. Beck *et al.*, *J. Am. Chem. Soc.*, **1992**, 114, 10834-43.

54) M. P. Kapoor, A. Vinu, W. Fujii, T. Kimura, Q. Yan, Y. Kasama, M. Yanagi, L. R. Juneja, *Microporous Mesoporous Mater.*, **2010**, 128, 187-93.

55) D. Khushalani, A. Kuperman, N. Coombs, G. A. Ozin, *Chem. Mater.*, **1996**, 8, 2188-93.

56) F. X. Chen, L. M. Huang, Q. Z. Li, *Chem. Mater.*, **1997**, 9, 2685.

57) M. Kimura, K. Wada, K. Ohta, K. Hanabusa, H. Shirai, N. Kobayashi, *J. Am. Chem. Soc.*, **2001**, 123, 2438-9.

58) A. Okabe, T. Fukushima, K. Ariga, T. Aida, *Angew. Chem. Int. Edn.*, **2002**, 41, 3414-7.

59) I. Honma, H. S. Zhou, *Adv. Mater.*, **1998**, 10, 1532-4.

60) (a) Y. Lu *et al.*, *Nature*, **2001**, 410, 913-7; (b) T. Aida K. Tajima, *Angew. Chem. Int. Edn.*, **2001**, 40, 3803-6; (c) H. S. Peng, J. Tang, L. Yang, J. B. Pang, H. S. Ashbaugh, C. J. Brinker, Z. Z. Yang, Y. F. Lu, *J. Am. Chem. Soc.*, **2006**, 128, 5304-5; (d) M. Ikegame, K. Tajima, T. Aida, *Angew. Chem. Int. Edn.*, **2003**, 42, 2154-7.

61) K. B. Yoon, *Chem. Rev.*, **1993**, 93, 321-339.

62) S. Hashimoto, *J. Photochem. Photobiol. C*, **2003**, 4, 19-49.

63) G. Calzaferri, S. Huber, H. Maas, C. Minkowski, *Angew. Chem., Int. Ed.*, **2003**, 42, 3732-3758.

64) J. K. Thomas, *Chem. Rev.*, **2005**, 105, 1683-1734.

65) L. Gartzia-Rivero, J. Banuelos, I. Lopez-Arbeloa, *Int. Rev. Phys. Chem.*, **2015**, 34, 515-556.

66) (a) Y. Nakamura, N. Aratani, A. Osuka, *Chem. Soc. Rev.*, **2007**, 36, 831-845; (b) J. Yang, M. C. Yoon, H. Yoo, P. Kim, D. Kim, *Chem. Soc. Rev.*, **2012**, 41, 4808-4826; (c) H. B. Rodríguez, E. San Román, *Photochem. Photobiol.*, **2013**, 89, 1273-1282.

67) T. Kumpulainen, B. Lang, A. Rosspeintner, E. Vauthey, *Chem. Rev.*, **2017**, 117, 10826-10939.

68) K. Lutkouskaya, G. Calzaferri, *J. Phys. Chem. B*, **2006**, 110, 5633-5638.

69) M. Busby, H. Kerschbaumer, G. Calzaferri, L. De Cola, *Adv. Mater.*, **2008**, 20, 1614-1618.

70) S. Ramachandra, Z. D. Popovic, K. C. Schuermann, F. Cucinotta, G. Calzaferri, L. De Cola, *Small*, **2011**, 7, 1488-1494.

71) G. Calzaferri, A. Devaux, *Manipulation of Energy Transfer Processes within the Channels of L-Zeolite. In Supramolecular Photochemistry: Controlling Photochemical Processes; John Wiley & Sons, Inc.*: Hoboken, NJ, **2011**; pp 285-387.

72) I. Lõpez-Duarte, D. Le-Quyenh, I. Dolamic, M. V. Martínez-Díaz, T. Torres, G. Calzaferri, D. Brühwiler, Chem. - Eur. J. 2011, 17, 1855-1862.

73) F. Cucinotta, F. Carniato, A. Devaux, L. De Cola, L. Marchese, *Chem. - Eur. J.*, **2012**, 18, 15310-15315.

74) N. Mizoshita, K. I. Yamanaka, S. Hiroto, H. Shinokubo, T. Tani, S. Inagaki, *Langmuir*, **2012**, 28, 3987-3994.

75) (a) P. Cao, O. Khorev, A. Devaux, L. Sägesser, A. Kunzmann, A. Ecker, R. Häner, D. Brühwiler, G. Calzaferri, P. Belser, *Chem. - Eur. J.*, **2016**, 22, 4046-4060; (b) D. D. Hu, L. Wang, J. Lin, F. Bu, T. Wu, *J. Mater. Chem. C*, **2015**, 3, 11747-11753; (c) A. Devaux, G. Calzaferri, I. Miletto, P. Cao, P. Belser, D. Brühwiler, O. Khorev, R. Häner, A. Kunzmann, *J. Phys. Chem. C*, **2013**, 117, 23034-23047; (d) G. Calzaferri, K. Lutkouskaya, *Photochem. Photobiol. Sci.*, **2008**, 7, 879-910; (e) S. Huber, G. Calzaferri, *ChemPhysChem*, **2004**, 5, 239-242.

76) M. Ziółek, C. Martín, M. T. Navarro, H. Garcia, A. Douhal, *J. Phys. Chem. C*, **2011**, 115, 8858-8867.

77) L. Wang, Y. Liu, F. Chen, J. Zhang, M. Anpo, *J. Phys. Chem. C*, **2007**, 111, 5541-5548.

78) F. d J. Trindade, E. R. Triboni, B. Castanheira, S. Brochsztain, *J. Phys. Chem. C*, **2015**, 119, 26989-26998.

79) A. Dhir, A. Datta, *Methods Appl. Fluoresc.*, **2016**, 4, 024003-024014.

80) A. Dhir, A. Datta, *J. Phys. Chem. C*, **2016**, 120, 20125-20131.

81) J. Hofkens, M. Cotlet, T. Vosch, P. Tinnefeld, K. D. Weston, C. Ego, A. Grimsdale, K. Müllen, D. Beljonne, J. L. Brédas, *et al.*, *Proc. Natl. Acad. Sci. U. S. A.*, **2003**, 100, 13146-13151.

82) S. Bonacchi, D. Genovese, R. Juris, M. Montalti, L. Prodi, E. Rampazzo, N. Zaccheroni, *Angew. Chem., Int. Ed.*, **2011**, 50, 4056-4066.

83) D. Bialas, A. Zitzler-Kunkel, E. Kirchner, D. Schmidt, F. Würthner, *Nat. Commun.*, **2016**, 7, 12949-12959.

84) (a) L. Malfatti, T. Kidchob, D. Aiello, R. Aiello, F. Testa, P. Innocenzi, *J. Phys. Chem. C*, **2008**, 112, 16225-16230; (b) J. Bujdak, N. Iyi, Y. Kaneko, A. Czimerova, R. Sasai, *Phys. Chem. Chem. Phys.*, **2003**, 5, 4680-4685; (c) V. Martínez-Martínez, F. López Arbeloa, J. Bañuelos Prieto, T. Arbeloa López, I. López Arbeloa, J. *Phys. Chem. B*, **2004**, 108, 20030-20037.

85) (a) E. Fois, G. Tabacchi, G. Calzaferri, *J. Phys. Chem. C*, **2012**, 116, 16784-16799; (b) V. Martínez-Martínez, R. García, L. Gómez-Hortigüela, J. Pérez-Pariente, I. López-Arbeloa, *Chem. Eur. J.*, **2013**, 19, 9859-9865; (c) M. Busby, C. Blum, M. Tibben, S. Fibikar, G. Calzaferri, V. Subramaniam, L. De Cola, *J. Am. Chem. Soc.*, **2008**, 130, 10970-10976; (d) R. García, V. Martínez-Martínez, L. Gómez-Hortigüela, I. López Arbeloa, J. Pérez-Pariente, *Microporous Mesoporous Mater.*, **2013**, 172, 190-199.

86) (a) G. Calzaferri, N. Gfeller, *J. Phys. Chem.*, **1992**, 96, 3428-3435; (b) W. Xu, M. Aydin, S. Zakia, D. L. Akins, *J. Phys. Chem. B*, **2004**, 108, 5588-5593.

87) (a) J. Bujdák, N. Iyi, *Chem. Mater.*, **2006**, 18, 2618-2624; (b) J. Bujdák, N. Iyi, *Colloid Polym. Sci.*, **2009**, 287, 157-165; (c) G. Chen, N. Iyi, R. Sasai, T. Fujita, K. Kitamura, *J. Mater. Res.*, **2002**, 17, 1035-1040.

88) (a) M. Kasha, H. Rawls, M. Ashraf El-Bayoumi, *Pure Appl. Chem.*, **1965**, 11, 371-392; (b) A. Eisfeld, J. S. Briggs, *Chem. Phys.*, **2006**, 324, 376-384.

89) A. Davydov, *Theory of Molecular Excitons*, *Springer*: Boston, **2013**.

90) T. Kobayashi, *J-Aggregates; World Scientific*: Singapore, **2012**; Vol. 2.

91) F. C. Spano, *Acc. Chem. Res.*, **2010**, 43, 429-439.

92) T. K. Shim, M. H. Lee, D. Kim, H. S. Kim, K. B. Yoon, *J. Fluoresc.*, **2012**, 22, 1475-1482.

93) M. Busby, A. Devaux, C. Blum, V. Subramaniam, G. Calzaferri, L. De Cola, *Phys. Chem. C*, **2011**, 115, 5974-5988.

Chapter 4

A New Heptanuclear Complex as Light-Harvesting Antenna

In Chapter 2 it has been discussed the issue of non-unidirectional energy transfer processes in Ru(II) and Os(II) polypyridine dendrimers of second generation, based on bis(2'-pyridyl)pyrazine (2,3-dpp) ligand. On the bases of these results we designed, in collaboration with the group of Garry Hanan in Montreal, a new bridging ligand based on three polypiridine chelating sites.

A representation of the tris-2'',4'',6''-(2,2'-bipyridin-4-yl)-1'',3'',5''-triazine) bridging ligand,[1] hereafter **L**, is shown in **Figure 4.1**. It has three bipyridine subunits (the chelating sites) and a 1,3,5-triazine core (unable to coordinate any metal centre).

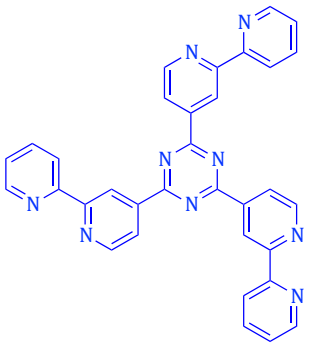

Figure 4.1 *Molecular structure of ligand **L**.*

*4.1 Synthesis and properties of ligand **L***

Ligand **L** has been prepared using liquefied (180°C) 4-cyano-2,2'-bipyridine (prepared by Negishi etero-coupling reaction)[2] in the presence of NaH (catalytic amount) in anhydrous condition under an inert atmosphere (**Scheme 4.1**). The resulting brown slurry was heated for eight hours and the reaction was then quenched with ethanol and water. The pure ligand **L** was recovered in moderate yield (60%) as a pure beige precipitate by simple filtration, without the need of any further purification.[1]

Single crystals suitable for X-ray diffraction were obtained by slow evaporation of a dichloromethane solution of **L**. As shown in **Figure 4.2**, the introduction of nitrogen atoms into the core heterocyclic ring permits the bipyridine and triazine portions of **L**

to lie co-planar, which in turn enhances electron delocalisation throughout the system. Two of the bipyridine subunits are almost perfectly coplanar with the triazine ring, with torsion angles of less than 5°. The torsion angle of the third bpy subunit is of 24.1°, which is significantly different from the two other "arms" of the molecule: π-stacking appears to be at the origin of the observed deviation from planarity, where the centroid–centroid separation (R_{cent}) and the distance between the closest atoms ($R_{closest}$) are found to be 4.09 Å and 3.65 Å, respectively, with an interplanar angle (θ_{plane}) of 18.5°. Moreover, the π-stacking explains the scarce solubility of ligand **L** in the most common solvents at room temperature.[1]

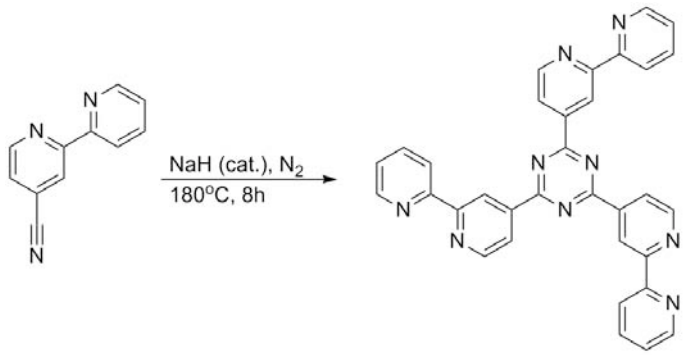

Scheme 4.1 *Synthesis of ligand **L**.*

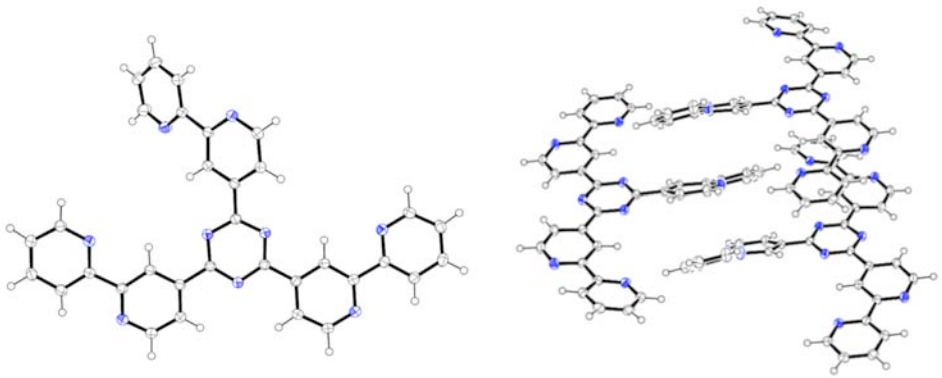

Figure 4.2 *X-ray structure of ligand **L**. On the right it is shown the packing of the ligand in solid state.*[1]

4.2 Synthesis of Ru(II) and Os(II) complexes

L have been used to resynthesize (through a different strategy) a series of Ru(II) and to prepare new Os(II) complexes, as well as a novel heterometallic trinuclear

complex, see **Figure 4.3** and **4.4**:

• the mono-, bi- and trinuclear Ru(II) complexes ($[Ru(bpy)_2L](PF_6)_2$ (**Ru1L**), $\{[Ru(bpy)_2]_2(\mu\text{-}L)\}(PF_6)_4$ (**Ru2L**) and $\{[Ru(bpy)_2]_3(\mu\text{-}L)\}(PF_6)_6$ (**Ru3L**) respectively);

• the mono-, bi- and trinuclear Os(II) complexes ($[Os(bpy)_2L](PF_6)_2$ (**Os1L**), $\{[Os(bpy)_2]_2(\mu\text{-}L)\}(PF_6)_4$ (**Os2L**) and $\{[Os(bpy)_2]_3(\mu\text{-}L)\}(PF_6)_6$ (**Os3L**) respectively);

• the mixed Ru(II)/Os(II) trinuclear complex $\{[Ru(bpy)_2]_2(\mu\text{-}L)[Os(bpy)_2]\}(PF_6)_6$ (**Ru2Os**).

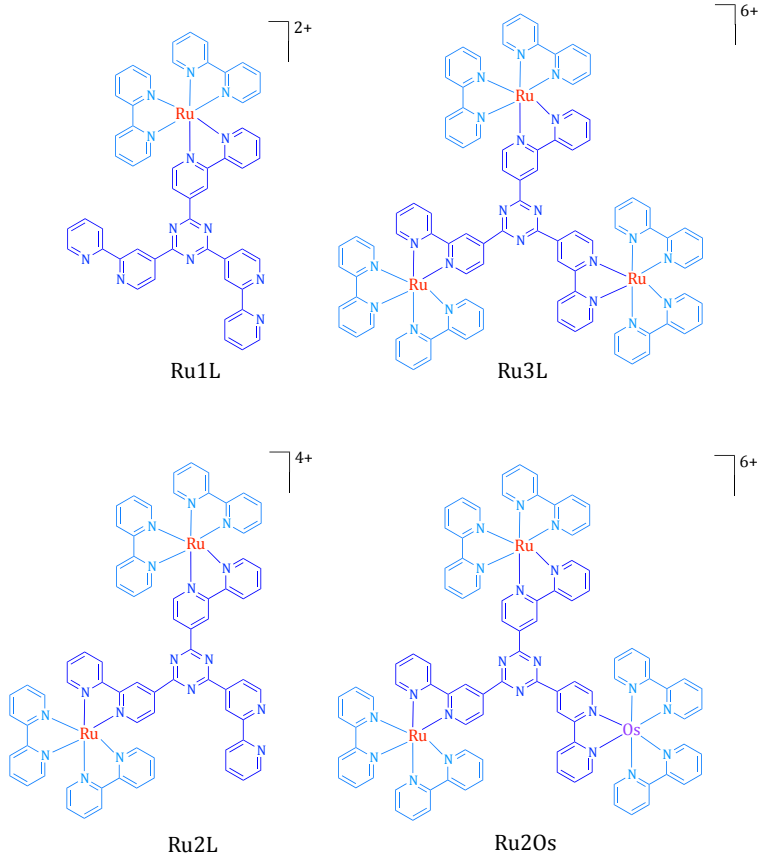

Figure 4.3 *Ru(II) and Ru(II)/Os(II) complexes taken as model. Counterions are omitted for clarity.*

Most of these species have been used as model and/or precursors for the synthesis and study of a new light-harvesting antenna: a dendritic heptanuclear species composed of six Ru(II) centre and on an Os(II) subunit $\{\{[Ru(bpy)_2]_2(\mu\text{-}L)\}_3Os\}(PF_6)_{14}$ (**Ru6Os**), shown in **Figure 4.5**.

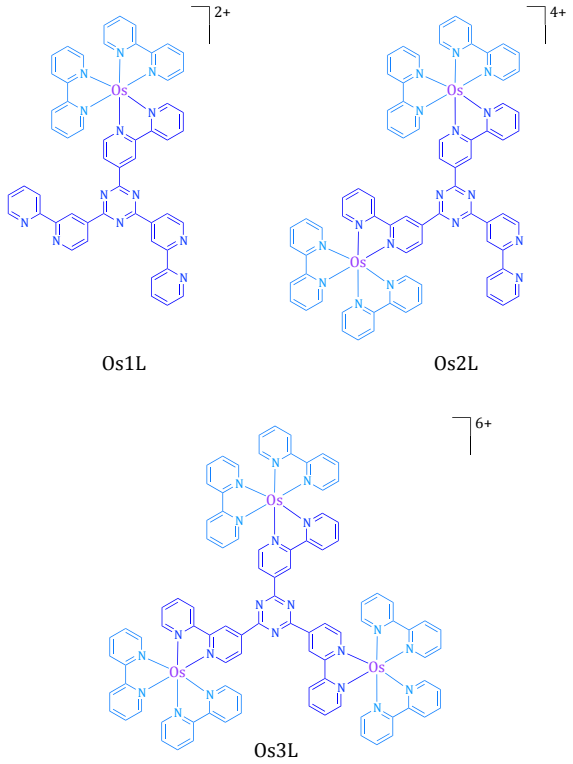

Figure 4.4 *Os(II) complexes taken as model. Counterions are omitted for clarity.*

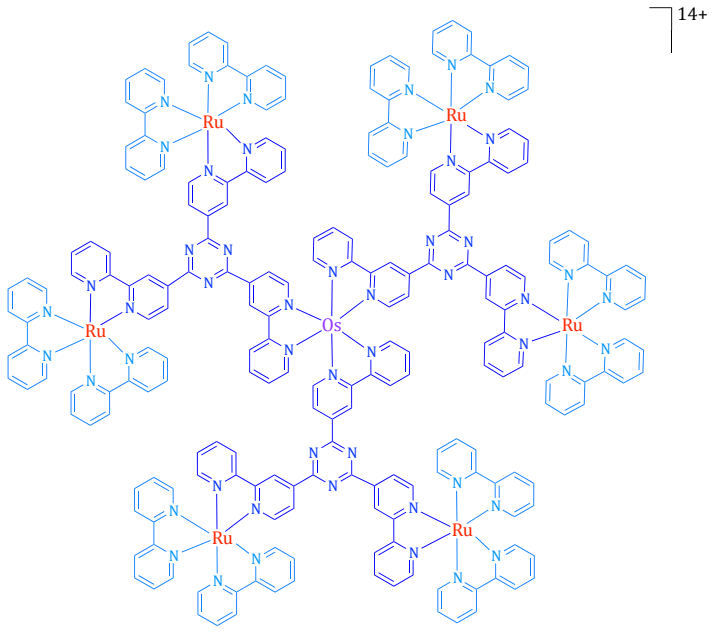

Figure 4.5 *Molecular structure of the **Ru6Os** complex synthesised. Counterion is omitted for clarify.*

The synthesis and, in particular, the purification procedures to obtain **Ru1L** and **Ru2L** have been quite difficult because the three coordination sites of **L** are chemically equivalent, so trying to obtain these ligand-complexes (that is complexes where there are present free coordinating sites) leads unavoidably to obtaining high-nuclear complexes, see Experimental Chapter. As the synthesis of the heptanuclear species has been planned to be convergent methodology shown below (see also Chapter 2, section 2.1), a large amount of the precursor **Ru2L** species is needed, therefore the strategy was focused on designing the more efficient synthetic procedure to yield **Ru2L**.

Ru2L has been obtained by the reaction between the metal-complex cis-$[Ru(bpy)_2Cl_2]$ and the bridging ligand **L** in DCM/MeOH mixture (**Scheme 4.2**). By this reaction there can obtain mono-, bi- and trinuclear species, so to increase the yield some precaution was taken: it was put a small excess of ligand **L** respect of the 2:1 stoichiometric ratio and a very concentrated solution of metal-complex was added drop wise within about 1 hour. These expedients helped achieving a good yield (65.5%); however the sub-products (both **Ru1L** and **Ru3L**) were present in the crude, especially **Ru3L**. The three species have been separated by ion exchange chromatography, thanks to the different charges of the three species (see Experimental Chapter).

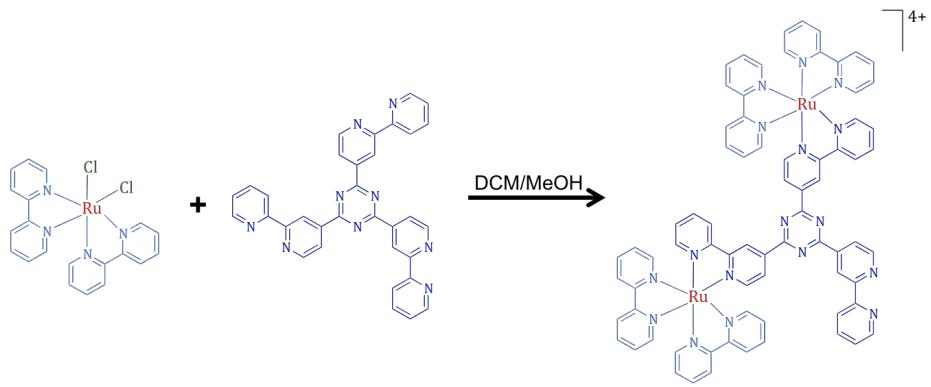

Scheme 4.2 *Synthesis of **Ru2L** complex. Counterion is omitted for clarify.*

Os_nL complexes have been synthesised by a similar methodology by the reaction between the complex-metal cis-$[Os(bpy)_2Cl_2]$ and the ligand **L** (**Os2L** synthesis

scheme is reported in **Scheme 4.3**). As previously said, the most favourable product is the trinuclear complex, so to obtain **Os1L** and/or **Os2L** species some precautions (like **Ru2L** synthesis shown above) are needed. The three species in the crude have been separated by ion exchange chromatography.

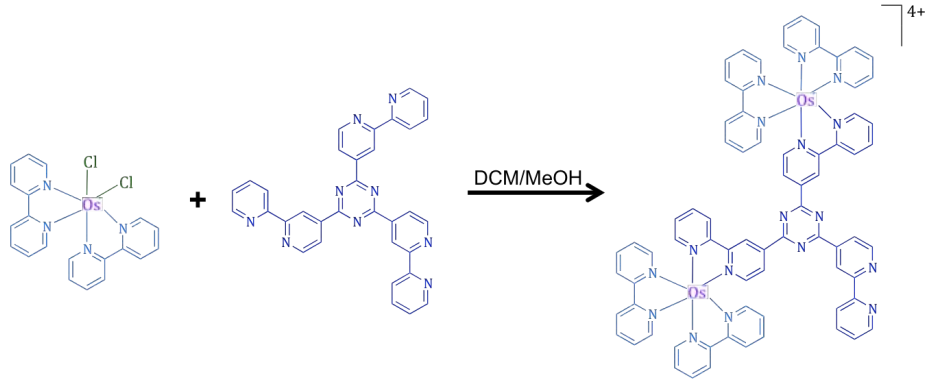

Scheme 4.3 *Synthesis of **Os2L** complex. Counterion is omitted for clarify.*

Ru2Os has been synthesised using **Ru2L** as complex-ligand and making it reacting with cis-$[Os(bpy)_2]Cl_2$ as complex-metal, in $EtOH/H_2O$ (**Scheme 4.4**).

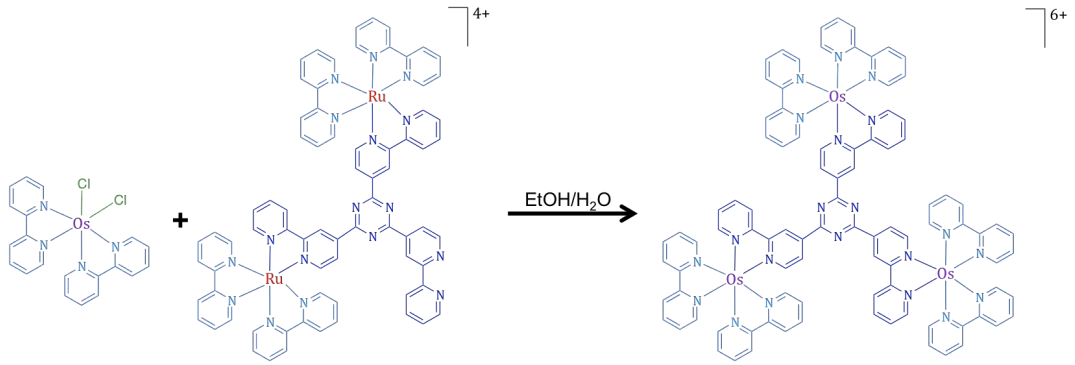

Scheme 4.4 *Synthesis of **Ru2Os**. Counterions are omitted for clarify.*

The reaction between **Ru2L** and K_2OsCl_6 in ethylene glycol (**Scheme 4.5**) allowed preparing **Ru6Os**. Since a side product is due to the incomplete coordination of the central osmium core (a pentanuclear complex bearing an Os(II) centre coordinated by two **Ru2L** and two Cl^-), to avoid its formation the reaction has been conducted with a 4:1 ratio of **Ru2L**/K_2OsCl_6. In K_2OsCl_6 the osmium is Os(IV): it is reduced to Os(III) simply in the reaction mixture; the Os(III)→Os(II) reduction is promoted by adding a sodium dithionite saturated solution. Heptanuclear complex has been

precipitated in ethanol by adding a hexafluorophosphate salt, filtered and isolated as a purple powder. The yield was 84%.

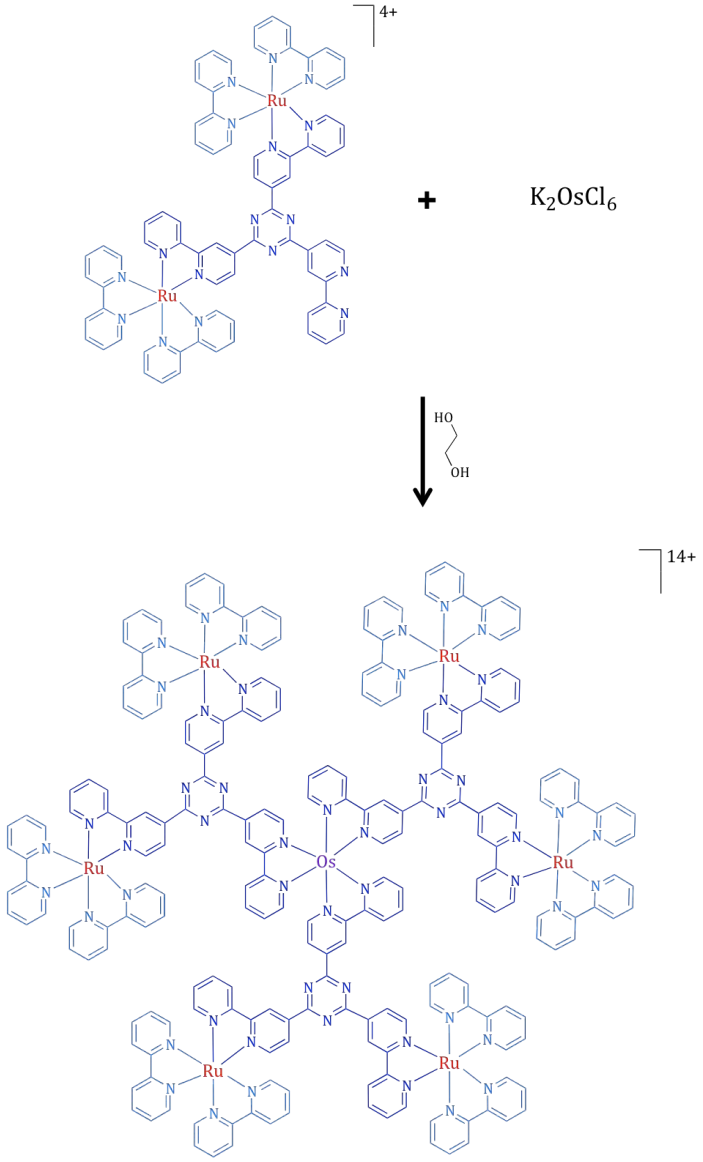

Scheme 4.5 *Synthesis of **Ru6Os** complex. Counterions are omitted for clarity.*

4.3 *Redox behaviour*

The redox behaviour of the species has been studied by cyclic and differential pulse voltammetry in degassed acetonitrile. Oxidation in Ru(II) and Os(II)

polypyridine complexes is typically centred on the metal centres and Ru(III) and/or Os(III) form, with a stable d^5 low-spin electronic configuration, in fact these oxidation processes are usually reversible. Reduction processes are instead typically centred on ligand orbitals.[3,4]

The redox properties of Ru(II) and Os(II) polypyridine species are well known and several reviews are available.[5]

In general, oxidation processes are reversible and metal centred, while reduction processes are reversible and ligand centred. Successive ligand reductions take place, even for homoleptic mononuclear compounds, and in this case reduction splitting is connected with ligand–ligand interaction as mediated by the metal-centred orbitals. In general, ligand–ligand interaction is larger for Os mononuclear species compared to homologous Ru species, as the metal-centred HOMO is closer in energy to the ligand-based LUMOs in the case of Os compounds. Each polypyridine ligand is usually reduced by one electron at mild potentials (typically, at potentials less negative than -2.00 V *versus* SCE). However, a second electron can be added to a single polypyridine ligand at more negative potentials: electron pairing takes place within 350–600 mV (*e.g.*, is 600 mV in the prototype $[Ru(bpy)_3]^{2+}$), depending on the size and delocalisation of the polypyridine ligand.[6]

Table 4.1 *Oxidation redox data in degassed acetonitrile. There are reported in square parenthesis the numbers of exchanged electron in the process.*

	$E_{1/2\ ox}$/ V *vs.* SCE	
Compound	E_{ox1}	E_{ox2}
2,2'-bpy	-	-
L	-	-
$[Ru(bpy)_3]^{2+}$	1.30 [1e]	-
Ru1L	1.31[1e]	-
Ru2L	1.33 [2e]	-
Ru3L	1.29 [3e]	-
Os2L	0.94 [2e]	-
Os3L	0.92 [3e]	-
Ru2Os	0.94 [1e]	1.30 [2e]
Ru6Os	1.02 [1e]	1.32 [6e]

A direct consequence is that when first reduction of a polypyridine ligand occurs at less negative potential, a second electron can be added to the same ligand even before first reduction of the other ligands occurs. This is actually found for the multinuclear dendrimers containing 2,3-dpp as bridging ligand, since first reduction of the bridge occurs at about -0.5 V.[7]

So, in multinuclear complexes if the metal-metal interaction is optimal it is possible seeing several consecutive processes whose separation is correlated to the electronic interaction magnitude. On the other hand, if the electronic interaction is negligible simultaneous and independent oxidations of the metal centres occur.[8]

The redox data recorded for all the investigated species, on oxidation, are shown in **Table 4.1**. In detail, **M1L**, **M2L** and **M3L** (M = Ru or Os) species show only a single reversible process attributed to the Ru(II)/Ru(III) oxidation at about +1.3 V *vs*. SCE for Ru(II) complexes and at about +0.94 V *vs.* SCE for Os(II) complexes. The absence of further processes at more positive potentials, at least in the investigated range, as well as the area peaks of these three complexes that increase proportionally with nuclearity, clearly confirm no significant communication between metal centres despite the ligand **L** electronic delocalisation.

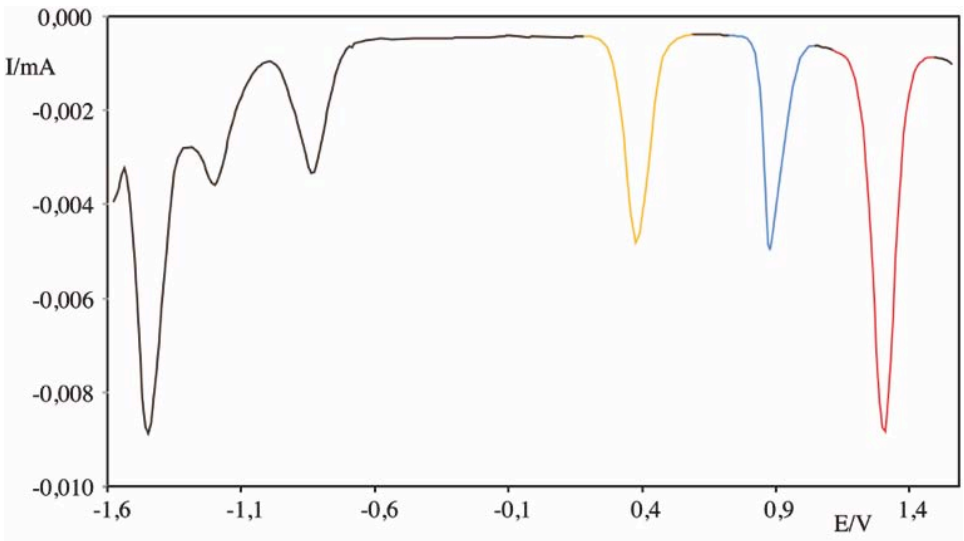

Figure 4.6 *Differential pulse voltammogram of **Ru2Os** in degassed acetonitrile. The yellow peak is correlated to oxidation of ferrocene, taken as reference. ([**Ru2Os**]= 0.5 mM, supporting electrolyte [$TBAPF_6$]= 0.1 M, SR: 10mV/s).*

The species **Ru2Os** exhibits two oxidation processes, see voltammogram in **Figure 4.6. Ru2Os** shows a first process at +0.94 V *vs.* SCE attributed to the monoelectronic reversible oxidation centred on Os(II) (easier to be oxidised than Ru(II)) and a second bielectronic reversible process at +1.30 V *vs.* SCE due to the simultaneous and independent oxidation of the two Ru(II) centres. It is noteworthy the oxidised osmium centre does not influence appreciably the ruthenium centres oxidation, confirming again the negligible electronic interaction of the system.

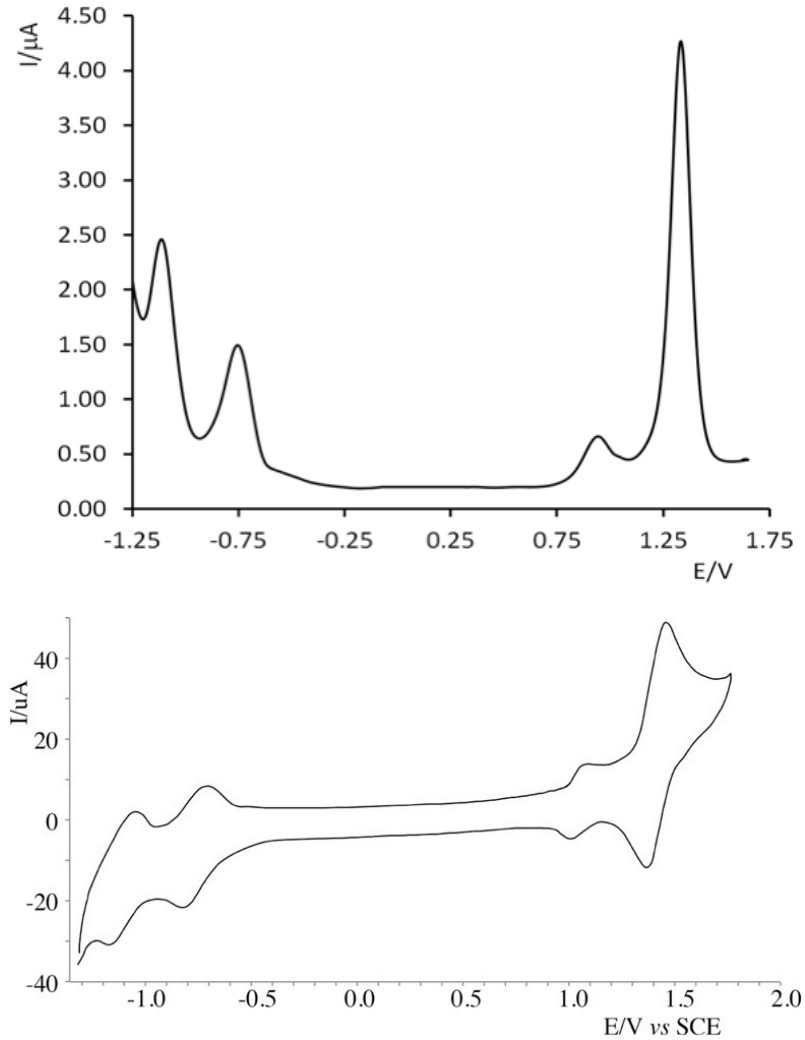

Figure 4.7 *Top) Differential pulse voltammogram (SR: 10mV/s) and bottom) Ciclic Voltammogram (SR: 100mV/s) of* ***Ru6Os*** *in acetonitrile ([**Ru6Os**]= 0.5 mM, supporting electrolyte [$TBAPF_6$]= 0.1 M).*

A similar behaviour have been observed for **Ru6Os**, see **Figure 4.7**, for which a reversible process takes place at +1.04 V *vs.* SCE, followed by a reversible process at +1.35 V *vs.* SCE whose intensity is six-fold the first one. The first process is associated to the Os(II)/Os(III) process, as already discussed for **Ru2Os**; the second one is associated to the simultaneous one-electron oxidation of the six Ru(II) centres. All of these attributions are in agreement with the discussion reported above and the behaviour exhibited by similar Ru(II) or (Os(II) polypyridine complexes and with $\mathbf{Ru_nL}$ species.[1]

Table 4.2 *Reduction redox data in degassed acetonitrile. numbers of exchanged electron in the process are reported in square parenthesis.*

	$E_{1/2\ rid}$/ V *vs.* SCE				
Compound	E_{red1}	E_{red2}	E_{red3}	E_{red4}	E_{red5}
2,2'-bpy	-	-2.10	-2.66	-	-
L	-1.15	-2.03	-2.21	-	-
$[Ru(bpy)_3]^{2+}$	-	-	-1.25	-1.43	-1.68
Ru1L	-0.85	-1.35	-	-	-
Ru2L	-0.76	-1.15	-	-	-
Ru3L	-0.70	-1.10	-1.26	-1.43	-1.7
Os2L	-0.74	-1.18	-	-	-
Os3L	-0.69	-1.09	-	-	-
Ru2Os	-0.70 [1e]	-1.11 [1e]	-1.25	-1.42	-1.68
Ru6Os	-0.69 [3e]	-1.09 [3e]	-	-	-

The reduction pattern of mono- bi- and trinuclear complexes is characterised by several processes (see **Table 4.2**). By comparison with the redox properties of the free ligand**,** the first process is attributed to the reduction of the bridging ligand. The potentials for this process become less negative along the $\mathbf{M_nL}$ series, because a higher nuclearity (higher positive charges) stabilises ligand **L**'s π* orbitals, see above.

In the case of the mono and binuclear complexes, the first and second reduction processes were attributed to the reduction of the central ligand, more specifically, an extended orbital that includes the triazine core. The case of complex **Ru3L** and **Ru2Os** is quite similar and the three subsequent reductions occurring at more negative potential were linked to reduction centred on the 2,2'-bipyridyl units, since their reduction potential are closely similar to the reported reduction values in the parent reference complex $[Ru(bpy)_3]^{2+}$.[9]

More complicated behaviour has been registered for **Ru6Os**. In this case the first two processes are associated to the simultaneous one-electron reduction of the three **L** ligands. This assignment is based on the fact that reduction processes centred on bpy in similar compounds occur at more negative potential than -1.20V[10] and is supported by the peaks intensities. These results indicate that these two reduction processes deal with bridge orbitals, which are delocalised over the whole **L** ligands, although the triazine moiety gives the larger contribution to the molecular orbitals; moreover, the circumstance that ligand **L** can be planar supports this hypothesis.[1] The separation between potentials, 390 mV, is attributed to electron pairing within the same orbital, and if we consider the large dimension of ligand **L** it appears plausible.[11]

4.4 UV/Vis characterisation

Absorption spectra are shown in **Figure 4.8**, **4.9** and **4.10**. Absorption data recorded in acetonitrile are resumed in **Table 4.3**.

All the spectra are similar to other Ru(II) and Os(II) polypyridine complexes, characterised by intense spin-allowed bands in UV region (200-350 nm) and bands in the visible region (350-800 nm). UV bands are assigned to π-π^* transitions, centred on ligands (LC bands); in the visible region, absorption bands are assigned to metal-to-ligand charge transfer (MLCT) transitions.

Table 4.3 *Absorption data of investigated species in acetonitrile.*

	Absorption
Compound	λ_{max}/nm ($\varepsilon/10^4$ $M^{-1}cm^{-1}$)
L[a]	246 (6.28), 253 (6.29), 279 (3.58), 322 (1.08)
$[Ru(bpy)_3]^{2+}$	244 (2.43), 254 (1.97), 287 (7.18), 423 (0.93), 452 (1.16)
Ru1L	475 (1.49), 285 (7.80), 245 (6.31)
Ru2L	482 (2.95), 284 (14.57), 246 (11.32)
Ru3L	496 (5.35), 286 (20.20), 247 (11.79)
Os2L	500 (2.71), 286 (11.73)
Os3L	508 (4.03), 287 (14,81)
Ru2Os	489 (3.55), 283 (23.09), 249 (12.42)
Ru6Os	494 (10.57), 285 (34.78), 247 (25.44)

[a] in dichloromethane.

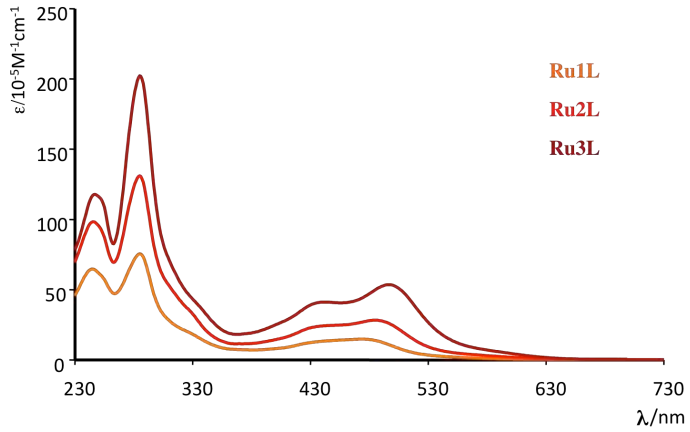

Figure 4.8 *Absorption spectra of mono-, bi- and trinuclear Ru(II) complexes in acetonitrile.*

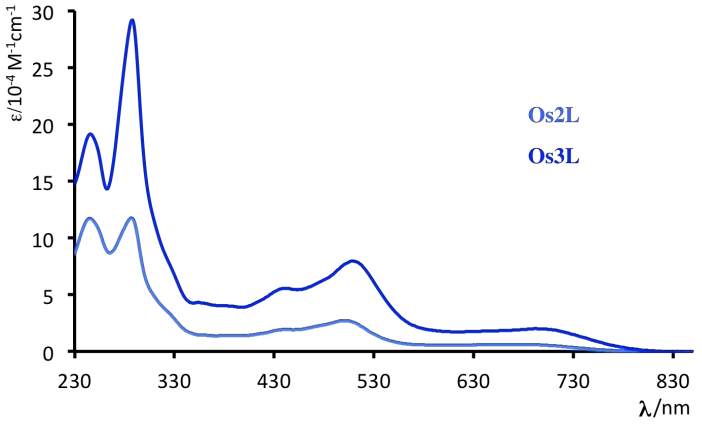

Figure 4.9 *Absorption spectra of bi- and trinuclear Os(II) complexes in acetonitrile.*

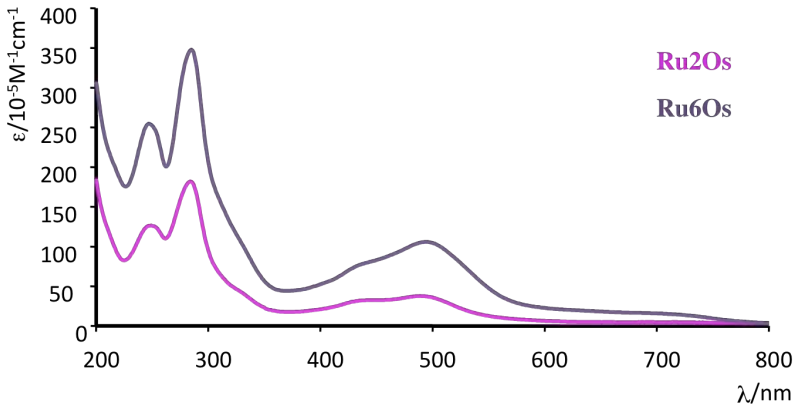

Figure 4.10 *Absorption spectra of **Ru2Os** and **Ru6Os** complexes in acetonitrile.*

From **Ru_nL** species data in **Table 4.3** it is noticeable a red shift of MLCT bands respect of $[Ru(bpy)_3]^{2+}$, taken as reference; in particular, there are trends concerning the maximum of MLCT bands (**Ru1L** (475 nm) < **Ru2L** (482 nm) < **Ru3L** (496 nm)) and the molar extinction coefficient ($[Ru(bpy)_3]^{2+}$ ($0.93 \cdot 10^4$ $M^{-1}cm^{-1}$) < **Ru1L** ($1.48 \cdot 10^4$ M^{-1} cm^{-1}) < **Ru2L** ($2.95 \cdot 10^4$ $M^{-1}cm^{-1}$) < **Ru3L** ($5.35 \cdot 10^4$ $M^{-1}cm^{-1}$)). The red shift correlated to a higher nuclearity, similarly to the reduction pattern, is due to a greater stabilisation of π^* ligand orbitals derived from the progressive coordination of the chelating sites. The increase of molar extinction coefficient is due to the higher number of metal centres. A similar trend occurs in **Os_nL** complexes with an additional weak absorption appearing around 700 nm, assigned to the spin-forbidden ^{3}MLCT transitions because of an easier spin-orbit coupling granted by the osmium centre.

4.5 Luminescence

All complexes are luminescent at room temperature. Emission spectra, recorded in acetonitrile, are shown in **Figure 4.11, 4.13** and **4.14** and data are reported in **Table 4.4**.

The red shift of **Ru_nL** species emission bands is in agreement with as said previously about UV/Vis spectra. **Ru_nL** species emissions are centred around 700 nm, whereas mixed species emission bands lie at less energy (**Figure 4.11**).

Table 4.4 *Luminescence data of investigated complexes in degassed acetonitrile.*

	Emission, 298 K	Lifetime	Quantum yield
Compound	λ_{max}, nm	τ, ns	Φ, %
L[a]	412	-	-
$[Ru(bpy)_3]^{2+}$	608	1100	9.5
Ru1L	687	664	2.0
Ru2L	698	499	1.3
Ru3L	709	264	0.7
Os2L	808	20	0.06
Os3L	818	15	0.04
Ru2Os	817	19	0.06
Ru6Os	820	13	0.07

[a] in degassed dichloromethane.

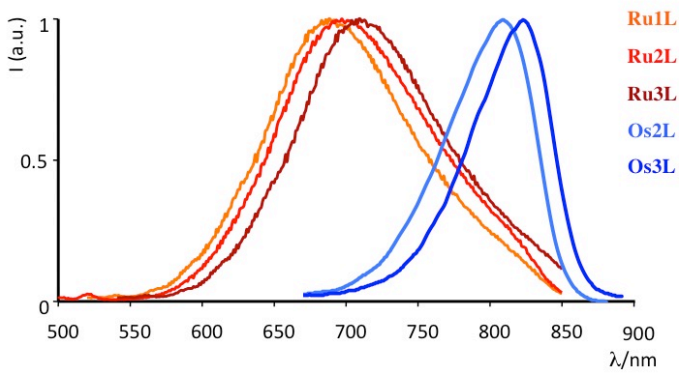

Figure 4.11 *Normalised emission spectra of Ru(II) and Os(II) species, in acetonitrile.*

The bridging ligand **L** has indeed unusual properties with respect to the bridges used in metal dendrimers: actually, in most of the metal dendrimers that have been reported so far, bridging ligands are bis-chelating species, that is a species capable of connecting two metal centres; a noticeable exception is the tris-chelating HAT ligand (HAT = 1,4,5,8,9,12-hexa-azatriphenylene, shown in **Figure 4.12**), capable of chelating three metal centres. However, the chelating sites of the HAT ligand are very strongly coupled to one another, so multiple metal coordination of a single HAT ligand induces a strong stabilisation of the bridging ligand π* orbital(s), the acceptor orbital(s) of the potentially emissive metal-to-ligand charge transfer (MLCT) excited state.

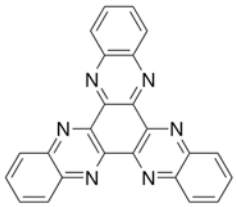

Figure 4.12 *Molecular structure of HAT bridging ligand.*

As a consequence, the low-lying ^{3}MLCT state of such multinuclear species are rather low in energy, lying in the near-infrared region even for compounds containing only Ru(II) centres, and the Franck–Condon factors for radiationless decay are very efficient, so reducing excited-state lifetime and hardly yielding luminescence. This is even more true when an Os(II) centre is introduced, because Os(II)-based MLCT

states are lower in energy than the analogous states involving Ru(II)-based compounds. In fact, no multinuclear species containing Os(II)-polypyridine subunits and tris-chelating bridging ligands is known, to the best of our knowledge. Like HAT, **L** also is a tris-chelating bridging ligand, with three bpy-type ligands linked to a central triazine moiety. However, the chelating sites of **L** are essentially decoupled, as suggested by the redox results, and this allows only a small electronic coupling among the three chelating subunits. As a consequence, multinuclear coordination of **L** does not decrease the energy of the ligand π* orbital(s) to such a large extent as to lead to inefficient luminescence. As a matter of fact, in acetonitrile solution at room temperature the mononuclear **Ru1L** compound exhibits ^{3}MLCT emission peaking at 698 nm, whereas the trinuclear species **Ru3L** emits with a maximum at 709 nm.

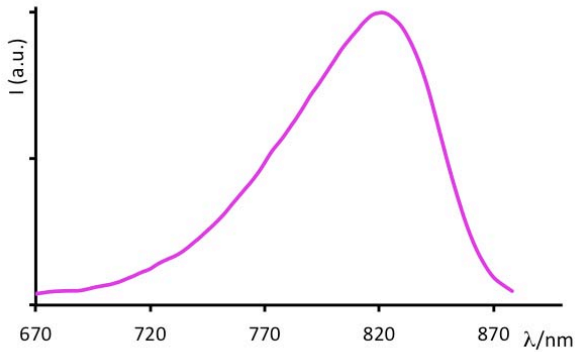

Figure 4.13 *Emission spectrum of **Ru2Os** at room temperature in acetonitrile.*

In **Ru2Os** species the lower-energy excited state involves the Os(II) core and the bridging ligand. This low-lying MLCT state decays radiatively to the ground state at around 817 nm (**Figure 4.13**). Because no residual luminescence from Ru(II)→**L** CT state has been detected, we may safely affirm that this species acts as antenna system.

Heptanuclear **Ru6Os** complex exhibits an emission band peaked at 820 nm (τ = 13 ns) at room temperature in acetonitrile, which is blue-shifted in a butyronitrile rigid matrix at 77 K (800 nm, τ = 500 ns), and no residual emission bands due to the Ru(II) subunits radiative deactivation (**Figure 4.14**). The comparison of the emission properties of **Ru6Os** with those of the bonafide model for the peripheral Ru-based subunit(s), **Ru3L** (acetonitrile fluid solution, room temperature: λ_{max} = 712 nm),[1] and those of **Ru2Os** complex allow us to assign the

luminescence of **Ru6Os** to the ^{3}MLCT state involving the Os(II) subunit, namely the Os → **L** ^{3}CT state.

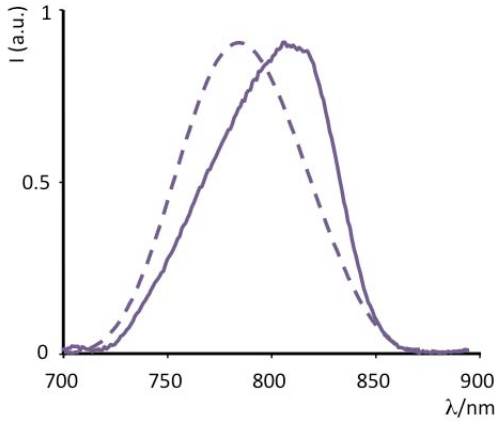

Figure 4.14 *Normalised emission spectra of **Ru6Os** at room temperature in acetonitrile (solid line) and in rigid matrix at 77 K in butyrontrile (dashed line).*

The emission properties of **Ru6Os** are independent of the excitation wavelength and the excitation spectrum (shown in **Figure 4.15**) matches well enough with the absorption one, meaning also Ru(II) subunits give their contribute to the population of the emissive state. This behaviour clearly indicates that in this species a quantitative energy transfer process from the MLCT states involving the Ru(II) subunits to the Os(II) core is active. The absence of residual emission from the ruthenium peripheral moieties at 77 K indicates that energy transfer process is quantitative also in these conditions.

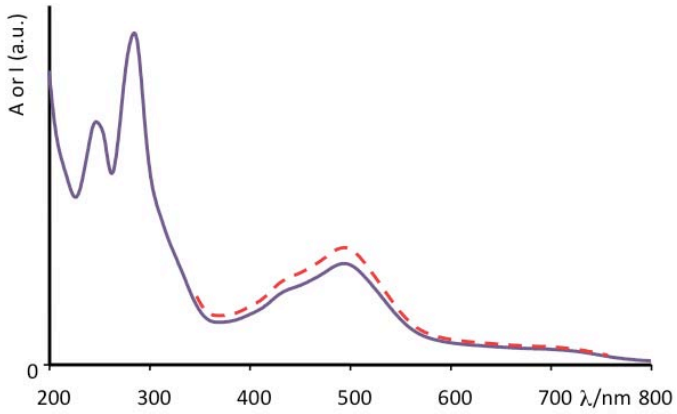

Figure 4.15 ***Ru6Os*** *absorption spectrum (solid purple line) and excitation spectrum (dashed red line, emission @800 nm) in acetonitrile.*

4.6 Pump-probe Transient Absorption Spectroscopy

Although downhill energy transfer from peripheral Ru(II)-based subunits to central Os(II)-based chromophores has been reported in metal dendrimers, the energy transfer kinetics and mechanisms have very rarely been studied. Probably, the case studied in most detail is the tetranuclear compound $[Os\{(\mu\text{-}2,3\text{-}dpp)Ru(bpy)_2\}_3]^{8+}$ (2,3-dpp = 2,3-bis(2'-pyridyl)pyrazine). For this species, Ru-to-Os energy transfer is biphasic, with a component faster than 60 fs, also involving non-equilibrated singlet MLCT states, and a slower component of about 600 fs, involving triplet MLCT states.[12]

As the metal-metal distance in **Ru6Os** is larger than that in $[Os\{(\mu\text{-}2,3\text{-}dpp)Ru(bpy)_2\}_3]^{8+}$, electronic coupling would be significantly smaller so the energy transfer process from peripheral Ru(II) subunits to Os(II) core is expected to be slower (driving force is approximated to -0.21 eV, calculated from the difference between emission energy of **Ru6Os** and **Ru3L** at room temperature). **Figure 4.16** shows the pump–probe transient absorption spectrum (TAS) of **Ru6Os** upon fs excitation (excitation wavelength = 400 nm, 120 fs pulse) and its time evolution.

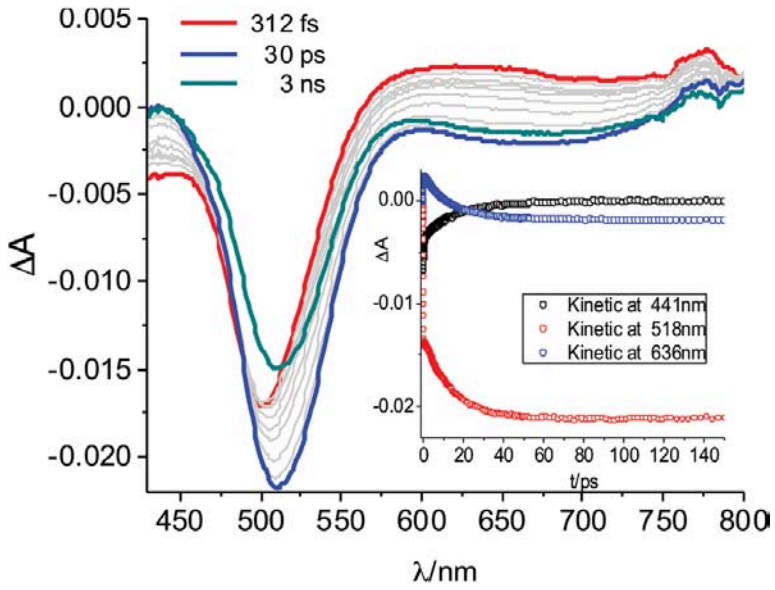

Figure 4.16 *Transient absorption spectra of **Ru6Os** at some delays after laser pulse (excitation: 400 nm). In the inset, kinetics at early times at three wavelengths are shown.*

The initial transient spectrum (after 312 fs from flash) exhibits a bleaching at about 505 nm with a small transient absorption in the 560–780 nm range. The

bleaching increases in intensity and red-shifts with time; simultaneously, another bleaching (with a negative peak around 700 nm) is formed and counter-balances the initial transient absorption in the red region (**Figure 4.16**, blue spectrum). During such spectral changes, an isosbestic point at about 480 nm is maintained. The process associated with these spectral changes, whose time constant is 11 ps (see **Figure 4.16**, inset), is assigned to triplet-triplet energy transfer process from the Ru-to-**L** CT state to the lower-lying Os-to-**L** CT state. The red shift of the absorption bleach at about 500-520 nm region – taking into account that spin-allowed MLCT transitions in Os(II) polypyridine compounds occur at a lower energy than that in the analogous Ru(II) species – and the appearance of the 640-740 nm bleach, typical of the spin-forbidden absorption band of the Os(II)-based chromophore, definitely identify the process. The time constant agrees with the expectation that the process is slower than that for $[Os\{(\mu\text{-}2,3\text{-}dpp)Ru(bpy)_2\}_3]^{8+}$, as mentioned above. Once energy transfer occurs, the TAS decays to the ground state on a timescale too long for our equipment (upper time limit, 3.3 ns), in agreement with the luminescence lifetime (13 ns, see **Table 4.4**). As far as the mechanism of the process is concerned, singlet–singlet energy transfer is ruled out since intersystem crossing in the Ru(II) centres is much faster (<200 fs).[12,13]

The calculated rate constant for Förster energy transfer k_{en}^F, in **Ru6Os** is based on **Equation 4.1**:[14]

$$k_{en}^{F} = 8.8 \cdot 10^{-25} \frac{K^2 \Phi}{n^4 r_{AB}^6 \tau} J_F \qquad \text{(eq. 4.1)}$$

where K is an orientation factor which accounts for the directional nature of the dipole-dipole interaction (from statistics considerations, assumed as 0.66), Φ and τ are the luminescence quantum yield and lifetime of the donor, respectively, n is the solvent refractive index, r_{AB} is the distance (in Å) between donor and acceptor, estimated to be 13 Å, from computer modelisation. The spectral overlap J_F is given by **Equation 4.2**:

$$J_F = \frac{\int F(\bar{\nu})\varepsilon(\bar{\nu}) / \bar{\nu}^4 \, d\nu}{\int F(\bar{\nu}) \, d\nu} \qquad \text{(eq. 4.2)}$$

where F($\overline{\nu}$) is the luminescence spectrum of the donor (**Ru3L** species taken as model), and ε($\overline{\nu}$) is the absorption spectrum of the acceptor (essentially, the spectrum of **Ru6Os**, since only the Os(II) core absorbs at relevant wavelengths), on an energy scale (cm^{-1}).

By using the experimental data, the calculated rate constant is $1.0 \cdot 10^{10}$ s^{-1}. This value is almost one order of magnitude smaller than the experimental result, which is $9.1 \cdot 10^{10}$ s^{-1}. As a consequence, the Förster mechanism is excluded as the main mechanism for energy transfer in **Ru6Os**. The main mechanism is therefore assumed to be the Dexter electron exchange energy transfer.[15] Assuming as valid the Landau-Zener and Fermi golden rules derived from a semi quantum mechanical approach (inherently non-adiabatic), **Equations 4.3** and **4.4** have to be considered, in which ν_{en} is the electronic factor and H_{AB} is the energy transfer matrix element for energy transfer between the subunits A and B.[16]

$$k_{en} = \nu_{en} e^{-\frac{\Delta G^{\neq}}{RT}} \qquad \text{(eq. 4.3)}$$

$$\nu_{en} = \left(\frac{2\pi H_{AB}^2}{h}\right)\left(\frac{1}{4\pi\lambda RT}\right)^{1/2} \qquad \text{(eq. 4.4)}$$

R and T have the usual values ($8.617 \cdot 10^{-5}$ eV K^{-1} $atom^{-1}$ and 298 K, respectively), and λ and $\Delta G^{\neq}$ are the reorganisation energy and the activation energy, respectively, expressed in **Equations 4.5** and **4.6**.[17]

$$\lambda = \left(\frac{1}{\mu} - \frac{1}{\varepsilon}\right)\left(\frac{1}{r_A} + \frac{1}{r_B} - \frac{1}{r_{AB}}\right) \qquad \text{(eq. 4.5)}$$

$$\Delta G^{\neq} = \frac{\left(\Delta G^{\circ} + \lambda\right)^2}{4\lambda} \qquad \text{(eq. 4.6)}$$

In **equations 4.5** and **4.6**, μ and ε are the optical and static dielectric constants,

respectively, r_A and r_B are the radii of the donor (A) and of the acceptor (B), r_{AB} is the donor acceptor distance, and $\Delta G°$ is the driving force of the energy transfer process. In the present case, r_A and r_B are both 3.5 Å, r_{AB} is 13 Å (from computer based calculations), so that λ is 0.343 eV, and $\Delta G^{\neq}$ is 0.013 eV. Therefore, ν_{en} is $1.5 \cdot 10^{11}$ and H_{AB} is 0.00105 eV, equivalent to 8.5 cm^{-1} that compares well with the averaged H_{AB} found for Ru(II)-to-Os(II) energy transfer in polymers (≈2 cm^{-1}) [18] and related complexes.[19]

4.7 Conclusions

A family of $[(M(2,2'\text{-bpy})_2)n(L)][(PF_6)_{2n}]$ complexes with n = 1–3, L = tris-2'',4''6''-(2,2'-bipyridin-4-yl)-1'',3'',5''-triazine and M Ru(II) or Os(II) have been prepared and characterised. For the ruthenium based complexes the ligand induced a bathochromic shift of the MLCT band in the absorption spectrum as compared to the parent complex $[Ru(2,2'\text{-bpy})_3][(PF_6)_2]$. More specifically, **$Ru_3$L** exhibits high intensity absorptions tailing out passed 600 nm. The central triazine component has a significant effect on the unoccupied molecule orbitals in spite of the fact that it is not directly bonded to the metal ions. This effect is most significant in the equilibrated ^{3}MLCT state, which emits at a considerably lower energy than the archetypical $[Ru(2,2'\text{-bpy})_3]^{2+}$ complex. Analogous results have been obtained for the Os(II) based compounds, whereas the mixed **Ru2Os** species shown an antenna behaviour. **L** has been also used for preparing the dendritic-shaped, heptanuclear, mixed-metal luminescent compound **Ru6Os**, in which all the light energy absorbed by the six Ru(II) chromophores is funnelled to the central Os(II) core, with a time constant of 11 ps. **Ru6Os** is the first mixed Os(II)–Ru(II) dendrimer built up with a trischelating bridging ligand and in which electronic coupling between nearby metal centres is practically negligible from a redox viewpoint, due to the relative electronic separation of the chelating sites in the bridging ligand. **Ru6Os** is also one of the very few examples of metal dendrimers whose energy transfer process has been studied by pump-probe TAS.

References

1) B. Laramée-Milette, F. Lussier, I. Ciofini and G. S. Hanan, *Dalton Trans.*, **2015**, 44, 11551.

2) Y.Q. Fang, G. S. Hanan, *Synlett*, **2003**, 6, 852.

3) A. A. Vlcek, *Coord. Chem. Rev.*, 1981, 36, 325.

4) M. K. De Armond, C. M. Carlin, *Coord. Chem. Rev.*, **1982**, 36, 325.

5) (a) A. Juris, V. Balzani, F Barigelletti, S. Campagna, P. Belser, A. von Zelewsky, *Coord. Chem. Rev.*, **1988**, 84, 85; (b) T. J. Meyer, *Acc. Chem. Res.*, **1989**, 22, 163; (c) K. Kalyanasundaram, *Photochemistry of Polypyridine and Porphyrin Complexes, Academic Press*, London, **1991**; (d) S. Campagna, F. Puntoriero, F. Nastasi, G. Bergamini, V. Balzani, *Top. Curr. Chem.*, **2007**, 280, 117; (e) D. Kumaresan, K. Shankar, S. Vaidya, R. H. Schmehl, *Top. Curr. Chem.*, **2007**, 281, 101.

6) (a) G. Farnia, S. Roffia, J. Electroanal. Chem., 1981, 122, 347; (b) S. Roffia, R. Casadei, F. Paolucci, C. Paradisi, C. A. Bignozzi, F. Scandola, *J. Electroanal. Chem.*, **1991**, 302, 157.

7) M. Venturi, S. Serroni, A .Juris, S. Campagna, V. Balzani, *Top.Curr.Chem.*, **1998**, 197, 193.

8) F. Puntoriero, S. Serroni, F. Nastasi, S. Campagna in *Electrochemistry of Functional Supramolecular Systems*, Wiley, **2010**, 121.

9) T. Matsumura-Inoue, *J. Electroanal. Chem.*, **1979**, 95, 109.

10) V. Balzani, G. Bergamini, S. Campagna and F. Puntoriero, *Top. Curr. Chem.*, **2007**, 280, 1.

11) S. Campagna, A. Mamo and J. K. Stille, *J. Chem. Soc., Dalton Trans.*, **1991**, 2545.

12) (a) J. Andersson, F. Puntoriero, S. Serroni, A. Yartsev, T. Pascher, T. Polivka, S. Campagna and V. Sundström, *Chem. Phys. Lett.*, **2004**, 386, 336; (b) J. Larsen, F. Puntoriero, T. Pascher, N. McClenaghan, S. Campagna, E. Åkesson and V. Sundström, *ChemPhysChem*, **2007**, 8, 2643.

13) (a) J. K. McCusker, *Acc. Chem. Res.*, **2003**, 36, 876; (b) H. Berglund Baudin, J. Davidsson, S. Serroni, A. Juris, V. Balzani, S. Campagna and L. Hammarström, *J. Phys. Chem. A*, **2002**, 106, 4312; (c) A. Cannizzo, F. van Mourik, W. Gawelda, C. Bressler and M. Chergui, *Angew. Chem., Int. Ed.*, **2006**, 45, 3174.

14) h. H. Förster, *Discuss. Faraday Soc.*, **1959**, 27, 7.

15) (a) V. Balzani, P. Ceroni and A. Juris, *Photochemistry and Photophysics, Wiley-VCH*, **2013**. (b) D. L. Dexter, *J. Chem. Phys.*, **1953**, 21, 836.

16) (a) V. Balzani, F. Bolletta and F. Scandola, *J. Am. Chem. Soc.*, **1980**, 102, 2552. (b) F. Scandola and V. Balzani, *J. Chem. Educ.*, **1983**, 60, 814.

17) R. A. Marcus and N. Sutin, *Biochim. Biophys. Acta*, **1985**, 811, 265.

18) C. N. Fleming, L. M. Dupray, J. M. Papanikolas and T. J. Meyer, *J. Phys. Chem. A*, **2002**, 106, 2328.

19) Z. A. Morseth, L. Wang, E. Poudziukynaite, G. Leem, A. T. Gilligan, T. J. Meyer, K. S. Schanze, J. R. Reynolds and J. M. Papanikolas, *Acc. Chem. Res.*, **2015**, 48, 818.

Chapter 5

Light-Harvesting with Organic Molecules inside Mesoporous Organosilica

Introduction

Boron-dipyrromethenes (known more simply as BODIPYs) molecules were first developed in 1968 by Treibs and Kreuzer,[1] and find several applications as laser dyes and fluorescent biosensors. These molecules are characterised by high molar absorption coefficient, high fluorescence quantum yield and small Stokes shift. BODIPYs are relatively insensitive to pH and temperature changes, when compared to other dyes. Moreover, their preparation is quite easy as also their chemical functionalisation, which allows for tuning their absorption and emission spectra across a large range of UV/Vis wavelengths up to the near-IR region.[2,3] They have been widely explored as components of light-harvesting arrays covalently linked or self-assembled.[3,4,5,6] Examples of multiBODIPY antenna systems are reported in **Figure 5.1**.

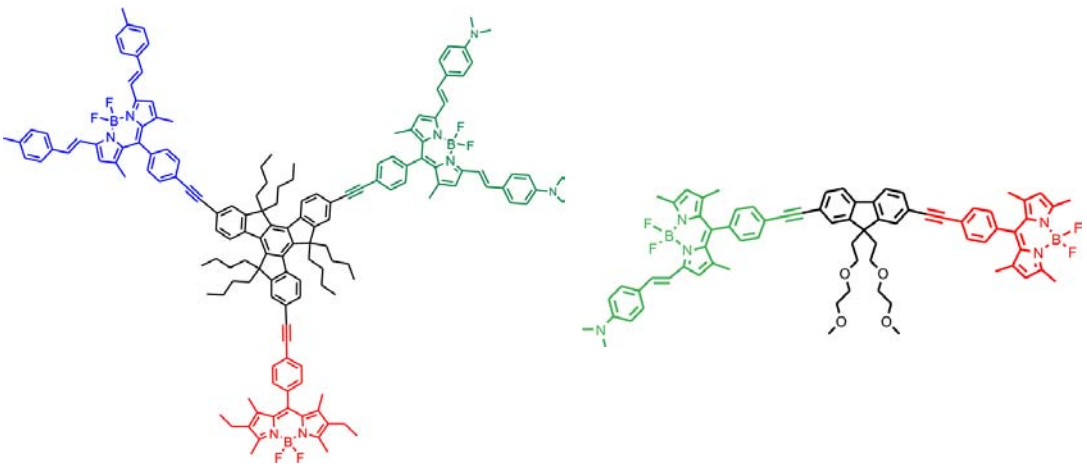

Figure 5.1 *Molecular structures of BODIPY-based light-harvesting antennas previously studied.*[4,5]

With the collaboration of prof. Cucinotta's research group in Newcastle upon Tyne (UK), in which I spent a 10 months research period, we have studied host-guest

chromophoric systems where a BODIPY is organised into mesoporous silica of MCM-41 type.[7]

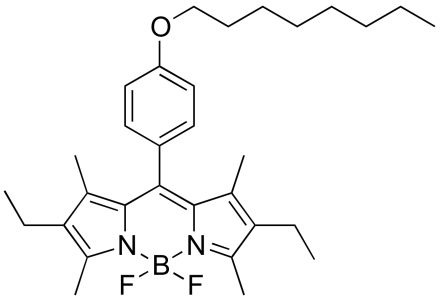

Figure 5.2 *Molecular structure of BPJ2 dye.*

The BODIPY used in this synthesis (hereafter labelled BPJ2 and shown in **Figure 5.2**) has been specifically designed to mimic the surfactant used (hexadecyltrimethylammonium bromide (CTAB)) in the nanoparticles syntheses, allowing the BODIPY molecules to self-assemble into the rod-like micellar phase. This leads the dyes to be evenly distributed among the surfactant molecules constituting the micelles due to the dynamic nature of such systems. While silica systems containing BODIPYs have been studied in the past, [8] systems in which BODIPY acts as both template and guest have not been widely explored.

5.1 *Hybrid BODIPY-silica nanomaterials*

5.1.1 *Synthesis*

The synthesis of MCM-41 with the BODIPY molecules as guest has been made following *Approach 1* described previously in Chapter 3, that is solidification from precursor solution containing soluble silica source and surfactant with dissolved functional guest species. BPJ2, which is insoluble in water, is dissolved in few drops of acetonitrile and such solution is added to a water mixture (pH = 12) containing CTAB rod-shaped micelles. This mixture is stirred for several hours and then heated to 80°C. Thereafter, tetraethyl orthosilicate (TEOS) is added to the mixture, which is refluxed for 2.5 hours. The basic aqueous environment is needed to induce the hydrolysis and then the polycondensation of TEOS in order to form the silica framework around the template. The mixture is eventually filtered and the obtained

powder left drying in oven. Through such methodology, BPJ2 has been integrated within the CTAB micellar phase at molar ratios of 1%, 5%, 10%, 20% and 50%. These new hybrid materials have been characterised structurally and spectroscopically.

5.1.2 *Structure and Morphology*

Small-angle X-ray scattering (SAXS) measurements have been performed to gain insights on the changes in structural order and the diagnostic signatures of the crystallographic planes (10), (11), (20) and (21) of the hexagonal columnar phase have been monitored (see **Table 5.1** and **Figure 5.3**). All samples contained one main peak, indexed as (10) on the 2D hexagonal structure, and up to three weaker additional peaks at higher q, indexed as (11), (20) and (21) signals, within the q range examined (see **Table 5.1** and **Figure 5.4**). The q-value of the (10) peak appears to decrease, and therefore the d-value to increase, with increasing dye loading up to 10%. The peak also broadens and concomitantly the resolution of the signals at higher q-values is gradually lost, indicating that the regular hexagonal arrangement of the porous structure is interrupted by the enhanced dye content within the template. This effect is accompanied by an increase in the pore spacing, shown by the TEM imaging of the 10% sample (bottom left in **Figure 5.3**), which also confirms the loss of the hexagonal arrangement and a disordered porosity.

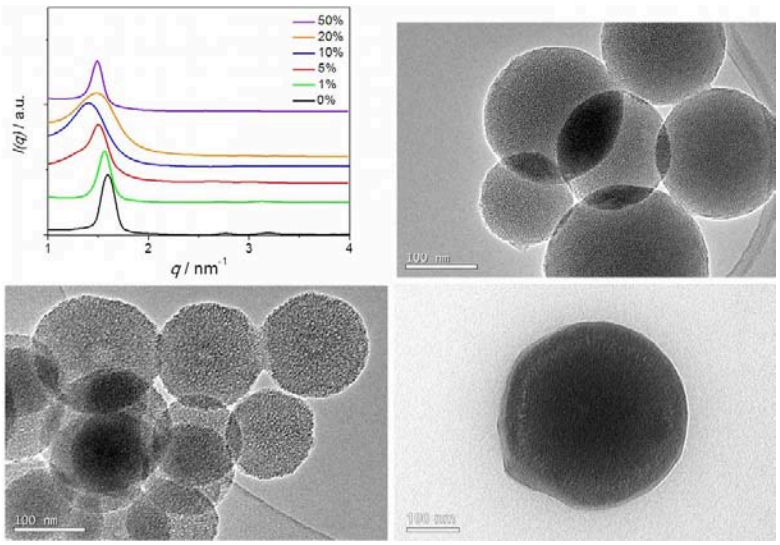

Figure 5.3 *SAXS profiles (top left) of the hybrid MCM-41 silica systems and TEM images of 1%-loaded (top right), 10%-loaded (bottom left) and 50%-loaded (bottom right) samples.*

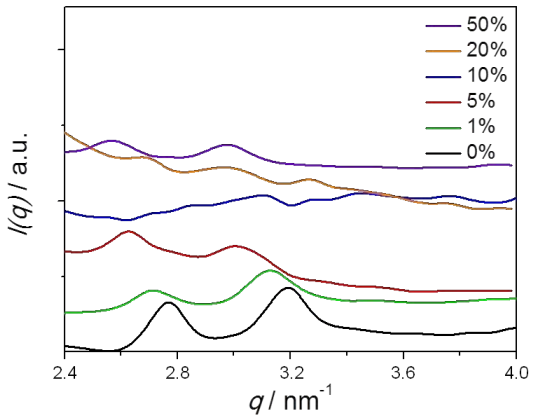

Figure 5.4 *SAXS profiles of the MCM-41 samples in the q range 2.4 – 4 nm.*

Table 5.1 *SAXS data for the MCM-41 silica hybrids.*

	SAXS Peaks				
	2θ/°	q /nm^{-1}	D /nm	ratio	2D hexagonal reflection
MCM-41	2.2 3.9 4.5	1.56 2.77 3.20	4.01 2.26 1.96	1 1.77 2.05	10 11 20
1% BPJ2@MCM-41	2.2 3.8 4.4	1.56 2.70 3.13	4.01 2.32 2.00	1 1.77 2	10 11 20
5% BPJ2@MCM-41	2.1 3.7 4.3	1.49 2.63 3.06	4.20 2.39 2.05	1 1.77 2.05	10 11 20
10% BPJ2@MCM-41	2.1 - -	1.49 - -	4.2 - -	-	-
20% BPJ2@MCM-41	2.1 3.8 4.2 4.6	1.49 2.70 2.99 3.27	4.2 2.3 2.1 1.9	1 1.81 2.1 1.9	10 11 20 20
50% BPJ2@MCM-41	2.1 3.6 4.2	1.49 2.56 2.99	4.2 2.5 2.1	1 1.68 2	10 11 20

Surprisingly, the trend appears to be inverted as the dye loading increases up to 50%, with the q value of the (10) diffraction peak shifting back to higher values and becoming narrower. This, alongside with a gradual return in resolution of the (11) and (20) signals, indicates that the order of the hexagonal columnar phase of the template is restored and the highest-loaded hybrid features a more crystalline structure.

5.1.3 *Photophysical properties and TAS*

For UV/Vis and luminescence spectroscopy studies the samples have been suspended in cyclohexane to reduce the effect of scattering. All absorption spectra (**Figure 5.5**) show the typical BODIPY band centred around 525 nm. In addition, if these systems are dried via thermic treatment, a higher-energy absorption band with a structured profile shows up, whereby it is possible identifying three main transitions, peaked at 390, 415 and 455 nm. The energy difference between these peaks matches with the stretching frequency of C=C and C=N bounds, which is typically a sign of the vibrational progression that accompanies electronic transitions localised on rigid organic chromophores.[9]

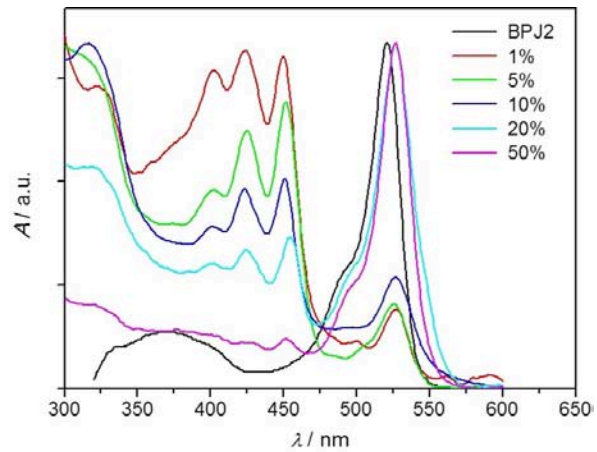

Figure 5.5 *Normalised absorption spectra of BPJ2 hybrid silica systems, in cyclohexane.*

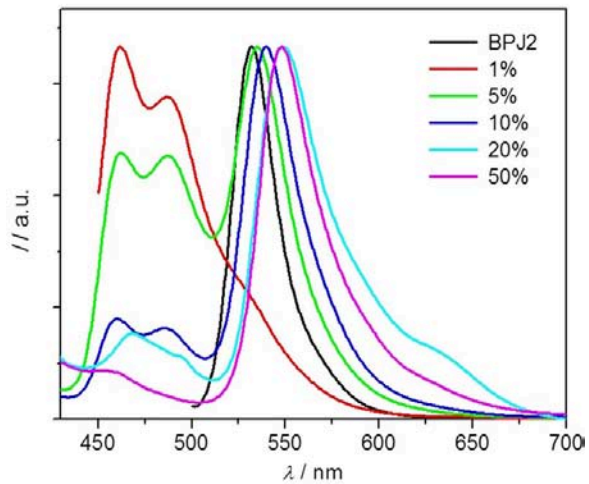

Figure 5.6 *Normalised emission spectra of BPJ2 hybrid silica systems, in cyclohexane.* λ_{ex} *= 430 nm.*

It is interesting that the intensity of this new band varies by varying the loading of dye inside the nano-channels: it is the major component in the 1% sample and gradually decreases as the loading reaches 50%, where the BPJ2 narrow band dominates.

Fluorescence spectra (**Figure 5.6**) confirm this trend: a new higher-energy band shows up (450-490 nm), alongside the BPJ2 band at 532 nm and it dominates the 1% emission spectrum losing intensity with the increase of loading percentage; in the 50% sample the typical BODIPY band is fully restored and red-shifted to 550 nm.

This behaviour has been explained considering the formation of a distinct chemical species when the silica formation around the template occurs. It was ruled out the possibility that such species could be the product of degradation of the dye-loaded micelles in the aqueous solution due to the high pH, as previous stability tests[10] on the dye-loaded micelles in basic aqueous solutions did not show the presence of additional high-energy bands. The next hypothesis has been considering that BPJ2 molecules within the template may form ground state dimers and H-aggregates, which leads to a blue-shifted absorption, compared to monomer. These kinds of aggregates are known to form for certain BODIPY systems in the solid state, at specific close-packing angles.[9,11,12] However, this type of aggregates is also known for showing unstructured and broad absorption bands, accompanied by a weak fluorescence, typically hard to be observed and fully characterised.[13]

The varying intensity ratio, between the two spectral components, is explicable if it is seen as different distribution equilibria that are reached in each sample between the two species. These distribution equilibria are the result of the dynamic conditions the micelles undergo while formation process; these conditions vary in each sample with the dye-loading, reaction times and ionic strength. The prevalence of one species over the other, as observed in 1% and 50% samples, is a sign of a homogeneous dispersion of one species within the template and is in good agreement with the SAXS data, which indicates a higher structural order for these two samples than in the other hybrids.

By Time-Correlated Single Photon Counting (TCSPC) technique the luminescence lifetimes of the two species have been measured, recorded on the respective emission wavelengths (**Table 5.2**). It is worth noting the lifetime of the high-energy species is

considerably shorter than the one of the BPJ2 dye. Moreover, from fluorescence excitation spectra, see **Figure 5.7,** recorded for all samples at the emission wavelength of the monomer, it has been observed a significant contribution from the high-energy species, suggesting that excitation energy is transferred from this species to the monomer.

Table 5.2 *Lifetimes of BPJ2 in solution and within MCM-41 nanoparticles.*

Sample	Lifetimes	
	450 nm[a]	540 nm[b]
in DCM	-	4.7 ns
1%	2.0 ns	4.9 ns
5%	1.5 ns	4.6 ns
10%	1.5 ns	5.2 ns
20%	1.3 ns	5.4 ns
50%	1.2 ns	5.1 ns

[a] Recorded using a 371.8 nm laser excitation source.
[b] Recorded using a 471.8 nm laser excitation source.

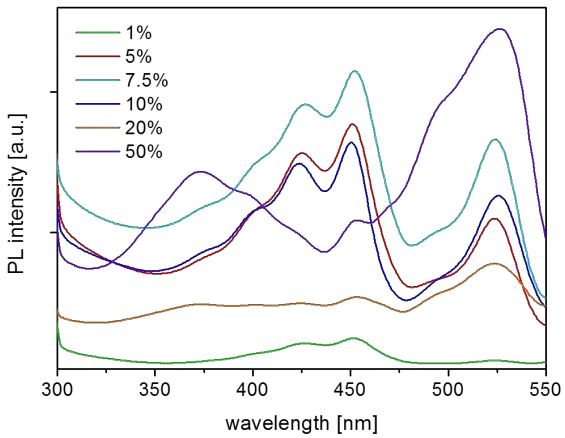

Figure 5.7 *Fluorescence excitation spectra of the BPJ2 hybrid silica systems, recorded from 0.3 mg/ml water suspensions, at* λ_{em} *= 580 nm.*

Further studies have been conducted by time-resolved transient absorption spectroscopy (spectra and kinetics shown in **Figures 5.8-5.12**). BPJ2 has also been investigated, taken as model for data interpretation. The transient spectrum recorded immediately after the excitation of BPJ2 is characterised by an intense bleaching centred at about 530 nm. This bleaching is recovered, without any spectral changes, within a time comparable to the luminescence excited state lifetime of 4.7 ns, recorded with the TCSPC.

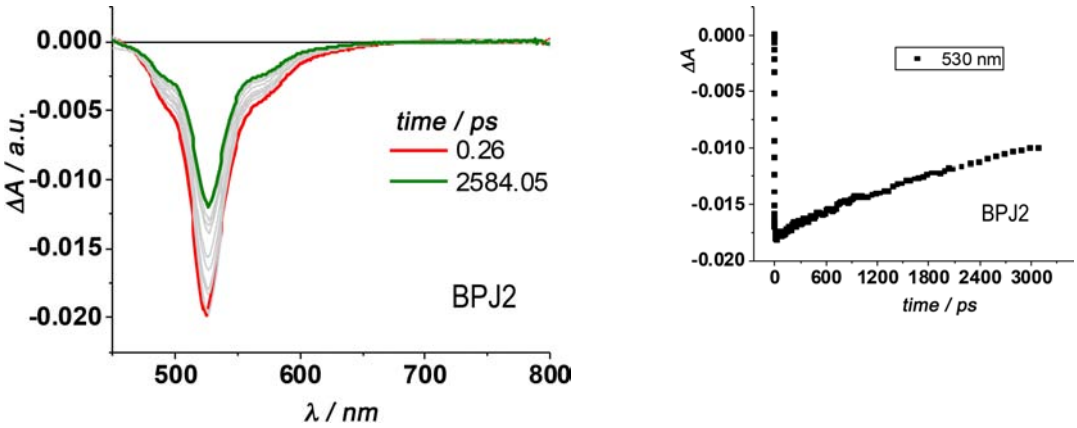

Figure 5.8 *Transient absorption spectra BPJ2 in ethanol (120 fs @ 400 nm). Inset right shows kinetic trace at 530 nm.*

The transient absorption spectra (TAS) of silica samples are more complex. For the 1%-loaded silica sample the TAS recorded (**Figure 5.8**) at 120 fs after the flash is characterised by a quite intense bleaching in the range between 440 and 500 nm, which can be assigned, by comparison with the steady state absorption spectra, to the direct excitation of the aggregate species. Further, in the spectral region between 500 and 750 nm it is possible observing an intense transient absorption band, absent in BPJ2, so attributable to the absorption to higher energy states of the aggregate. The spectrum evolves biphasically and, whereas the bleaching at 480 nm is completely recovered in about 1 ns, as well as the absorption band, a low intense bleaching at 530 nm is still evident and disappears with a longer time constant.

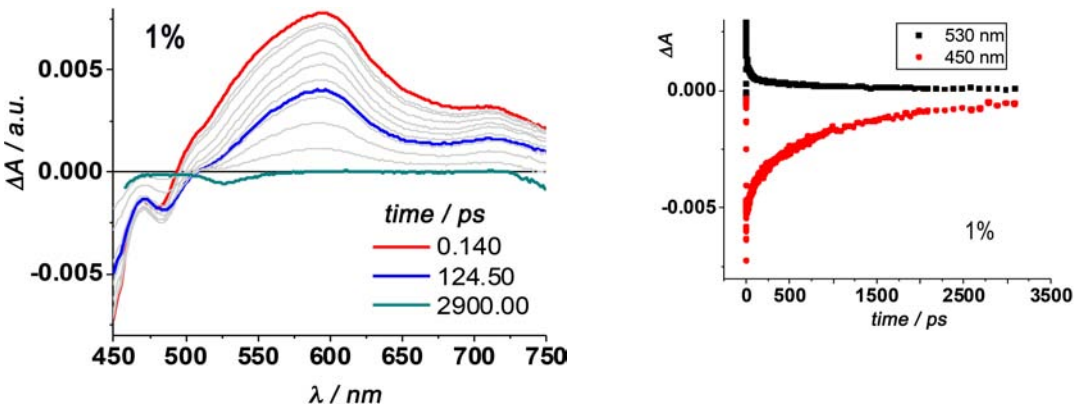

Figure 5.9 *Transient absorption spectra of 1%-loaded hybrid samples, recorded from water suspensions (120 fs @ 400 nm). Inset right shows kinetic traces at 530 nm (black) and at 450 nm (red).*

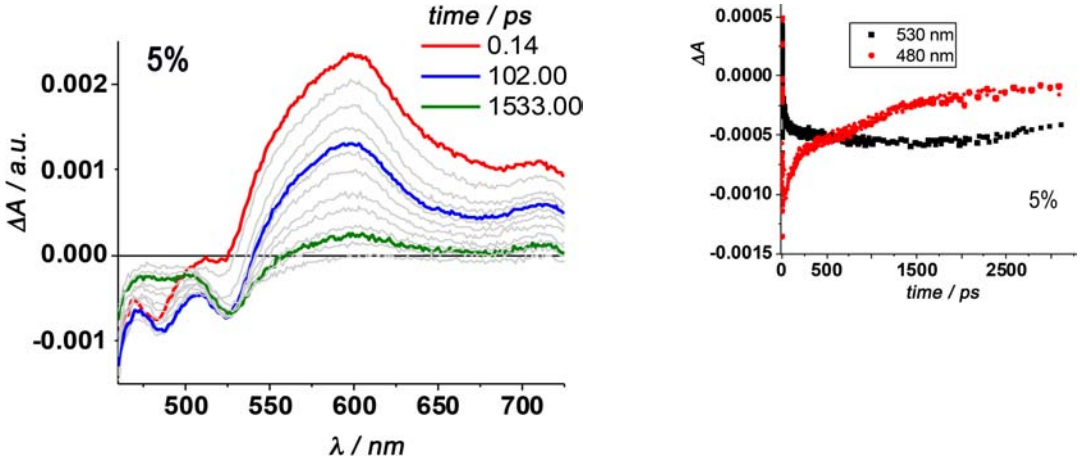

Figure 5.10 *Transient absorption spectra of 5%-loaded (right) hybrid samples, recorded from water suspensions. Inset right shows kinetics at 530 nm (black) and at 480 nm (red).*

For the 5%-loaded silica sample a similar trend can be observed (**Figure 5.10**) but in this case, because the lower percentage of the aggregates species respect to the monomeric one, a bleaching peaked at 530 nm is present in the initial TAS. This signal increases in about 100 ps and, at the same time the bleaching at 480 nm is partially recovered. More precisely, from the kinetics traces recorded for the 1% and 5% samples, a partial recovery of the bleaching at 480 nm is observed within about 80 ps, with a simultaneous increase of the bleaching at 530 nm due to the monomeric species. After this tie, the kinetics trace at 480 nm decays completely to zero in 1.2 ns, whereas the ground state of the monomer is fully recovered in a time scale of about 4.5 ns (± 0.6 ns).

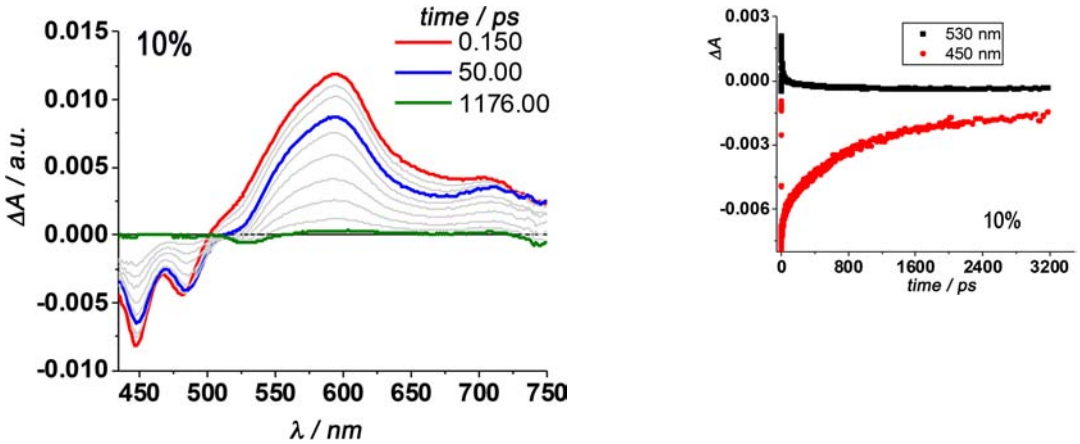

Figure 5.11 *Transient absorption spectra of 10%-loaded hybrid samples, recorded from water suspensions. Inset right shows kinetic traces registered at 530 nm (black) and at 450 nm (red).*

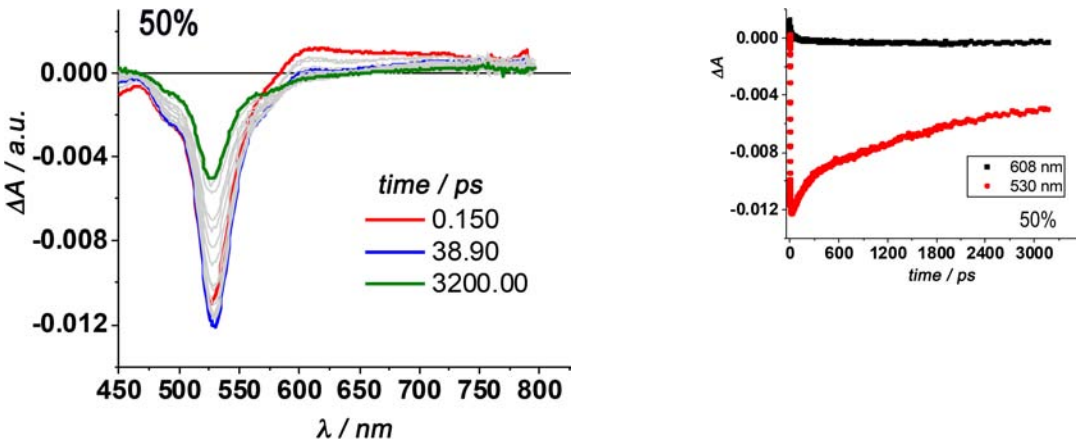

Figure 5.12 *Transient absorption spectra of 50%-loaded hybrid samples, recorded from water suspensions (120 fs @ 400 nm). Inset right shows kinetic traces registered at 608 nm (black) and at 530 nm (red).*

This scenario can be rationalised by assuming that the relative location of aggregated and monomeric species within the silica nanopores is random, so the distances between the species are statistically distributed. It is therefore possible assuming that, in approximately 80 ps, an energy transfer process occurs from the excited state localised on the aggregated form of the dyes to the excited state of the monomeric species. From calculations performed using this kinetic trace, the average donor-acceptor distance has revealed being around 20 Å. However, there are not only such donor-acceptor pairs, but also a certain amounts of isolated aggregates and monomers within the nanopores and this is proved by the long kinetic traces of the excited states of the aggregated and the monomeric forms, which decay independently in 1.2 ns and 4.5 ns, respectively. These two time constants are consistent with the luminescence lifetimes measured by the TCSPC experiments.

This behaviour remains constant (**Figures 5.11-5.12**) throughout the series of samples, although the relative spectral contributions from the aggregated form changes compared to the ones of the monomers; specifically, it decreases as the dye loading increases. Also, the time constant for the intermolecular energy transfer decreases from the 1% to the 50% samples. In particular, the spectral evolution, recorded for the 50%-loaded sample (**Figure 5.12**), is essentially dominated by the monomeric form, as also supported by the steady-state absorption spectra. However, in the first dozen of ps, it is possible observing an increase of the bleaching at 530 nm, which is attributed to the energy transfer from the excited state of the aggregated

form. In this case, as the concentration of the monomeric form is higher than the one of the aggregate species, statistically the distance between the two species is the lowest in the sample series. Indeed, the TAS results show that the energy transfer is very efficient for this system and occurs in less than 20 ps, as shown by the disappearance of the small transient absorption band between 550 nm and 700 nm in this short time scale, accompanied by the simultaneous increase in the bleaching of the monomer's ground state at 530 nm. The mean donor-acceptor distance in this case has been calculated to be lower than 15 Å.

On the bases of these results we continued the studies focusing on hybrid host-guest mesoporous silica systems (MCM-41 type) based on a pyridinium species as guest.

5.2 *Hybrid piridinium-silica nanoparticles*

Pyridinium and bipyridinium [14] compounds are extensively used functional species[15] because their appealing electron-withdrawing (pull effect)[16,17] and electron-accepting (redox)[18,19] properties. By virtue of their reduction properties they are suited to artificial systems developed for solar energy conversion, both in bimolecular schemes and in supramolecular (multicomponent) arrangements in which they play the role of electron acceptor (electrophores).[20] Their mild and reversible reduction processes also make them a valid choice as components in supramolecular assemblies designed to behave as electron-storage systems (*e.g.*, polyviologen dendrimers)[21,22] or molecular machines[23,24] whose organisation and machinery are based on charge-transfer interactions and redox inputs, respectively.[15,25]

Nevertheless, pyridinium salts have attracted attentions not only for their well-known redox properties, but also for their electro-optical and photophysical properties.[26] Indeed, there is great interest in designing new types of pyridinium that behave not only as good electrophores, but also as luminophores and chromophores, that is multifunctional and polyvalent entities. This can be achieved by expanding the molecular scaffold of pyridiniums[27] and, particularly, of their π system.[28] Similarly to macromolecular unsaturated hydrocarbon architectures in which connecting patterns[29] are based on single-bond linkages and/or edge-fused linkages, skeletal

expansion of pyridiniums can take the form of aryl-substituted [30, 31] and pericondensed[26c] species.

5.2.1 Piridinium properties

Several pyridinium and bipyridinium species have been studied by the research group where I have worked; the chosen one for my research (hereafter labelled PS1), synthesised by prof. Lainé's research group and isolated as PF_6^- salt, is represented in **Figure 5.13**.

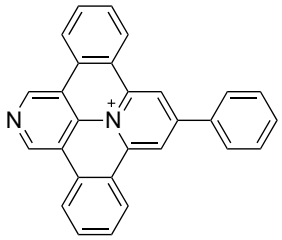

Figure 5.13 *Molecular structure of PS1, isolated as PF_6^- salt.*

PS1 shows interesting photophysical behaviours. As consisting in several fused aromatic rings, it has a rigid structure, which leads its absorption spectrum to be partially structured (**Figure 5.14**). The nuclear configurations of ground and excited states are similar and, therefore, electronic transitions between these states yield structured spectra.

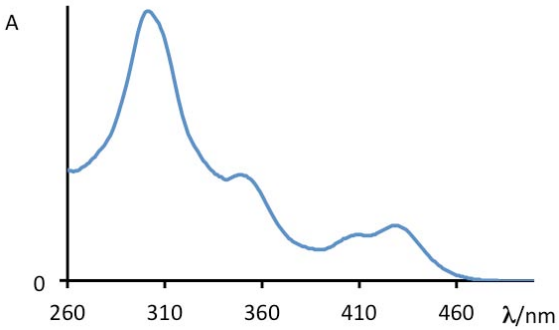

Figure 5.14 *Absorption spectrum of PS1 in water.*

Moreover, a pronounced vibronic effect ascribable to the coupling of intramolecular charge transfer (ICT) transition that involves the dangling phenyl terminus and its torsional motion[32,33,34] also contribute to the absorption features. This effect is clearly visualised at the red edge of the absorption spectrum.

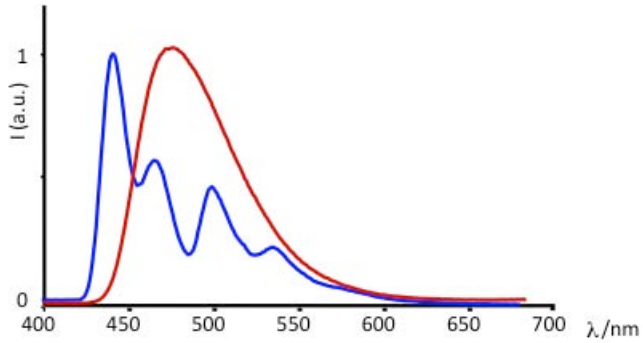

Figure 5.15 *Normalised PS1 luminescence spectra recorded at room temperature in acetonitrile (red curve) and in rigid matrix at 77 K in MeOH/EtOH 4:1 (blue curve).*

PS1 exhibits luminescence (**Figure 5.15**), both in fluid acetonitrile solution at room temperature and in rigid matrix at 77 K in MeOH/EtOH 4:1 (v/v), with monoexponential decays; in both cases, luminescence properties are independent of excitation wavelengths. At room temperature, PS1 shows an emission band centred at 465 nm, with a relatively small Stockes shift due to its rigidity, which does not allow a significant structural reorganisation of the molecule in the excited state. The measured luminescence lifetime has a value of 3.3 ns, with a quantum yield of 0.21.

At 77 K, the luminescence spectrum is structured (vibrational progression of about 1300 cm^{-1}, corresponding to C=C and C=N stretching) and can be assigned to locally excited π–π* singlet and triplet states. The first two luminescence peaks (**Figure 5.15**) are due to the radiative decay of an excited singlet state (fluorescence lifetime: 5.3 ns); at lower energy it is possible to detect a second structured band deriving from the radiative decay of an excited triplet state, characterised by a very long lifetime (phosphorescence lifetime: 800 ms).

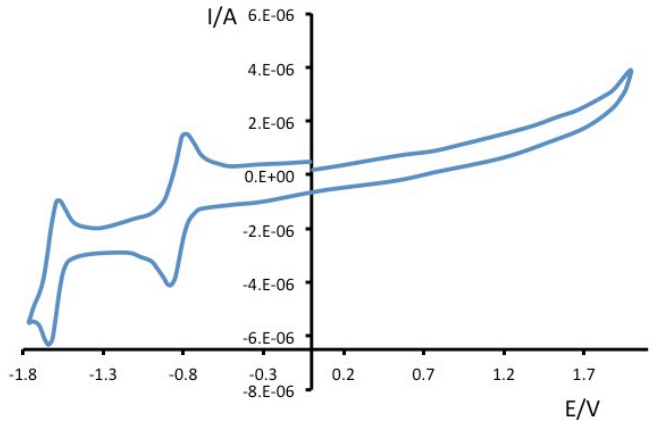

Figure 5.16 *Cyclic voltammetry of PS1 in acetonitrile (0.3 mM) with $TBAPF_6$ (0.1 M).*

We have selected this species not only because of it photophysical properties but also because its redox behaviour. In fact, PS1 species undergo monoelectronic reversible reduction processes at mild potentials in acetonitrile solution (-0.81 V *vs.* SCE and -1.61 V *vs.* SCE) as shown in **Figure 5.16**.

5.2.2 *Hybrid nanoparticles synthesis and morphology*

Similarly to the synthesis of MCM-41 loaded with BPJ2 reported above, an adapted template procedure has been used to prepare the hybrid silica samples. Also in this case, the synthesis has been performed in a basic (pH = 12) aqueous environment. The PS1 (guest) has been integrated within the CTAB micellar phase at varied molar ratios of 1%, 5% and 10%. The nanoparticles so obtained have been dried at room temperature.

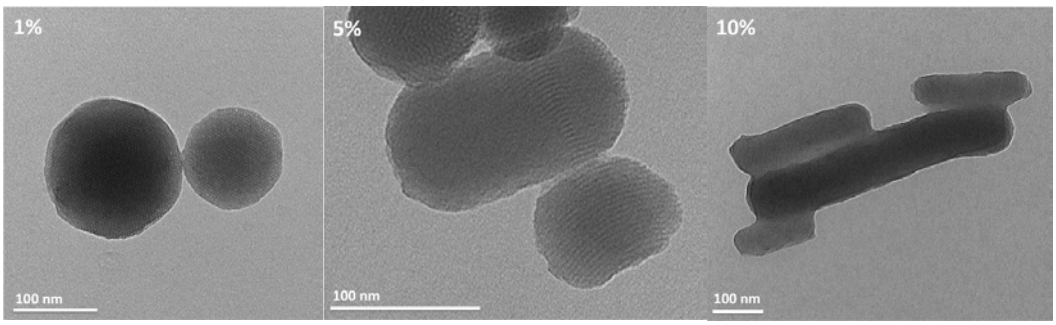

Figure 5.17 *TEM images of 1%- (left), 5%- (centre) and 10%-loaded (right) samples.*

TEM images are shown in **Figure 5.17**. It is easy to notice the increase of PS1 loaded within nanopores leads to more lengthened nanoparticles, as the mesoporous 2D hexagonal array becomes less orderly; in fact, the presence of PS1 among the rod-shaped micelles causes them a distortion, which is as high as the amount of species extraneous to the surfactant.

5.2.3 *Photophysical properties*

MCM-41 hybrid silica materials have been characterised by UV/Vis absorption and luminescence spectroscopy. Their properties have been compared with those of PS1 in solution. Optical measurements can be performed from suspensions of the silica nanoparticles in water, although they are limited by the intense scattering that is

generated by the suspended particles and increases as the wavelength decreases. Cyclohexane proved to be a better choice and so the spectra were recorded from stable suspensions in this solvent.

The scattering generated by 1%- silica nanoparticles is too high, so there are only reported the spectra of the 5%- and 10%-loaded hybrid particles (**Figure 5.18**). In this case the scattering is still high, but it is possible distinguishing the absorption bands due to the presence of PS1 as guest within the silica nanopores.

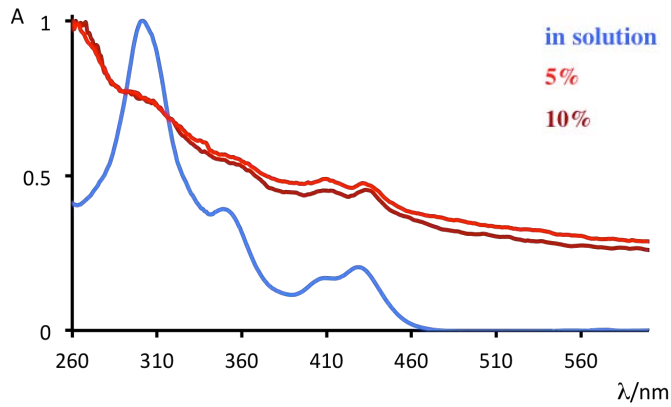

Figure 5.18 *Normalised absorption spectra of PS1 in water (blue) and as hybrid system with a 5% and a 10% loading suspended in cyclohexane.*

A more interesting behaviour of these hybrid species, compared to PS1's in solution, is present in luminescence (**Figure 5.19**).

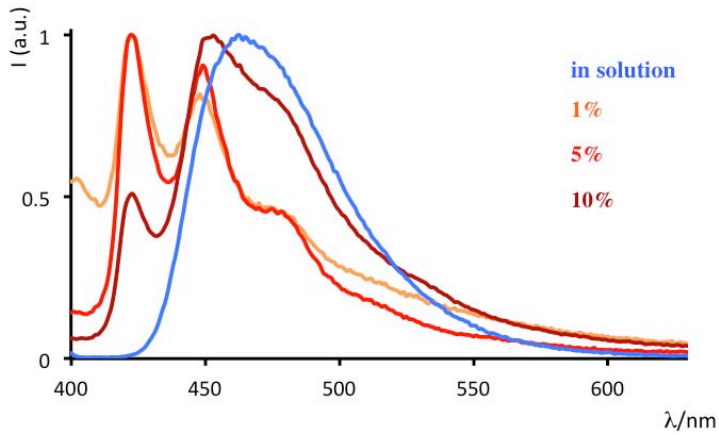

Figure 5.19 *Normalised fluorescence spectra of PS1 in water (blue) and at different percentage loadings in MCM-41 nanoparticles.*

PS1 in solution exhibits a broad emission band peaked at 460 nm, but when it is within the silica nanopores of MCM-41 nanoparticles the luminescence spectra show a new high-energy structured emission band, peaked at 420 and 450 nm, in addition to a broad band centred at 470 nm. By comparison of the emission spectra of PS1 in the hybrid systems with those in solution, it is possible to attribute the band at around 470 nm to the decay of PS1 present within the nanochannels as monomer, whereas the structured band, registered at higher energy, is tentatively attributed to the species that are sterically constrained (so reducing the excited state rearrangement) in the structure. Moreover, the intensity ratio between the high-energy peaks and the lower energy band gets less intense with the increase of the percentage of the MCM-41's loading, even with no thermic treatment. This behaviour is quite similar to the one observed in the BPJ2 hybrid systems, hence the monomeric form becomes predominant as the loading percentage gets higher.

In **Table 5.3** there are resumed the principal components for the excited state lifetimes registered both at high and low energy for all the samples. The comparison of the data suggests that the excited species emitting at higher energy live for around 6 ns whereas the monomeric one (emitting a around 470 nm) at least 2 ns. In fact the decay trace registered at 420 nm is essentially monoexponential for the 1% system while, moving to 450nm and 470 nm biexponential decays can be registered, yielding a new contribution (with increasing weight moving to lower energy) of about 1.8 ns.

Table 5.3 *Lifetimes of PS1 in solution and within MCM-41 nanoparticles.*

Sample	Lifetimes		
	420 nm[a]	450 nm[a]	470 nm[a]
in MeCN	-		4.7 ns
		5.8 ns (70%)	5.6 ns (40%)
1%	6.0 ns	1.9 ns (30%)	1.9 ns (60%)
		5.6 ns (56%)	5.7 ns (45%)
5%	5.9 ns	1.8 ns (44%)	1.9 ns (55%)
		5.6 ns (49%)	5.7 ns (32%)
10%	5.8 ns	1.8 ns (51%)	1.9 ns (68%)

[a] Recorded using a 371.8 nm laser excitation source.

By increasing the amount of dye, the contribution at higher energy becomes less evident as well as multiexponential its lifetime, suggesting a behaviour similar to the one observed for BODIPY containing hybrid systems, with a partial (distance depending) energy transfer from the high energy emitting species the low energy ones.

5.3 *Hybrid systems for energy/electron transfer*

5.3.1 *Synthesis*

On the basis of the obtained results on the PS1-hybrid system, we prepared multichromophoric hybrid mesoporous silica systems containing both PS1 and BPJ2.

Following the same synthetic methodology of the PS1-MCM-41, hybrids nanoparticles containing only BPJ2 (with several loadings) have been resynthesized without drying thermic treatments and used as model systems. The amount of BPJ2 in such silica systems has been the same of the PS1-silica hybrid systems, so it has been obtained 1%-, 5% and 10%-loaded MCM-41 nanoparticles. As it is possible to observe in **Figure 5.20** and **5.21**, the MCM-41 hybrids obtained in these experimental conditions (no heating) do not show evidence of dyes associations, in fact the high-energy bands, observed in the absorption and emission spectra for the previously discussed samples, are in this case absents.

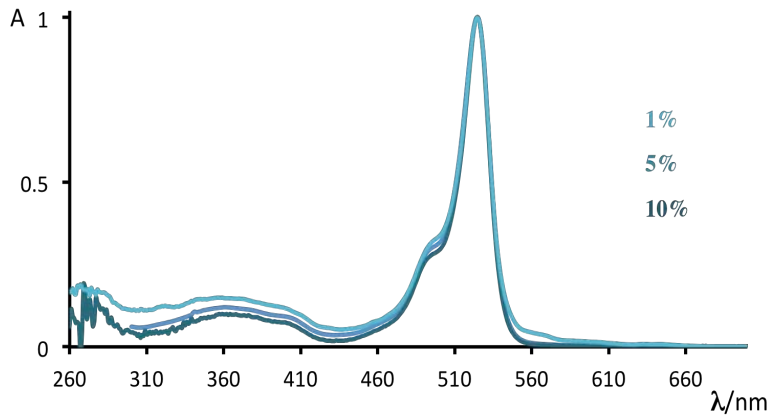

Figure 5.20 *Normalised absorption spectra of BPJ2 MCM-41 systems suspended in cyclohexane.*

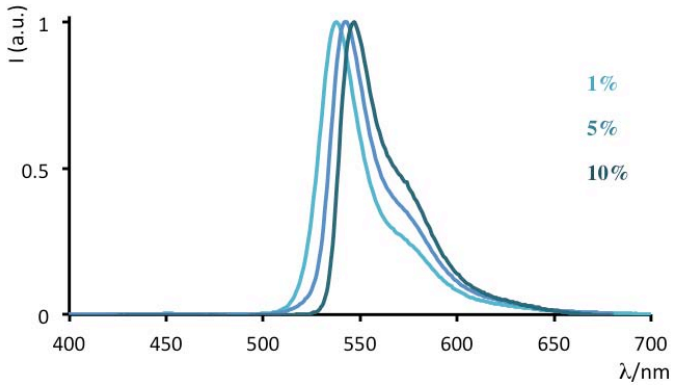

Figure 5.21 *Normalised fluorescence spectra of BPJ2 MCM-41 systems suspended in cyclohexane.* λ_{ex} *= 350 nm.*

Table 5.4 *Percentages of compounds used for the micellar phases in the hybrid silica nanoparticles syntheses.*

Sample	Compounds		
	PS1	BPJ2	CTAB
1%-1% MCM	1%	1%	98%
5%-5% MCM	5%	5%	90%
10%-10% MCM	10%	10%	80%
10%-1% MCM	10%	1%	89%

The same experimental procedure has been used for the preparation of mixed-chromophore hybrid systems, so obtaining three samples having a PS1:BPJ2 ratio of 1:1, loaded at 1%, 5% and 10% (these percentages have been chosen to be able to compare data results with the PS1- and BPJ2-silica systems'). A fourth sample has been synthesised with a PS1:BPJ2 ratio of 10:1 (with a loading of 10% for PS1 and 1% for BPJ2), see **Table 5.4**.

5.3.2 *Photophysical properties*

The absorption spectra of the samples (1:1 ratio) are reported in **Figure 5.22**. The profile and the energy of the absorption bands are quite similar for all the prepared mixed samples. By a comparison between the spectrum of the mixed-dye silica nanoparticles and those of the two mono-dye systems, the more intense band registered the UV region is attributed to the presence of the PS1, confirmed by the small band peaked at 430 nm in the visible region (**Figure 5.22**).

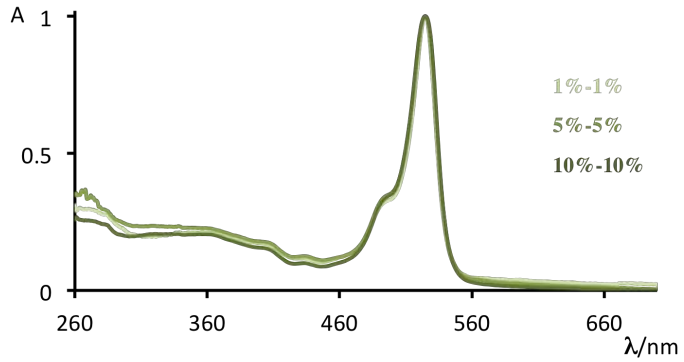

Figure 5.22 *Normalised absorption spectra of PS1-BPJ2 mixed (1:1 ratio) hybrid systems suspended in cyclohexane.*

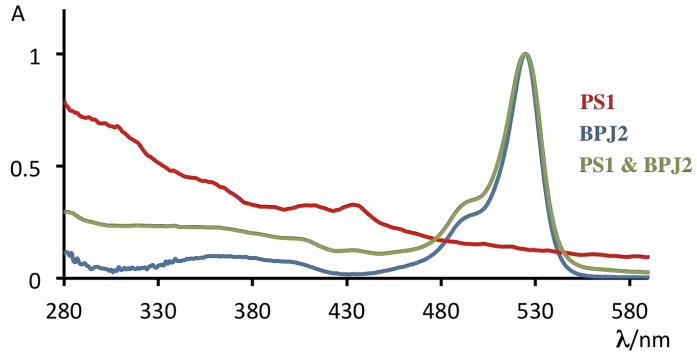

Figure 5.23 *Normalised absorption spectra of hybrid systems containing PS1 (red), BPJ2 (blue) and both of them (green).*

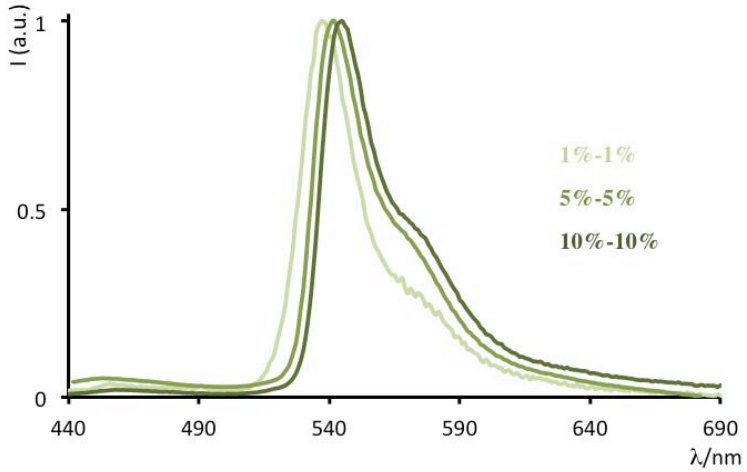

Figure 5.24 *Normalised luminescence spectra of PS1-BPJ2 mixed (1:1 ratio) hybrid systems suspended in cyclohexane.* λ_{ex} *= 430 nm.*

All the samples, dispersed in cyclohexane, are emissive. The spectra of all the 1:1 mixed-hybrid systems are essentially dominated by the BPJ2 bands at around 545 and 580 nm (**Figure 5.24**). No clear evidence of emission from the excited state localised on PS1 have been registered except in the case of the 10:1 PS1:BPJ2 ratio, as it possible to observe in **Figure 5.24 and 5.25**.

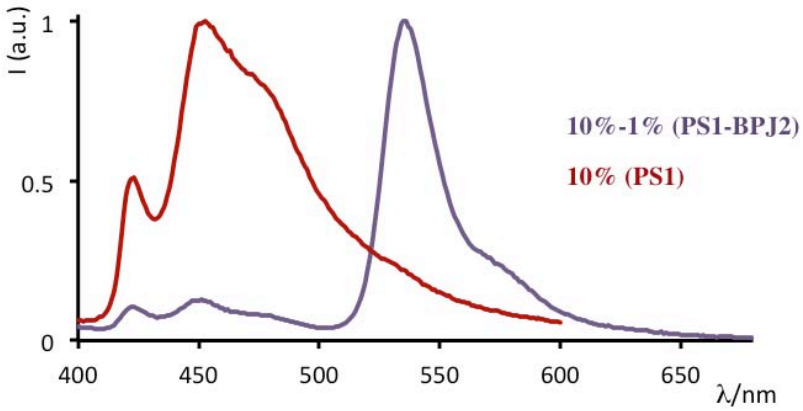

Figure 5.25 *Normalised luminescence spectra of PS1-BPJ2 mixed (10:1 ratio) hybrid systems (purple curve) and 10% PS1 systems (red curve), shown for comparison, suspended in cyclohexane.* λ_{ex} *= 350 nm.*

Table 5.5 *Luminescence lifetimes of mixed dye-loaded MCM-41 nanoparticles.*

Sample	Lifetimes	
	470 nm[a]	550 nm[a]
1%-1% MCM	5.8 ns	4.7 ns
		4.8 ns
5%-5% MCM	5.9 ns	
	5.8 ns	4.0 ns (52%)
10%-10% MCM	4.5 ns	4.8 ns (48%)
	5.8 ns	1.2 ns (20%)
	3.4 ns	3.6 ns (45%)
10%-1% MCM	1.0 ns	4.5 ns (35%)

[a] Recorded using a 371.8 nm laser excitation source.

It has been measured the luminescence lifetimes and the values are reported in **Table 5.5.** The values have been registered at 470 nm, to analyse the PS1 behaviour, and 550 nm, for the BPJ2's. The 1%-1% and 5%-5% mixed samples do not show any

detectedable differences compared to the hybrid systems containing a single dye with the same percentages.

The increase of the percentage of chromophores induces a different photophysical behaviour, in particular in the case of the 10%-10% mixed MCM-41, whose decay traces show a partial reduction of the luminescence lifetimes on PS1 contribution, and, moreover, a slight reduction of the one registered at 550 nm dues to the deactivation of the excited BPJ2.

In 10%-1% sample the decay traces are more complexes, with a multiexponential decay, which indicates a compresence of unquenched PS1 in both the high-energy and low-energy forms and PS1 molecules whose luminescence lifetime (high- and low-energy form) is partially reduced, due in first approximation to the partial energy transfer process from the excited PS1 to BPJ2. At the same time, the quenching of BPJ2 becomes more significant (τ = 3.6 ns).

To rationalise this behaviour, it has been quantified the quantum yield (Φ) of 10%-10% and 10%-1% PS1-BPJ2 mixed systems referred to the luminescence of 10% and 1% BPJ2 samples, respectively, by the **Equation 5.1**:

$$\Phi = \Phi_r \cdot \frac{I}{I_r}\frac{A_r}{A}\frac{\eta^2}{\eta_r^2} \qquad \text{(eq. 5.1)}$$

where Φ_r is the quantum yield of the reference species, I and I_r are the areas of the emission bands of sample and reference, respectively, excited at the same wavelength; A and A_r are the intensities of the absorption spectrum at the excitation wavelength of sample and reference, respectively; η and η_r are the solution refractive indexes of sample and reference, respectively.

Exciting at wavelengths in the spectral area between 465 nm and 490 nm (BPJ2 absorption region) it has been found out for 10%-10% MCM-41 sample a reduction of luminescence intensity (referred to 10% BPJ2 MCM-41) of about 10% (averaged value) and, for 10%-1% MCM-41 sample a reduction (referred to 1% BPJ2 MCM-41) of about 75% (averaged value), that is in agreement with the luminescence lifetimes data obtained.

This quite complicate comportment can be rationalised, in first approximation, taking into account the fact that PS1 can play the role of both luminophore and

electron acceptor, depending if it directly excited or not. The driving force for the electron transfer process from the excited state of BODIPY subunits and PS1 can be estimated by using **Equation 5.2**:

$$\Delta G = (eE_{ox}\text{-}eE_{red}) - E_{00} \qquad \text{(eq. 5.2)}$$

where E_{ox} is the oxidation potential of BODIPY dye, E_{red} is the reduction potential of the Acceptor, and E_{00} is the energy of the involved excited state. The E_{00} for the excited state of BODIPY can be estimated (+/-5 %) from the tangent of the high-energy part of the emission peaks and is shown to be around 2.33 eV. Non-substituted BODIPY dyes are reversibly oxidised around 1.02 V *versus* SCE,[35] and PS1 undergoes to monoelectronic reduction at -0.84 V *versus* SCE. In first approximation (by using the "in solution" values) the driving force for the photoinduced reductive electron transfer process is around -0.47 eV.

This process is strongly dependent of the relative concentration of the dyes and their interdistances. So, in the case of 10%-1% sample, because of the higher amount of PS1 molecules that are statistically localised around BPJ2 species, within the nanopores by a distance that makes efficient these kinds of processes, the excited BPJ2 can be quenched (with a distance dependence) by PS1. This stochastic behaviour has been further demonstrated by synthesising another mixed hybrid silica system using methyl viologen (MV) as quencher instead of PS1, with a MV:BPJ2 ratio of 10:1. MV is well known for his quenching capabilities towards the excited state of BODIPY dyes[36] and, in addition, does not play the role of chromophore or luminophore as PS1.

The new MV:BPJ2 (10:1) system exhibits a quenched luminescence referred to the BPJ2, with luminescence lifetimes (multiexponential in the range of 1 and 3 ns) slightly shorter than the BPJ2 1%-loaded MCM-41 system and comparable to the mixed PS1:BPJ2 (10:1) system's lifetimes.

To further demonstrate the possibility of a bimolecular quenching mechanism, there have been conducted Stern-Volmer experiments on the free BPJ2 chromophore. The emission variations have been analysed by using the equation (**Equation 5.3**):

$$\frac{I_0}{I} = 1 + k_q \tau_0 [Q] \qquad \text{(eq. 5.3)}$$

where I_0 and I are the steady-state fluorescence intensities at the same emission wavelength in the absence and in presence of quencher, respectively; [Q] is the concentration of quencher; τ_0 is the emissive species' lifetime in the absence of quencher; k_q is the rate constant of the quenching process. Usually, the product $k_q\tau_0$ is expressed as Stern-Volmer constant (K_{SV}).

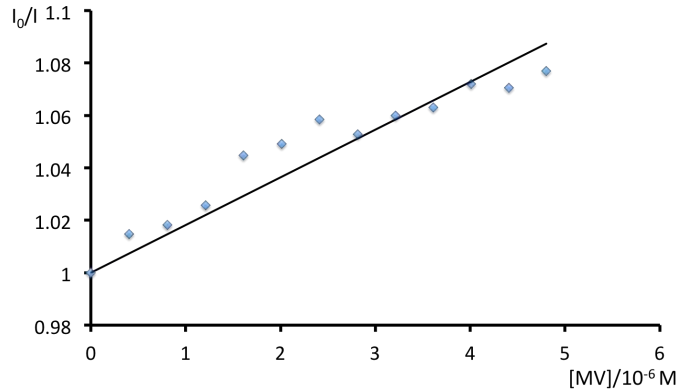

Figure 5.26 *Stern-Volmer plot relative to the quenching of a BPJ2 solution (MeOH, 10^{-6}M) by additions of 20μL of a MV solution (MeOH, 10^{-3}M).*

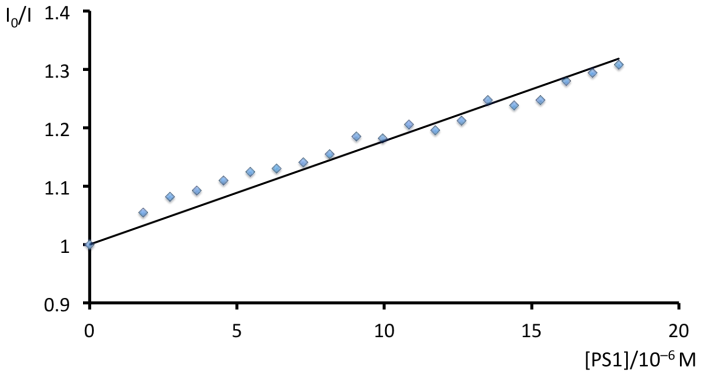

Figure 5.27 *Stern-Volmer plot relative to the quenching of a BPJ2 solution (MeOH, 10^{-6}M) by additions of 20μL of a PS1 solution (MeOH, 10^{-3}M).*

It has been conducted two experiments on BPJ2 solutions (10^{-6} M in methanol), using both MV (**Figure 5.26**) and PS1 (**Figure 5.27**) as quenchers: in both cases a linear dependence has been obtained, suggesting that the quenching process is dynamic (diffusion dependence). Two similar K_{SV} values (MV: $1.82 \cdot 10^4$ M^{-1}; PS1: $1.77 \cdot 10^4$ M^{-1}) have been calculated.

All these results could help to justify also the results obtain in the case of the

10%-10% mixed sample at least in the BODIPY region. The reduction of lifetimes in the PS1 (quite evident in that case) can be justified taking into account of a partial energy transfer process as suggested by the excitation spectra registered at 600 nm. The difference spectrum (**Figure 5.28**) between the excitation spectrum of 10%-10% sample and the excitation spectrum of 10% BPJ2 sample (both of them recorded at λ_{em}=600 nm) shows a small but not negligible band at 430 nm (PS1 absorption band), letting us suppose there is a (small) contribute of PS1 on the population of the luminescent excited state of BPJ2.

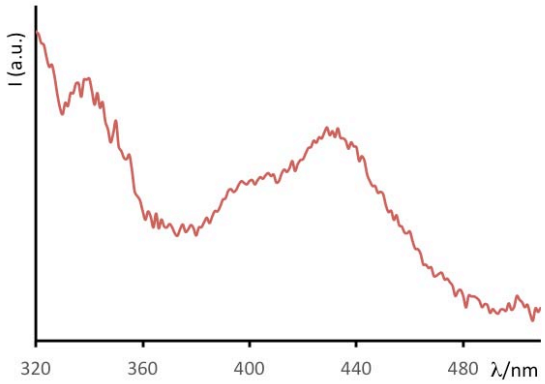

Figure 5.28 *Difference spectrum between 10%-10% sample's excitation spectrum and 10% BPJ2 sample's.*

This overall scenario, which will be supported by further studies (such as transient absorption spectroscopy experiments), suggests that in the cavities PS1 can act in a multimodal way: if it is excited, it leads to an energy transfer process to BPJ2; otherwise, if PS1 is *not* excited, it acts as a quencher to BPJ2.

5.4 Conclusions

A new class of light-harvesting antennae has been prepared by exploiting the template-assisted host-guest chemistry of mesoporous organosilica. By employing green-yellow emitting BODIPY dye (BPJ2), specifically functionalised to self-assemble into two types of micellar templates, there have been obtained hybrid materials, which display peculiar optical activity. A new blue light-absorbing species formed as a result of aggregation phenomena and its content varies depending on the

dye-loading. This species is able to transfer the excitation energy quantitatively to the BODIPY monomers, which in turn act as acceptor units, and the migration process is complete in a time range between 20 and 80 ps.

The MCM-41 matrices have been also used to encapsulate pyridinium chromophore, which exhibits a similar behaviour, at least, in emission with a dual luminescence as function of the dyes loaded amounts.

Because of the dual properties of the chosen piridinium subunits, mixed hybrid species have been obtained, loading both BJP2 and PS1 into MCM-41.

The co-loading leads new properties to the systems with, depending on the excitation wavelength, the opportunity to observe energy transfer from the excited state of PS1 to the BODIPY acceptor or oxidative electron transfer from the ground state of PS1 to the excited BODIPY.

References

1) A. Treibs, F. H. Kreuzer, Justus Liebigs, *Ann. Chem.*, **1968**, 718, 208.223.

2) (a) A. Loudet, K. Burgess, *Chem. Rev.*, **2007**, 107, 4891-4932; (b) R. Ziessel, G. Ulrich, A. Harriman, *New J. Chem.*, **2007**, 31, 496-501.

3) O. Altan Bozdemir, S. Erbas-Cakmak, O. O. Ekiz, A. Dana, E. U. Akkaya, *Angew. Chem. Int. Ed.*, **2011**, 50, 10907–10912; *Angew. Chem.*, **2011**, 123, 11099-11104.

4) S. Diring, F. Puntoriero, F. Nastasi, S. Campagna, R. Ziessel, *J. Am. Chem. Soc.*, **2009**, 131, 6108-6110.

5) F. Puntoriero, F. Nastasi, S. Campagna, T. Bura, R. Ziessel, *Chem. Eur. J.*, **2010**, 16, 8832-8845.

6) (a) J. Iehl, J. F. Nierengarten, A. Harriman, T. Bura, R. Ziessel, *J. Am. Chem. Soc.*, **2012**, 134, 988-998; (b) R. Ziessel, G. Ulrich, A. Haefele, A. Harriman, *J. Am. Chem. Soc.*, **2013**, 135, 11330–11344; (c) A. Kaloudi-Chantzea, N. Karakostas, F. Pitterl, C. P. Raptopoulou, N. Glezos, G. Pistolis, *Chem. Commun.*, **2012**, 48, 12213-12215.

7) F. Cucinotta, B. P. Jarman, C. Caplan, S. J. Cooper, H. J. Riggs, J. Martinelli, K. Djanashvili, E. La Mazza, F. Puntoriero, *ChemPhotoChem*, **2018**, 2, 196-206.

8) (a) X. Yu, X. Jia, X. Yang, W. Liu, W. Qin, *RSC Adv.*, **2014**, 4, 23571-23579; (b) S. Guo, H. Zhang, L. Huang, Z. Guo, G. Xiong, J. Zhao, *Chem. Commun.*, **2013**, 49, 8689-8691; (c) X. Hong, Z. Wang, J. Yang, Q. Zheng, S. Zong, Y. Sheng, D. Zhu, C. Tang, Y. Cui, *Analyst*, **2012**, 137, 4140-4149.

9) J. B. Birks, *Photophysics of Aromatic Molecules, Wiley*, London, **1970**.

10) B. P. Jarman, F. Cucinotta, *Faraday Discuss.*, **2015**, 185, 471-479.

11) T. T. Vu, M. Dvorko, E. Y. Schmidt, J. F. Audibert, P. Retailleau, B. A. Trofimov, R. B. Pansu, G. Clavier, R. Méallet-Renault, *J. Phys. Chem. C*, **2013**, 117, 5373-5385.

12) F. Würthner, T. E. Kaiser, C. R. Saha-Möller, *Angew. Chem. Int. Ed.*, **2011**, 50, 3376–3410; *Angew. Chem.*, **2011**, 123, 3436-3473.

13) S. Choi, J. Bouffard, Y. Kim, *Chem. Sci.*, **2014**, 5, 751-755 and references 11-12 therein.

14) W. Sliwa, *Curr. Org. Chem.*, **2003**, 7, 995-1048.

15) V. Balzani, G. Bergamini, P. Ceroni, *Coord. Chem. Rev.*, **2008**, 252, 2456-2469.

16) (a) C. Reichardt, *Chem. Rev.*, **1994**, 94, 2319-2358, and references therein; (b) P. Chen, T. J. Meyer, *Chem. Rev.*, **1998**, 98, 1439-1477; (c) U. Narang, C. F. Zhao, J. D. Bhawalkar, F. V. Bright, P. N. Prasad, *J. Phys. Chem.*, **1996**, 100, 4521-4525.

17) (a) S. R. Marder, J. W. Perry, C. P. Yakymyshyn, *Chem. Mater.*, **1994**, 6, 1137-1147; (b) S. R. Marder, J. W. Perry, W. P. Schaefer, *Science*, **1989**, 245, 626-628; (c) B. J. Coe, *Acc. Chem. Res.*, **2006**, 39, 383-393; (d) M. Konstantaki, E. Koudoumas, S. Couris, P. Lainé, E. Amouyal,

S. Leach, *J. Phys. Chem. B*, **2001**, 105, 10797-10804; (e) S. R. Marder, J. W. Perry, B. G. Tiemann, W. P. Schaefer, *Organometallics*, **1991**, 10, 1896-1901.

18) S. Hünig, H. Berneth, *Top. Curr. Chem.*, **1980**, 92, 1-44.

19) C. L. Bird, A. T. Kuhn, *Chem. Soc. Rev.*, **1981**, 10, 49-82.

20) (a) V. Balzani, L. Moggi, F. Scandola, *In Supramolecular Photochemistry; Balzani, V., Ed.; D. Reidel Publishing Co.*: Dordrecht, The Netherlands, **1987**, pp 1-28; (b) T. J. Meyer, *Acc. Chem. Res.*, **1989**, 22, 163-170; (c) J. P. Sauvage, J. P. Collin, J. C. Chambron, S. Guillerez, C. Coudret, V. Balzani, F. Barigelleti, L. De Cola, L. Flamigni, *Chem. Rev.*, **1994**, 94, 993-1019; (d) E. H. Yonemoto, R. L. Riley, Y. Il Kim, S. J. Atherton, R. H. Schmehl, T. E. Mallouk, *J. Am. Chem. Soc.*, **1992**, 114, 8081-8087; (e) H. Dürr, S. Bossmann, *Acc. Chem. Res.*, **2001**, 34, 905-917.

21) C. M. Ronconi, J. F. Stoddart, V. Balzani, M. Baroncini, P. Ceroni, C. Giansante, M. Venturi, *Chem. – Eur. J.*, **2008**, 14, 8365-8373.

22) (a) A. Juris, *Annu. Rep. Prog. Chem., Sect. C*, **2003**, 99, 177-241; (b) R. Toba, J. M. Quintela, C. Peinador, E. Roman, A. E. Kaifer, *Chem. Commun.*, **2002**, 1768-1769; (c) W. S. Baker, B. I. Lemon III, R. M. Crooks, *J. Phys. Chem. B*, **2001**, 105, 8885-8894; (d) P. Ceroni, M. Venturi, *Electrochemistry of Functional Supramolecular Systems; Ceroni, P., Credi, A., Venturi, M., Eds.; Wiley*: Hoboken, NJ, **2010**, pp 145-184.

23) W. Sliwa, B. Bachowska, T. Girek, *Curr. Org. Chem.*, **2007**, 11, 497-513.

24) (a) P. L. Anelli, N. Spencer, J. F. Stoddart., *J. Am. Chem. Soc.*, **1991**, 113, 5131-5133; (b) P. L. Anelli, *et al.*, *J. Am. Chem. Soc.*, **1992**, 114, 193-218; (c) R. Ballardini, V. Balzani, M. T. Gandolfi, L. Prodi, M. Venturi, D. Philp, H. G. Ricketts, J. F. Stoddart, *Angew. Chem., Int. Ed. Engl.*, **1993**, 32, 1301-1303; (d) V. Balzani, M. Gomez-Lopez, J. F. Stoddart, *Acc. Chem. Res.*, **1998**, 31, 405-414.

25) A. Credi, M. Venturi, *Electrochemistry of Functional Supramolecular Systems; Ceroni, P., Credi, A., Venturi, M., Eds.; Wiley*: Hoboken, NJ, **2010**, pp 377-424 and references therein.

26) (a) M. I. Knyazhanskii, Y. R. Tymyanskii, V. M. Feigelman, A. R. Katritzky, *Heterocycles*, **1987**, 26, 2963-2982; (b) C. Peltier, P. P. Lainé, G. Scalmani, M. J. Frisch, C. Adamo, I. J. Ciofini, *Mol. Struct.: THEOCHEM*, **2009**, 914, 94-99; (c) J. Fortage, F. Tuyèras, P. Ochsenbein, F. Puntoriero, F. Nastasi, S. Campagna, S. Griveau, F. Bedioui, I. Ciofini, P. P. Lainé, *Chem. – Eur. J.*, **2010**, 16, 11047-11063; (d) C. Peltier, C. Adamo, P. P. Lainé, S. Campagna, F. Puntoriero, I. J. Ciofini, *Phys. Chem. A*, **2010**, 114, 8434-8443; (e) V. Balzani, A. Credi, S. J. Langford, A. Prodi, J. F. Stoddart, M. Venturi, *Supramol. Chem.*, **2001**, 13, 303-311; (f) R. Ballardini, A. Credi, M. T. Gandolfi, C. Giansante, G. Marconi, S. Silvi, M. Venturi, *Inorg. Chim. Acta*, **2007**, 360, 1072-1082.

27) S. Arai, M. Hida, *Adv. Heterocycl. Chem.*, **1992**, 55, 261-358.

28) M. Bendikov, F. Wudl, D. F. Perepichka, *Chem. Rev.*, **2004**, 104, 4891-4945, and references therein.

29) (a) S. Müller, K. Müllen, *Phil. Trans. R. Soc. A*, **2007**, 365, 1453-1472; (b) M. D. Watson, A. Fechtenkoötter, K. Müllen, *Chem. Rev.*, **2001**, 101, 1267-1300.

30) (a) P. P. Lainé, F. Bedioui, P. Ochsenbein, V. Marvaud, M. Bonin, E. Amouyal, *J. Am. Chem. Soc.*, **2002**, 124, 1364-1377; (b) P. P. Lainé, F. Bedioui, E. Amouyal, V. Albin, F. Berruyer-Penaud, *Chem. – Eur. J.*, **2002**, 8, 3162-3176. (c) P. P. Lainé, E. Amouyal, *Chem. Commun.*, **1999**, 935-936.

31) (a) P. P. Lainé, S. Campagna, F. Loiseau, *Coord. Chem. Rev.*, **2008**, 252, 2552-2571; (b) P. P. Lainé, F. Bedioui, F. Loiseau, C. Chiorboli, S.; Campagna, *J. Am. Chem. Soc.*, **2006**, 128, 7510-7521; (c) P. P. Lainé, F. Loiseau, S. Campagna, I. Ciofini, C. Adamo, *Inorg. Chem.*, **2006**, 45, 5538-5551; (d) P. P. Lainé, I. Ciofini, P. Ochsenbein, E. Amouyal, C. Adamo, F. Bedioui, *Chem. – Eur. J.*, **2005**, 11, 3711- 3727; (e) I. Ciofini, P. P. Lainé, F. Bedioui, C. Adamo, *J. Am. Chem. Soc.*, **2004**, 126, 10763-10777.

32) C. Peltier, P. P. Lainé, G. Scalmani, M. J. Frisch, C. Adamo, I. Ciofini, *J. Mol. Struct.: THEOCHEM*, **2009**, 914, 94-99.

33) J. Fortage, F. Tuyèras, P. Ochsenbein, F. Puntoriero, F. Nastasi, S. Campagna, S. Griveau, F. Bedioui, I. Ciofini, P. P. Laineé, *Chem. – Eur. J.*, **2010**, 16, 11047-11063.

34) C. Peltier, C. Adamo, P. P. Lainé, S. Campagna, F. Puntoriero, I. Ciofini, *J. Phys. Chem. A*, **2010**, 114, 8434-8443.

35) A. C. Benniston, G. Copley, K. J. Elliott, R. W. Harrington, W. Clegg, *Eur. J. Org. Chem.*, **2008**, 2705-2713.

36) D. Frath, J. E. Yarnell, G. Ulrich, F.N. Castellano, R. Ziessel, *ChemPhysChem,* **2013**, 14, 3348-3354

Chapter 6

Ru(II) Complexes Appended with Additional Organic Chromophores in Hybrid Silica Nanostructures

On the basis of the results obtained for the hybrid systems based on organic chromophores, discussed in the previous chapter, we decided to investigate the effect of the mesoporous matrix on the intramolecular energy-transfer processes of organic/inorganic dyads.

Transition metal complexes, such as those derived from $[Ru(bpy)_3]^{2+}$, have been extensively studied due to their unique combination of luminescence and redox properties, see Chapter 2. Within this class of compounds, species with prolonged excited-state lifetimes are highly desirable in view of their use in diffusion-rate limited bimolecular processes and in multicomponent (supramolecular) systems featuring photoinduced energy and/or electron transfer processes, where Ru(II) complexes play the role of photo-active subunits.[1] The luminescence lifetimes of Ru(II) polypyridine complexes can be increased if there is the presence of coupled aromatic chromophores, whose lowest-energy triplet excited state (with a long lifetime) has a comparable energy to the luminescent metal triplet state one.[2] This behaviour is due to the thermal equilibrium that arises between the excited triplet states of the two species (**Figure 6.1**), although the resulting emission derives almost exclusively from the radiative decay of ^{3}MLCT state.[3,4,5]

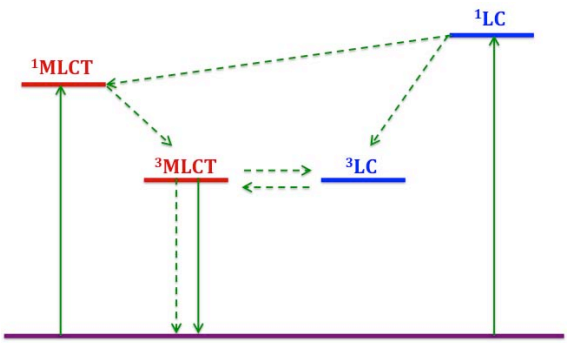

Figure 6.1 *Schematic representation of the energy level diagram and of the possible relaxation processes, at room temperature. Solid and dashed lines are referred to radiative and non-radiative decays, respectively.*

Ru(II) complexes consisting on polypyridine ligands substituted with pyrenyl chromophores follow this equilibrium model and the luminescence lifetimes increase with a higher number of pyrenyl chromophores.[6] Therefore, these complexes exhibit an efficient antenna effect, because the light collected by the peripheral organic chromophores is funnelled to a single one, the central metal core.

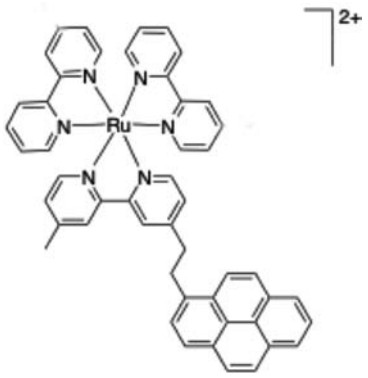

Figure 6.2 *Molecular structure of **Ru-1P**, used as gest for hybrid silica systems. The counterion (chloride) is omitted for clarity.*

To reach our goal we decided to use the species bearing one pyrenyl ([Ru(2,2'-bipyridine)$_2$(bpy-pyr)](PF$_6$)$_2$, bpy-pyr = 4-Methyl-4'-[2-(1-pyrenyl)ethyl]-2,2'-bipyridine), hereafter called **Ru-1P** and depicted in **Figure 6.2**, previously studied by the photochemistry group in Messina. This species, that have been freshly reprepared, is characterised by a long luminescence lifetime (see **Table 6.1**), which is an important property: it may be used in diffusion-rate limited bimolecular processes and in multicomponent (supramolecular) systems where the Ru(II) complex acts as photo-active subunit for photoinduced energy and/or electron transfer processes.

Table 6.1 *Spectroscopic and photophysical data of **Ru-1P** in solution and inside MCM-41 at room temperature.*

	absorption	luminescence		
sample	λ/nm (ε/M^{-1} cm^{-1})	λ_{em}/nm	τ/μs	ϕ
Ru-1P[a]	343 (43 840)	614	2.5 (0.21[b])	0.065
	461 (15 730)			
Ru-1P MCM-41[b]	349 (-)	632	0.98 (1.24[c])	–
	458 (-)			

[a] in degassed acetonitrile; [b] in air equilibrated water; [c] in degassed water.

6.1 Hybrid MCM-41 nanoparticles

I started studying **Ru-1P** MCM-41 hybrid systems. The synthesis has been conducted with the same strategy described for PS1 MCM-41 nanoparticles (see Chapter 4), with a dye loading of 5%. Sample has been washed several times with small amounts of acetonitrile to remove the complexes that are not trapped within template micelles or adsorbed on the surface. Release experiments have been performed to test the stability of the hybrid nanomaterials. No release of dye has been observed in water after at least 2 hours of stirring.

TEM images (**Figure 6.3**), compared to pure MCM-41 silica nanoparticles, show a less-ordered mesoporous structure in **Ru-1P** hybrid silica systems, due to the distortions caused by the metal complex as an extraneous species within the micellar arrays (as explained previously in Chapter 4).

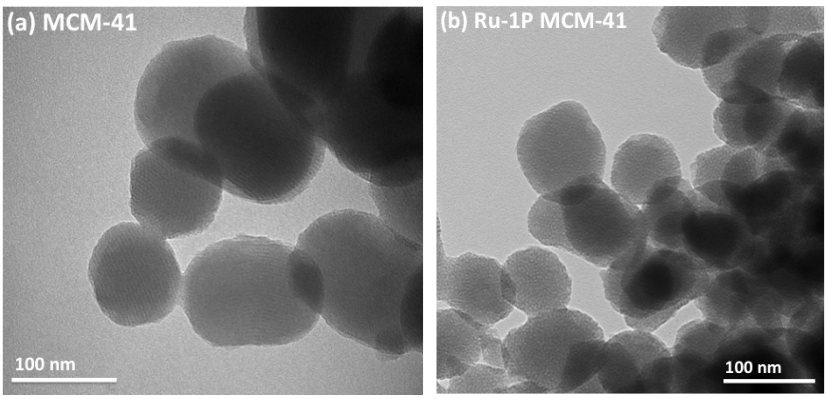

Figure 6.3 *TEM images of hollow MCM-41 (a) and **Ru-1P** MCM-41 hybrid systems.*

Ru-1P MCM-41 nanoparticles exhibit absorption bands (**Figure 6.4**, data stored in **Table 6.1**) that retain the structured shape of the species in acetonitrile solution. The UV region is very rich, because of the several LC transitions. The relatively intense bands in the visible (between 400 and 500 nm) are attributed to spin-allowed MLCT transitions.

The hybrid systems are emissive (see **Figure 6.5** and **Table 6.1**) and such radiative decay is attributed, by comparison with the luminescence properties of the free dye in solution, to ^{3}MLCT excited states,[7,8,9] according to the model above

descripted: the equilibrium between pyrene-based triplet state and ^{3}MLCT state causes a prolonged luminescence from the low-lying ^{3}MLCT state (at least at room temperature).

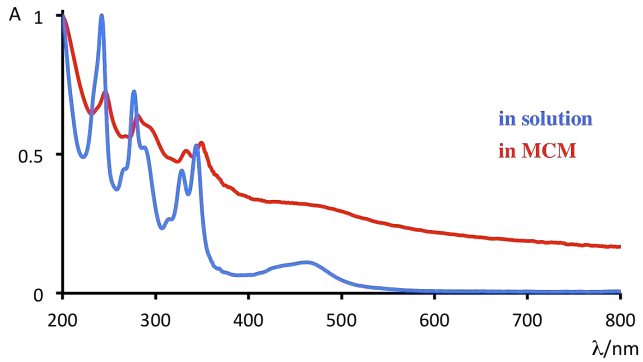

Figure 6.4 *Normalised absorption spectra of **Ru-1P** in acetonitrile (blue) and in silica hybrid system (red).*

In the hybrid MCM-41 nanoparticles the emission band is slightly red-shifted, most probably because of the different environment of the dye inside the nanopores. The absence of residual emission from the pyrene moiety and the comparison between absorption and excitation spectra (**Figure 6.6**) suggest that, even though the antenna system is confined within nanostructure, the energy transfer process from pyrene excited states to Ru(II) core ones is still efficient.

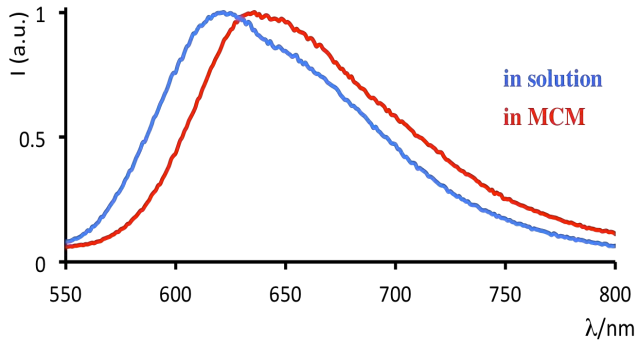

Figure 6.5 *Normalised emission spectra of **Ru-1P** in acetonitrile (blue) and inside MCM-41 nanoparticles in water suspension (red). λ_{ex} = 460 nm.*

The luminescence lifetime registered for the hybrid species in air equilibrated solution is longer with respect to the free dye in same experimental conditions. From results, collected in **Table 6.1**, it is possible to observe that the reduction of O_2

percentage present in the suspension does not influence significantly the emission in the case of the hybrid system, with respect to the effect on the free dye, so suggesting that the antenna within the nanopores is essentially protected by the presence of O_2.

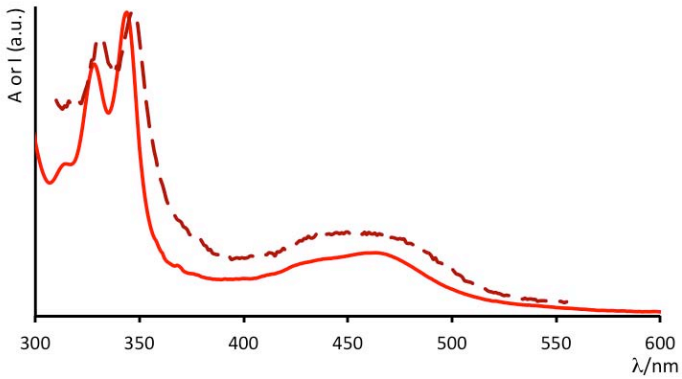

Figure 6.6 *Absorption spectrum of **Ru-1P** in water solution (solid line) and excitation spectrum, registered at 610 nm (dashed line) of **Ru-1P** within MCM-41 in water suspension.*

6.2 Hybrid mesoporous silica spheres

With the aim to investigate this behaviour, we decided to prepare a different kind of silica nanostructure characterised by a higher porosity and so allowing for a higher permeability. The new systems are based on mesoporous silica spheres (MSS), which present a high-surface-area.[10,11]

The synthesis of MSS consists on a modified approach of the methodology reported by Qu *et al.*.[11,12] A mixture of TEOS, cyclohexane and isopropyl alcohol has been added to a mixture of CTAB and urea in water and heated under stirring. TEOS molecules are hydrolysed by urea and, as negatively charged silicate molecules, get arranged in the space available between the self-assembled template molecules. Through such process, they aggregate along the free radial directions and the restricted tangential direction. Condensation of self-assembled silicate leads to the crystallisation of the silica material within the isolated micelles (dispersed in the solvent), yielding fibrous nanospheres. The product obtained has then been collected by centrifugation, dried and, eventually, calcinated at 550°C. **Ru-1P** has been trapped inside nanoparticles letting stir a EtOH suspension of MSS containing **Ru-1P** dissolved. Again, the sample has been washed several times with small amounts of acetonitrile, so removing complex adsorbed on the surface. The amount of complex retained by nanoparticles has been about 27%. Also in this case, release experiments

have been performed to test the stability of the hybrid nanomaterials. No release of dye has been observed in water after at least 2 hours of stirring.

TEM images have been recorded (**Figure 6.7**). Each particle is made by silica fibres, which grow from the centre and spread three-dimensionally, forming a spherical-shaped nanoparticle. The density of these fibres is dependent to the distance from the centre, as in the central part there is a restricted space for the growth of the fibres, resulting in a denser substructure.[12] Since **Ru-1P** has been inserted via a post-synthetic approach, the morphologies of both hollow MSS and **Ru-1P** MSS are similar, as the silica network was already formed. The nanoparticles appear to be monodispersed as demonstrated by the particle-size distribution obtained by DLS experiments (see e.g. panel (c) in **Figure 6.7**).

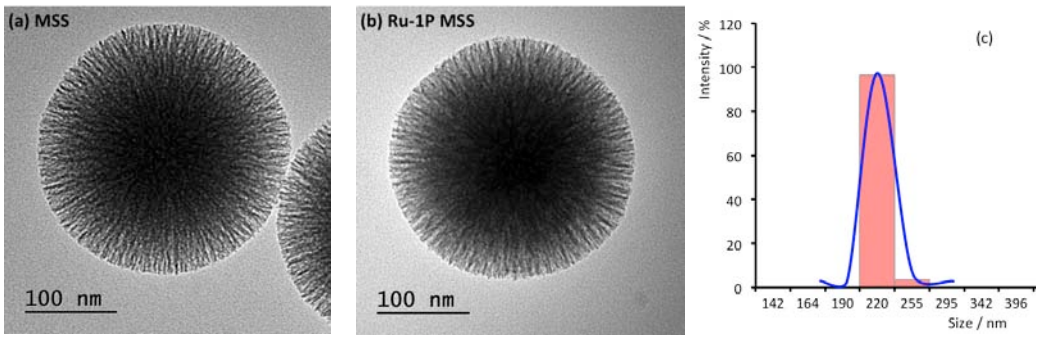

Figure 6.7 *TEM images of hollow MSS (a) and **Ru-1P** MSS hybrid system (b). In panel (c) size distribution of **Ru-1P** MSS is reported.*

Photophysical properties are analogue to those of hybrid MCM-41 nanoparticles. The absorption spectrum (see **Figure 6.8** and **Table 6.2**) exhibits features that could be ascribed to the transition exhibited by **Ru-1P**.

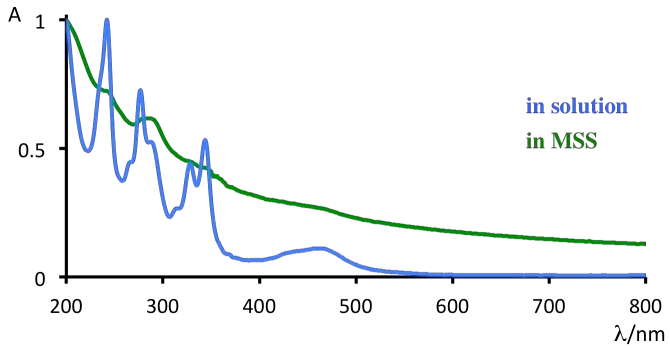

Figure 6.8 *Normalised absorption spectra of **Ru-1P** in acetonitrile (blue) and inside MSS nanoparticles suspended in water (green).*

As well as for the hybrid MCM-41 systems, **Ru-1P** MSS nanoparticles are emissive (**Figure 6.9** and **Table 6.2**). There is no evidence of residual luminescence of pyrene, suggesting that also in this kind of system the energy transfer process from the triplet state centred on the pyrene to the ^{3}MLCT excited state remains active. This is confirmed by the comparison between absorption and excitation spectra (**Figure 6.10**). In this case, the emission band of **Ru-1P** MSS is slightly blue-shifted, compared to **Ru-1P** luminescence band in acetonitrile solution. This result can be rationalised taking into account the higher dimension of the pores with respect to the hybrid MCM-41, that allow for a stronger interaction with the solvent

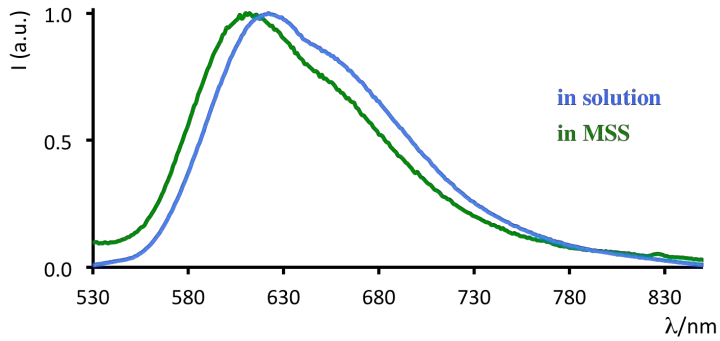

Figure 6.9 *Normalised emission spectra of **Ru-1P** in acetonitrile (blue) and inside MSS nanoparticles suspended in water (green).* λ_{ex} *= 440 nm.*

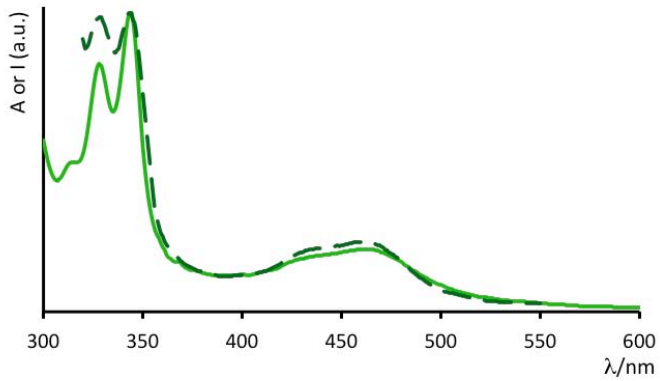

Figure 6.10 *Absorption spectrum of **Ru-1P** in water solution (solid line) and excitation spectrum, registered at 610 nm (dashed line) of **Ru-1P** within MSS in water suspension.*

This higher exposition of the dye to the environment it is also confirmed by the difference in excited state lifetime between the air equilibrated and degassed

suspensions. The results, in fact, show that reducing the amount of O_2 present in the mixture leads to a significant increase of lifetime (**Table 6.2**).

Table 6.2 *Spectroscopic and photophysical data of **Ru-1P** in solution and inside MSS at room temperature.*

sample	absorption	luminescence		
	λ/nm (ε/M^{-1} cm^{-1})	λ_{em}/nm	τ/μs	ϕ
Ru-1P[a]	343 (43 840)	614	2.5 (0.21[b])	0.065
	461 (15 730)			
Ru-1P MSS[b]	344 (-)	610	2.07 (4.70[c])	–
	462 (-)			

[a] in degassed acetonitrile; [b] in air equilibrated water; [c] in degassed water.

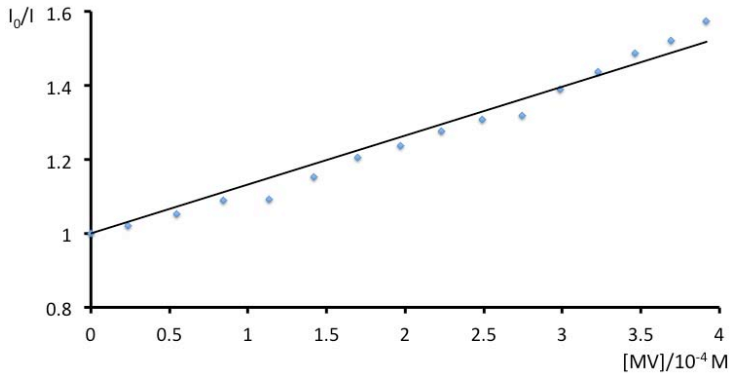

Figure 6.11 *Stern-Volmer plot relative to the quenching of a **Ru-1P** solution (water, 10^{-6} M) by sequential additions of a MV solution (water, $2.4 \cdot 10^{-3}$ M).*

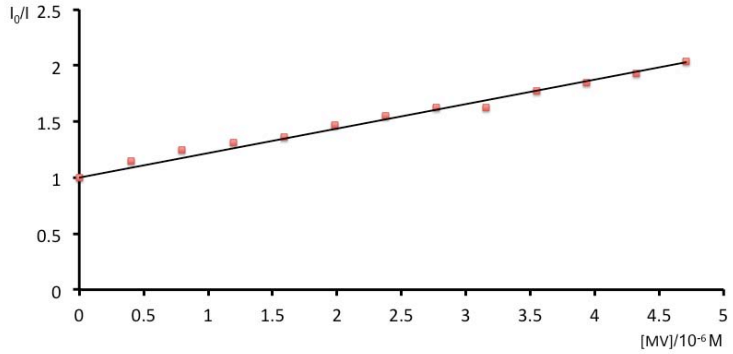

Figure 6.12 *Stern-Volmer plot relative to the quenching of a **Ru-1P** MSS suspension (water) by sequential additions of a MV solution (water, $2.4 \cdot 10^{-4}$ M).*

Quenching studies have also been conducted performing Stern-Volmer

experiments on **Ru-1P** in solution, **Ru-1P** MCM-41 and **Ru-1P** MSS nanoparticles (**Figure 6.11 and 6.12**) using methyl viologen (MV) as quencher.

As expected, by adding MV to a solution of **Ru-1P** in water a quenching of the luminescence is registered, see **Figure 6.11**, with a K_{SV} equal to $1.32 \cdot 10^3$ M^{-1}. The quenching profile, as well as the K_{SV} value, strongly supports a diffusional quenching. Considering an excited state lifetime of 0.2 μs, the bimolecular quenching constant k_q, strongly dependent on the viscosity of the solvent, results equal to $6.6 \cdot 10^9$ $M^{-1}s^{-1}$, confirming that a diffusion controlled process is active.

Stern-Volmer experiments on **Ru-1P** MCM-41 have been inconclusive, confirming the ruthenium complex within nanopores is isolated from external species, which cannot reach the dye inside the structures. On the other hand, experiments on hybrid MSS showed **Ru-1P** within this kind of nanoparticle can be quenched by MV. The high porosity structure of the MSS allows for direct interaction of the quencher with the metal complex. In this case, see **Figure 6.12**, the Stern-Volmer plot is linear but the constant (K_{SV}: $2.19 \cdot 10^5$ M^{-1}) results two order of magnitude higher with respect to the one obtained for free **Ru-1P.** Anyway, taking into account the longer excited lifetime of **Ru1-P** inside MSS, the k_q ($1.1 \cdot 10^{11}$ $M^{-1}s^{-1}$) result one order of magnitude higher. This behaviour could be rationalised as an energy hopping process along the chromophores inside the silica, so one MV subunit could, in this case, quench more than one excited state of **Ru-1P** with respect to the free species.

6.3 Adding new functionalities

It is worth thinking systems containing an antenna and another active species may be assembled. New functionalities may be so introduced. Since MSS's permeability to water, a possible application could be trapping inside the nanoparticle both chromophore and water oxidation catalysts as iridium oxide nanoparticles (IrO_x).[13,14] The **Ru-1P** antenna would act, in this case, as photosentiser for the process.

As preliminary study, IrO_x nanoparticles have been synthesised within MSS via a new photochemical hydrolysis approach.[12,15] MSS nanoparticles have been suspended in an $IrCl_3$ solution (water, 2 mM) and the pH has been adjusted to 12 through a

concentrated KOH solution. The mixture has been then left stirring at room temperature under UV irradiation (390 nm, 5 mW) overnight. It has been finally centrifuged and the precipitate dried at room temperature.

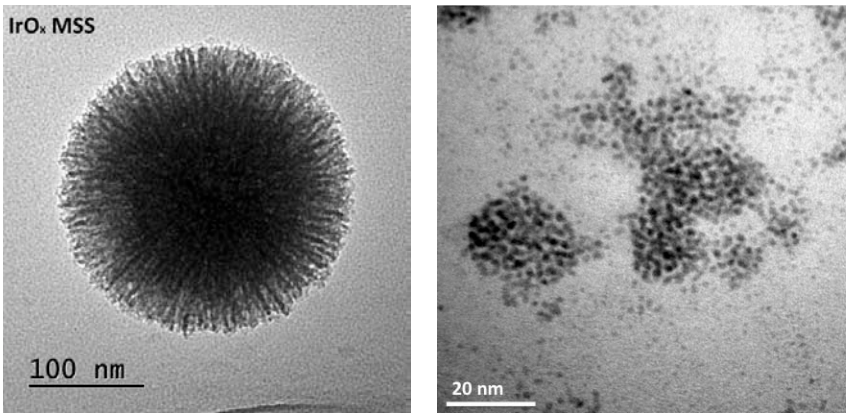

Figure 6.13 *Left: TEM image of MSS nanoparticles with iridium oxide nanoparticles inside. Right: TEM image of iridium oxide nanoparticles.*

TEM images (**Figure 6.13**) show IrO_x nanoparticles are retained by MSS, accumulating especially among the most external MSS branches. As model, the TEM images referred to the free IrO_x nanoparticles are also shown in **Figure 6.13**, demonstrating that, by this photochemical procedure, quite small particles (few nm) can be produced. These results suggest that the new system is able to encapsulate totally inorganic structures, so yielding stable (with no release in solution) hybrid systems. Further photocatalysis studies on these systems (with also **Ru-1P** trapped inside) will have to be done to verify the capacity of them to take part in water oxidation processes.

6.4 *Conclusions*

Excited-state equilibration which governs the photo-physical properties of a pyrene-appended $[Ru(bpy)_3]^{2+}$–type complex in homogeneous solution appears equally to be operational when the complex is hosted in MCM-41 or adsorbed on mesoporous silica spheres leading to long luminescence lifetimes. While the specific role of mesoporous silica supports on the properties of ruthenium polypyridine complexes often requires clarification, different environmental effects when hosted, in the case studied in this thesis, seem to only subtly affect the energy levels of the

excited state. In fact, the processes of equilibration of the excited state by the pyrenil fragment and the consequent prolongation of the excited state remain unaffected allowing to measure life-times that vary in the range of 0.9 – 2 μs. In the case of the MCM-41, however, a decreased sensitivity to the quenching by dissolved oxygen and MV has been observed. This sensitivity, on the other hand, is still active, for both quenchers, in the case of nano-spheres hybrid materials. Moreover, the latter, as a function of their higher open-pore structure, have been used, with good results (although preliminary) as support for the photochemical synthesis of IrO_x nanoparticles as possible catalysts for photoinduced water oxidation.

References

1) (a) V. Balzani, A. Juris, M. Venturi, S. Campagna, S. Serroni, *Chem. Rev.*, **1996**, 96, 759; (b) C. A. Bignozzi, J. R. Schoonover, F. Scandola, Progr. *Inorg. Chem.*, **1997**, 44, 1; (c) F. Barigelletti, L. Flamigni, *Chem. Soc. Rev.*, **2000**, 29, 1.

2) W. E. Ford, M. A. Rodgers, *J. Phys. Chem.*, **1992**, 96, 2917.

3) (a) D. S. Tyson, F. N. Castellano, *J. Phys. Chem. A*, **1999**, 103, 10 955; (b) D. S. Tyson, K. B. Henbest, J. Bialecki, F. N. Castellano, J. *Phys. Chem. A*, **2001**, 105, 8154.

4) G. J. Wilson, A. Launikonis, W. H. F. Sasse, A. W.-H. Mau, *J. Phys. Chem. A*, **1997**, 101, 4860.

5) (a) J. A. Simon, S. L. Curry, R. H. Schmehl, T. R. Schatz, P. Piotrowiak, X. Jin, R. P. Thummel, *J. Am. Chem. Soc.*, **1997**, 119, 11 012; (b) M. Hissler, A. Harriman, A. Khatyr, R. Ziessel, *Chem. Eur. J.*, **1999**, 5, 3366; (c) N. B. Thornton, K. S. Schanze, *New J. Chem.*, **1996**, 20, 791; (d) D. S. Tyson, C. R. Luman, X. Zhou, F. N. Castellano, *Inorg. Chem.*, **2001**, 40, 4063; (e) A. Juris, L. Prodi, *New J. Chem.*, **2001**, 25, 1132.

6) B. Maubert, N. D. McClenaghan, M. T. Indelli, S. Campagna, *J. Phys. Chem. A*, **2003**, 107, 447-455.

7) (a) V. Balzani,; F. Scandola, *Supramolecular Photochemistry*; Horwood: Chichester, **1991**; (b) J.-P. Sauvage, J. P. Collin, J.-C. Chambron, S.Guillerez, C. Coudret, V. Balzani, F. Barigelletti, L. De Cola, L. Flamigni, *Chem. Rev.* **1994**, 94, 993; (c) V. Balzani, A. Juris, M. Venturi, S. Campagna, S. Serroni, *Chem. Rev.*, **1996**, 96, 956 and references therein; (d) A. Harriman, R. Ziessel, *Chem. Commun.*, **1996**, 1707; (e) C. A. Bignozzi, J. R. Schoonover, F. Scandola, *Progr. Inorg. Chem.*, **1997**, 44, 1. (f) L. De Cola, P. Belser, *Coord. Chem. Rev.*, **1998**, 177, 301; (g) F. Barigelletti, L. Flamigni, *Chem. Soc. Rev.*, **2000**, 29, 1; (h) L. Sun, L. Hammarstroem, B. Akermark, S. Styring, *Chem. Soc. Rev.*, **2001**, 30, 36; (i) R. Ballardini, V. Balzani, A. Credi, M. T. Gandolfi, Venturi, *Acc. Chem. Res.*, **2001**, 34, 445; (l) D. Pomeranc, V. Heitz, J.-C. Chambron, J.-P. Sauvage, *Am. Chem. Soc.*, **2001**, 123, 12215; (m) C. N. Fleming, K. A. Maxwell, J. M. De Simone, T. J. Meyer, J. M. Papanikolas, J. *Am. Chem. Soc.*, **2001**, 123, 10336.

8) A. Juris, V. Balzani, F. Barigelletti, S. Campagna, P. Belser, A. von Zelewsky, *Coord. Chem. Rev.*, **1988**, 84, 85.

9) (a) S. Boyde, G. F. Strouse, W. E., Jones Jr, T. J. Meyer, *J. Am. Chem. Soc.*, **1989**, 111, 7448; (b) J. N. Younathan, W. E. Jones, T. J. Meyer, *J. Phys. Chem.*, **1991**, 95, 488; (c) P .Belser, R. Dux, M. Baak, L. De Cola, V. Balzani, *Angew. Chem., Intern. Ed. Engl.*, **1995**, 34, 595.

10) V. Polshettiwar, D. Cha, X. Zhang, J. M. Basset, *Angew. Chem. Int. Ed.*, **2010**, 49, 9652–9656; *Angew. Chem.*, **2010**, 122, 9846-9850.

11) X. Deng, R. Rin, J.-C. Tseng, C. Weidenthaler, U.-P. Apfel, H. Teysez, *ChemCatChem*, **2017**, 9, 4238-4243

12) Q. Qu, Y. Min, L. Zhang, Q. Xu, Y. Yin, *Anal. Chem.*, **2015**, 87, 9631-9638.

13) G. La Ganga, F. Nastasi, S. Campagna, F. Puntoriero, *Dalton Trans.*, **2009**, 45, 9997-9999.

14) (a) H. Hara, C. C. Waraksa, J. T. Lean, B. A. Lewis, T. E. Mallouk, *J. Phys. Chem. A*, **2000**, 104, 5275-5280; (b) N. D. Morris, M. Suzuki, T. E. Mallouk, *J. Ohys. Chem. A*, **2004**, 108, 9115-9119; (c) P. G. Hoertz, Y.-I. Kim, W. J. Youngblood, T. E. Mallouk, *J. Phys. Chem B*, **2007**, 111, 6845-6856; (d) M. Hara, J. T. Lean, T. E. Mallouk, *Chem. Mater.*, **2001**, 13, 4668-4675.

15) D. Xu, P. Diao, T. Jin, O. Wu, X. Liu, Xin Guo, H. Gong, F. Li, M. Xiang, Y. Ronghai, *ACS Appl. Mater. Interfaces*, **2015**, 7, 16738-16749.

Chapter 7

Interaction with Bio-Materials

Introduction

Nucleic acids are the building blocks of life and, consequently, the subject of innumerable investigations. In carrying out its role, DNA is assisted by the action of ions, small molecules, proteins, enzymes which, interacting with it in a reversible way, stabilise it, protect it, repair it and regulate the opening of the double helix at the base of the processes of duplication and transcription. The non-covalent interactions that a small species can establish with the nucleic acids are widely studied, not only to understand the mechanisms at the base of the interaction,[1] but also to realise if the interaction can be exploited, for example, in the medical field or in cell biology.[2] Some species, in fact, are able to interact with the DNA of tumour cells, interfering with their proliferative mechanism and activating the apoptotic process;[3] some others make the cell luminescent and can be used to stain the DNA.[4]

Over the past few decades, small molecules that bind to DNA have shown significant promise as diagnostic probes, reactive agents and therapeutics.

Much attention has focused on the design of organic, DNA-binding agents. However, over the past twenty five years, increasing interest has focused on another class of noncovalent DNA-binding agents: substitutionally inert, octahedral transition metal complexes that can bind or react with specific DNA sites provide a means to access this cellular information. To this goal we followed this path taking advantage of the structure of Ru(II)-based building blocks discussed in Chapter 2 and 4.

***7.1** DNA structure*

Deoxyribonucleic acid (DNA) is a biopolymer composed by nucleotides, which are monomers containing three components: a phosphate group, a pentose monosaccharide (deoxyribose) and a nitrogenous base bonded to deoxyribose by a N-glycosidic bond. The nitrogenous bases that constitute DNA are four: adenine (A) and guanine (G), purine derivatives; cytosine (C) and thymine (T), pyrimidine derivatives. They are shown in **Figure 7.1**.

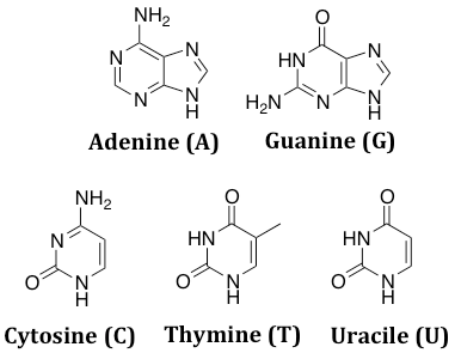

Figure 7.1 *Nitrogenous bases contained in nucleic acids.*

There exists a fifth nitrogenous base (pyrimidine derivative), the uracil (U), but this base is present in RNA (ribonucleic acid) filaments instead of thymine. Uracil is present in DNA molecule only as degradation product derived from the degradation of cytosine. The order of the nitrogenous bases disposition determines the genetic information that leads to the amino acids syntheses.

Each monosaccharide molecule is bonded to the nitrogenous bases by glycosidic bond to C1. Nucleotides bind covalently reciprocally to form polynucleotides by phosphodiester bonds, linking the 3' carbon atom of one sugar molecule to the 5' carbon atom of a second one via a phosphate group (**Figure 7.2**).[5]

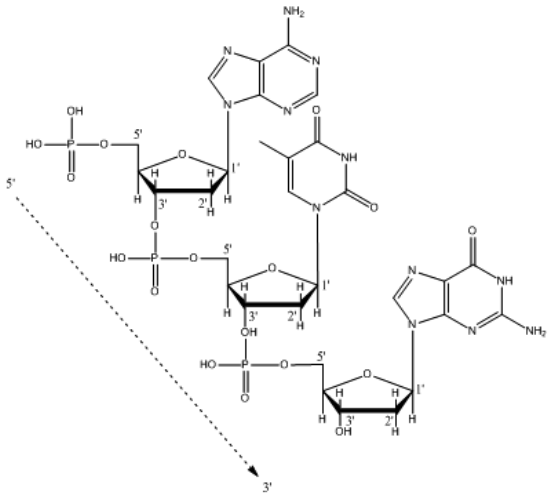

Figure 7.2 *Phophodiester bonds between nucleotides to form polynucleotides.*

The classic 3D-model, proposed by Watson and Crick in 1953, describes the DNA (in B conformation) as two polynucleotide chains that coil around each other to form

a right-handed double helix (**Figure 7.3**).[6] The two filaments of the DNA run in opposite directions to each other, so they are antiparallel and, according to the model, this is the reason such winding is present. In the centre of the double helix there are the nitrogenous bases, which keep the two chains bound by hydrophobic π-π interactions (which reduce the interaction with water molecules) and by hydrogen bond between complementary bases, each of them belonging to a different chain. It is exclusively the interaction between a purine and pyrimidine derived base which grants the necessary distance in order that the hydrogen bond can form: this can happen only by the A-T and G-C pairs (**Figure 7.3**).

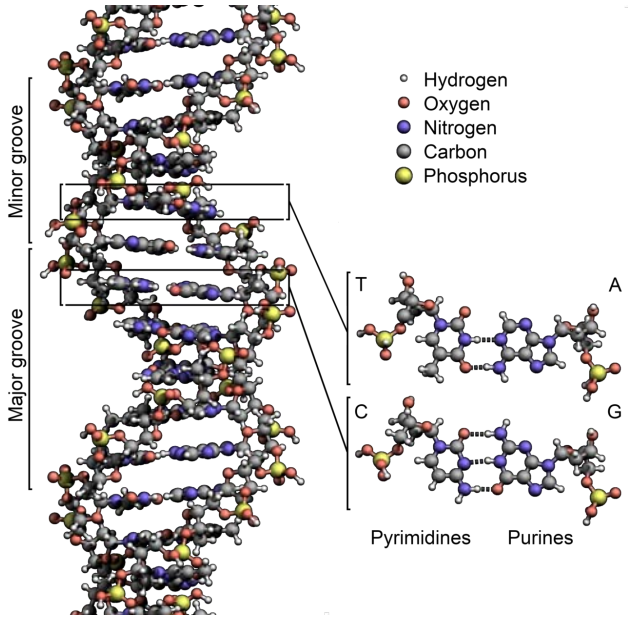

Figure 7.3 *Double helix model of B-DNA. On the right, complementary hydrogen bonds in A-T and G-C pairs are highlighted.*

Since hydrogen bonds are weak, it is relatively easy breaking and forming them again, like a zip, due to, for example, high temperature or by mechanic interactions. As a consequence, in addition of the bases complementary, DNA molecules may be replicated so that all the biological information within contained may be duplicated: such is the DNA replication.[7]

As shown in **Figure 7.3**, it is evident the G-C stability (three hydrogen bonds) is higher than the A-T one (two hydrogen bonds), therefore the global stability of a DNA helix is related to the amount of G-C pairs, as well as the chain length.

B conformation is the most common DNA conformation found within cells.[8] B-DNA winds up in a right-handed way (**Figure 7.3**). There are ten nitrogenous bases per turn, paired on the same plane and arranged perpendicularly to the DNA axis; they have an anti conformation. The stacking of the nucleobases leads to the formation of a major and a minor groove in the DNA comformation. In B-DNA the major groove is 11.6 Å wide and the minor one is 6.0 Å wide: this difference leads to a different accessibility to the nitrogenous bases, depending their position. Since on these grooves the nitrogenous bases are exposed to solvent, they may interact specifically with other species without implicating modifications to the double helix. The majority of DNA-specific proteins interact with it right in one of the two grooves. Of course, also specific interactions may occur.

7.2 Interaction of small molecules with DNA

It is possible distinguish two kinds of interactions with DNA: reversible and irreversible interactions.[9] Irreversible interactions involve the formation of a covalent or coordination bond between a species and an atom site of the helix; such a linkage implicates the total inhibition of DNA processes (and the cell death as a consequence). Very often, the steric hindrance of species bound irreversibly may cause a distortion of the phosphate groups, which leads to negative effects about DNA transcription and replication as prevents, for example, the identification protein-complex.[10]

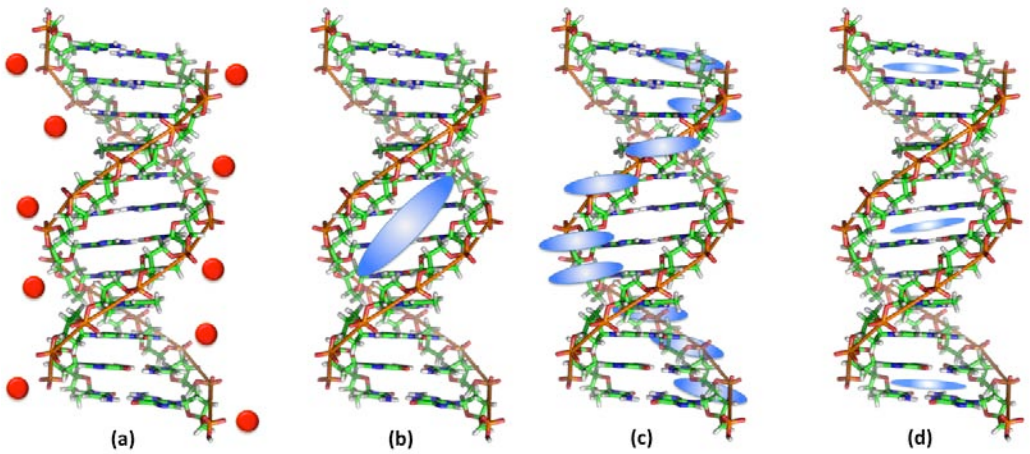

Figure 7.4 *Schematisation of the main reversible interactions species may form with DNA: (a) external electrostatic interaction, (b) major groove binding, (c) external self-aggregation and (d) intercalation.*

Reversible interactions are usually less toxic than the irreversible ones. They can be classified in four types: (i) external electrostatic interaction, (ii) major groove binding, (iii) external self-aggregation and (iv) intercalation (**Figure 7.4**).

The external electrostatic interaction (i) is due to the presence of the phosphate groups in the chain because their negative charge may attractively interact above any positive ion (**Figure 7.4a**). In particular, simple cations like alkaline ones associates with nucleic acids in base of the density charge generated by the phosphate groups, resulting in a stabilisation of the DNA itself. This association is called *condensation*, because ions are associated to the overall charge of the biomolecule but not to any specific site, remaining capable to move around the double helix. The typical DNA counterions are Na^+ ions, which compensate the most of phosphate groups' negative charge. The remaining charges are neutralised by others cations by the classic Debye-Huckel mechanism.

The major groove binding (ii) occurs for species having the right dimension and conformation to "lay down" in one of the grooves, interacting via electrostatic interactions, Van der Waals forces and, especially, hydrogen bonds (**Figure 7.4b**).[11] The typical molecules able to make this kind of interaction have an appropriate length and flexibility with which may assume an optimal conformation. Usually, these molecules have several aromatic rings (like pyrroles, furans or benzenes) bound to substituents capable to rotate around the bonds, letting them adapt to the double helix shape without perturbing significantly the DNA structure.

External self-aggregation (iii) occurs when molecules, especially aromatic planar species, stack along the external part of double helix (**Figure 7.4c**), forming dimers or even huge aggregates by a non-specific bond called external stacking. It is known interactions of porphyrin and metal-porphyrin with DNA, which lead to the formation of chiral supramolecular structures,[12] Pt(II) organometal complexes coordinated by terpyridine[13] or extended aromatic ligands like dipyrido[3,2-a:2',3'-c]phenazine or benzodipyrido[b:3,2-h:2',3'-j]phenazine in the case of low [DNA]/[complex] ratio and presence of few intercalative sites.[14] Pasternack *et al.* highlighted the structure of intercalators influences the interaction type with DNA and may lead an external interaction to be preferred rather than intercalation.[15]

Intercalation (iv) is the insertion of an aromatic planar molecule between two

adjacent nitrogenous pairs (**Figure 7.4d**). Intercalation is permitted by a significant overlap between π orbitals of the intercalative species and those of nitrogenous bases. This is the kind of interaction on which the study explained in this chapter focuses on.

7.3 Intercalation model

In 1961, Lerman, studying interactions between DNA and cationic aromatic planar acridines, hypothesised a model about this interaction, then called intercalation: intercalating molecules arranges perpendicularly between nitrogenous bases pairs, forming a system stabilised by Van der Waals forces, hydrophobic interaction and, especially, π-π stacking (**Figure 7.5**).[16,17]

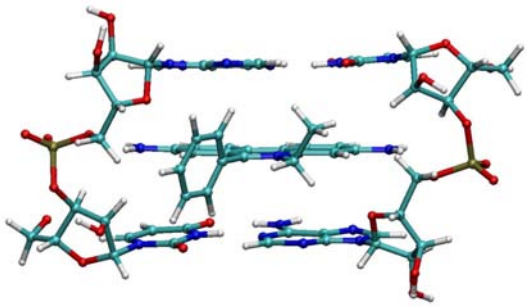

Figure 7.5 *Intercalation model.*

To permit this intercalation process it is necessary a "cavity" forms between the nucleobases, so they have to distance each other; this process causes the elongation of DNA.[18] Vertical separation between nucleobases (about 3.4 Å in the B-DNA) when a huge aromatic molecule intercalates may increase from 1.8 to 4.5 Å per intercalated molecule. The angle of rotation may vary from 11° to 48°, depending on intercalator structure and the type of nucleotides involved.[19] The process causes distortions in the DNA structure that can be used to study DNA-molecule interactions by, for example, viscosity measurements, [20] sedimentation studies, [21] circular dichroism (CD) variations,[20,21,22] and electrophoresis studies on circular DNA supercoil.[23]

The intercalation model proposed by Lerman, however, did not take in account the possibility of the intercalator to insert itself between nucleobases pairs until the double helix saturation. Crothers introduced the neighbour exclusion model:[24] in the

case a molecule intercalates in a site it distorts the vicinal ones, so that they will not be available to permit an intercalation with other molecules (**Figure 7.6**). There arises that intercalation is anti-cooperative at adjacent sites and, therefore, only the 50% of DNA sites can undergo to an intercalation interaction. Moreover, it is also (highly) possible the molecules do not occupy every other site, obstructing more than two of them; also, huge molecules may prevent this kind of interaction due their steric hindrance.

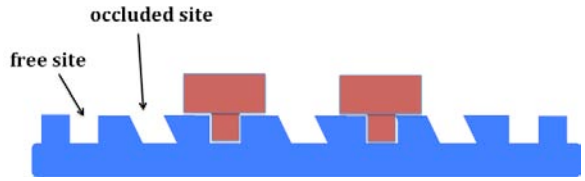

Figure 7.6 *Schematisation of neighbour exclusion intercalating model.*

It has been conducted several studies to know if there exists a specificity in intercalation interactions related to the type or the sequence of nucleobases. Some intercalators showed preferential interactions, but almost all of them interact aspecifically with the nucleobases.

At first it was believed only small molecules, with a planar structure, could intercalate, but after several studies during the years it was made a distinction between *classical* and *non-classical* intercalators. Classical intercalators are characterised by aromatic condensed rings and positive charge(s) laying on the rings themselves or the side chains.

Among non-classical intercalators there are compounds that have huge and/or polar (or charged) substituents on the opposite sites of intercalating aromatic system. These compounds have to insert at least one of the substituents between nucleobases pairs to intercalate. Among these species there are known compounds like naphthalene bisimide and cationic porphyrins, which, although they are not supposed to intercalate, they may interact efficiently with DNA through such an interaction.[25] Even if thermodynamically favourable, this interaction is kinetically unfavourable, as needs the elongation of the double helix (so that the distortion and/or breaking of hydrogen bonds); such effect makes the DNA-molecule interaction slow.

The initial studies of the intercalative process were about simple organic molecules, but they were followed by studies focused on the interaction between

DNA and metal complexes. The presence of a transition metal provides indeed several advantages:[26]

- The presence of d orbitals grants more ways (bonds and geometries) the species may interact with DNA than those of organic molecules;
- Steric and electronic properties can be modulated choosing opportune ancillary ligands;
- Bridging ligands of certain dimensions may modify the size of the intercalator;
- It is possible taking advantages from their spectroscopic, magnetic, redox, photophysical and photochemical properties.

Since their antitumoral properties, square planar Pt(II) complexes were the first species whose interaction with DNA was studied. Lippard, in the '70s, demonstrated Pt(II) complexes with heterocyclic aromatic ligands (like 2,2':6',2''-terpyridine) intercalate into DNA.[27] It is worth noting Pt(II) complexes geometry is compatible with steric requisites for the intercalation process and, modifying the ligands bounded, it is possible modulating their steric and electronic properties.

7.3.1 *Ru(II) complexes as intercalators*

In the last decades more attention has been put on metal complexes with an octahedral geometry, to verify if species with high steric hindrance may intercalate and how it influences the process. In fact, ancillary ligands could prevent the insertion of small molecules between adjacent nucleobases pairs.

Ru(II) complexes containing rigid aromatic rings (stable, inert and soluble in water) were among the first classes of octahedral complexes studied.

One of these was $[Ru(phen)_3]^{2+}$ species (phen = phenanthroline) (**Figure 7.7**).[28] In this complex each ligand has an aromatic planar structure that may intercalate; moreover, the three ligands give a chiral effect to the species. Chirality may have a relevant effect on intercalation process: according to Barton,[28d] the intercalation is favoured for Δ isomers of these kinds of complexes. This is due to the orientation of ligands in the Δ isomers, which interfere sterically less than those in Λ isomers with the structure of DNA. Such discrimination is the base for designing probes able to recognise the double helix chirality.

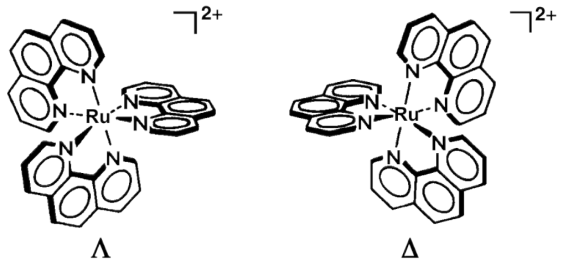

Figure 7.7 *Λ and Δ configurations of $[Ru(phen)_3]^{2+}$ complex.*

Taking enantioselectivity of Ru(II) tris-phenanthroline complexes as a starting point, there have been synthesised complexes that can bind selectively to DNA. For example, Λ isomers of metal complexes based on 4,7-diphenylphenanthroline (DIP) are efficient probes for Z-DNA. [29] $[Ru(TMP)_3]^{2+}$ (TMP = 3,4,7,8-tetramethylphenanthroline, **Figure 7.8**) is, instead, a selective probe for A-DNA.[30] Methyl substituents do not allow the complex to intercalate between nucleobases; it interacts with DNA by electrostatic and hydrophobic interactions. This complex is too huge to insert into B-DNA minor groove, but can insert into the major one of A-DNA and, by photoactivation and subsequent generation of $^1O_2$, can break the double helix.

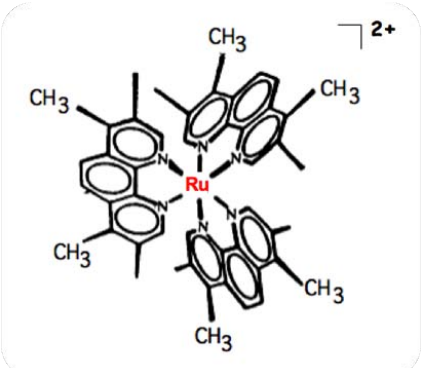

Figure 7.8 *Molecular structure of $[Ru(TMP)_3]^{2+}$.*

Ru(II) complexes may be used also by virtue of their photophysical properties, which are usually (significantly) altered as a result of interactions with DNA. An application is the use of these species as DNA luminescent probes, also called *light switches*. Ru(II) complexes are indeed very used because their relative stability and their photophysical properties described in Chapter 2.

Interaction of Ru(II) complexes with DNA usually generates an increase of

luminescence intensity, due to the reduced probability of:

- non-radiative decay, because the intercalated luminophore is surrounded by the DNA hydrophobic environment and so protected from water-induced deactivation;
- intersystem crossing to the ^{3}MC excited state, as the complex is caged into double helix and its rigidity results enhanced;
- O_2 luminescence quenching.

On the other hand, if there occur photoinduced reactions between metal complex and nucleobases, luminescence is quenched.

In **Figure 7.9** there are shown two Ru(II) complexes with such properties; they are based on TAP (1,4,5,8-tetra-azaphenanthrene) and PHEHAT (1,10-phenanthroline[5,6-b]-1,4,5,8,9,12-hexa-azatriphenylene) ligands. In the presence of DNA, the behaviour of these two complexes is different: the first complex acts as an ON-OFF molecular switch; the second one acts, instead, as an OFF-ON molecular switch.[31]

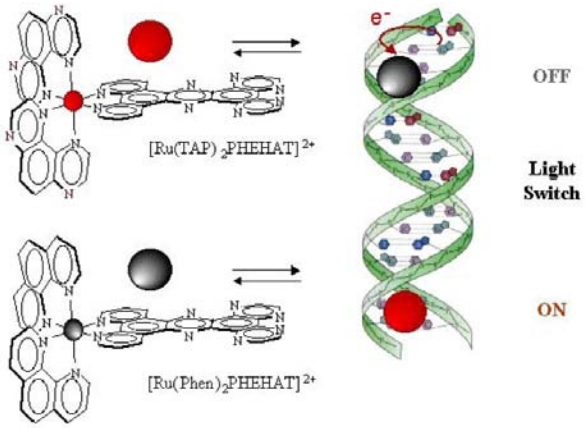

Figure 7.9 Examples of light-switches ON-OFF (top) and OFF-ON (below).

$[Ru(TAP)_2PHEHAT]^{2+}$ is a photo-oxidant complex (the two TAP ligands confer a high reduction potential to it) and shows a great affinity for the DNA thanks the PHEHAT ligand, which can intercalate. DNA efficaciously quenches its luminescence because the *electron transfer* process with the guanine; such is a *light-switch ON-OFF*.

$[Ru(phen)_2PHEHAT]^{2+}$ in water solution at room temperature does not exhibit any luminescence; the lone pairs present on nitrogen atoms in the ligands, interacting with water molecules, stabilise a non-emissive excited state. If the complex is

intercalated into DNA the stabilisation by water molecules cannot happen. Therefore, the non-emissive excited state is not stabilised and so the complex exhibits luminescence; such is called *light-switch OFF-ON*.

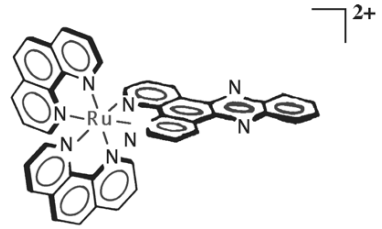

Figure 7.10 *Molecular structure of [Ru(phen)$_2$(dppz)]$^{2+}$.*

The first Ru(II) complex whose light switch properties have been observed was, however, [Ru(phen)$_2$(dppz)]$^{2+}$ (dppz = dipyrido[3,2-a:2',3'-c phenazine]) (**Figure 7.10**).[32] When it is intercalated, it exhibits an intense luminescence due to the radiative decay of an MLCT excited state. In water solution, the luminescence is, instead, quenched because *proton-transfer* from water molecules to phenazine's nitrogen atoms. As seen before, intercalation does not permit the interaction between water molecules and the Ru(II) complex, so it becomes luminescent.

The presence of the free binding fragment on the dinuclear complex **Ru2L**, (see Chapter 4 and **Figure 7.11**) allows an aromatic surface sufficiently extended, in principle, to be able to interact with the double helix of DNA.

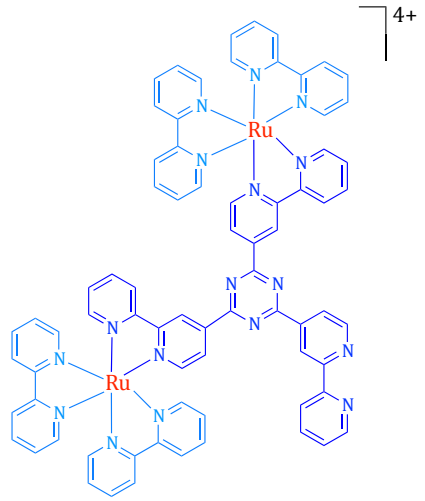

Figure 7.11 *Molecular structure of **Ru2L** complex.*

On these bases, we investigated, in collaboration with Prof. Maria Letizia di Pietro of the University of Messina, the interaction of this compound with polynucletides. To increase the solubility of this species in aqueous solvent, we changed the counter-anion from PF_6^- to Cl^-.

*7.4 Interaction of **Ru2L** with DNA*

The absorption spectrum of this species in buffered solution is reported in **Figure 7.12** (red curve).

As it possible to observe, the main spectral features (see Chapter 4) have been retained in the aqueous solvent. It has been done a spectrophotometric titration of **Ru2L** by adding DNA to the mixture (titration shown in **Figure 7.12**). Spectral variation is characterised by hypochromism and bathochromic shift. This trend, which is reversible by adding NaCl, is compatible with a non-covalent interaction where an electronic interaction between aromatic moieties is present. Moreover, the presence of two isosbestic points that are kept present within the entire titration confirms that in solution there are only two absorbing species: free and bound **Ru2L** species.

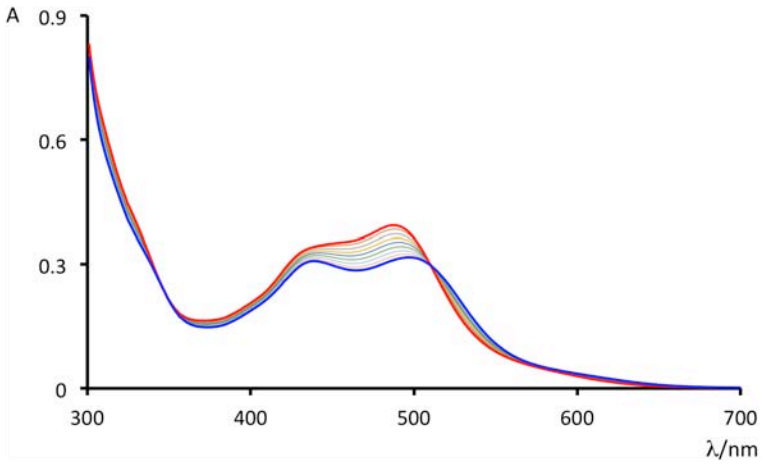

Figure 7.12 *Spectrophotometric titration of **Ru2L** ($1.67 \cdot 10^{-5}$ M) with DNA at 298 K and I = $2.2 \cdot 10^{-2}$ M ($2.1 \cdot 10^{-2}$ M in NaCl and 10^{-3} M in phosphate buffer, pH = 7). Initial **Ru2L** spectrum is red coloured; final one is blue coloured.*

To verify **Ru2L** affinity for DNA, spectrophotometric data have been analysed by McGhee–von Hippel equation.[33] Binding constant (K_b) value has been founded being 4.2 (±0.05)$\cdot 10^6$ M^{-1}, at 298 K and with an ionic strength of $2.2 \cdot 10^{-2}$ M ($2.1 \cdot 10^{-2}$ M in

NaCl and 10^{-3} M in phosphate buffer (pH = 7)).

Presence of a non-covalent interaction is also strongly confirmed by the appearance, after adding DNA, of a circular dichroism signal induced in the spectral region where only the Ru(II) complex absorbs, as a result of the rigid orientation of **Ru2L** caused by its interaction with the chiral double helix. Spectropolarimetric titration of **Ru2L** species by addition of DNA is shown in **Figure 7.13**. However, these experimental results are not enough to confirm an intercalation process of **Ru2L** between DNA nitrogenous bases or just an interaction on the external surface of the double helix.

To examine in depth the nature of the interaction it has been measured the denaturation temperature of DNA in presence of **Ru2L**. In fact, if a complex is intercalated it stabilises the double helix and gets the denaturation temperature higher. With an ionic strength of $2.2 \cdot 10^{-2}$ M ($2.1 \cdot 10^{-2}$ M in NaCl and 10^{-3} M in phosphate buffer (pH = 7)) and the presence of **Ru2L** species, DNA melting point increases (ΔT_f=20 K); the increment is similar to the one of the well-known intercalator $[Ru(bpy)_2(dppz)]^{2+}$ (dppz=dipyridophenazine) (ΔT_f=13.2 K),[34] whereas $[Pt(en)(py)_2]^{2+}$ (en=ethylenediamine; py=pyridine), which cannot intercale, leads only to a little increase of DNA melting point (ΔT_f=3 K).

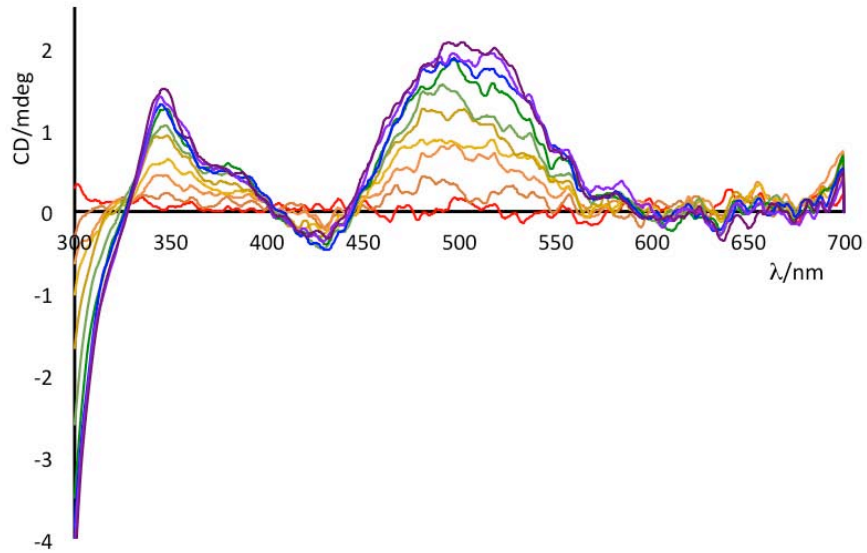

Figure 7.13 *Spectropolarimetric titration of **Ru2L** ($1.7 \cdot 10^{-5}$ M) with DNA at 298 K and I = $2.2 \cdot 10^{-2}$ M ($2.1 \cdot 10^{-2}$ M in NaCl and 10^{-3} M in phosphate buffer, pH = 7). In purple is represented the spectrum at the end of titration.*

The intercalation of a molecule among its nucleobases, as well as stabilising the DNA double helix, causes an elongation and a simultaneous stiffening of the structure of the biopolymer, which reflects in a significant increase in viscosity of its solutions.[35] In **Figure 7.14** are reported the increments of the viscosity of the DNA solution in presence of **Ru2L**; these increments are comparable to the ones induced from $[Ru(bpy)_2(dppz)]^{2+}$, used as standard.

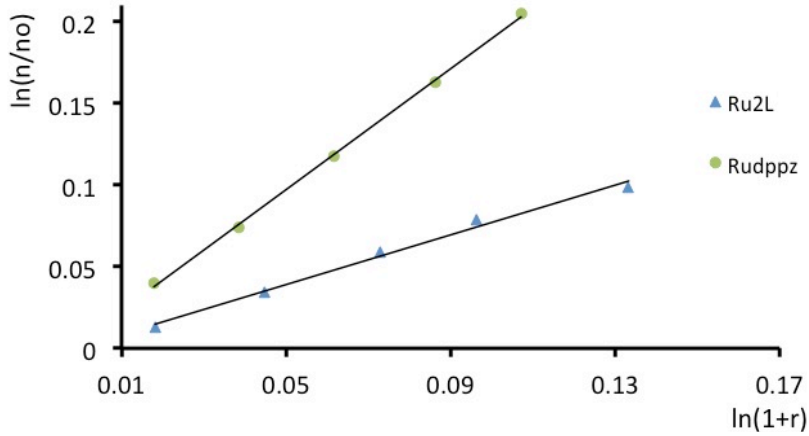

Figure 7.14 *Viscosimetric titration of a DNA solution with **Ru2L** (blue triangles) and $[Ru(bpy)_2(dppz)]^{2+}$ (green circles). Measurements have been conducted at 298 K and $I = 2.2 \cdot 10^{-2}$ M ($2.1 \cdot 10^{-2}$ M in NaCl and 10^{-3} M in phosphate buffer, pH = 7). h_0 is the reduced viscosity of the DNA solution; h is the reduced viscosity of the DNA solution in presence of complex; $r = [complex]_{bound}/[DNA]_{tot}$.*

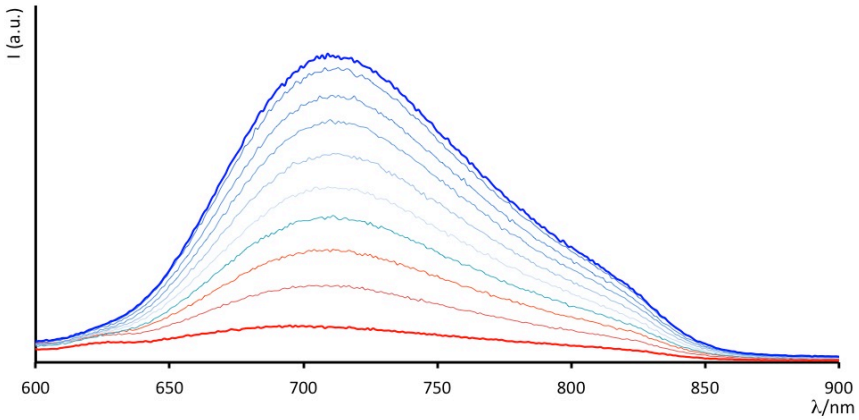

Figure 7.15 *Spectrofluorimetric titration of **Ru2L** ($8.01 \cdot 10^{-6}$ M) with DNA at 298 K and $I = 2.2 \cdot 10^{-2}$ M ($2.1 \cdot 10^{-2}$ M in NaCl and 10^{-3} M in phosphate buffer, pH = 7). λ_{exc} = 510 nm. Initial **Ru2L** spectrum is red coloured; final one is blue coloured.*

Ru2L species, in phosphate buffer (pH = 7) exhibits a very low luminescence signal (quantum yield less than 0.01% vs 1.3% in ACN), possibly because of the interaction between nitrogen atoms of triazine moiety and the water's protons, which stabilise a non-luminescent lower-energy state, as for $[Ru(phen)_2PHEHAT]^{2+}$ and $[Ru(phen)2(dppz)]^{2+}$ complexes.[36]

Adding DNA to a **Ru2L** solution leads to a growing of the emission band, centred at 701 nm, which increases with the increment of DNA concentration (**Figure 7.15**). So, it is evident the interaction of **Ru2L** with DNA grants an intense emission due to MLCT transitions, similar to other well-known intercalators, like $[Ru(bpy)_2(dppz)]^{2+}$. In fact, whereas in water solution **Ru2L** luminescence is quenched by proton transfer from water to nitrogens, intercalation prevents this kind of interaction, causing an increasing of the luminescence lifetime of the excited state.[37] The lifetime has resulted at least biexponential (t_1=190 ns; t_2=480 ns), which suggests there are several ways the complex intercalates between bases.[38] This behaviour will be investigated in detail in future works.

These experimental data leads us to consider **Ru2L** as an "OFF-ON" molecular light-switch for DNA.

As a first test towards a possible application, *cellular internalisation* studies have been performed with erythrocytes. These experiments have been performed in collaboration with the group of Prof. Davide Barreca at the University of Messina.

7.5 Cellular internalisation studies and cytotoxicity

The internalisation of **Ru2L** has been analysed by fluorescence microscopy after incubation of erythrocyte for 24 h in the absence or in the presence of different amounts of the tested compound, see Experimental Section for more details. In the fluorescence images, although at a different concentration values, it is possible to observe a clear fluorescence of the cytosol, supporting that the tested compound is able to cross the plasmatic membrane. The luminescence is probably partially turned-on thanks to the interactions with protein material inside the cell. Detectable amount of the compounds has been found in the range of concentration of 0.125–10 μM (**Figure 7.16**). These results clearly indicate that **Ru2L** is able to permeate the cellular membrane and its luminescence can be detected up to the nanomolar scale.

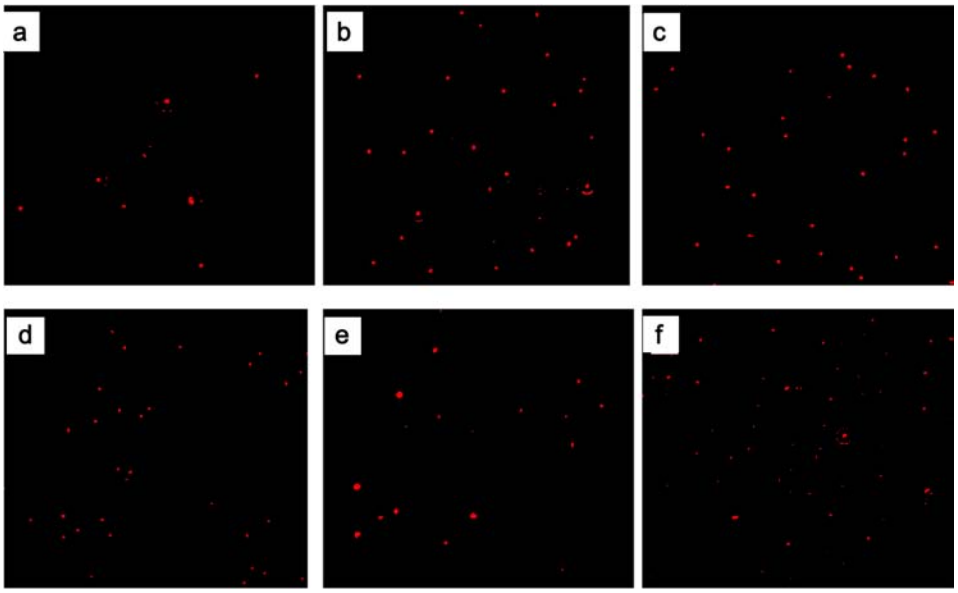

Figure 7.16 *Fluorescence microscopy images of erythrocytes incubated with 10 (a), 5 (b), 1 (c), 0.5 (d), 0.25 (e) and 0.125 μM (final concentrations) of* ***Ru2L****.*

On the basis of these results we decided to test also the cellular permeation of **Ru-1P** (see Chapter 6), because of its prolonged excited state lifetime (that in principle could be useful for singlet oxygen sensitisation). Tests have been performed for the free **Ru-1P** as well as encapsulated in the MCM-41 or MSS structures (see Chapter 6).

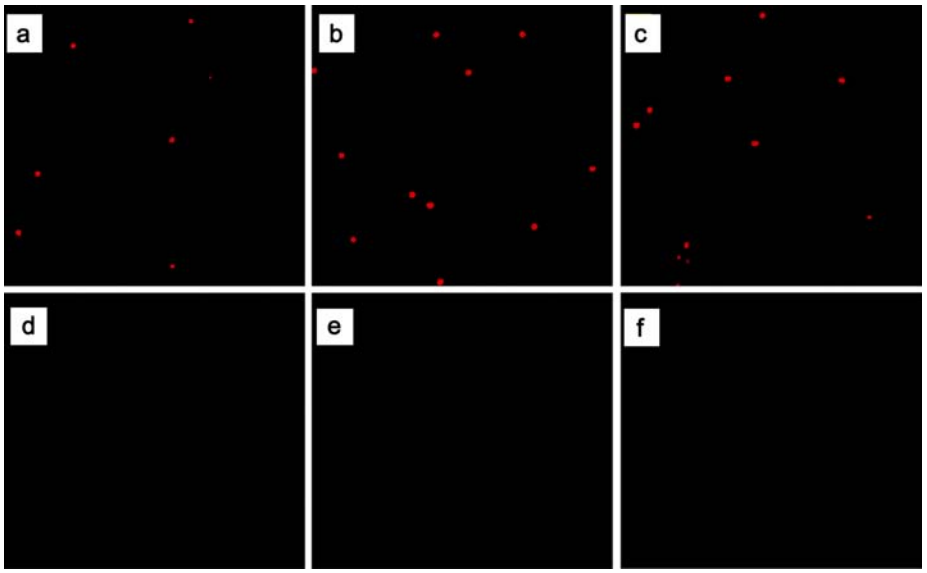

Figure 7.17 *Fluorescence microscopy images of erythrocytes incubated with 10 (a), 5 (b), 1 (c), 0.5 (d), 0.25 (e) and 0.125 μM (final concentrations) of* ***Ru-1P****.*

Again, internalisation of the species has been analysed by fluorescence microscopy after incubation of erythrocyte for 24 h in the absence or in the presence of different amounts of the tested compound. The results are shown in **Figure 7.17, 7.18** and **7.19**.

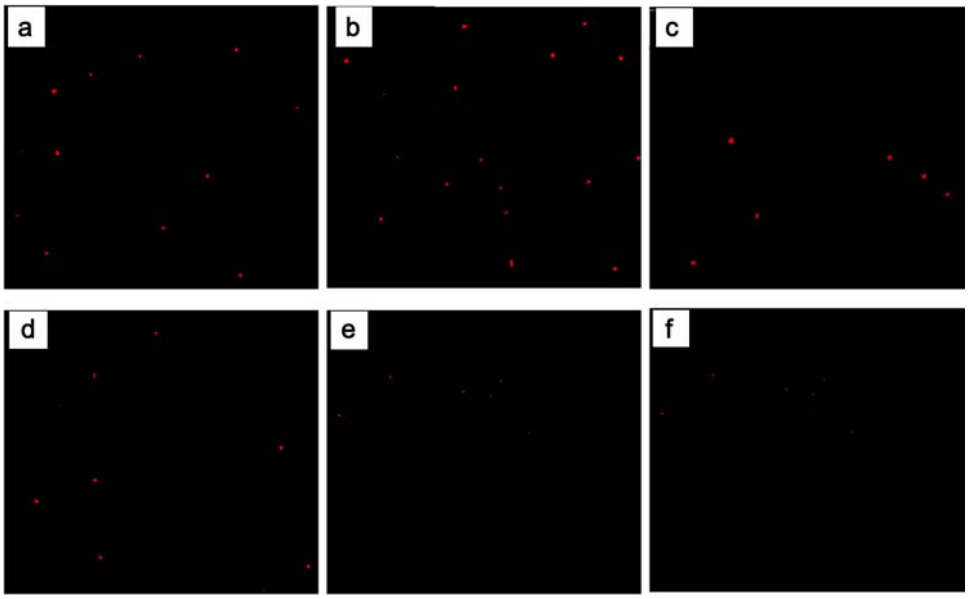

Figure 7.18 *Fluorescence microscopy images of erythrocytes incubated with 5.00 (a), 2.50 (b), 1.00 (c), 0.50 (d), 0.250 (e) and 0.12 μg/mL (final concentrations) of* ***Ru-1P*** *inside MCM-41.*

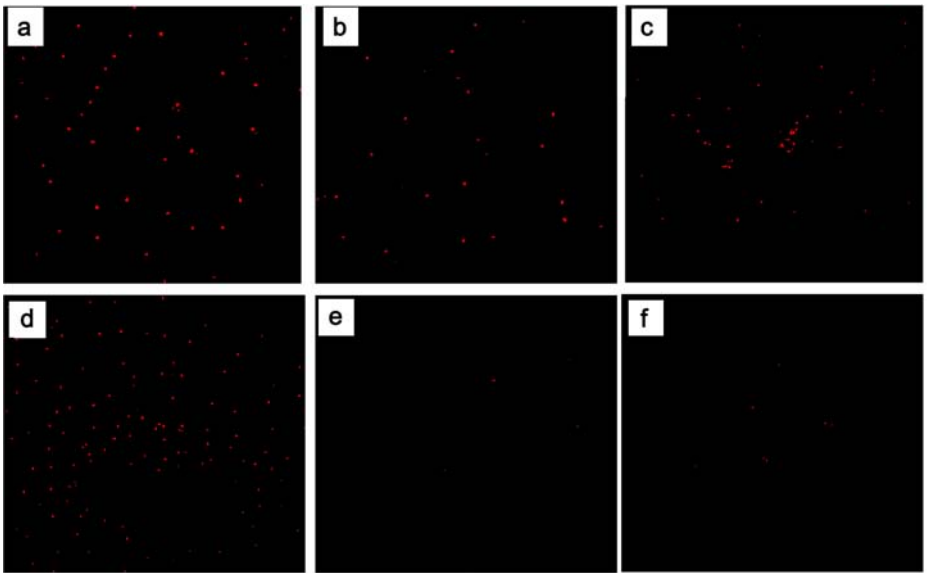

Figure 7.19 *Fluorescence microscopy images of erythrocytes incubated with 10.00 (a), 5.00 (b), 1.00 (c), 0.50 (d), 0.25 (e) and 0.12 μg/mL (final concentrations) of* ***Ru-1P*** *inside MSS.*

All the species are detected inside the cells. Whereas **Ru-1P** was not detectable at concentrations lower than 1 μM, in the case of the nanohybrid structures the luminescence, inside the cells, can be observed at all the concentration used, as low as 0.12 μg/mL. Taking into account that in the case of MCM-41 each mg of hybrid material contains 160 nmol of **Ru-1P** (averaged value) a concentration of 0.12 μg/mL correspond to 20 nM in dye. In the case of MSS, the **Ru-1P** contained is 13.2 nmol/mg, so the lowest concentration used corresponds to 1.6 nM. It is interesting to note that the nanostructure seems allowing for a more efficient internalisation.

The internalisation of the compounds is a fundamental point for the tested compounds, but at the same time it is essential to test their biological safety. To test the eventual cytotoxicity, we have monitored the release of LDH from cells and compared with the data obtained with tert-butyl hydroperoxide, a well-known cytotoxic compound. Analyses of LDH release from the tested cells have highlighted that, in the range of concentrations utilised during our experiments, all the tested compounds do not have cytotoxic effects (**Figure 7.20**).

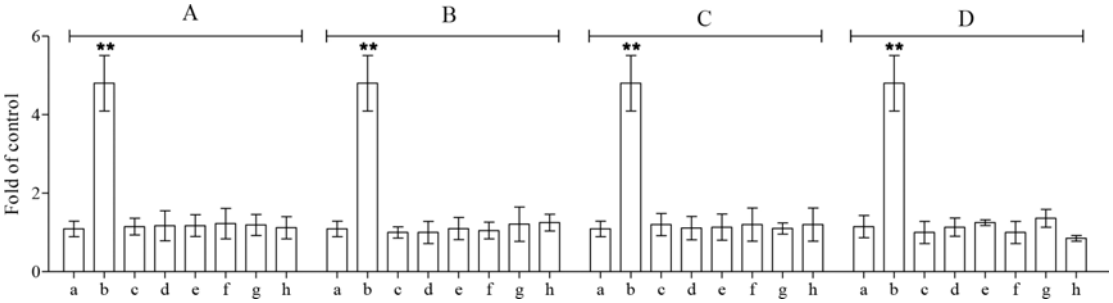

Figure 7.20 *Spectroscopic determination of LDH release from erythrocytes incubated for 24 h in the absence (a) or in the presence of tert-butyl hydroperoxide (b), 10.00 (c), 5.00 (d), 1.00 (e), 0.50 (f), 0.25 (g) or 0.12 (h) μM of **Ru2L** or **Ru-1P** or 10.00 (c), 5.00 (d), 1.00 (e), 0.50 (f), 0.25 (g) or 0.12 (h) μg/mL of MSS or MCM-41 containing **Ru-1P**. Samples were analysed by one-way ANOVA, followed by Turkey's test. Asterisks (**) indicate a significant difference with respect to controls (P<0.05).*

7.6 Conclusions

The overall scenario suggests that the new prepared di-nuclear **Ru2L** species strongly interact with DNA. The species is quite luminescent in organic aprotic solvents and substantially quenched in aqueous environment. The demonstrated interaction with polynucleotides switches on its luminescent, so **Ru2L** acts as light switch for DNA. As preliminary step, its permeability to the cellular membrane has

been tested with erythrocytes, demonstrating that **Ru2L** can be internalised. Further studies with more complex cellular lines are needed to test, also, the nucleus entrance of this species.

Moreover, it has been demonstrated that **Ru-1P** is able to cross the cellular membrane of erythrocytes and to be detected as luminophores in the cytosol at concentration higher than 1 mM, whereas if encapsulated or adsorbed on the silica nanostructures the luminescence it detectable inside the cell at the nanomolar scale.

References

1) (a) M. Cusumano, M. L. Di Pietro, A. Giannetto, *Inorg. Chem.*, **1999**, 38, 1754-1758; (b) M. Cusumano, M. L. Di Pietro, A. Giannetto, *Inorg. Chem.*, 2**0**06, 45, 230-235; (c) M. Cusumano, M. L. Di Pietro, A. Giannetto, M. A. Messina, F. Romano*, J. Am. Chem. Soc.*, **2001**, 123, 1914-1919; (d) M. Cusumano, M. L. Di Pietro, A. Giannetto, P. A. Vainiglia, *Inorg. Chem.*, **2007**, 46, 7148-7153;(e) E. Trovato, M. L. Di Pietro, F. Puntoriero, *Eur. J. Inorg. Chem.*, **2012**, 3984-3988.

2) (a) G. Marverti, M. Cusumano, A. Ligabue, M. L. Di Pietro, P. A. Vainiglia, A. Ferrari, M. Bergomi, M. S. Moruzzi, C. Frassineti, *Journal of Inorganic Biochemistry*, **2008**, 102, 699-712; (b) G. Marverti, A. Ligabue, M. Montanari, D. Guerrieri, M. Cusumano, M. L. Di Pietro, L. Troiano, E. Di Vono, S. Iotti, G. Farruggia, F. Wolf, M. G. Monti, C. Frassineti, *Investigationals New Drugs*, **2011**, 29, 73-86; (c) S. Petralia, E. L. Sciuto, M. L. Di Pietro, M. Zimbone, M. G. Grimaldi, S. Conoci, *Analyst*, **2017**, 142, 2090-2093.

3) (a) J. Chaires, *Nucleic Acid–Drug Interaction, Eds.: B. Pullman, J. Jortner, Kluwer Academic Press*, Dordrecht, **1990**, 123-136; (b) F. Arcamone, *Doxorubicin Anti-Cancer Antibiotics, Academic Press*, New York, **1981**.

4) (a) S. A. Latt, G. Stetten, L. A. Juergens, H. F. Willard, C. D. Scher, *Journal of Histochemistry & Cytochemistry*, **1975**, 23, 493-505; (b) S. A. Latt, G. Stetten, *Journal of Histochemistry & Cytochemistry*, **1976**, 24, 24-33; (c) J. Kapuscinski, *Biotech. Histochem*. **1995**, 70, 220-233.

5) A. L. Lehninger, *Principles of Biochemistry*, W. H. Freeman, **1983**.

6) J. D. Watson, F. H. C. Crick, *British Journal Nature*, **1953**, 171, 738.

7) B. Alberts, A. Johnson, J. Lewis, M. Raff, K. Roberts, P. Walters, *Molecular Biology of the Cell. 4th Edition*, New York: Garland Science, **2002**.

8) A. G. Leslie, S. Arnott, R. Chandrasekaran, R. L. Ratliff, *J. Mol. Biol.*, **1980**, 143, 49.

9) (a) A. Carrier, P. Le Ber, C. Auclain, *Biochemistry,* **1990**, 29, 6002; (b) Y. Matsuzawa, K. Minagawa, K. Yoshikawa, M. Matsumoto, M. Doi, *Nucleic Acids Symp Ser.*, **1991**, 25, 131.

10) H. K. Liu, P. J. Sadler, *Acc. Chem. Res.*, **2011**, 44, 349.

11) (a) L. H. Hurley, *J. Med. Chem.*, **1989**, 32, 2027; (b) H. Iida, G. Jia, J. W. Lown, *Current Opinion in Biotechnology*, **1999**, 10, 29.

12) (a) R. F. Pasternack, C. Bustamante, P. J. Collings, A. Giannetto, E. J. Gibbs, *J. Am. Chem. Soc.*, **1993**, 115, 5393; (b) R. F. Pasternack, K. F. Schaefer, *Inorg. Chem.*, **1994**, 33, 2062; (c) B. P. Hudson, J. Sou, D. J. Berger, D. R. McMillin, *J. Am. Chem. Soc.*, **1992**, 114, 8997; (d) K. Kano, K. Fukuda, H. Wakami, R. Nishiyabu, R. F. Pasternack, *J. Am. Chem. Soc.*, **2000**, 122, 7494.

13) (a) G. Arena, L. Monsù Scolaro, R. F. Pasternack, R. Romeo, *Inorg. Chem.*, **1995**, 34, 2994; (b) M. Casamento, G. E. Arena, C. Lo Passo, I. Pernice, A. Romeo, L. Monsù Scolaro, *Inorg.*

Chim. Acta, **1998**, 275, 242.

14) M. Cusumano, M. L. Di Pietro, A. Giannetto, *Inorg. Chem.*, **2006**, 45, 230.

15) (a) R. F. Pasternack, E. J. Gibbs, J. J. Villafranca, *Biochemistry*, **1983**, 22, 2046; (b) E. J. Gibbs, M. C. Mauer, H. F. Zhang, W. M. Reiff, D. T. Hill, M. M. Blaszkiewicz, R. E. Mckinnie, H-Q. Liu, R. F. Pasternack, *J. Inorg. Biochem.*, **1988**, 32, 39.

16) L. S. Lerman, *J. Mol. Biol.*, **1961**, 3, 18.

17) I. Haq, *Arch. Bioch. and Bioph.*, **2002**, 403, 1.

18) (a)W. Bauer, J. Vinograd, *J. Mol. Biol.*, **1968**, 33, 141; (b) W. Bauer, J. Vinograd, *J. Mol. Biol.*, **1970**, 47, 419; (c) M. J. Waring, *J. Mol. Biol.*, **1970**, 54, 247; (d) J. Cairns, *Cold Spring Harbor Symp. Quant. Biol.*, **1962**, 27, 311.

19) M. J. Waring, *Ann. Rev. Biochem.*, **1981**, 50, 159.

20) J. B. Chairs, M. J. *Drug-nucleic acid interactions, Waring, Eds., Academic Press*, San Diego, **2001**, 340.

21) C. R. Cantor, P. R. Schimmel, *Biophysical Chemistry, W. H. Freeman. and Co.*, San Francisco, **1980**.

22) K. Sauer, *Methods of Enzymology: Biochemical spectroscopy, ed., Academic Press*, San Diego, **1995**, 246.

23) K. Utsuno, M. Tsuboi, *Chem. Pharm. Bull.*, **1997**, 45, 1551.

24) D. M. Crothers, *Biopolymers*, **1975**, 6, 575.

25) D. Barton, K. Nakanishi, O Meth-Cohn, *"DNA Intercalators" in "Comprehensive Natural Products Chemistry", W. D. Wilson*, *eds. Pergamon*, Oxford, **1999**, 427.

26) (a) V. Balzani, A. Credi, M. Venturi, *Coord. Chem. Rev.*, **1998**, 171, 3; (b) N. J. Turro, *Chem. Commun.*, **2002**, 2279; (c) S. S. Sun, A. J. Lees, *Coord. Chem. Rev.*, **2002**, 230, 171; (d) V. Balzani, G. Bergamini, S. Campagna, F. Puntoriero, *Photochemistry and Photophysics of Coordination Compounds I, V. Balzani, S. Campagna, eds.*, Berlin: Springer-Verlag, **2007**, 1.

27) K. W. Jenette, S. J. Lippard, G. A. Vassiliades, W. R. Bauer, *Proc. Natl. Acad. Sci. USA*, **1974**, 71, 3839.

28) (a) C. V. Kumar, J. K. Barton, N. J. Turro, *J. Am. Chem. Soc.*, **1985**, 107, 5518; (b) J. K. Barton, A. T. Danishefsky, J. M. Goldberg, *J. Am. Chem. Soc.*, **1984**, 106, 2172; (c) J. K. Barton, J. M. Goldberg, C. V. Kumar, N. J. Turro, *J. Am. Chem. Soc.*, **1986**, 108, 2081; (d) J. P. Rehmann, J. K. Barton, *Biochemistry*, **1990**, 29, 1701.

29) (a) S. J. Lippard, P. J. Bond, K. C. Wu, W. R. Bauer, *Science* **1976**, *194,* 726; (b) A. H. J. Wang, J. Nathans, G. van der Marel, J. H. van Boom, A. Rich, *Nature* **1978**, *276*, 471.

30) H.-Y Mei, J. K. Barton, *J. Am. Chem. Soc.*, **1986**, 108, 7414.

31) C. Moucheron, A. Kirsch-De Mesmaeker, *J. Phys. Org. Chem.*, **1998**, 11, 577.

32) a) A. E. Friedman, J.-C. Chambron, J.-P. Sauvage, N. J. Turro, J. K. Barton, *J. Am. Chem. Soc.*, **1990**, 112, 4960; b) C. H. Hiort, P. Lincoln, B. Nordén, *J. Am. Chem. Soc.*, **1993**, 115, 3448.

33) J. D. McGhee, P. H. von Hippel, *J. Mol. Biol.*, **1974**, 86, 469.

34) E. Friedman, J.-C. Chambron, J.-P. Sauvage, N. J. Turro, J. K. Barton, *J. Am. Chem. Soc.*, **1990**, 112, 4960.

35) a) L. S. Lerman, *J. Mol. Biol.*, **1961**, 3, 18; b) G. Cohen, H. Eisenberg, *Biopolymers*, **1966**, 4, 429; c) M. A. Schwaller, G. Dodin, J. Aubard, *Biopolymers*, **1991**, 31, 519; d) S. Satyanaryana, J. C. Daborusak, J. B. Chaires, *Biochemistry*, **1993**, 32, 2573.

36) (a) A. E. Friedman, J. C. Chambron, J. P. Sauvage, N. J. Turro, J. K. Barton, *J. Am. Chem. Soc.*, **1990**, 112, 4960; b) C. H. Hiort, P. Lincoln, B. Nordén, *J. Am. Chem. Soc.*, **1993**, 115, 3448.

37) J. Bolger, A. Gourdon, E. Ishow, J.-P. Launay, *Inorg. Chem.,* **1996**, 35, 2937.

38) A. W. McKinley, P. Lincoln, E. M. Tuite, *Dalton Trans.,* **2013**, 42, 4081-4090.

CONCLUSIONS

The aim of this thesis was the designing and the investigation of molecular antennas (dendrimer of nanometric size) and nanohybrid systems able to collect and use light.

Most of the compounds here illustrated are based on Ru(II)- or Os(II)-polypyridine subunits as chromophores and polyaromatic organic moieties as electron acceptor or energy donor in photoinduced processes. A new heptanuclear, mixed-metal luminescent compound have been assembled to act efficiently as light-harvesting device. In this nanosized molecular dendrimer all the light energy absorbed by the ancillary Ru(II) chromophores is efficiently funnelled to the central Os(II) one, which acts as energy trap. All the intrinsic photoinduced processes have been investigated in details by pump-probe transient absorption spectroscopy.

A new class of light-harvesting antennae has been prepared by exploiting the template-assisted host-guest chemistry of mesoporous organosilica. A new blue light-absorbing species formed as a result of aggregation phenomena of BODIPY dye inside mesoporous silica. This species has been demonstrated to be able to transfer its excitation energy quantitatively to BODIPY monomers inside the nanopores of mesoporous silicas, in a time range between 20 and 80 ps depending on the relative localisation and distribution.

Because of the dual properties of a piridinium species, able to act as luminophore and electron acceptor subunit, mixed hybrid nano-silica have been prepared loading both BODIPY dye and poly-aromatic pyridinium salt, into MCM-41.

The excited-state equilibration that governs the photophysical behaviour of a pyrene-appended Ru(II) complex in solution has been demonstrated to be equally performing when the dyad is hosted in mesoporous silica nanoparticles. The excited state of this species, if protected from dynamic quenching when hosted by MCM-41 silicas, retains a quite long luminescence lifetime. The higher porosity of new silica nanospheres compared to the MCM-41 allows for higher permeability and so they have been used as support for the photochemical synthesis of IrO_x nanoparticles as possible catalysts for photoinduced water oxidation.

Moreover, it has been demonstrated that **Ru-1P** is able to cross the cellular membrane of erythrocytes and to be detected as luminophores in the cytosol at concentration higher than 1 mM, whereas if encapsulated into nano-silica the luminescence is detectable inside cells at concentration lower than 10 nM.

The ability of permeating erythrocytes membrane has been revealed also for a Ru(II) dinuclear complex. This species, used as precursor in the synthesis of the heptanuclear **Ru6Os** antenna dendrimer, has been demonstrated to be able to intercalate into DNA and to play the role of DNA light-switch.

All the obtained results on this topic indicate that the optical bandwidth and the energy collection in artificial antennae can be manipulated not only choosing different chomophores to link covalently but also by employing chromophores able to self-assemble into host-guest systems.

Moreover, mesoporous silica materials prove to be an excellent playground for a fine tuning of the light-harvesting properties in artificial photo-systems, as well as vector for luminophores in bio-imaging applications. The obtained results could open the way for further investigations in order to fully unravel and control the mechanisms of formation of such systems and of energy migration within them.

Experimental Chapter

EC.1 *Materials and methods*

UV/Vis absorption spectra were taken on a Jasco V-560 spectrophotometer. For steady-state luminescence measurements, a Jobin Yvon-Spex Fluoromax 2 spectrofluorimeter was used, equipped with a Hamamatsu R3896 photomultiplier. The spectra were corrected for photomultiplier response using a program purchased with the fluorimeter. For the luminescence lifetimes, an Edinburgh OB 900 time-correlated single-photon-counting spectrometer was used. As excitation sources, a Hamamatsu PLP 2 laser diode (59 ps pulse width at 408 nm) and/or the nitrogen discharge (pulse width 2 ns at 337 nm) were employed. Emission quantum yields for deaerated solutions were determined using the optically diluted method.[1] As luminescence quantum yield standards, we used $[Ru(bpy)_3]^{2+}$ (bpy=2,2'-bipyridine).[2]

Time-resolved transient absorption experiments were performed using a pump probe setup based on the Spectra-Physics MAI-TAI Ti:sapphire system as the laser source and the Ultrafast Systems Helios spectrometer as the detector. The output of laser beam was split to generate pump and probe beam pulses with a beam splitter (85 and 15%). The pump pulse (400 nm, 1-2 mJ) was generated with a Spectra-Physics 800 FP OPA and was focused onto the sample cuvette. The probe beam was delayed with a computer controlled motion controller and then focused into a 2 mm sapphire plate to generate a white light continuum (spectral range 450–800 nm). The white light is then overlapped with the pump beam in a 2-mm quartz cuvette containing the sample. The effective time resolution was ca. 200 fs, and the temporal chirp over the white-light 450–750 nm range ca. 150 fs; the temporal window of the optical delay stage was 0–3200 ps. All the transient spectra shown in the work are chirp corrected. The chirp correction was done by using the pump-induced absorption signals themselves in the same conditions (same cuvette, solvent, temperature, stirring frequency, and so on) used for each single experiment. The time resolved data were analysed with the Ultrafast Systems Surface Explorer Pro software.

Electrochemical measurements were carried out in the dry and argon-purged

stated acetonitrile, at room temperature with an Autolab multipurpose equipment interfaced to a PC. The working electrode was a glassy carbon (8 mm^2, Amel) electrode. The counter electrode was a Pt wire, and the pseudo-reference electrode was a silver wire. The reference was set using the redox couple ferrocene/ferrocinium as internal reference (395 mV vs. SCE in acetonitrile). The concentration in analyte was about 0.5 mM, unless otherwise stated. Tetrabutylammonium hexafluorophosphate was used as supporting electrolyte and its concentration was 0.10 M. Cyclic voltammograms were obtained at scan rates between 50 and 500 mV/s and were stated in each case. The criteria for reversibility were the separation of 60 mV between cathodic and anodic peaks, the close to unity ratio of the intensities of the cathodic and anodic currents, and the constancy of the peak potential on changing scan rate. The number of exchanged electrons reported in the main text was established using the areas of the peaks in differential pulse voltammetry (DPV).

Experimental uncertainties are as follows: absorption maxima, 2 nm; molar absorption, 15%; luminescence maxima, 4 nm; luminescence lifetimes, 10%; luminescence quantum yields, 20%; transient absorption decay and rise rates, 10%; redox potentials, 20 mV.

Transmission electron microscopy images were taken on a 100 kV CM100 TEM (FEI).

SAXS measurements were performed on a Bruker Nanostar SAXS machine, with cross-coupled Gobel mirrors and pin-hole collimation for point focus geometry, using a sealed tube X-ray source operating at 40 kV and 35 mA to produce Cu Kα radiation of wavelength 1.54 Å. The SAXS camera was fitted with a Vantec 2000 detector. The optics and sample chamber were under vacuum to minimise air scatter. The powder samples were wrapped in aluminum foil to facilitate introduction into the cuvette. Scattering experiments were run for 10 minutes and temperature-controlled at 20°C, using a Peltier system accurate to ±0.1 °C. Sample C1 was also run for 40 min. The nominal sample-to-detector distance was 650 mm, which provides a q range of 0.2–6.2 nm^{-1}. Primary beam scattering dominated the curves up to q=0.35 nm^{-1}. A background of aluminum foil was subtracted from the scattering files. Scattering files

were integrated between a q range of 0.2–4.0 nm^{-1} to give the one-dimensional scattering function I(q), where q is the length of the scattering vector, defined by $q=(4\pi/\lambda)\sin\theta/2$, λ being the wavelength and θ the scattering angle. In addition, the q range 0.85–4.00 nm^{-1} was integrated separately, to remove the dominant peak which occurred at q=0.8–0.9 nm^{-1} in all samples, and thus enhance the peaks which occurred at q=1.4–2.3 nm^{-1} in all samples.

The results from the SAXS scattering frames are presented below in image, graphical and tabular form. "D" spacings were calculated with Excel using values for 2θ and the operation: D = 0.154/(2(SIN(RADIANS(*cell*/2)))).

The thermal denaturation temperature of compound–DNA mixtures (1:10) was determined in 1 x 10^{-3} M phosphate buffer (pH = 7) solutions containing the compound (7.8 x 10^{-6} M) and 2 x 10^{-3} M NaCl.

Melting curves were recorded at 260 nm. The temperature has been increased at a rate of 0.5 °C/min by using a GBC Peltier system.

Viscosity titrations were performed by means of a Cannon-Ubbelhode semimicro dilution viscometer (Series No. 75, Cannon Instrument Co.), thermostatically maintained at 25°C in a water bath. The viscometer contained 2 mL of sonicated DNA solution, 1 x 10^{-3} M phosphate buffer (pH = 7) and 1 x 10^{-2} M NaCl. The compound solution (2.5 x 10^{-4} M), containing also DNA (6.0 x 10^{-4} M) at the same concentration as that in the viscometer, was delivered in increments of 90÷380 µL from a micro-pipet. Solutions were freed of particulate material by passing them through nylon Acrodisc syringe filters before use. Flow times were measured by hand with a digital stopwatch. Reduced viscosities were calculated by established methods and plotted as $\ln(\eta/\eta_0)$ against $\ln(1 + r)$ for rod-like DNA (600 base pairs) (η = reduced viscosity of the biopolymer solution in the presence of compound; η_0 = reduced viscosity of the biopolymer solution in the absence of compound; $r = [\text{compound}]_{\text{bound}}/[\text{biopolymer}]_{\text{tot}}$).

Spectrophotometric titrations were performed by adding to a complex solution (1.7 x 10^{-5} M] successive aliquots of DNA, containing also the complex, in a 10 mm stoppered quartz cell and recording the spectrum after each addition. The data were

analysed by a nonlinear least-squares fitting program, applied to the McGhee and von Hippel equation.[3] The binding constant, K_B, was determined by the program, using the extinction coefficient of the compounds, the free complex concentration, and the ratio of bound complex per mole of DNA. Extinction coefficient for bound compound was determined by Beer's law plots in the presence of a large excess of DNA.

EC.1.1 *Erythrocytes isolation*

Donors volunteers participating in the study were informed of all risks, discomforts and benefits relating to the study, in accordance with the Declaration of Helsinki for research protocols approved by the institutional review boards of the National Institutes of Health (NIH). All subjects provided medical histories, using a standardised questionnaire and declared they had not taken anti-inflammatory medication or nutritional supplements. Blood was obtained by venipuncture from healthy male volunteers and collected in heparinised tubes. Erythrocytes were separated from plasma and buffy coat and washed three times with l0 volume of 0.9% NaCl and centrifuged at 2,500 rpm for 5 min. During the last washing the packed cells were resuspended in the incubation buffer (phosphate saline buffer), at pH 7.4 and utilised for subsequent experiments.

EC.1.1.1 *Cellular internalisation and cytotoxic effects*

Erythrocytes were incubated for 24 hours at 37°C in the absence or in the presence of the investigated species. The same experiment has been repeated incubating the cells in the presence of 100 mM tert-butyl hydroperoxide to check the maximum release of LDH from damage cells. At the end of incubation time, cells were centrifuged at 2,500 rpm for 5 min. The supernatant was analyzed to detect the release of lactate dehydrogenase, while the pocked cells were resuspended and washed three times in incubation buffer and finally used for fluorescence and visible microscopy. The supernatant was utilised to check cytotoxicity by measuring lactate dehydrogenase (LDH) release from damaged cells into culture medium. LDH activity in the medium was determined using a commercially available kit from BioSystems S.A. The texted compounds, at the concentrations utilised in the experiments, did not interfere with LDH determination. For fluorescence and visible microscopy 10 µL of

each sample was placed on a glass slide covered with a coverslip and monitored with a fluorescence microscope.

EC.1.1.2 *Statistical analysis*

Data are presented as means ± standard deviation (S.D.). Data were analyzed by one-way analysis of variance (ANOVA). The significance of the difference from the respective controls for each experimental test condition was assayed by using Tukey's for each paired experiment. A $P<0.05$ was regarded as indicating a significant difference.

EC.2 *Syntheses*

Tris-2'',4'',6''-(2,2'-bipyridin-4-yl)-1'',3'',5''-triazine (L). An oven-dried 10 mL microwave vial was charged with 4-cyano-2,2'-bipyridine (100 mg, 0.55 mmol) and sodium hydride (2 mg, 0.08 mmol). The vial was equipped with a stirring bar and sealed. After several vacuum/N_2 cycles the mixture was left at 190°C for 8 h. The resulting brown solid was cooled to room temperature before adding ethanol (10 mL). The slurry was sonicated for 5 minutes and solvent was evaporated under vacuum. Water (10 mL) was added and the resulting mixture was filtered over paper. The resulting precipitate was washed with ethanol (10 mL), yielding a pure colourless solid (40 mg, 40%), which was used without further purification.

^{1}H NMR ($CDCl_3$, 400 MHz, 330 K): δ (ppm) 9.74 (s, 3H, Ha,a',a''), 9.03 (d, J^d = 5.0 Hz, 3H, Hb,b',b''), 8.88 (d, J^d = 4.2 Hz, 3H, Hd,d',d''), 8.76 (d, J^d = 4.9 Hz, 3H, Hc,c',c''), 8.59 (d, J^d = 7.9 Hz, 3H, Hg,g',g''), 7.97 (t, J^t = 7.8 Hz, 3H, Hf,f',f''), 7.47 (t, J^t = 5.3 Hz, 3H, He,e',e''). ^{13}C{^{1}H}NMR ($CDCl_3$-d_1, 400 MHz, 330 K): 171.5, 157.5, 155.5, 150.3, 149.4, 143.6, 137.0, 124.1, 122.5, 121.4, 120.0. ESI-MS (TFA : CH_2Cl_2): $[M]^+$ = 544.4.

cis-[Ru(bpy)$_2$Cl$_2$]·2H$_2$O. In 12.5 mL of dimethylformamide, $RuCl_3 \cdot H_2O$ (1.95 g, 7.46 mmol), 2,2'-bipyridine (2.34 g, 15 mmol) and LiCl (2.1 g, 49.6 mmol) were added. The mixture was refluxed for 8 h, then cooled to room temperature and 62.5 mL of acetone were added. It was left at 0°C for 12h. A precipitate formed in these conditions and was isolated through filtration with H_2O and Et_2O. A microcystalline purple solid was obtained (2.5g, 65% yield).

cis-[Os(bpy)$_2$Cl$_2$]·2H$_2$O. In 3 mL of ethylene glycol, K_2OsCl_6 (300 mg, 0.62 mmol) and 2,2'-bipyridine (203 mg, 1.30 mmol) were added and this mixture was refluxed for 45 min. To the crude, cooled to room temperature, 5 mL of a $Na_2S_2O_4$ saturated solution were added. The solid formed was filtered with H_2O, dried for 12 h and washed with Et_2O. A dark violet powder was obtained (298 mg, 79% yield).

{[Ru(2,2'-bpy)$_2$]L}(PF$_6$)$_2$ (Ru1L). A 100 mL round-bottomed flask was charged with ligand **L** (50 mg, 0.092 mmol) and dichloromethane (25 mL). cis-[Ru(bpy)$_2$Cl$_2$] (45 mg, 0.092 mmol) and silver nitrate (40 mg, 0.23 mmol) were separately dissolved in methanol (25 mL each). The methanol solutions were then added dropwise to the flask over 30 minutes with vigorous stirring. The reaction mixture was left at reflux for 24 h. After this time, a few drops of hydrazine were added to convert any Ru(III) to Ru(II). The resulting slurry was filtered over a fine glass frit. The filtrate was extracted with dichloromethane and evaporated under vacuum. The residue was then purified on Spehadex CM-25, using a mixture of $H_2O/(CH_3)_2CO$ 5:3 (v/v) containing NaCl (0.05 M) as eluent. The band eluted in these conditions contains the product. The counter-anions were exchanged twice with a solution of NH_4PF_6 in water, resulting in the precipitation a pure red solid (33 mg, 29%).

^{1}H NMR (CD_3CN, 400 MHz, 330 K): δ (ppm) 9.62 (s, 1H), 9.02 (s, 1H), 8.65-8.57 (m, 6H), 8.47-8.45 (d, J^d = 8.0 Hz, 1H), 8.41-8.40 (d, J^d = 4.8 Hz, 2H), 8.28-8.27 (d, J^d = 3.9 Hz, 2H), 8.16-8.08 (m, 5H), 8.02-7.96 (m, 4H), 7.81-7.69 (m, 7H), 7.50-7.36 (m, 5H), 7.34-7.33 (t, J^t = 5.1 Hz, 2H). ^{13}C{^{1}H}NMR (MeCN-d_3, 400 MHz, 330 K): 157.8, 157.7, 157.6, 155.6, 152.9, 152.6, 152.4, 151.1, 150.3, 139.2, 139.1, 138.2, 128.8, 128.7, 128.6, 125.7, 125.5, 125.4, 123.1, 121.8, 119.8.

{[Ru(2,2'-bpy)$_2$]$_2$L}(PF$_6$)$_4$ (Ru2L). A 100 mL round-bottomed flask was charged with **L** (50 mg, 0.092 mmol) and dichloromethane (25 mL). cis-[Ru(bpy)$_2$Cl$_2$] (90 mg, 0.18 mmol) and silver nitrate (80 mg, 0.46 mmol) were separately dissolved in methanol (25 mL each). The methanol solutions were then added dropwise to the flask over 30 minutes with vigorous stirring. The reaction mixture was left under reflux for 24 h. After this time, a few drops of hydrazine were added to convert any Ru(III) to Ru(II). The resulting slurry was filtered over a glass frit. The filtrate was

extracted with dichloromethane and evaporated under vacuum. The residue was then purified on Spehadex CM-25, using a mixture of $H_2O/(CH_3)_2CO$ 5:3 (v/v) containing NaCl (0.05 M) as eluent. The concentration of NaCl was increased to 0.1 M to obtain the pure product as chloride salt. The counter-anions were exchanged by addition of a saturated aqueous solution of NH_4PF_6, resulting in the precipitation of a pure red solid (117 mg, 65%).

^{1}H NMR (CD_3CN, 400 MHz, 330 K): δ (ppm) 9.63 (s, 2H), 9.57 (s, 1H), 9.06-9.05 (d, J^d = 4.4 Hz, 1H), 8.94-8.92 (d, J^d = 8.1 Hz, 2H), 8.82-8.78 (m, 2H), 8.68-8.67 (d, J^d = 5.6 Hz, 2H), 8.55-8.53 (d, J^d = 7.0 Hz, 8H), 8.19-8.06 (m, 13H), 7.88-7.86 (d, J^d = 5.1 Hz, 2H), 7.82-7.76 (m, 8H), 7.64-7.61 (t, J^t = 6.3 Hz, 1H), 7.51-7.40 (m, 10H). ^{13}C{^{1}H}NMR (MeCN-d_3, 400 MHz, 330 K): 171.0, 157.9, 157.8, 157.6, 157.4, 154.0, 152.7, 152.5, 144.1, 139.0, 138.9, 129.0, 128.6, 128.5, 126.6, 126.0, 125.3, 123.2.

{[Ru(2,2'-bpy)$_2$]$_3$L}(PF$_6$)$_6$ (Ru3L). A 25 mL round-bottomed flask was charged with **L** (25 mg, 0.046 mmol), cis-[Ru(bpy)$_2$Cl$_2$] (66.84 mg, 0.138 mmol) and silver nitrate (68 mg, 0.40 mmol). A mixture of ethylene glycol : water (9:1) (20 mL) was added and then left at reflux for 4 h. The resulting solution was added to an aqueous NH_4PF_6 solution. The resulting red precipitate was filtered over celite and dissolved in a minimum amount of acetonitrile. The solution was reduced under vacuum and the residue was then purified on Spehadex CM-25, using a mixture of $H_2O/(CH_3)_2CO$ 5:3 (v/v) containing NaCl (0.05 M) as eluent. The concentration of NaCl was increased to 0.15 M to obtain the pure product as chloride salt. The solution was then reduced under vacuum and an aqueous solution of NH_4PF_6 was added, resulting in the precipitation of the title compound as a pure red solid (77 mg, 61%).

^{1}H NMR (CD_3CN, 400 MHz, 330 K): δ (ppm) 9.62 (s, 3H), 8.93-8.92 (d, J^d = 8.1 Hz, 3H), 8.70-8.69 (d, J^d = 6.1 Hz, 3H), 8.55-8.52 (m, 12H), 8.16-8.04 (m, 18H), 7.84-7.82 (d, J^d = 5.6 Hz, 3H), 7.80-7.74 (m, 12H), 7.49-7.37 (m, 15H). ^{13}C{^{1}H}NMR (MeCN-d_3, 400 MHz, 330 K): 171.3, 159.7, 157.9, 157.8, 157.7, 157.6, 157.5, 154.0, 152.7, 152.6, 152.5, 143.9, 139.0, 128.9, 128.6, 125.3, 123.5.

Homonuclear Os(II) complexes with bridging ligand L.

General procedure: A round-bottomed flask was charged with ligand **L** (51.2 mg,

0.094 mmol) and 3 mL of a 1,2-dichloroethan/methanol 1:1 (v/v) solution and, by small additions, cis-$[Os(bpy)_2Cl_2]\cdot 2H_2O$ (100.4 mg, 0.165 mmol) was added. The mixture was refluxed under N_2 atmosphere for 3 days. Then it was cooled to room temperature and evaporated under reduce pressure. The crude was purified by cation-exchange chromatography on Spehadex CM-25, using a mixture of $H_2O/(CH_3)_2CO$ 5:3 (v/v) containing NaCl (0.05 M) as eluent. Such NaCl concentration permitted uniquely the elution of the bi-charged species (Os1L or aquo-precursor). Increasing NaCl concentration (0.1 M for Os2L and 0.2 M for Os3L) led to the selective elution of the two other Osmium complexes. Each Os(II) complex was further purified on alumina with DCM/MeOH 9:1 (v/v) as eluent, precipitated with NH_4PF_6 and filtered with water and Et_2O. Additionally, each product was purified by flash chromatography on Sephadex G-10, precipitated in Et_2O and filtered. A green solid was isolated in both cases with a 54% yield for Os2L and 20 % yield for Os3L.

Os2L: ^{1}H NMR (CD_3CN, 400 MHz, 330 K): δ (ppm) 9.64 (s, 2H), 9.59 (s, 1H), 9.02 (d, J^d = 4.4 Hz, 1H), 8.89-8.87 (d, J^d = 8.1 Hz, 2H), 8.81-8.79 (m, 2H), 8.69 (d, J^d = 5.6 Hz, 2H), 8.55-8.53 (d, J^d = 7.0 Hz, 8H), 8.41 (m, 1H), 8.05-7.9 (m, 12H), 7.92-7.91 (d, J^d = 5.1 Hz, 2H), 7.78-7.71 (m, 8H), 7.67-7.65 (t, J^t = 6.3 Hz, 1H), 7.52-7.31 (m, 10H).

Os3L: ^{1}H NMR (CD_3CN, 400 MHz, 330 K): δ (ppm) 9.59 (s, 3H), 9.03-8.94 (d, J^d = 8.1 Hz, 3H), 8.75 (d, J^d = 6.1 Hz, 3H), 8.56-8.48 (m, 12H), 8.11-8.04 (m, 18H), 7.96-7.91 (d, J^d = 5.6 Hz, 3H), 7.73-7.71 (m, 12H), 7.41-7.32 (m, 15H).

$\{[Ru(bpy)_2]_2(\mu\text{-}L)[Os(bpy)_2]\}(PF_6)_6$ (Ru2Os). A round-bottomed flask was charged with cis-$[Os(bpy)_2Cl_2]\cdot H_2O$ (4 mg, 0.00882 mmol) and 4 mL of a solution EtOH/H_2O 3:1 (v/v). There were added $\{[Ru(2,2'\text{-}bpy)_2]_2L\}(PF_6)_4$ (15.1 mg, 0.00738 mmol) and a minimal amount of $AgNO_3$. The mixture was refluxed for 48 h under N_2 atmosphere. Therefore, it was rotary-evaporated and purified on alumina through a gradient elution by $CH_3CN/PhCH_3$ 3:1 (v/v). The eluted complex was precipitated in EtOH and further purified by washing several times with EtOH. Finally, a brown-orange powder is obtained (12.3 mg, 58% yield).

^{1}H NMR (CD_3CN, 400 MHz, 330 K): δ (ppm) 9.62 (s, 3H), 8.93-8.92 (d, J^d = 8.1 Hz, 3H), 8.70-8.69 (d, J^d = 6.1 Hz, 3H), 8.55-8.52 (m, 12H), 8.16-8.04 (m, 18H), 7.84-7.82 (d, J^d = 5.6 Hz, 3H), 7.80-7.74 (m, 12H), 7.49-7.37 (m, 15H). $^{13}C\{^1H\}$NMR (MeCN-d_3,

400 MHz, 330 K): 171.3, 159.7, 157.9, 157.8, 157.7, 157.6, 157.5, 154.0, 152.7, 152.6, 152.5, 143.9, 139.0, 128.9, 128.6, 125.3, 123.5.

{Os[(μ-L)[Ru(bpy)$_2$]$_2$]$_3$}(PF$_6$)$_{14}$ (Ru6Os). A 50 mL round-bottomed flask was charged with 9.29 mg (0.00476 mmol) of {[Ru(bpy)$_2$]$_2$(μ-L)}(PF$_6$)$_4$, 0.77 mg (0.00159 mmol) of K_2OsCl_6 and 1.5 mL of ethylen glycole. The reaction mixture was left stirring under reflux for 48 h, under a N_2 atmosphere. After this time, at room temperature, 5 mL of a saturated solution of $Na_2S_2O_8$ were added. The resulting slurry was filtered over a glass frit. The solid was treated with water several times and at the end with Et_2O. The dried solid was dissolved in the minimum amount (few drops) of acetonitrile and treated with an excess of EtOH and NH_4PF_6. The solid recovered by filtration was washed at least 10 times with ethanol. A further purification was made by flash chromatography on Sephadex G-15. The pure sample was recovered by precipitation in Et_2O, as a violet solid. (yield = 84%).

^{1}H NMR (CD_3CN, 300 MHz, 298 K): δ (ppm) 9.66 (m, 9H), 8.98 -8.69 (m, 16H), 8.68 (s, 9H), 8.53–8.51 (m, 24H), 8.16–8.04 (m, 34 H), 7.90–7.60 (m, 33H), 7.58–7.27 (m, 34H). TOF-SIMS: [M(PF$_6$)$_{13}$]+ = 6188.3368 (theoretical = 6188.3334). Elemental analysis Calc. for $C_{219}H_{159}N_{51}OsRu_6P_{14}F_{84}$: C, 41.62; H, 2.67; N, 11.25; Elemental analysis Found: C, 41.55; H, 2.53; N, 11.28.

N,N'-difluoroboryl-2,8-diethyl-1,3,7,9-tetramethyl-5-(4-octyloxyphenyl)-dipyrrin (BPJ2). Ocytloxybenzaldehyde (240 mL, 1.1 mmol) was dissolved in dry DCM (20 mL). 3-ethyl-2,4-dimethylpyrrole (270 mL, 2.2 mmol) was then added and the mixture was stirred for 30 min. TFA (15 mL, 0.2 mmol) was then added under N_2 atmosphere and the resulting red mixture was stirred overnight. Consumption of the aldehyde was confirmed by TLC (SiO_2, DCM). DDQ (233 mg, 1.0 mmol) was then added and the dark red mixture was stirred for 3.5 h. Dry Et_3N (1.1 mL, 7.0 mmol) was added followed by immediate dropwise addition of $BF_3{\cdot}OEt_3$ (1.15 mL, 7.6 mmol) causing the mixture to change colour to yellow and dark green, respectively. It was stirred overnight under N_2 atmosphere. It was then washed with H_2O (10 mL, three times), dried over anhydrous Na_2SO_4 and rotary-evaporated resulting in a viscous purple oil with green tints. The crude product was then purified by column

chromatography (SiO_2, petrol ether/DCM 50/50, Rf=0.42). Evaporation of the eluent resulted in an orange-red solid with green tints with a 36% yield (181 mg, 0.40 mmol).

^1H NMR (300 MHz, $CDCl_3$): d=7.07 (d, J=9 Hz, 2H, CHAr), 6.91 (d, J=9 Hz, 2H, CH_{Ar}), 3.93 (t, J=6 Hz, 2H, OCH_2), 2.45 (s, 6H, pyrrole-CH_3), 2.22 (q, J=7 Hz, 4H, pyrrole-CH_2-CH_3), 1.80–1.64 (m, 2H, OCH_2-CH_2), 1.47–1.37 (m, OCH_2CH_2-CH_2), 1.33–1.18 (m, 8H, -CH_2-), 1.26 (s, 6H, pyrrole-CH_3), 0.90 (t, J=7.5 Hz, 6H, pyrrole-CH_2-CH_3), 0.82 ppm (t, J=6 Hz, 3H, -CH_3). ^{13}C NMR (300 MHz, $CDCl_3$): d=159.6 (C_{Ar}), 153.4 (C_{Ar}), 140.5 (CAr), 138.5 (C_{Ar}), 132.6 (C_{Ar}), 131.2 (C_{Ar}), 129.8 (C_{Ar}), 129.4 (C_{Ar}), 127.6 (C_{Ar}), 68.2 (O-CH_2-), 31.9 (-CH_2-), 29.5 (-CH_2-), 29.3 (-CH_2-), 26.1 (-CH_2-), 22.7 (-CH_2-), 17.3 (-CH_2-), 17.1 (-CH_3), 14.7 (pyrrole-CH_2-CH_3), 14.2 (pyrrole-CH_2), 12.5 (pyrrole-CH_3), 9.4 ppm (pyrrole-CH_3). HRMS (pNSI) calcd for $C_{31}H_{44}N_2OBF_2$ $[M+H]^+$: 509.3515, found 509.3520.

MCM-41 mesoporous silica with 100% CTAB. Cetyltrimethylammonium bromide (CTAB, 350 mg, 1 mmol) was dissolved in H_2O (180 mL) using an ultrasound bath. 2 M sodium hydroxide (1.3 mL) was then added, causing the cloudy mixture to turn clear. This was heated to 80°C and tetraethylorthosilicate (1.8 mL, 8.2 mmol) was added. The mixture was then stirred under reflux at 80°C for 2 h after which it was filtered under vacuum. The filtrate was washed with H_2O until reaching a neutral pH and dried in an oven overnight. This resulted in a powdery white solid.

MCM-41 nanoparticles with mixed cetyltrimethylammonium bromide (CTAB) and BPJ2 micelles. CTAB and BPJ2 dye were mixed in the following ratios, to achieve the intended dye loadings: 99:1 (0.949 mmol CTAB, 9.6 μmol BPJ2), 95:5 (0.911 mmol CTAB, 48 μmol BPJ2), 92.5:7.5 (0.887 mmol CTAB, 72 μmol BPJ2), 90:10 (0.863 mmol CTAB, 96 μmol BPJ2), 80:20 (0.767 μmol CTAB, 0.192 μmol BPJ2) and 50:50 (0.167 mmol CTAB, 0.167 μmol BPJ2). CTAB was dissolved in H_2O (100 mL), while, in parallel, BPJ2 was dissolved in a minimum amount of acetonitrile and transferred in H_2O (80 mL) resulting in a homogeneous turbid pink-orange mixture. Once the CTAB had dissolved with use of an ultrasound bath, the BPJ2 in acetonitrile/H_2O was added. This was stirred before addition of 2 M NaOH (1.3 mL,

2.6 mmol), which did not result in the mixture clarifying. It was then heated to 80°C at which point tetraethyl orthosilicate (1.7 g, 1.8 mL, 8.2 mmol) was added. The mixture was then refluxed in the dark at 80°C for 2.5 h before being filtered under vacuum and washed with H_2O until the filtered solution was neutralised. A small amount of BODIPY could be seen in the filtered solutions. The filtrate was dried in an oven resulting in powdery solids with colours from pale yellow (99:1), to pink (95:5, 92.5:7.5, 90:10 and 80:20), to red (50:50) that fluoresced under UV light.

MCM-41 nanoparticles loaded with PS1. CTAB and PS1 were mixed in the following ratios, to achieve the intended dye loadings: 99:1 (0.949 mmol CTAB, 9.6 μmol PS1), 95:5 (0.911 mmol CTAB, 48 μmol PS1) and 90:10 (0.863 mmol CTAB, 96 μmol PS1). CTAB was dissolved in H_2O (100 mL), while, in parallel, PS1 was dissolved in a minimum amount of acetonitrile and transferred in H_2O (80 mL) resulting in a homogeneous turbid yellow mixture. Once the CTAB had dissolved with use of an ultrasound bath, the PS1 in acetonitrile/H_2O was added. This was stirred before addition of 2 M NaOH (1.3 mL, 2.6 mmol), which did not result in the mixture clarifying. It was then heated to 80°C at which point tetraethyl orthosilicate (1.7 g, 1.8 mL, 8.2 mmol) was added. The mixture was then refluxed in the dark at 80°C for 2.5 h before being filtered under vacuum and washed with H_2O until the filtered solution was neutralised. A small amount of PS1 could be seen in the filtered solutions. The obtained powder was dried at room temperature.

MCM-41 nanoparticles loaded with PS1 and BPJ2. CTAB, PS1 and BPJ2 were mixed in the following ratios, to achieve the intended dye loadings: 98:1:1 (0.939 mmol CTAB, 9.6 μmol PS1, 9.6 μmol BPJ2), 90:5:5 (0.863 mmol CTAB, 48 μmol PS1, 48 μmol BPJ2), 80:10:10 (0.767 mmol CTAB, 96 μmol PS1, 96 μmol BPJ2) and 89:10:1 (0.852 mmol CTAB, 96 μmol PS1, 9.6 μmol BPJ2). CTAB was dissolved in H_2O (100 mL), while, in parallel, both PS1 and BPJ2 were dissolved separately in a minimum amount of acetonitrile and transferred in H_2O (40 mL each) resulting in homogeneous turbid mixtures. Once the CTAB had dissolved with use of an ultrasound bath, the PS1 and BPJ2 in acetonitrile/H_2O were added. This was stirred before addition of 2 M NaOH (1.3 mL, 2.6 mmol), which did not result in the mixture clarifying. It was then heated to 80°C at which point tetraethyl orthosilicate (1.7 g, 1.8 mL, 8.2 mmol) was

added. The mixture was then refluxed in the dark at 80°C for 2.5 h before being filtered under vacuum and washed with H_2O until the filtered solution was neutralised. The obtained powder was dried at room temperature.

MCM-41 nanoparticles loaded with MV and BPJ2. CTAB, MV (as PF_6^- salt) and BPJ2 were mixed in an 89:10:1 ratio (0.852 mmol CTAB, 96 μmol MV, 9.6 μmol BPJ2). CTAB was dissolved in H_2O (100 mL), while, in parallel, both MV and BPJ2 were dissolved separately in a minimum amount of acetonitrile and transferred in H_2O (40 mL each) resulting in homogeneous turbid mixtures. Once the CTAB had dissolved with use of an ultrasound bath, the MV and BPJ2 in acetonitrile/H_2O were added. This was stirred before addition of 2 M NaOH (1.3 mL, 2.6 mmol), which did not result in the mixture clarifying. It was then heated to 80°C at which point tetraethyl orthosilicate (1.7 g, 1.8 mL, 8.2 mmol) was added. The mixture was then refluxed in the dark at 80°C for 2.5 h before being filtered under vacuum and washed with H_2O until the filtered solution was neutralised. The obtained powder was dried at room temperature.

4-Methyl-4'-[2-(1-pyrenyl)ethyl]-2,2'-bipyridine (bpy-pyr). 4,4'-Dimethyl-2,2'-bipyridine (0.50 g, 2.71 mmol) was dissolved in dry THF (40 mL) under a N_2 atmosphere. After cooling to –10°C, lithium diisopropylamide (1.2 mL) was added dropwise over a 5 min. period. After stirring for an additional 45 min., a solution of 1-(chloromethyl)pyrene (0.48 g, 1.92 mmol) in THF (25 mL) was introduced dropwise. The reaction mixture was stirred at –10°C for 30 min, and then allowed to warm to ambient temperature and reacted for a further 20 h. After this time, water (5 mL) was added dropwise and solvents were removed under reduced pressure. The residue was then dissolved in dichloromethane and washed with water. The separated organic phase was dried over magnesium sulfate, filtered and the solvent was removed. The residue was then triturated with MeOH : H_2O, 4:1 (v/v) (20 mL). The resulting solid was collected and then triturated with methanol (25 ml). The product, which was collected by filtration and dried under vacuum, was an off-white powder. (yield = 63%).

^{1}H NMR ($CDCl_3$): d 8.58-8.55 (m, 2H), 8.40-7.81 (m, 11H), 7.17-7.10 (m, 2H), 3.73 (t, 2H, J = 8 Hz), 3.26 (t, 2H, J = 8 Hz), 2.45 (s, 3H). Elemental analysis data (for

$C_{29}H_{22}N_2$), calc. (found): C, 87.40 (87.28); H, 5.57 (5.59); N, 7.03% (6.99%). MS (FAB): m/z 398.

[Ru(2,2'-bipyridine)$_2$(bpy-pyr)](PF$_6$)$_2$ (Ru-1P). The synthesis was optimised modifying methodology reported in previous work.[4] Ru(2,2'-bipyridine)$_2$Cl$_2$ (0.23 mmol) and bpy-pyr (0.25 mmol) were suspended in methanol (30mL) and refluxed for 24 h while stirring under nitrogen, before cooling the reaction mixture to room temperature. Solid NH_4PF_6 was added and stirring was continued for 30 min. The precipitate formed was collected by filtration through a fine glass frit and washed with water, followed by diethyl ether to afford the crude orange product. The product was purified by chromatography, eluting with MeCN : toluene 2:1 (v/v). The complex was further purified through Sephadex G-10, eluting with acetonitrile, before reprecipitating from acetonitrile/toluene.

MCM-41 nanoparticles loaded with Ru-1P. CTAB and Ru-1P (as PF_6^- salt were mixed in an 90:10 ratio (26 μmol CTAB, 2.93 μmol Ru-1P). CTAB was dissolved in H_2O (3 mL), while, in parallel, Ru-1P was dissolved in a minimum amount of acetonitrile and transferred in H_2O (2.5 mL) resulting in a homogeneous turbid orange mixture. Once the CTAB had dissolved with use of an ultrasound bath, the Ru-1P in acetonitrile/H_2O was added. This was stirred before addition of 2 M NaOH (40 μL, 79.5 μmol), which did not result in the mixture clarifying. It was then heated to 80°C at which point tetraethyl orthosilicate (52 mg, 55 μL, 250 μmol) was added. The mixture was then refluxed in the dark at 80°C for 2.5 h before being filtered under vacuum and washed with H_2O until the filtered solution was neutralised. The powder was centrifuged several times with acetonitrile (10 000 rpm for 5 minutes) and dried at room temperature.

Mesoporous silica spheres (MSS). CTAB (0.47 g, 1.29 mmol) as surfactant and urea (0.93 g, 0.015 mole) were first added into deionised water (27 mL). Then, a mixture containing 18.6 mL cyclohexane, 4 mL TEOS, and 0.86 mL of isopropyl alcohol was added. The solution was first stirred at 300 rpm under room temperature and then heated to 70°C in an oil bath with constant stirring at 300 rpm. After a

reaction time of 42 h, the solution turned into milky white color and the product was collected by centrifugation, washed with ethanol for three times and dried at 60°C overnight. Finally, the solid was obtained after calcination at 550°C for 6 h (1.056 g).

MSS loaded with Ru-1P. Ru-1P (1.36 mg, 1.56 μmol) was dissolved in ethanol (3 mL). MSS (30.7 mg) were then added to the solution and such mixture was stirred for 45 h in the dark. Therefore, the product was collected by centrifugation, washed with acetonitrile several times. The obtained orange powder was dried at room temperature.

Iridium oxide (IrO_x) nanoparticles. IrO_x nanoparticles were prepared via a photochemical hydrolysis approach. An aqueous solution of 2 mM $IrCl_3$ was prepared in a beaker, and the pH of solution was adjusted to 12 with concentrated KOH. Then, the beaker was placed under light irradiation (390 nm, 5 mW/cm^2). During photochemical synthesis, the reaction system was kept at room temperature by a circulating water bath. The UV light was generated from 390 nm LED with 5 mW/cm^2 power. During irradiation, the colour of the solution changed from clear yellow to dark blue. The reaction was monitored by UV/Vis spectra recorded at fixed time intervals.

MSS with IrO_x nanoparticles trapped inside. Reaction to obtain IrO_x nanoparticles was done in presence of MSS. In an aqueous solution (2 mL) of 2 mM $IrCl_3$ (pH = 12) MSS (9.7 mg) were added and such suspension was placed stirring under light irradiation (390 nm, 5 mW/cm^2) for 24 h. During irradiation, the colour of the suspension changed from clear yellow to dark blue. Then, the solid was collected by centrifugation, washing several times with water.

EC.3 Supplemental Ru6Os characterisations

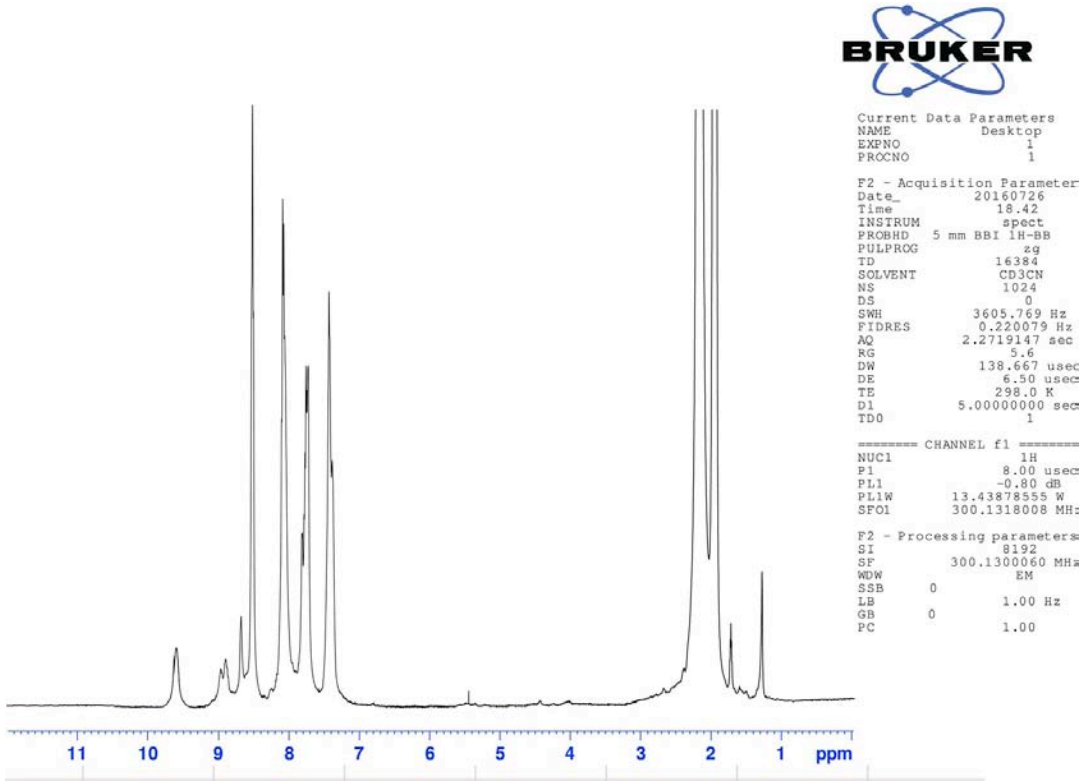

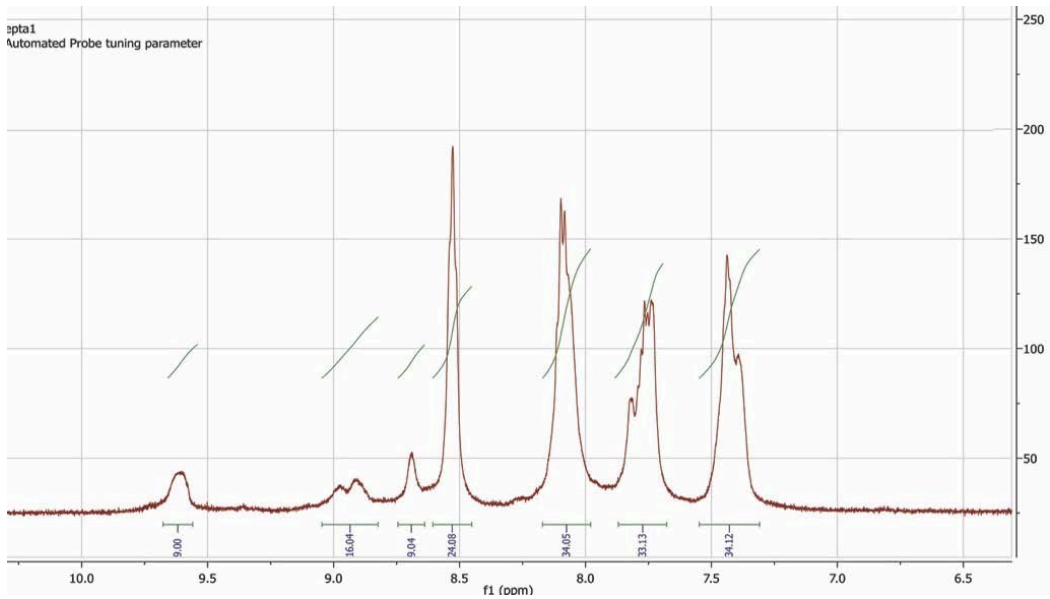

Figure E1 *^{1}H NMR spectrum of **Ru6Os** in CD_3CN, range 0-12 ppm (top). In the bottom, the range 7-10 is expanded and peak integrations are shown.*

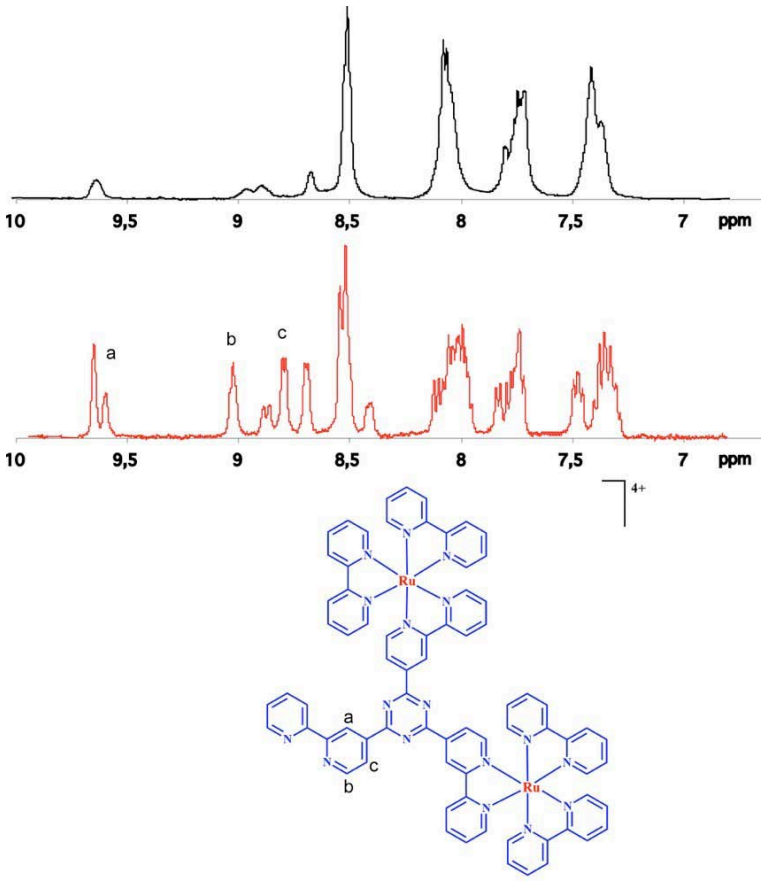

Figure E2 *^{1}H NMR spectra of **Ru6Os** (top) and of the precursor [[Ru(bpy)$_2$]$_2$(μ-L)](PF$_6$)$_4$ (bottom) in CD$_3$CN.*

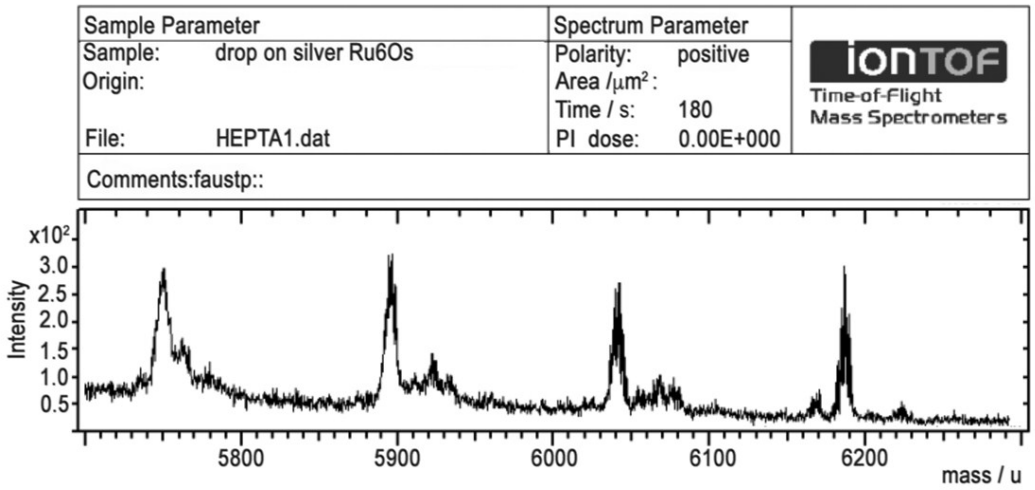

Figure E3 *TOF-SIMS spectrum of **Ru6Os** (range 5700 – 6300).*

References

1) J. N. Demas and G. A. Crosby, *J. Phys. Chem.*, **1971**, 75, 991.

2) N. Nakamaru, *Bull. Chem. Soc. Jpn.*, **1982**, 55, 2697.

3) J. D. McGhee, P. H. von Hippel, *J. Mol. Biol.*, **1974**, 86, 469.

4) N. D. McClenaghan, F. Barigelletti, B. Maubert, S. Campagna, *Chem. Commun.*, **2002**, 0, 602-603.